

Genesis and evolution of a Neoproterozoic magmatic arc: the cordilleran-type granitoids of the Araçuaí Belt, Brazil

by
Francesco Narduzzi

Dissertation presented for the joint-Degree of Doctor of Geology in the Faculty of Science at Stellenbosch University (South Africa) and Universidade Federal de Ouro Preto (Brazil)



Supervisor: Prof. Herminio Arias Nalini Jr.
Co-supervisor: Dr. Federico Farina
Co-supervisor: Prof. Cristiano de Carvalho Lana
Co-supervisor: Prof. Gary Stevens

UNIVERSITEIT
iYUNIVESITHI
STELLENBOSCH
UNIVERSITY

100
December 2018

Declaration

By submitting this dissertation electronically, I declare that the entirety of the work contained therein is my own, original work, that I am the sole author thereof (save to the extent explicitly otherwise stated), that reproduction and publication thereof by Stellenbosch University will not infringe any third party rights and that I have not previously in its entirety or in part submitted it for obtaining any qualification. This dissertation has also been presented at Universidade Federal de Ouro Preto in terms of a joint-/double-degree agreement.

Signature:
Francesco Narduzzi

Date:
December 2018

Copyright © 2018 Stellenbosch University

All rights reserved

ABSTRACT

The Araçuaí orogen (SE Brazil) is one of the largest (350,000 km²) and long-lived (ca. 630 – 480 Ma) granitic province in the world. Its wide variety of granitoids recording mid- to lower crustal P - T conditions allow direct investigation of petrological processes occurring in the deepest part of the continental crust. This study investigates the field, textural, geochemical, geochronological and isotopic evolution of the pre-collisional Galiléia Batholith (ca. 15,000 km²) outcropping in the central part of the Araçuaí orogen. This weakly foliated Neoproterozoic (ca. 632–550 Ma), metaluminous to slightly metaluminous (ASI = 0.97–1.07), calc-alkaline granitoid body is characterized by the widespread occurrence of grossular-rich garnet and epidote. This is a rare mineral association in Cordilleran-I-type granitoids and of special petrogenetic significance. Field, petrographic, and mineral chemistry evidence indicate that garnet, epidote, biotite as well as white mica crystals (low-Si phengite), are magmatic. There is no difference in bulk rock major and trace element composition between the Galiléia and other garnet-free cordilleran-type granitoids worldwide. The uncommon garnet+epidote parageneses are related to the pressure, temperature and water content conditions of magma crystallization. Comparison with the mineral assemblages and mineral compositions obtained from crystallization experiments from garnet-bearing metaluminous calc-alkaline magmas, indicates that the supersolidus coexistence of grossular-rich garnet, epidote and white mica is consistent with crystallization at pressures greater than 0.8 GPa (above 25 km depth). This shows that the Galiléia batholith was assembled in the lower crust during the accretionary/collisional stages of the Neoproterozoic Brasiliano Orogeny. However, the lifetime of deep magma chambers and the duration of magmatic activity in them remains a puzzle, contrary to young upper crustal magmatic systems. Despite being homogeneous with respect to mineralogy/texture and major/trace elements, all samples from the central part of the batholith record extreme variability in U-Pb magmatic ages from ca. 630 to 555 Ma. Trace element geochemistry and Hf isotopes from the igneous zircons – here interpreted as autocrysts (ca. 555 – 560 Ma) and antecrysts (> 560 Ma) – are all consistent with an open-system crystallization, rather than a simple cooling following fractional crystallization at the level of magma emplacement. We interpret the age variability as the result of a long-lived, uninterrupted injection of compositionally similar magmas in the lower crust during the batholith assembling. These conditions kept the system above its solidus through the 80 Ma of zircon crystallization. Unradiogenic ¹⁷⁶Hf/¹⁷⁷Hf and ¹⁴³Nd/¹⁴⁴Nd isotopic values of the Galiléia samples indicate no direct mixing with mantle-derived magmas. This explains the scarcity of mafic products in the region. Mineral textural, geochronological and isotopic similarities with other younger and older granitic plutons constructed

within accretionary / fore-arc settings, better explain the characteristics showed by the Galiléia granitoids. Thus it is suggested that this giant batholith was assembled in an accretionary prism during the Brasiliano Orogenic stages. Eventually, it is likely that during the Brasiliano/Pan-African orogeny, accretionary prism, fore- and back-arc setting were sites of voluminous silicic magmatism and commonplaces for the stabilization of continental crust and its differentiation.

RESUMO

O orógeno Araçuaí (sudeste do Brasil), é uma das maiores províncias graníticas (ca. 350,000 km²) de longa duração (ca. 630 – 480 Ma) do mundo. A sua ampla variedade de granitoides que registram condições de P e T de crosta média a inferior permitem a investigação direta de processos petrológicos que ocorrem na crosta inferior continental. Através de estudos de campo, texturais, geoquímicos, geocronológicos e isotópicos o presente estudo investiga a evolução do batólito Galiléia (ca. 15,000 km²) aflorante na parte central do Orógeno Araçuaí. Este batólito fracamente foliado, Neoproterozoico (ca. 630 – 550 Ma), metaluminoso a levemente peraluminoso (ASI = 0.97 – 1.07) e calcio-alcálico, é caracterizado pela ocorrência de granada grossulária e epidoto. Esta associação mineralógica em granitoides cordilheiranos tipo I é rara e de grande significado petrológico. Evidências de campo, texturais e de química mineral indicam que granada, epidoto, biotita e também mica branca (fengita de baixo silício) são minerais magmáticos. Os elementos maiores e traços dos granitoides Galiléia não mostram diferenças composicionais quando comparados com granitos cordilheiranos sem granada descritos no mundo. Isso sugere que a paragênese granada+epidoto esteja relacionada às condições de pressão, temperatura e teor de água do magma cristalizante. Comparações com as assembleias e composições dos minerais produzidas durante experimentos de cristalização que utilizam magmas calcio-alcálicos metaluminosos com granada magmática, indicam que a existência de granada enriquecida em grossulária, epidoto e mica branca está relacionada a uma cristalização sob pressões superiores a 0.8 GPa (acima de 25 km de profundidade). Estas evidências mostram que o batólito Galiléia foi construído na crosta profunda durante os estágios de acreção e colisão do Ciclo Orogenético Brasileiro (Neoproterozoico). Contudo, ao contrário dos sistemas magmáticos jovens de crosta superior, tanto o tempo de vida quanto a duração da atividade magmática das câmaras magmáticas profundas permanecem um enigma. Apesar de ser homogêneo em relação a mineralogia/textura e elementos maiores/traços, todas as amostras da parte central do batólito registram uma extrema variabilidade nas idades magmáticas U-Pb, de aproximadamente 630 Ma até 550 Ma. Elementos traços e isótopos de Hf em zircões magmáticos – aqui interpretados como *auto-cristais* (ca. 555 – 560 Ma) e *ante-cristais* (> 560 Ma) – são consistentes com um processo de cristalização em sistema aberto, ao invés de um simples processo de resfriamento e cristalização fracionada no nível da colocação do magma. A variabilidade de idades é interpretada como resultado de uma prolongada e ininterrupta injeção de magmas de composição similar na crosta inferior ao longo da construção do batólito. Tudo isso, manteve o sistema acima do solidus durante 80 Ma de contínua cristalização de zircão. Os valores não radiogênicos dos isótopos de ¹⁷⁶Hf/¹⁷⁷Hf e ¹⁴³Nd/¹⁴⁴Nd das amostras evidenciam que não houve mistura com magmas de manto. Isso explicaria a carência de magmas máficos na área. As

semelhanças minerais, geocronológicas e isotópicas com outros plutons graníticos mais novos e/ou mais velhos construídos dentro de prismas acrecionários / bacias de antearco e retroarco, explicam melhor as características mostradas pelos granitos Galiléia. Assim, sugere-se que este batólito foi edificado em um prisma de acreção durante os estágios orogênicos Brasilianos. Enfim, é provável que ao longo das orogenias Brasilana/Pan-Africana, prismas acrecionários, bacias de antearco e retroarco se comportaram como sítios de geração de grandes volumes de magmas silicáticos, e estabilização e diferenciação da crosta continental.

ACKNOWLEDGEMENTS

Let me start to express my special thanks to my supervisors Prof. Dr. Herminio Arias Nalini Jr., Dr. Federico Farina and Prof. Dr. Cristiano Lana, who four years ago trusted and gave to me this incredible opportunity. You have been a tremendous example to follow and together with your advice in these years, I grew as a researcher. Most of all, your encouragement even during “not-happy periods” were simply priceless.

I would like to express my acknowledgements also to my other supervisor, Prof. Dr. Gary Stevens for its important suggestions, comments and scientific challenges that helped me along this thesis. My appreciation goes also to Prof. Dr. Fernando Alkmim for his kindness and important insights into the geology of the Araçuaí Orogen, and to Prof. Dr. Leonardo Gonçalves that helped me in the first part of this thesis.

If I am here, if I grew up as a man but especially if *virei o gringo mais Brasileiro de Ouro Preto (e também mais de Chimarrão)* is only because I was lucky to meet so many Important Friends which never abandoned me. My profound thanks are for: Marcha, Samuel, Camila, Alice, Marcus, Cris, Ana, Teodoro, Federico, André, GLeo, Chimarrão, Marilane, Stefano, Bacana, Ricardo, Paolo, Carmen Aguilar, Carmen Martinez, Lorena, Livia, Maria-Eugenia, Ramon, Taynara, Paula, Debora, Mathias, Hugo, Rosana Tako, Camila Schuch, Fabiana, Ariela, Maristela, Max, Glauçia, Marco, Edgar Daiana and Capucine. Please forgive me if have forgot someone.

My life in Brazil was a great time also because I have splendid friends in Italy, with whom I had so many fun and were always ready to support me. I will be forever in debt with Luca, Sula, Mattia, Alessia, Glenda, Arianna, Sandro, Pav, Daniela, Stefania, Elena, Michele, Willy e Elisa.

Eventually, there are three persons in my life that I must acknowledge the most. Long time ago when I have decided to leave my small hometown Martignacco, it has was a big heart-breaking moment for them because they understood that they could see me only one month or less, per year. Mum, Dad and Fede, if I am here, I have reached this goal is also your merit. Even across the billions of Skype-calls that we have had in order to make smaller our distance, you were able to make feel as I have never left home. I believe that no word can express how grateful I am.

I would like to express my gratitude also to my uncles and cousins that never stop thinking about me. Thanks a lot!

TABLE OF CONTENTS

Declaration	i
Abstract	ii
Resumo	iv
Acknowledgments	vi
Table of contents	vii
List of figures	ix
List of tables	xi
1. Introduction	1
1.1 - I-type, or cordilleran I-type granitoids?	1
1.1.1 - Generalities.....	1
1.1.2 - Garnets and epidotes in I-type rocks	2
1.1.3 - Two main geochemical models for the I-type granitogenesis	4
<i>1.1.3.1 - The mantle - crustal magma mixing model</i>	4
<i>1.1.3.2 - The peritectic entrainment model</i>	6
1.2 - Aims of the project	7
1.3 - Localization of the study area.....	9
1.4 - Methods	10
1.4.1 - Literature review	10
1.4.2 - Field work.....	11
1.4.3 - Sample analyses.....	12
<i>1.4.3.1 - Thin sections</i>	12
<i>1.4.3.2 - Mineral chemistry and whole rock geochemistry</i>	12
<i>1.4.3.3 - U-Pb geochronology</i>	13
<i>1.4.3.4 - Lu-Hf method</i>	13
<i>1.4.3.5 - Oxygen isotopes</i>	13
1.4.4 - Scientific contributions and future works.....	13
1.5 - Structure of the thesis	14
2. The geology of the Araçuaí-West Congo Orogenic belt	24
2.1 - General geology	24
2.2 - Architecture of the Araçuaí orogen	25
2.3 - Overview of the stratigraphy of the Araçuaí orogen	29
2.3.1 - The basement of the Araçuaí Orogen.....	29
2.3.2 - Late Paleoproterozoic to Mesoproterozoic sequences.....	30
2.3.3 - Neoproterozoic rift-related rock successions.....	31
2.3.4 - Neoproterozoic pre- and orogenic-related rock units	33
<i>2.3.4.1 - The Rio Doce metasedimentary Group</i>	34

2.3.4.2 - <i>The Jequitinhonha and Nova Venecia complexes</i>	36
2.4 - Geodynamic evolution of the Araçuaí orogenic belt.....	36
2.4.1 - The Nutcracker model.....	37
2.4.2 - The Araçuaí ensialic belt	39
2.4.3 - The Araçuaí Hot Orogen: deformation in a pervasively molten middle crust?.....	34
2.4.3.1 - <i>The partially molten Araçuaí Crystalline Core</i>	41
2.4.3.2 - <i>The Central Plutonic Unit</i>	41
2.4.3.3 - <i>An almost ensialic Neoproterozoic Orogen</i>	42
3. The granitoids of the G1 Supersuite - a state of the art	51
3.1 - Generalities.....	51
3.2 - The Galiléia and São Vitor batholiths	53
3.2.1 - Brief geochronologic review	53
3.2.2 - São Vitor and Galiléia field relationships.....	57
3.2.3 - Mafic enclave abundance as a tool for subdividing the Galiléia batholith in different intrusive suites	59
3.2.4 - Micro-textural features of the São Vitor and Galiléia granitoids	59
3.2.5 - Mineral chemical review	62
3.2.6 - Whole rock geochemistry	64
3.3 - The São Vitor and Galiléia granitoids and cordilleran-type granitoids.....	69
3.3.1 - Petrogenetic models for the G1 EGT and GT plutonic rocks and tectonic implications	76
4. Magmatic garnets in cordilleran-type Galiléia granitoids of the Araçuaí belt (Brazil): evidence for crystallization in the lower crust	84
5. Extreme U-Pb age variability in a Neoproterozoic, lower crustal batholith: implications for magma storage in an accretionary prism	100
6. Conclusions	128
6.1 - Genesis and evolution of a Neoproterozoic magmatic arc: the cordilleran-type granitoids of the Araçuaí belt, Brazil.....	128
APPENDICES	132
Appendix A - Supplementary material of the manuscript presente in the chapter 4	133
Appendix B - Supplementary material of the manuscript presente in the chapter 5	162
Appendix C - Abstract to conferences	233

LIST OF FIGURES

Figure 1.1. - Experimental pressure and temperature field stability for garnet and epidote crystallizing from metaluminous magmas	3
Figure 1.2. - Example of $^{87}\text{Sr}/^{86}\text{Sr}$ vs. $^{143}\text{Nd}/^{144}\text{Nd}$ mantle-crust hybrid signature shown by some South American Cordilleran I-type batholiths.....	6
Figure 1.3. - Map with the localization of the main road used to get in the study area. Modified from Google maps.....	10
Figure 2.1. - The Araçuaí-West Congo Orogen.	25
Figure 2.2. - The Araçuaí Orogen.....	26
Figure 2.3. - Structural domains of the Araçuaí-West Congo Orogen..	29
Figure 2.4. - Stratigraphic column for the Espinhaço Supergroup in the Araçuaí belt.....	31
Figure 2.5. - Stratigraphic succession for the Neoproterozoic rift-related, pre-and orogenic-related rocks units.	33
Figure 2.6. - Palinspastic reconstruction of the Nutcracker model for the AWC orogen.....	38
Figure 2.7. - E-W schematic cross section of the Araçuaí belt in which are shown the three domains... ..	40
Figure 2.8. - Map showing structural (left) and AMS (right) measurements within central unit.	43
Figure 2.9. - 3D diagram showing the structural interpretation of the central plutonic unit.	43
Figure 3.1. - Simplified map of the Araçuaí Orogen... ..	52
Figure 3.2. - U-Pb ages distribution histograms for the Rio Doce Arc.	56
Figure 3.3. - Typical appearance of the Galiléia batholiths in the field.....	57
Figure 3.4. - Petrographic features of Galiléia and São Vitor granitoids.	61
Figure 3.5. - Main discrimination geochemical diagrams..	66
Figure 3.6. - Major (K_2O and CaO) and trace elements (V, Ni, Rb and Sr) against SiO_2	67
Figure 3.7. - Map showing the location of the Cordilleran I-Type Batholiths	69
Figure 3.8. - $\text{K}_2\text{O}/\text{Na}_2\text{O}$ vs SiO_2	71
Figure 3.9. - (A/CNK) vs $(\text{Fe}+\text{Mg})$	72
Figure 3.10. - MALI vs SiO_2 for granitoid rocks.....	73
Figure 3.11. - Fe^* vs SiO_2 diagram to discriminate between ferroan and magnesium granitoids.....	74
Figure 3.12. - MgO vs SiO_2	75

LIST OF FIGURES IN ATTACHED PUBLICATIONS

Figure 4.1. - Schematic geological map of the Araçuaí Orogen and Galiléia granitoids... ..	86
Figure 4.2. - Field features of the Galiléia granitoids.....	87
Figure 4.3. - Garnet and mafic enclave counting.....	88
Figure 4.4. - Garnet field relationships.....	89
Figure 4.5. - Garnet petrography	90
Figure 4.6. – General petrography.....	91
Figure 4.7. - Garnet chemical maps and profiles.....	92

Figure 4.8. - Mineral chemistry.....	93
Figure 4.9. - Whole rock geochemistry.....	94
Figure 4.10. – CaO against MnO wt.%.....	95
Figure 4.11. – Comparison between Galiléia, experimental and natural magmatic garnets.....	96
Figure 4.12. – A/CNK vs. FeO _{Tot} + MgO diagram.....	96
Figure 5.1. – Comparison of duration of magmatism from different ages and tectonic settings.....	103
Figure 5.2. – The Araçuí Orogen and the Galiléia granitoids.....	105
Figure 5.3. – Hacker diagrams.....	106
Figure 5.4. – Cathodoluminescence images of the Galiléia zircons.....	109
Figure 5.5. – Concordia diagrams and weighted mean plots of LA-SF-ICP-MS dating.....	110
Figure 5.6. – Weighted mean plots for the two high-precision multi-collector dated samples.....	111
Figure 5.7. – a) Comparison between concordia diagrams from high-precision and LA-SC-ICP-MS date. b) Density plot diagram showing for the MC dates.....	112
Figure 5.8 – Hf isotopes analyses vs. SF ²⁰⁶ Pb/ ²³⁸ U dates.....	113
Figure 5.9. – Zircon trace elements vs. high-precision multi collector dates.....	114
Figure 5.10. – Accretionary prism evolutionary model for the Galiléia granitoids.....	118

LIST OF TABLES

Table 3.1.- Table showing the location coordinates (UTM), granitoid ages for the central area of the Galiléia Batholith and methodology implied.54

LIST OF TABLES ATTACHED TO PUBLICATIONS

Table 5.1.- Summary of the grossular, pyrope, almandine and spessartine content in mol.% of magmatic garnets in metaluminous to slightly peraluminous natural granitoids and experimental melts.....92

CHAPTER 1

INTRODUCTION

1.1 - I-TYPE, OR CORDILLERAN I-TYPE GRANITOIDS?

1.1.1 – Generalities

The major components of Earth's continental crust are granitic and silicic rocks which can occur in different tectonic setting. One of the biggest and still on-going debates in granite petrology is what process(es) govern the granitoid geochemical variability and thus their mineralogical assemblage (Clemens *et al.*, 2011). In the 1970's Chappell & White, (1974) recognized two groups of granitoids in the Lachlan Fold Belt, eastern Australia. They suggested that one group was derived from the partial melting of (meta)sedimentary protoliths while a different one was formed by the reworking of (meta)igneous rocks. Then the suffix I and S was meant as indication of the type of the source generating these silicic magmas: I for igneous and S for sedimentary-derived.

I-type granites are mainly composed of granodiorites and tonalites, with subordinate amounts of granites *sensu strictu* (Roberts & Clemens, 1993). Between the possible granitoid types defined in the literature (Chappell & White, 1974; Frost *et al.*, 2001; Brown, 2013), these granites are by far the most voluminous. Because I-type granitoids are mostly found in arc settings, where both silicic and mafic magmas can have juvenile signature, I-type granites are therefore considered to be the main crust-forming component (i.e., Castro *et al.*, 2010 and references therein). They form small plutons to big batholiths commonly containing variable amounts of magmatic enclaves, metasedimentary xenoliths and closely associated with volcanic rocks, typically andesites and rhyolites.

In thin section the mafic mineral assemblage of I-type granites are composed by low Al-biotite \pm hornblende and more rarely clinopyroxene. K-feldspar is generally less abundant, and with quartz, it is usually one of the last to crystallize. An-rich plagioclase (An > 70 mol.%) can be present. Accessory minerals are zircon, allanite, titanite, epidote and sometimes magnetite (Kemp and Hawkesworth, 2004; Clemens *et al.*, 2011). These granitoids are slightly peraluminous to metaluminous (Clemens *et al.*, 2011) with SiO₂ content ranging from 50 up to ca. 77 wt.%, with a low K₂O/Na₂O ratio (< 1), although some also have high K₂O content (ca. > 2 wt.%; Roberts & Clemens, 1993; Clemens *et al.*, 2009).

In contrast, S-type granitoids are recognized by the stable presence of garnet and cordierite (anhydrous Al-rich ferromagnesian silicate phases), muscovite and Al-rich biotite in the major rock-forming minerals. Accessory minerals are mostly zircon, monazite and ilmenite. In S-type granites, the SiO₂ content is more restricted (64 – 77 wt.%) and the K₂O/Na₂O ratio is high, above 1. Moreover, I-type granitoids generally have the tendency to not carry inherited zircons as it is generally seen for S-type rocks. Importantly, as noted by Clemens *et al.* (2011), igneous-derived granites *sensu lato* have A/CNK (Al/2Ca+Na+K in mol.%; Alumina Saturation Index) and CaO content showing negative and positive correlation with maficity index (FeO_{Tot} + MgO wt.%), respectively. The opposite is shown by S-type granites *sensu lato*.

1.1.2 Garnet and epidote in metaluminous magmatic rocks

It is widely accepted that the main difference between S- and I-type granites is the higher A/CNK index of the S-type rocks. This is due to the presence of garnet and/or cordierite as stable mafic minerals. In contrast, I-type granites, being slightly peraluminous to metaluminous, are characterized by having stable biotite and hornblende (\pm clinopyroxene). However, in rare cases, this mineralogical classification between I- and S-type rocks is not valid. In fact Green & Ringwood (1968), Green (1972; 1977; 1992), Evans & Vance (1987), Dawes & Evans (1991), Day *et al.* (1992), Schmidt (1993), Schmidt & Thompson (1996), Harangi *et al.* (2001), Barnes & Allen (2006), Alonso-Perez *et al.* (2009), Bach *et al.* (2012) and Samadi *et al.* (2014) have shown that metaluminous silicic plutonic rocks and their volcanic equivalents can contain garnet. The occurrence of Al-silicate mineral in Al₂O₃-poor rocks is quite rare because requires specific and restricted conditions.

Crystallization experiments (Green & Ringwood 1968; Green 1972, 1977, 1992; Harangi *et al.*, 2001) have shown that garnet is stable when the magma crystallizes at high pressure condition, usually above 0.8 GPa (Fig. 1.1). The high CaO content in garnet is taken as indication of high pressure (> 0.8 GPa) crystallization because plagioclase breaks down at pressure > 0.8 GPa liberating CaO which is accommodated within garnet. Such high CaO content in garnet is also taken as indication that the magma was at high water content (5 – 10 wt.% H₂O), implying then low crystallization temperatures. Indeed, Alonso-Perez *et al.* (2009) found a correlation between water content dissolved in the melt, garnet CaO content and T of crystallization. That is, as the crystallization temperatures decreases and water dissolved in the magma increases, garnet became more FeO- and CaO-rich, but depleted in MgO.

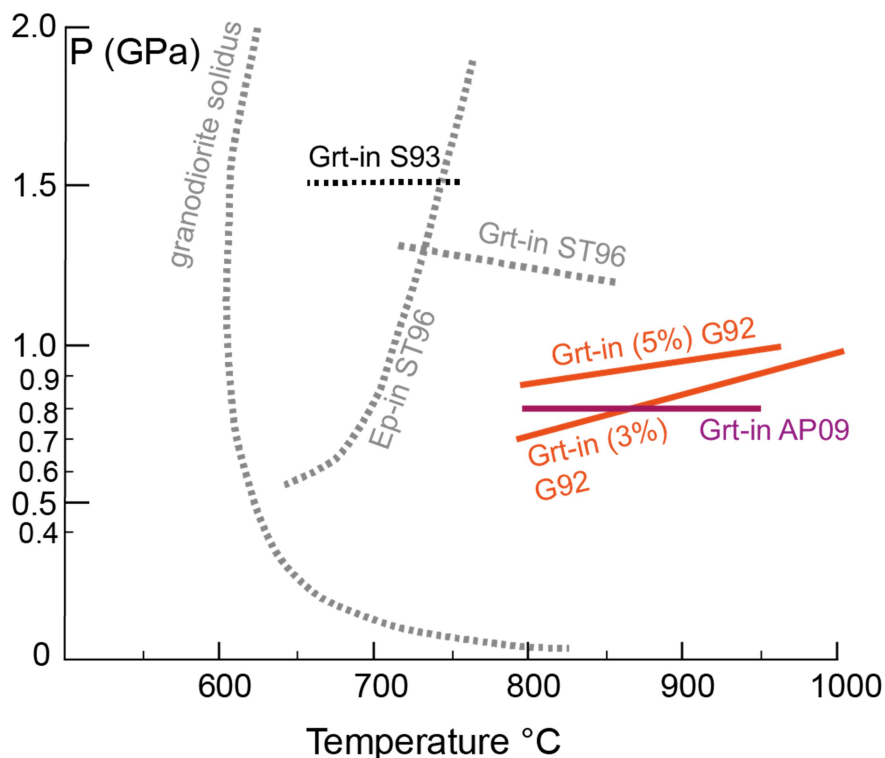


Figure 1.1. Experimental pressure and temperature field stability for garnet and epidote crystallizing from metaluminous magmas. Grt: garnet; Ep: epidote. 3% and 5% in G92 indicate that water was added at the experimental starting material. G92: Green (1992); S93: Schmidt (1993); ST96: Schmidt & Thompson, (1996); AP09: Alonso-Perez *et al.* (2009).

Within the range of 5 to 10 wt.% H₂O content, granitic magmas are also able to crystallize another accessory mineral phase, epidote. It is widely recognized (Zen & Hammarstrom, 1984a, 1984b; Zen, 1985; Schmidt & Thompson, 1996) that epidote in silicic melts crystallizes as last mineral, and only at determined pressure, that is, above 0.6 GPa. Thus the lack of epidote is able to give important indications about the final depth of magma emplacement and crystallisation. However, the presence of epidote reflects also magma composition, water content and oxygen fugacity (i.e. NNO oxygen buffer) (Brandon *et al.*, 1996; Schmidt & Poli, 2004).

Epidote is widespread in metaluminous, I-type *sensu lato* granitoids (i.e. Sial *et al.*, 1999) but it is truly rare that these plutonic rocks include also garnet. Crystallization experiments of Schmidt & Thompson, (1996) indeed indicate that both minerals are stable together at relatively high pressure conditions, above approximately 1.2 GPa, that is between 32 and 36 km of depth (considering a density between $2.7 - 3.1 \times 10^3 \text{ kg/m}^3$; i.e. Rudnick & Fountain, 1995). From a literature revision and from Zen & Hammarstrom, (1984a, 1984b), Zen (1985), Evans & Vance (1987), Dawes & Evans (1991), Nalini (1997), Sial *et al.* (1999), Schmidt & Poli, (2004), Xu *et al.*

(2013), Samadi *et al.* (2014) and more recently from Pribavkin *et al.* (2013) only 4 locations have evidence for the rare coexistence of magmatic garnet and epidote, within the same mineralogical assemblage. One of these locations is the Araçuaí orogen, in which the I-type metaluminous Galiléia granitoids - also called Galiléia batholith - beside the typical biotite and hornblende assemblage, these rocks contain also garnet and epidote as accessory minerals (Nalini, 1997).

1.1.3 Two main geochemical models for the I-type granitogenesis

1.1.3.1 The mantle – crustal magma mixing model

I-type granitoids are not “pure magmas”, but have a hybrid geochemical signature suggesting that both mantle- and crustal-derived magmas, in variable proportion, contributed to shape their chemical composition (DePaolo 1981; McCulloch & Chappel, 1982; Castro *et al.*, 2010). This isotopic heterogeneity together with the fact that generally I-type granites crop out in subduction-related setting such as those along the Cordilleran margins have generated an misuse of the alphabetic classification proposed by Chappell & White, (1974). The inconsistent use of the term I-type granite creates a circular misunderstanding regarding the relationship between the rock-source, the chemistry of the granite, the processes that shaped the magmatic composition and the tectonic settings (Pankhurst *et al.*, 1999; Parada *et al.*, 1999; Harvé *et al.*, 2007; Lee *et al.*, 2007; Castro *et al.*, 2010; Clemens *et al.*, 2011; Castro 2013; Clemens & Stevens, 2016).

The main models used to explain the petrogenesis of these subduction-related I-type granites are the so-called MASH model (i.e. mixing, assimilation, storage and homogenisation) (Hildreth & Moorbarth, 1988) and/or the Deep Crustal Hot Zone (DCH; Annen *et al.*, 2006; 2008; 2015). The MASH model assumes that silicic magmatism basically originates from mantle-wedge-derived basaltic to andesitic magmas that, once emplaced at the base of the continental crust (i.e storage), are able to assimilate and/or partially melt the surrounding crustal rocks to produce crustal magmas whose composition is similar to I-type magmas (DePaolo, 1981; Patiño-Douce, 1995; Thompson *et al.*, 2002). The Deep Crustal Hot Zone (DCHZ) model is similar to the previous one but it focus on the deep lower crust where numerous basaltic sills are able to intrude. These multiple intrusions generate mafic to intermediate melts by the re-melting of former mafic intrusions. The release of heat and fluid by crystallization causes partial melting of the surrounding country rocks with the production of crustal melts. Thus, mantle and crustal magmas mix in these zones for long enough to produce large volumes of hybrid magma (Annen *et al.*, 2006; 2008; 2015).

Despite their wide acceptance, these models fail to explain three important aspects of I-type granites. i) They do not account for the generally broad Sr and Nd isotopic variability (Fig. 1.1), associated with a rather homogeneous major element character ($\text{SiO}_2 = 63 - 70$ wt.%; $\text{FeO}_{\text{Tot}} 2 - 5$ wt.%, $\text{MgO} 1 - 3$ wt.%, $\text{CaO} 3 - 5$ wt.%, $\text{Na}_2\text{O} 2 - 4$ wt.% and $\text{K}_2\text{O} 2 - 4$ wt.%; Castro *et al.*, 2010). ii) Especially for the MASH model that is more stationary than the DCH, the incorporation of solid wall rocks (i.e. assimilation) and/or during magma ascent is severely limited by the energy required to melt xenoliths (Glazner, 2007). This process appears to be self-limiting since the energy consumed by the mantle-derived magmas in assimilating the surrounding crustal rocks leads to a temperature drop, causing higher crystal contents in the hybridizing magma thus limiting further assimilation. Additionally, iii) fluids released from the mafic magma crystallization that cause fluid-fluxed partial melting of the surrounding crustal rocks (Annen *et al.*, 2006) provoke a negative volume change (i.e. increase of magma density) in the generated crustal magma thus making it impossible to escape from the source (i.e. Clemens & Droop, 1998; Clemens & Stevens, 2015).

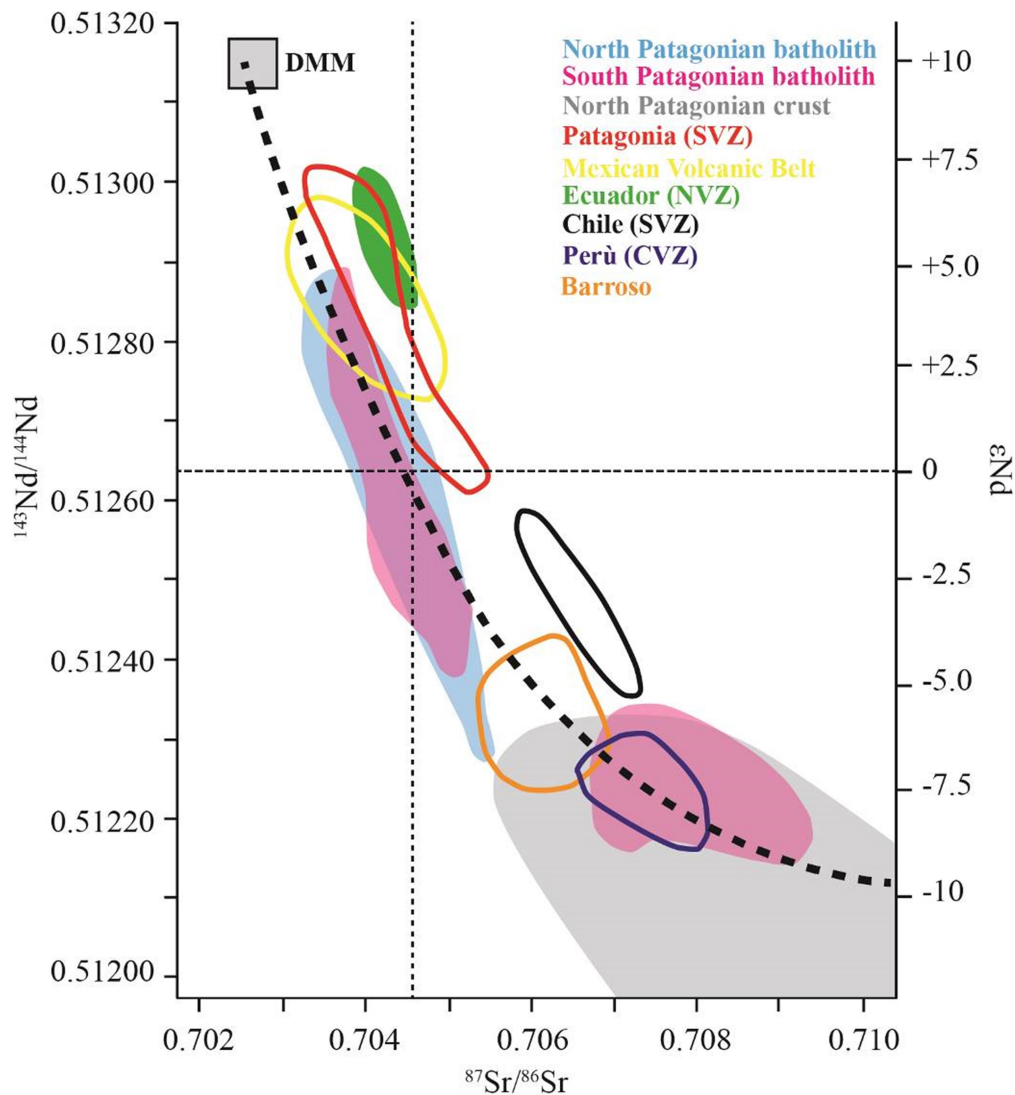


Figure 1.2 Example of $^{87}\text{Sr}/^{86}\text{Sr}$ vs. $^{143}\text{Nd}/^{144}\text{Nd}$ mantle-crust hybrid signature shown by some South American Cordilleran I-type batholiths; black thick dotted line is the mixing curve (modified from Castro *et al.*, 2010). The colour of the names in legend is relative to the field covered within the diagram; DMM: Depleted Mantle Morb; CVZ: Central Volcanic Zone; SVZ: Souther Volcanic zone.

1.1.3.2 The peritectic entrainment model.

Recently Stevens *et al.* (2007), Clemens *et al.* (2011) and Clemens & Stevens (2012; 2016) proposed an alternative model. They propose that the chemical variability exhibited by S- and I-type granitic suites is controlled by the different degree of peritectic mineral assemblage entrained in the magma during the partial melting process. In the case that the source is an Al_2O_3 -rich metasedimentary rock, the fluid-absent melting of biotite, produce a peritectic assemblage mainly constituted by garnet, ilmenite, and \pm k-feldspar. This assemblage once entrained in the magma is responsible for the production of S-type granitoids. Instead, if the source is formed by immature greywackes and/or volcanic and plutonic rocks having andesite affinity, the dehydration melting involves also the presence of hornblende besides biotite, and the peritectic minerals will be,

clinopyroxene (playing a major role), plagioclase, ilmenite and orthopyroxene. The resulting melts will be I-type Al_2O_3 -depleted with the more mafic melts derived by mixing of melts and peritectic assemblage, while leucocratic melts derive directly from crustal anatexis. This model has two important implications: 1) it can explain the puzzling problem of invariant major element compositions with highly variable isotopic signature (both mantle and crust-derived); and 2), I-type granitic magmatism reflects to the recycling of the continental crust during continent-continent collision, where lithospheric subduction is not involved. With reference to the second point, Clemens & Stevens, (2016) pointed out that most of the voluminous granitic magmatism is not directly related to subduction zone settings, that is, atop the subducting slab, but in more distal settings. For example, the I- and S-type granites of the Lachlan Fold belt were produced in a back-arc scenario. Likewise, Clemens *et al.* (2017a and references therein) reports that many other extensive batholiths were produced from, and intruded into accretionary wedge sequences constituting the foreland domain of a collisional system. These settings are geological areas for the deposition of fertile (volcano)clastic material derived from the erosion of continental arc. Once subjected to suitable P-T conditions, this fertile material undergoes partial melting and is able to deliver voluminous quantities of felsic magmas.

1.2 AIMS OF THE PROJECT

During the Neoproterozoic, the Brasiliano/Pan-African orogeny was responsible for the build-up of the Araçuaí-West Congo orogen as the consequence of the closure of the Macaubas Basin and the related westward-subduction of oceanic lithosphere. This process triggered the production and emplacement of pre-collisional (ca. 630 - 585 Ma) metaluminous I-type Galiléia granitic magmatism, belonging to the G1 Supersuite. Notably the Galiléia granitoids cover an area of more than 15,000 km². Because the strong geological implication that assumes the study of these Cordilleran-I-type granitoids, and most importantly the petrogenetic and geodynamic meaning for the rare coexistence of garnet and epidote in these rocks, the aims of this project are the following.

- 1) Investigate the nature and the origin of garnet and epidote in the Galiléia granitoids.

The origin of garnet and epidote remains a debated topic in granite petrogenesis. While epidote could be either magmatic or metamorphic, garnet could be: 1) a peritectic mineral due to incongruent melting of biotite in the source or during wall rock assimilation (Erdmann *et al.*, 2009; Lackey *et al.*, 2012; Melo *et al.*, 2017a, 2017b), 2) a crystal phase in the source not involved in the partial melting event (resistate crystal; Vernon 2007), 3) a xenocryst from the wall rocks

incorporated during magma ascending and emplacement (Clarke, 2007), 4) a product of primary crystallization (Allan & Clarke, 1981; Miller & Stoddard, 1981; Harrison, 1988; Dalquist *et al.*, 2007; Villaros *et al.*, 2009; Barnes *et al.*, 2012; Lackey *et al.*, 2012) 5) a metamorphic mineral growth from very high pressure conditions that the rock experienced (Vielzeuf & Schmidt, 2001).

To answer at these questions, the review of natural and experimental scientific contributions concerning garnets and epidotes in granitoids will give a better knowledge of: i) their pressure-temperature stability within intermediate to silicic melts, ii) the pressure, temperature and petrogenetic meaning for their interplay in silicic rocks like the Galiléia granitoids and eventually iii) since this mineral assemblage is reported in metaluminous granitoids thus it means that it is possible also understand better what geotectonic situation(s) within the Araçauí orogen allowed such petrological conditions.

Once these questions have been answered, part of these will be able to serve the key(s) to solve other open debates.

2) Why the Galiléia granitoids record a protracted and vast granitic magmatism lasted over a period of 55 Myrs (from ca. 630 to 575 Ma)?

The prolonged granitic magmatism so far reported for these granites is at odds with the general belief that mid- to upper crustal granitoids emplace and crystallize in less than 10 Myr (Coleman *et al.*, 2004; Schartegger *et al.*, 2009; Shoene *et al.*, 2012; Miller *et al.*, 2011; Barboni *et al.*, 2013 and references therein). Moreover in literature (for instance Fig. 6 and table 2 in Pedrosa-Soares *et al.*, 2011) it appears that each single hand sample have concordant zircons recording the same age variability (ca. > 60 Myrs) suggested using different samples (> 40 granitoid samples). The answer to these paradoxes must be found. Additionally, the long-lived history of the Galiléia granitoids is not dissimilar from i) plutonic rocks intruding accretionary prism and back-arc settings and ii) mid- to lower-crustal Precambrian plutonic rocks found in similar accretionary settings and/or cratonic nuclei terrains (Farris *et al.*, 2010; Sharkov, 2010; Jeon *et al.*, 2012; Farina *et al.*, 2015; Jiang *et al.*, 2016; Clemens *et al.*, 2017 and others).

3) Were mantle-derived magmas involved in the genesis of the Galiléia magmas and 4) was there crustal growth during the G1 I-type genesis or just crustal recycling (Pedrosa-Soares *et al.*, 2001, 2011; Gonçalves *et al.*, 2014, 2016, 2018; Tedeschi *et al.*, 2016)?

If mantle magmas were involved in the genesis of the G1 granitoids, the subduction of oceanic lithosphere could truly have produced the G1 granitoids, despite their strong high K₂O/N₂O content and crustal signature (i.e. high radiogenic Sr and unradiogenic Nd and Hf values, see later).

Thus the long-lived history of the Galiléia granitoids indeed could be explained by MASH/DCH zones models. In contrast, if the magmatism was controlled only by pre-existent crustal protoliths, then another mechanism for the production of such and prolonged voluminous granitic magmatism must be found. Whatever would be the answer, the nature of the protolith involved in the genesis of the Galiléia granites would be likely understood. Then answering correctly the third point would automatically lead to answer the question at the fourth point.

To address the questions at points 2), 3) and 4) detailed U-Pb geochronological and Lu-Hf isotopic study on carefully selected Galiléia granitoids and relative zircons is planned. Detailed zircon trace element analyses will be also performed. Furthermore as for the first point, a review of time span of magmatism in different settings, at different crustal depths and relative duration of it is necessary. Thus comparison between young and upper crustal magmatism versus old and mid- to lower crustal plutonism would possibly highlight a geochronological bias caused by the geological record and so far poorly reported. Thus the Galiléia granitoids could be a starting point to understand better why old silicic magmatism appear to have time spans bigger than generally reported.

1.3 LOCALIZATION OF THE STUDY AREA

The study area is localized within the Minas Gerais State, between the cities of Governador Valadares and Resplendor, and covers almost 4,000 km². Other main and small cities included in the area are: São Vitor, Linópolis, Divinos das Laranjeiras, Sapucaia do Norte, Galiléia, Conselheiro Pena, Penha do Norte, Independencia, João Pinto, São Roque, Barra do Cuite, Tumiritinga, Cuieté Velho e Divino. The area is well represented within the following geological maps: Governador Valadares (SE.24-YA-IV), Itabirinha de Mantena (SE.24-Y-A-V), Conselheiro Pena (SE.24-Y-C-I) and Itanhomi (SE24-Y-C-I). The scale adopted is 1:100000 and these maps were mapped by the CPRM and/or as a collaboration project between CPRM and UFMG. The Galiléia batholith extends approximately from north at the parallel 17°90" S, above the city of Teófilo Otoni, till the south, around the 21°75" S parallel, close to the city of Juiz de Fora. Some intrusions belonging to the Galiléia granitic magmatism occur also further to the north around the 16°00" S (Gonçalves *et al.*, 2016). The batholith is generally confined to the area between the 42°60" and 41°40" W meridians. In general, it covers a minimum area of ca. 15,000 km² with a general N-S direction (> 300 km long and > 50 km wide). These main roads pass through main cities as Ponte Nova, Caratinga, Inhapim, Governador Valadares and Conselheiro Pena (Fig. 1.3).

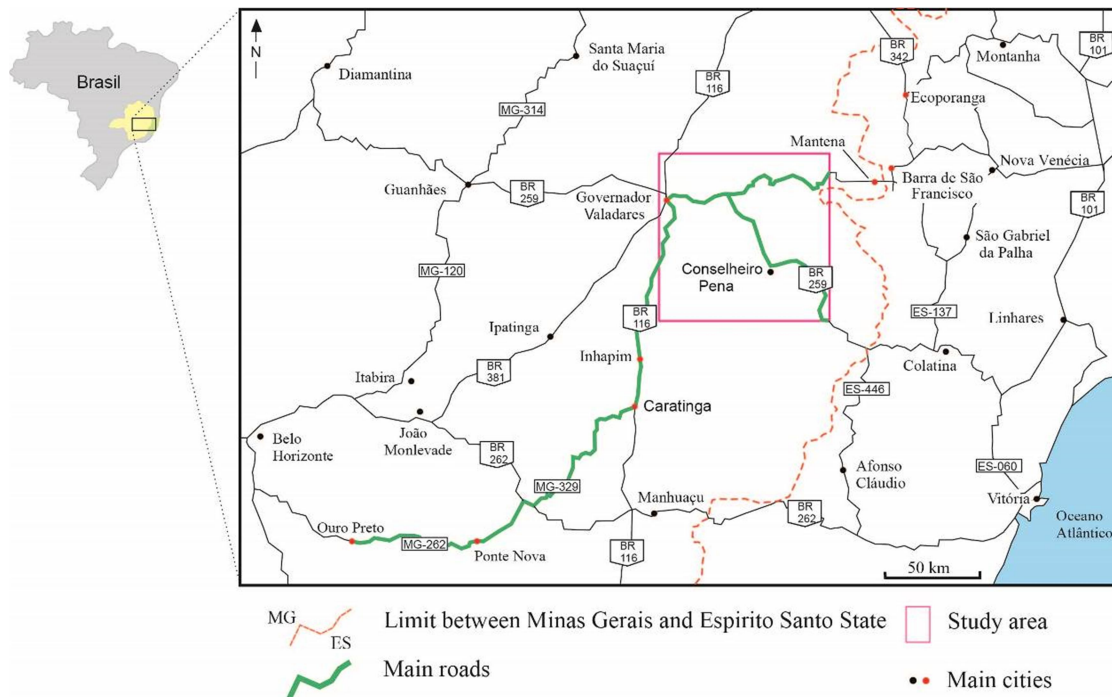


Figure 1.3: Map with the localization of the main roads used to get the study area. Modified from Google Maps.

1.4 METHODS

1.4.1 Literature review

The papers that I have considered in this literature review address the following broad themes:

- the geology of the area comprised between the São Francisco Craton and the Congo Craton, focussing on the Araçuaí-West Congo orogen. The period spanning from the Rodinian rifting stages (ca. 1.0 Ga), until the end of the Brasiliano Orogeny was investigated, with special attention to the geological and geotectonic events occurred during the pre-collisional period, which led to the genesis and emplacement of the I-type G1 granitoids;
- the field occurrence, the mineral and textural features, the major and trace element variability, the isotope signature as well as the age of I-type G1 granitoids which are the focus of this study;
- another issue considered for this project, and directly correlated with granite petrogenesis and geochronology, is the study of the petrogenetic models adopted for the genesis of I-type granitoids, occurring along the Cordilleran margin, from Alaska to the Antarctica Region, as well as in continental-continental collision. This part aims to understand the physical and chemical aspects of granitoid rocks, through natural and experimental data regarding the

mineralogical and textural relationships, and their control on major and trace elements. Since the G1 granitoids have rare occurrence of garnet in coexistence with epidote, more attention has been giving to literature that deals with: 1) the stability of these two specific minerals within Al-poor intermediate to acidic melts, 2) the possible textures that could help to identify their different forms, and 3) their petrogenetic significance. Moreover isotopic and geochronological studies reviewing and their possible applications on granite petrogenesis, have been reviewed, as well.

- **1.4.2 Field work**

Since the study area is vast (ca. 4000 km²), a few weeks were spent planning the field work and plotting previously collected data from Nalini (1997), Paes (1999), Feboli (2000), Feboli & Paes (2000), Oliveira (2000) and Paes *et al.* (2010), Mondou *et al.* (2012) and Gonçalves *et al.*, (2009, 2014) on a map. Using the Google Earth Software, this pre-field work has provided an invaluable tool: that is to individuate, once in the field, the main outcrops avoiding those which are weathered. The area investigated occurs between Governador Valadares and Resplendor Cities. So far three field campaigns were performed.

Field campaign 1 (07 - 12/12/2013, 5 days). The main areas covered were along the BR-259 and BR-381 roads, i.e. Governador Valadares, São Vitor, Galileia, Conselheiro Pena, Penha do Norte and Independecia. In this field work 23 samples of granitoids and 4 enclaves were collected. One migmatite associated with the São Vitor granitoids was also observed and sampled.

Field campaign 2 (10 – 19/12/2014, 9 days). The main areas investigated, were 1) between Conselheiro Pena, João Pinto and São José do Ituieto Cities, 2) between Conselheiro Pena, Barra do Cuiete and Tumiritinga Cities and 3) Between São Vitor, Central de Sant’Helena, Linopolis, Divino de Laranjeiras, Sapucaia do Norte and Galiléia. In the second field campaign, 18 samples (mainly granitoids and few enclave) were collected.

Field campaign 3 (16 – 21/08/2016, 5 days). This was the last field campaign scheduled. Was attained between Conselheiro Pena and Cuieté Velho areas, right to the south of the Rio Doce River. This sampling activity was scheduled in order to sample rocks that Mondou *et al.* (2012) have previously dated but for which no geochemical data was reported. Moreover this period helped to have a better and clear “image” about the granitoids around that area. In total 7 granitoids and 1 enclave were collected.

1.4.4 Sample analyses

1.4.4.1 Thin sections

From a total of 50 samples 22 (granitoids and enclaves) thin sections were prepared. Thin sections were prepared at the Department of Geology of the Federal University of Ouro Preto. Thin sections have been used to give as much as possible detailed interpretation of the São Vitor and Galiléia granitoid rocks. Moreover a special attention was given to the more important minerals so far discussed, that is, garnet and epidote. Petrographic investigations on these minerals had the meaning to understand their genesis and their textural relationships.

1.4.3.2 Mineral chemistry and whole-rock geochemistry

Mineral chemistry was done by means Scanning Electron Microprobe (SEM) at the Department of Earth Science of the University of Stellenbosch, South Africa. Chemical analyses were carried out especially on garnets and epidotes, beside plagioclase, biotite and hornblende.

From the 50 samples chosen for the thin section, 29 were crushed and powdered at the Department of Geology of the Federal University of Ouro Preto and sent to the Department of Earth Science of the University of Stellenbosch (South Africa) to determine the major and trace element composition by X-Ray Fluorescence (XRF) instrumentation.

1.4.3.3 U-Pb geochronology

From the 50 samples used for whole-rocks geochemistry, 18 have been crushed and prepared for U-Pb zircon geochronology. One of these samples comes from the new migmatitic outcrop associated to the São Vitor granitoids. Sample preparation was conducted at the Department of Geology of the Federal University of Ouro Preto. Once crushed to mineral scale, the sample had their magnetic minerals removed (usually Fe-Ti-Mg-rich ones), by means magnetic separation. After this stage, 50 - 100 zircons grains are hand-picked and mounted in epoxy-resin disk. The zircons are then imaged using cathodoluminescence imaging using a scanning electron microscope at the Department of Earth Science of the University of Stellenbosch (South Africa). Subsequently, U-Pb zircon ages were obtained using the ELEMENTTM 2 ICP-MS, made available by the LOGPAGE/AIR Group of the Department of Geology of the Federal University of Ouro Preto. Furthermore, it will be performed also *in-situ* U-Pb ages in few zircons inclusions in the magmatic garnets. Additionally, zircon from two already dated samples, were again handpicked and chosen to

be dated by means high-precision multi-collector LA-ICP-MS at the Department of Geology of the Federal University of Ouro Preto.

1.4.3.4 Lu-Hf method

Lu-Hf isotope will be measured on the same zircons that were used to obtain LA-ICP-MS U-Pb ages. This will be on the new facility, NEPTUNE PLUS high-performance Multi-collector ICP-MS made available by the LOGPAGE/AIR Group of the Department of Geology of the Federal University of Ouro Preto.

1.4.3.5 Oxygen isotopes

Oxygen isotopes were measured on garnet and quartz. These minerals were handpicked from 7 samples (6 granitoids and 1 enclave) samples in which previously mineral chemistry, whole rock and U-Pb ages and Hf isotopes have been analysed. In order to separate mineral inclusions from the garnet crystals, these were crushed. Overall, a quantity of 2 mg for each mineral is required. Oxygen isotopes in minerals were measured at the Department of Earth Sciences, University of Cape Town, South Africa using the laser fluorination method which uses a 20 W New Wave CO₂ laser mounted on a movable stage.

1.4.4 Scientific contributions and future works

1. The first scientific work was focussed on the occurrence of garnet and epidote in the G1 granitoids. These mineral phases are uncommon in metaluminous I-type granitoids and may be both peritectic, metamorphic or magmatic. The backbone of this study was the detailed study in thin sections of the petrography of the rock. The petrography was coupled with mineral chemistry analyses. The whole rock was discussed as well.
2. The aim of the second scientific contribution is to try to give a better explanation for the wide U-Pb ages so far obtained from other workers, determine if different intrusion/plutons with different ages may be identified as well as to detect possible inherited cores in the zircon population. Zircon trace elements will play a fundamental role in understanding internal magma chamber processes (i.e. mixing, magmatic zircon recycling, magma fractionation etc.). The Hf isotopic composition of zircon will also be determined. Applied in granitoid studies, this systematic have the power to discern the granitic sources, from that having deep crust origin, from that having upper mantle derivation. It is hence able to

individuate crustal recycling or juvenile crust production, that otherwise would be hidden using just major and trace elements (see for example Castro *et al.*, 2010).

A third and fourth contribution are scheduled to be written during year 2018.

3. The recognition that the Galiléia garnets are magmatic crystallized in metaluminous granitoids and indicating a deep origin, opens new windows in understanding metaluminous granite petrogenesis. These findings allow studying these garnets and then their felsic host using new petrologic tools, like oxygen isotopes. Information of these isotopes in non-metamorphic garnets belonging to granites are scarce. The few available data are related only to peraluminous granites where garnets is commonly found. Then, since garnets have high closure temperature for oxygen diffusion ($> 800^{\circ}\text{C}$), oxygen isotopes in garnets are of potential significance because $\delta^{18}\text{O}$ will not change its value after crystallization, thus oxygen isotopes could be correlated with that of the granitic magma source. Oxygens were measured in quartz, because the coupling the $\delta^{18}\text{O}$ of these minerals with that one of garnets is a strong geothermometer able to give information about coexistence between minerals and open and/or closes magma systems. Fluid related processes (i.e. fluid present melting and/or internal magma fluid circulation) are able to be investigated. Eventually, garnet trace elements will be measured as well. This allow us to understand the geochemistry of the melt from which these garnets crystallized with the possibility to understand better some petrogenetic processes that otherwise will remain cryptic.
4. Peraluminous Urucum and Palmital S-type granitoids (Nalini 1997; Nalini *et al.*, 2005; 2015) have been found showing the same age and Hf variability of the Galiléia metaluminous granitoids. Besides confirming that these I- and S-type granites in the central part of the Crystalline core have an isotopically similar source (Nalini *et al.*, 2005), this fact, once more, rise the fact that both are contemporaneous and thus there is no evidence neither in age nor in geochemistry for different steps in the geodynamic evolution of the Arçuaí belt. That is, there no need to call for pre and syn-collisional granites

1.5 STRUCTURE OF THE THESIS

This thesis addresses important geological and petrological aspects of the Galiléia batholith. This work includes field, petrographic, mineral chemistry, geochemical, geochronological and isotopic data. The obtained outcomes offer important aspects regarding the genesis and evolution of

lower crustal I-type granitoids formed during subduction-related processes. The document is structured as follows:

Chapter 1 introduce some of the main concepts regarding I- and S-type granite classification and I-type granite petrogenesis, the aims of the project, the localization of the area and the methodology used along this work.

Chapter 2 discusses in detail the geology of the Araçuaí Orogen and the tectonic models adopted to explain the evolution of this orogenic belt.

Chapter 3 offers a detailed review about the field, geochemical, geochronological and isotopic data so far published for the Galiléia granitoids and compares these data with those from other well-studied I-type batholiths from other parts of the world.

Chapter 4 hosts the manuscript “Magmatic garnets in cordilleran-type Galiléia granitoids of the Araçuaí belt (Brazil): evidence for crystallization in the lower crust”. This manuscript discusses the widespread occurrence of magmatic garnet and epidote in the Galiléia granitoids, a rare mineral parageneses in I-type granitoids. It is discussed the petrological meaning of these two minerals through field, textural, mineral chemical and geochemical data. It is shown as the Galiléia batholith, together with few other similar granitoids is related to lower crustal crystallization in an old accretionary prism.

Chapter 5 host the manuscript “Extreme U-Pb age variability in a Neoproterozoic, lower crustal batholith: implications for magma storage in an accretionary prism”. This paper reports zircon trace elements, U- Pb ages and Hf isotopes and whole rock geochemical data. Here it is investigated the possibility that lower crustal granitoids found in accretionary prism and fore to back-arc settings record a more long-lived history than the shallower counterparts found atop of subduction zone. These data are also supported by comparison with ages from older and younger granitic bodies found in different tectonic settings.

Chapter 6 addresses and summaries the main conclusions of this project achieved through the two manuscripts.

Appendix includes detailed description of the methods used during this research and the tables hosting data of mineral chemistry, whole rock geochemistry, zircon trace elements, U-Pb geochronology and Hf isotopes.

References

- Allan B.D. & Clarke D.B. 1981. Occurrence and origin of garnets in the South Mountain Batholith, Nova Scotia. *The Canadian Mineralogist* **19**:19-24
- Annen C., Blundy J.D., Leuthold J., Sparks R.S.J. 2015. Construction and evolution of igneous bodies: Towards an integrated perspective of crustal magmatism. *Lithos* **230**:206-2217
- Annen C., Blundy J.D., Sparks R.S.J. 2006. The genesis of intermediate and silicic magmas in deep crustal hot zones. *Journal of Petrology*, **47**:505-539.
- Annen C., Blundy J.D., Sparks R.S.J. 2008. The source of granitic melt in Deep Hot Zones. *Transactions of the Royal Society of Edinburgh: Earth Sciences*, **97**:297-309.
- Bach P., Smith I.E.M. Malpas J.G. 2012. The Origin of Garnets in Andesitic Rocks from the Northland Arc, New Zealand, and their Implication for Sub-arc Processes. *Journal of Petrology*, **53**:1169-1195.
- Barboni M., Boehnke P., Schmitt A.K., Harrison T.M., Shane P., Bouvier A.-S., Baumgartner L., 2016. Warm storage for arc magmas. *Proceedings Of Natural Academy of Science* **113**:13959–13964
- Barnes C.G. & Allen C.M. 2006. Depth of origin of late Middle Jurassic garnet andesite, Southern Klamath Mountains, California. In: Snoke AW, Barends CG (eds) Geological studies in the Klamath Mountains Province, California and Oregon. *Geological Society of American Special Paper*, **410**:269-286
- Brandon A.D., Creaser R.A., Chacko T. 1996. Constraints on rates of granitic magma transport from epidote dissolution kinetics. *Science*, **271**:1845-1848
- Brown M. 2013. Granite: From genesis to emplacement. *Geological Society of American Bulletin*, **7-8**:1079-1113
- Castro A. 2013. Tonalite-granodiorite suite as cotectic system: a review of experimental studies with applications to granitoid petrogenesis. *Earth-Sciences Review*, **124**:68-95.
- Castro A., Gerya T., García-Castro A., Fernández C., Díaz-Alvarado J., Moreno-Ventas I., Lowe I. 2010. Melting relations of MORB-sediment mélanges in underplated mantle wedge plumes. Implications for the origin of Cordilleran-type batholiths. *Journal of Petrology*, **51**:1267-1295.

Chappell B.W. & White A.J.R. 1974. Two contrasting granite types. *Pacific Geology*, **8**:173-174.

Clarke B.D. 2007. Assimilation of phenocryst in granitic magmas: principles, processes, proxies and problems. *The Canadian Mineralogist* **45**:5-30

Clemens J.D. Helps P.A. Stevens G., 2009. Chemical structure in granitic magmas – a signal from the source? *Transactions of the Royal Society of Edinburgh: Earth Sciences*, **100**:159-172

Clemens J.D. & Stevens G., 2012. What controls chemical variations in granitic magmas? *Lithos*, **134-135**:317-329.

Clemens J.D., Buick I.S., Kisters A.F.M., Frei D. 2017a. Petrogenesis of the granitic Donkerhuk batholith in the Damara Belt of Namibia: protracted, syntectonic, short-range, crustal magma transfer. *Contribution to Mineralogy and Petrology*, **172**:50

Clemens J.D. & Droop G.T.R. 1998. Fluids, P-T paths and the fates of anatectic melts in the Earth's crust. *Lithos*, **44**:21-36

Clemens J.D. & Stevens G. 2015. Comment on “Water-fluxed melting of the crust: A review” by Weinberg RF, Hasalová P. *Lithos*, **234-235**:100-101

Clemens J.D. & Stevens G. 2016. Melt segregation and magma injections during crustal melting: Breaking out of the matrix. *Earth-Science Reviews*, **160**:333-349

Clemens J.D., Stevens G., Farina F. 2011. The enigmatic sources of I-type granites: the peritectic connexion. *Lithos*, **126**:174-181.

Dalquist J.A., Galindo C., Pankhurst R.J., Rapela C.W., Alasino P.H., Saavedra J., Fanning C.M. 2007. Magmatic evolution of the Peñón Rosado granite: petrogenesis of garnet-bearing granitoids. *Lithos* **95**:177-207

Dawes R.L. & Evans B.W., 1991. Mineralogy and geothermobarometry of magmatic epidote-bearing dyke, Front Range, Colorado. *Geological Society of American Bulletin* **103**:1017-1031

Day R.A, Green T.H., Smith I.E.M. 1992. The origin and significance of garnet phenocrysts and garnet-bearing xenoliths in Miocene calc-alkaline volcanics from Northland, New Zealand. *Journal of Petrology*, **33**:125-161

DePaolo D.J. 1981. A neodymium and strontium isotopic study of the Mesozoic calc-alkalin granitic batholiths of the Sierra Nevada and Peninsular Ranges, California. *Journal of Geophysical Research*, **86**:10470-10488.

Erdmann S., Jamieson R.A., Macdonald M.A. 2009. Evaluating the origin of garnet, cordierite and biotite in granitic rocks: a case study from the South Mountain Batholith, Nova Scotia. *Journal of Petrology*, **50**:1477-1503

Evans B.W. & Vance J.A., 1987. Epidote phenocrysts in dacitic dikes, Boulder Country, Colorado. *Contribution to Mineralogy and Petrology*, **96**:178-185

Farina F., Albert C., Lana C., 2015. The Neoproterozoic transition between medium- and high-K granitoids: Clues from the Southern São Francisco Craton (Brazil). *Precambrian Research*, **266**:375–394.

Farris D.W. 2010. Tectonic and petrologic evolution of the Kodiak batholith and the trenchward belt, Kodiak Island, AK: Contact fault juxtaposition? *Journal of Geophysical Research - Solid Earth*, **115**:1–29

Féboli W.L. & Paes V.C. 2000. *Folha Itanhomi. Projeto Leste*. CPRM-CODEMIG. <http://www.portatgeologia.com.br/mapa/>.

Féboli, W.L., 2000. *Folha Governador Valadares. Projeto Leste*. CPRM-CODEMIG. <http://www.portatgeologia.com.br/mapa/>.

Frost B.R., Arculus R.J., Barnes C.G., Collins W.J., Ellis D.J., Frost C.D. 2001. A geochemical classification of granitic rocks. *Journal of Petrology*, **42**:2033-2048.

Glazner A.F. 2007. Thermal limitations on incorporation of wall rocks into magma. *Geology*, **35**:319-322.

Gonçalves L., Alkmim F.F., Pedrosa-Soares A., Gonçalves C.C., Vieira V. 2018: From the plutonic root to the volcanic roof of a continental magmatic arc: a review of the Neoproterozoic Araçuaí orogen, southeastern Brazil. *International Journal of Earth Science*, **107**:337-358

Gonçalves L.E. 2009. *Características Gerais e História Deformacional da Suíte Granítica G1, entre Governador Valadares e Ipanema, MG*. Master Thesis. Universidade Federal de Ouro Preto, Ouro Preto, Brasil, p. 112.

Gonçalves L.E., Alkmim F.F., Pedrosa-Soares C.A., Dussin I.A., Valeriano, C.d.M., Nalini Jr.H.A. Lana C., Tedeschi M. 2016. Granites of the intracontinental termination of a magmatic arc:

an example from the Ediacaran Araçuaí orogen, southeastern Brazil. *Gondwana Research*, **36**:439-458

Gonçalves L.E., Farina F., Lana C., Pedrosa-Soares C.A., Alkmim F.F., Nalini Jr.H.A. 2014. New U-Pb ages and lithochemical attributes of the Ediacaran Rio Doce Magmatic Arc, Araçuaí confined orogen, southeastern Brazil. *Journal of South American Earth Sciences*, **52**:1-20.

Green T.H. 1972. Crystallization of Calc-Alkaline Andesite under Controlled High-Pressure Hydrous Conditions. *Contributions to Mineralogy and Petrology*, **34**:150-166

Green T.H. 1977. Garnet in Silicic Liquids and Its Possible Use as P-T indicator. *Contributions to Mineralogy and Petrology*, **69**:59-67.

Green T.H. 1992. Experimental phase equilibrium studies of garnet-bearing I-type volcanics and high-level intrusive from Northland, New Zealand. *Transactions of the Royal Society of Edinburgh: Earth Sciences*, **83**:429-438.

Green T.H., & Ringwood A.E. 1968. Origin of the garnet phenocrysts in calc-alkaline rocks. *Contribution to Mineralogy and Petrology*, **18**:163-174.

Harangi S.Z., Downes H., Kósa L., Szabo C.S., Thirlwall M.F., Mason P.R.D., Matthey D. 2001. Almandine Garnet in Calc-alkaline Volcanic Rocks of the Northern Pannonian Basin (Eastern-Central Europe): Geochemistry and Geodynamic Implications. *Journal of Petrology*, **42**:1813-1843.

Harrison T.N. 1988. Magmatic garnets in the Cairngorm granite, Scotland. *Mineralogical Magazine*, **52**:659-667

Hervé F., Pankurst R.J., Fanning C.M., Calderon M., Yaxely G.M. 2007. The south Patagonian batholith: 150 my of granite magmatism on a plate margin. *Lithos*, **97**:373-394

Hilderth W. & Moorbarth S. 1988. Crustal contributions to arc magmatism in the Andes. *Contributions to Mineralogy and Petrology*, **98**:455-489

Jeon H., Williams I.S., Chappell B.W. 2012. Magma to mud to magma: Rapid crustal recycling by Permian granite magmatism near the eastern Gondwana margin. *Earth and Planetary Science Letters*, **319–320**:104–117.

Jiang Y.D., Schulmann K., Sun M., Štípská P., Guy A., Janoušek V., Lexa O., Yuan C. 2016. Anatexis of accretionary wedge, Pacific-type magmatism, and formation of vertically stratified continental crust in the Altai Orogenic Belt. *Tectonics*, **35**:3095–3118

Kemp A.I.S. & Hawkesworth C.H. 2004. Granitic prospective on the generation and secular evolution of the continental crust. In: Rudnick, R.L. (Eds.). *The Crust. Treatise on Geochemistry*. Elsevier, Amsterdam, 4:349-431.

Lackey J.S, Romero G.A., Bouvier A-S., Valley J.W. (2012) Dynamic growth of garnet in granitic magmas. *Geology*, **40**:171-174

Lee C-T.A., Morton D.M., Kistler R.W., Baird A.K. 2007. Petrology and tectonics of Phanerozoic continent formation: from island arcs to accretion and continental arc magmatism. *Earth and Planetary Science Letters*, **263**:370-387.

McCulloch M.T. & Chappell B.W., 1982. Nd isotopic characteristics of S- and I-type granites. *Earth and Planetary Science Letters*, **58**:51-64

Melo M.G., Lana C., Stevens G., Pedrosa-Soares A.C., Gerdes A., Alkmim L.A., Nalini Jr. H.A., Alkmim F.F. 2017a. Assessing the isotopic evolution of S-type granites in the Carols Chagas Batholith: clues from U-Pb, Hf isotopes, Ti geothermometry and trace element composition of zircon. *Lithos*, **284-284**:730-750

Melo M.G., Stevens G., Lana., Pderosa-Soares A.C., Frei D., Alkmim F.F., Alkmin L.A. 2017b. Two cryptic anatectic events within the syn-collisional granitoid from the Araçuaí orogen (southeastern Brazil): Evidence from the polymetamorphic Carlos Chagas batholith. *Lithos*, **277**:51-71

Miller C.F. & Stoddard E.F., 1981. The role of manganese in the parageneses of magmatic garnet: an example from the Old Woman-Piute Range, California. *Journal of Geology*, **89**:233-246

Miller C.F., Furbish D.J., Walker B.A., Claiborne L.L., Koteas G.C., Bleick H.A., Miller J.S. 2011. Growth of plutons by incremental emplacement of sheets in crystal-rich host: Evidence from Miocene intrusions of the Colorado River region, Nevada, USA. *Tectonophysics*, **500**:65–77

Mondou M., Egydio-Silva M., Vauchez A., Raposo M.I.B., Bruiguiet O., Oliveira A.F. 2012. Complex, 3D strain patterns in a synkinematic tonalite batholith from the Araçuaí Neoproterozoic orogen (Eastern Brazil): Evidence from combined magnetic and isotopic chronology studies. *Journal of Structural Geology*, **39**:158-179.

Nalini Jr.H.A. 1997. *Caractérisation des suites magmatiques néoprotérozoïques de la région de Conselheiro Pena et Galiléia (Minas Gerais, Brésil): étude géochimique et structurale des suites Galiléia et Urucum et leur relation avec les pegmatites à éléments rares associées*. These Docteur, Ecole Nationale Supérieure des Mines de Paris, pp. 237

Nalini Jr.H.A., Machado R.M., Bilal E. 2005. Geoquímica e petrogênese da Suíte Galiléia: exemplo de magmatismo tipo I, metaluminoso, pré-colisional, neoproterozóico da região do Médio Vale do Rio Doce. *Revista Brasileira de Geociências*, **35**:23-24.

Nalini Jr.H.A., Machado R., Bilal E. 2015. Petrogenesis and tectonic of the Urucum granitic suite, Rio Doce Valley (Minas Gerais – Brazil): an example of syn to late collisional peraluminous magmatism associated with high-angle transcurrent shear zone. *Brazilian Journal of Geology*, **45**:127-141

Oliveira M.J.R. 2000. *Folha Conselheiro Pena. Projeto Leste*. CPRM-CODEMIG. <http://www.portalgeologia.com.br/mapa/>.

Paes V.J. de C. 1999. *Geologia e Geoquímica da Região de Alvarenga, Minas Gerais: implicações geotectônicas e metalogenéticas*. Master Thesis. Universidade Federal de Minas Gerais, Belo Horizonte, Brasil, pp. 149.

Paes V.J. de C., Raposo F.O., Pinto P.C. Oliveira F.A.R. 2010. *Geologia e Recursos Minerais das Folhas Comercinho, Jequitinhonha, Almenara, Itaobim, Joáima e Rio do Prado*. Projeto Jequitinhonha, CPRM-CODEMIG, pp. 376.

Pankhurst R.J., Weaver S.D., Hervé F., Larrondo P. 1999. Mesozoic-Cenozoic evolution of the North Patagonian Batholith in Aysen, southern Chile. *Journal of the Geological Society of London*, **156**:673-694.

Parada M. A., Nyström J.O. & Levi B. 1999. Multiple sources for the Coastal Batholith of central Chile 31-34°S: geochemical and Sr-Nd isotopic evidence and tectonic implications. *Lithos*, **46**:504-521.

Patiño-Douce A.E. 1995. Experimental generation of hybrid silicic melts by reaction of high-Al basalt with metamorphic rocks. *Journal of Geophysical Research*, **100**:15623–15639.

Pedrosa–Soares A.C., De Campos C., Noce C.M., Silva L.C., Novo T., Roncato J., Medeiros S., Castañeda C., Queiroga G., Dantas E., Dussin I., Alkmim F.F. 2011. Late Neoproterozoic–Cambrian granitic magmatism in the Araçuaí Orogen (Brazil), the Eastern Brazilian Pegmatite Province and related mineral resources. *Geological Society London Special Publications*, **350**:25-51.

Pribavkin S.W., Avdonina I.S., Zamyatin D.A. 2013. Mineralogy, conditions of crystallization and melt generation of epidote-bearing porphyries from the Middle Urals, Russian Federation. *Mineralogy and Petrology*, **107**:125-147

Roberts M.P. & Clemens J.D. 1993. Origin of high potassium, calc-alkaline, I-type granitoids. *Geology*, **21**:825–828.

Rudnick R.L. & Fountain D.M. 1995. Nature and composition of the continental crust: a lower crust perspective. *Reviews of Geophysics*, **33**:267-309.

Samadi R., Mirnejad H., Kawabata H., Harris C., Valizadeh M.V., Gazel E. 2014. Magmatic garnet in the Triassic (215 Ma) Dehnow pluton of NE Iran and its petrogenetic significance. *International Geology Review*, **56**:596-691.

Schaltegger U., Brack P., Ovtcharova M., Peytcheva I., Schoene B., Stracke A., Marocchi M., Bargossi G.M. 2009. Zircon and titanite recording 1.5 million years of magma accretion, crystallization and initial cooling in a composite pluton (southern Adamello batholith, northern Italy). *Earth and Planetary Science Letters*, **286**:208–218.

Schmidt M.V. & Thompson A.B. 1996. Epidote in calc-alkaline magmas: An experimental study of stability, phase relationships, and the role of epidote in magmatic evolution. *American Mineralogist*, **81**:462-474.

Schmidt M.W. 1993. Phase relations and compositions in the tonalite as a function of pressure: an experimental study at 650°C. *American Journal of Science* **293**:1011-1060

Schmidt M.W. & Poli S. 2004. Magmatic Epidote. *Review in Mineralogy and Geochemistry*, **56**:399-430.

Schoene B. & Bowring S.A. 2010. Rates and mechanism of Mesozoic magmatic arc construction, eastern Kaapvaal craton, Swaziland. *Geological Society of America Bulletin*, **122**:408-429

Schoene B., Schaltegger U., Brack P., Latkoczy C., Stracke A., Günther D., 2012. Rates of magma differentiation and emplacement in a ballooning pluton recorded by U-Pb TIMS-TEA, Adamello batholith, Italy. *Earth and Planetary Science Letters*, **355–356**:162–173

Sial A.N., Toselli A.J., Saavedra J., Parada M.A., Ferreira V.P. 1999. Emplacement, petrological and magnetic susceptibility characteristics of diverse magmatic epidote-bearing granitoid rocks in Brazil, Argentina and Chile. *Lithos*, **46**:367-392.

Stevens G., Villaros A., Moyen J.-F. 2007. Selective peritectic garnet entrainment as the origin of geochemical diversity in S-type granites. *Geology*, **35**:9-12.

Tedeschi M., Novo T., Pedrosa-Soares A.C., Dussin I., Tassinari C., Silva L.C., Gonçalves L., Alkmim F.F., Lana C., Figueiredo C., Dantas E., Medeiros S., De Campos C., Corrales F.,

Heilbron M. 2016. The Ediacaran Rio Doce magmatic arc revisited (Araçuaí-Ribeira orogenic system, SE Brazil). *Journal of South American Earth Science*, **68**:167-186

Thompson A.B., Matile L., Ulmer P. 2002. Some thermal constraints on crustal assimilation during fractionation of hydrous, mantle-derived magmas with examples from central alpine batholiths. *Journal of Petrology*, **43**:403-422.

Vernon R.H., 2007. Problems in identifying restite in S-type granites in southeastern Australia, with speculation on source of magma and enclaves. *The Canadian Mineralogist*, **45**:147-178

Vielzeuf D. & Schmidt M.W. 2001. Melting relations in hydrous systems revisited: application to metapelites, metagreywakes and metabasalts. *Contribution Mineralogy and Petrology*, **141**:251-267

Villaros A., Stevens G., Buick I.S. 2009. Tracking S-type granite from source to emplacement: clues from garnet in Cape Granite suite. *Lithos*, **112**:217-235

Xu L., Xiao Y., Wu F., Li S., Simon K, Wörner G. 2013. Anatomy of garnets in a Jurassic granite from the south eastern margin of the North China Craton: magma sources and tectonic implication. *Journal of Asian Earth Science*, **78**:198-221

Zen E., 1985. Implications of magmatic epidote-bearing plutons on crustal evolution in the accreted terranes of northwestern North-America. *Geology*, **13**:266-269.

Zen E-an. & Hammarstrom J.M. 1984a. Magmatic epidote and its petrologic significance. *Geology*, **12**:515-518.

Zen E-an. & Hammarstrom J.M., 1984b. Mineralogy and a petrogenetic model for the tonalite pluton at Bushy Point, Revillagigedo Island, Ketchikan 1° x 2° Quadrangle, South-eastern Alaska. *U.S. Geological Survey, Circular 939*:118-123.

CHAPTER 2

THE GEOLOGY OF THE ARAÇUAÍ-WEST CONGO OROGENIC BELT

2.1 GENERAL GEOLOGY

Before the Cretaceous rifting that between 132 to 100 Ma opened the southern part of the Atlantic ocean (e.g. Torsvik *et al.*, 2009), the Araçuaí-West Congo (AWC) orogen (Fig. 2.1a) was an orogenic block surrounded to the west, north and east by the São Francisco - Congo Craton (Pedrosa-Soares & Wiedemann-Leonardos, 2000; Pedrosa-Soares *et al.*, 2001, 2008, 2011, Alkmim *et al.*, 2006; Pedrosa-Soares & Alkmim, 2011). This orogen formed during the Brasiliano/Pan-African Orogeny, a series of events that between the Neoproterozoic and early Paleozoic (640-520 Ma) led to the complete amalgamation of West Gondwana (Trompette, 1994, 1997, 2000; Brito-Neves *et al.*, 1999; Almeida *et al.*, 2000; Pedrosa-Soares *et al.*, 2001, 2011; Alkmim *et al.*, 2006). Contemporary other orogenic belts formed on the Atlantic side of both the South American and African cratons. Along the Brazilian eastern coast occurs the southern continuation of the Araçuaí orogen, the so-called Ribeira orogen which continues to the south as the Dom Feliciano orogen (Fig. 2.1b). Importantly, these orogens together form the Mantiqueira Province (da Silva *et al.*, 2005). On the African side from north to south there are the West Congo Belt, western flank of the AWC orogen, followed by the Kaoko, Damara and Gariep belts (Porada, 1989; Pedrosa-Soares *et al.*, 2001; Pedrosa-Soares & Alkmim, 2011).

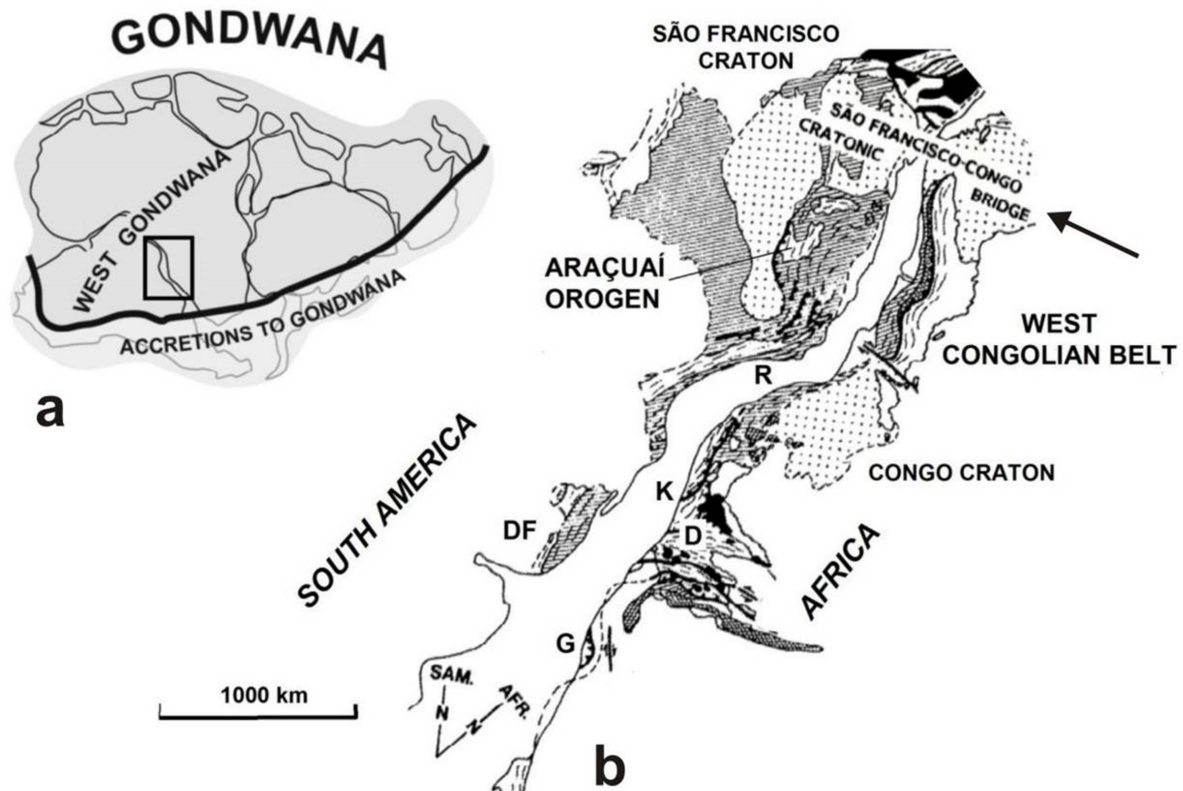


Figure 2.1: The Araçuaí-West Congo orogen. In a) location (black square) of the AWC orogen during the complete amalgamation of the West Gondwana; b) Distribution of the various orogens in both of the Atlantic sides. The Araçuaí and the West Congolian Belt as well as the São Francisco-Congo Craton and the Bahia-Gabon Bridge (black arrow) are also shown. DF: Dom Feliciano orogen; R: Ribeira Orogen; K: Kaoko orogen; D: Damara orogen; G: Gariiep belt (modified from Pedrosa-Soares & Alkmim, 2011).

2.2 ARCHITECTURE OF THE ARAÇUAÍ OROGEN

The Araçuaí orogen, represents about two thirds of the AWC orogen (Figs 2.1 and 2.2). This orogen occurs between the eastern border of São Francisco Craton and the eastern coast of the Atlantic Ocean, with its northern and southern limits drawn between the 15° and 21° latitude, respectively (Fig. 2.2; Pedrosa-Soares & Wiedemann-Leonardos, 2000; Pedrosa-Soares, *et al.*, 2001, 2011; Heilbron *et al.*, 2004; Alkmim *et al.*, 2006; 2017; Pedrosa-Soares & Alkmim, 2011). The northern boundary ends at the northern lobe of the São Francisco Craton, while the southern limit is marked by a NE deflection of the general NNE structural trend characterizing the Araçuaí belt (Pedrosa-Soares & Wiedemann-Leonardos, 2000). This orogen has been tectonically subdivided into the Araçuaí belt and Crystalline core (Fig. 2.2b) (Alkmim *et al.*, 2017 and references therein). Some authors (Pedrosa-Soares and Wiedemann-Leonardos, 2000; Pedrosa-Soares *et al.*, 2001) also subdivide the Araçuaí orogen in external and northern domain, whereas

they refer to the Crystalline as the high grade internal domain. According to Alkmim *et al.* (2017), the Araçuaí Belt is a N-S trending fold and thrust belt, juxtaposed over the eastern border of the São Francisco Craton by west-verging thrusts and made up of units showing greenschist to lower amphibolite facies metamorphism (Fig. 2.2c) (Pedrosa-Soares & Wiedemann-Leonardos, 2000; Heilbron *et al.*, 2004; Pedrosa-Soares *et al.*, 2001). The high grade internal domain is the Crystalline core of the orogen, recording the highest metamorphic grade and characterized by the widespread occurrence of granitic rocks. In the northern domain, both the tectonic features of the two former domains occur and are characterized by an E-W curvature direction. In this area the metamorphic grade increases from greenschist to upper amphibolite facies from north to south, and a northward thrusting system is present (Pedrosa-Soares & Wiedemann-Leonardos, 2000).

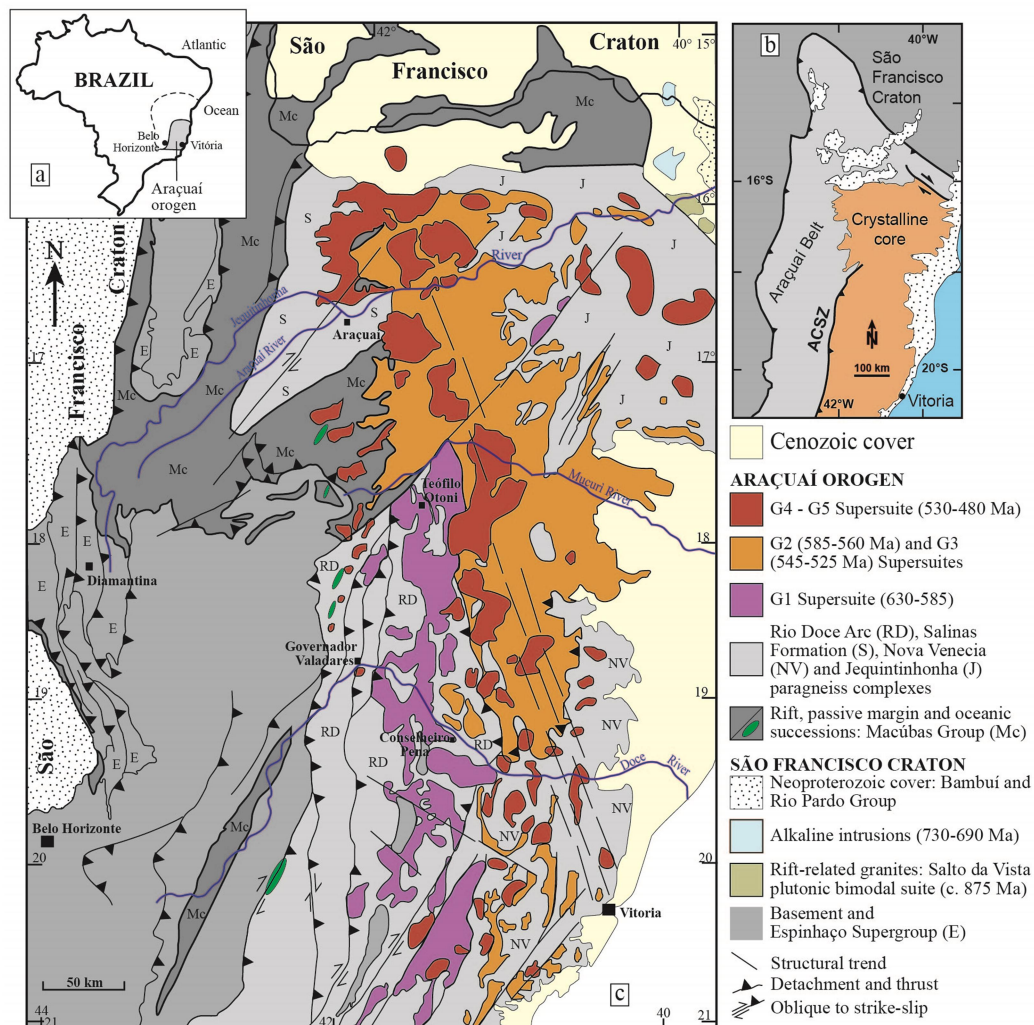


Figure 2.2: The Araçuaí orogen. (a) Localization of the Araçuaí orogen in SE Brazil; (b) subdivision of the Araçuaí orogen in Araçuaí belt and Crystalline core; (c) geotectonic map of the Crystalline core; the green ellipsoids represent the location of the ophiolitic slivers (modified after Pedrosa-Soares & Alkmim, 2011 and Alkmim *et al.*, 2017).

Based on deformation history, shear sense and structural style Alkmim *et al.* (2006) proposed an alternative subdivision of the AWC (Fig. 2.3). These authors identified the following ten domains.

1-The Serra do Espinhaço Fold-Thrust Belt is a 700 km N-S west-verging structure, fringing the eastern side of the Sao Francisco Craton and containing rocks from the Archean basement, the Espinhaço Supergroup and the Macaúbas Group.

2-The Chapada Acauã shear zone (Marshak *et al.*, 2006) shows that the relative plateau with an area of 50 km wide and 150 km long on the eastern side of the Serra do Espinhaço and covered by lithologies belonging to Macaúbas Group is the hanging wall of this regional east-dipping shear zone.

3- The Minas Novas Corridor is a 30 km wide and 150 km long hallway with dextral strike-slip shear zone cutting the Macaúbas Group metapelites.

4- The Rio Pardo Salient domain comprises a zone (latitude 16°S) in which the internal trend-lines of the Serra do Espinhaço Fold-Thrust Belt deviates in a regional-scale, convex-to- the foreland curve. This domain includes rocks of both the Espinhaço Supergroup and Macaúbas Group (Cruz & Alkmim, 2006). All together form the Paramirim Aulacogen, a N-NW-trending suture which is also the boundary between the north-eastern and southern lobe of the São Francisco Craton. This aulacogen formed when the Espinhaço rift was reactivated during the opening of the Macaúbas basin and was subsequently partially inverted during the Barsiliano orogeny (Cruz & Alkmim, 2006). In fact, the main reason for joining these two domains together is because in the southern portion of this aulacogen, the extensional structures were inverted during the Brasiliano orogeny, creating thrusts folds and folds associated with the Rio Pardo Salient domain.

5- The Guanhães Basement Block is located south of the Serra do Espinhaço Fold-Thrust Belt. This domain, exposed over an area of ca. 35000 km², is formed by Archean basement and Palaeoproterozoic meta-sedimentary units with granitic intrusions (1.75 Ga) with anorogenic affinities (e.g. Silva *et al.*, 2008). The boundaries of the Guanhães basement block are defined by is surrounded by shear zones. The western margin is a foreland-west verging thrust that juxtaposes the Guanhães Block over the Espinhaço Supergroup; the south-eastern margin is delimited by the Dom Silvério shear zone that places the Rio Doce metapelites against the basement rocks. Finally, the northern margin is characterized by a shallowly dipping shear zone bringing the Macaúbas Group over the Guanhães Block.

6- The Dom Silvério shear zone is ca. 100 km long and 4 km wide sinistral NNE-trending steeply dipping belt consisting of mylonitic rocks and terminating on the northern sector on the dextral strike-slip Abre Campo shear zone (Peres *et al.*, 2004).

7- The Itapebi shear zone is a NW-trending shear zone having a general dextral transpressive movement that delineates the northern limit of the Araçuaí Belt. It cuts the Archean basement, the Salto da Vista anorogenic granites and the Jaquitinhonha Complex.

8- The high grade, internal zone is made up of granitoid rocks of the G1-G5 Supersuites (Pedrosa-Soares & Wiedemann-Leonardos, 2000; Pedrosa-Soares *et al.*, 2011; Gonçalves *et al.*, 2014; 2016; 2018; Tedeschi *et al.*, 2016; Alkmim *et al.*, 2017) as well as of the Jequitinhonha and Paraíba do Sul paragneiss complexes (Dias Gonçalves *et al.*, 2016). This internal zone is further subdivided into two structural subdomains (Alkmim *et al.*, 2006). The northern subdomain (between 16° and 19°S) is characterized by SW vergence formed by shallowly- to moderately-dipping thrusts with a dextral strike-slip component (Pedrosa-Soares *et al.*, 1992, 2001; Pedrosa-Soares & Wiedemann-Leonardos, 2000; Heilbron *et al.*, 2004; Pedrosa-Soares & Alkmim, 2011, Alkmim *et al.*, 2006). In the western side of this subdomain remnants of ocean-floor mafic to ultramafic rocks (ophiolitic slivers) have been identified and interpreted as evidence of a Neoproterozoic subduction event (e.g. Pedrosa-Soares *et al.*, 1992, 1998, 2001; Peixoto *et al.*, 2013 and references therein). The southern subdomain (S of 19°S), is characterized by granulite facies rocks and granitic plutons, and shows steeply-dipping dextral shear zones. These features have been related to the exhumation of the deepest crustal levels of the Araçuaí orogen (Pedrosa-Soares & Wiedemann-Leonardos, 2000; Pedrosa-Soares *et al.*, 2001; Heilbron *et al.*, 2004). In this domain the Abre-Campo shear zone represents a major geophysical and structural discontinuity, whose role and significance is still debated (cf. Alkmim *et al.*, 2006). This shear zone marks the transition between the Araçuaí belt and the Crystalline core and was initially interpreted as Paleoproterozoic in age because it juxtaposes the Archean amphibolite facies Mantiqueira complex to the west with the granulite facies Paleoproterozoic Juiz de Fora Complex and Pocrane complexes to the east (i.e. Crystalline core) (Cunningham *et al.*, 1998, Fischel *et al.*, 1998; Brueckner *et al.*, 2000; Noce *et al.*, 2007a, 2007b). North of the 19°S, the pre-collisional arc-related G1 granitoids lie just to the east of this tectonic suture, leading some workers (Cunningham *et al.*, 1996, 1998) to consider the Abre-Campo Shear zone as having been active during the Brasiliano Orogeny, because this tectonic evidence could suggest the shear zone is the closure suture of the oceanic portion of the Macaúbas basin.

9- The West Congo belt defines an ENE-verging fold-thrust belt and it is generally believed to have been formed by the closure of the eastern portion of the Macaúbas basin (e.g. Alkmim *et al.*, 2006). Along this orogen the basement rocks were thrust eastward over Neoproterozoic high-grade metasediments (i.e. the Zadinian and Mayumbian Group; Tack *et al.*, 2001). These in turn were thrust over the diamictites of the West Congolian Group characterized by greenschist facies metamorphism. Magmatism in this belt is related to the Rodinian rifting stages (1.0 – 0.9 Ga; Tack *et al.*, 2001).

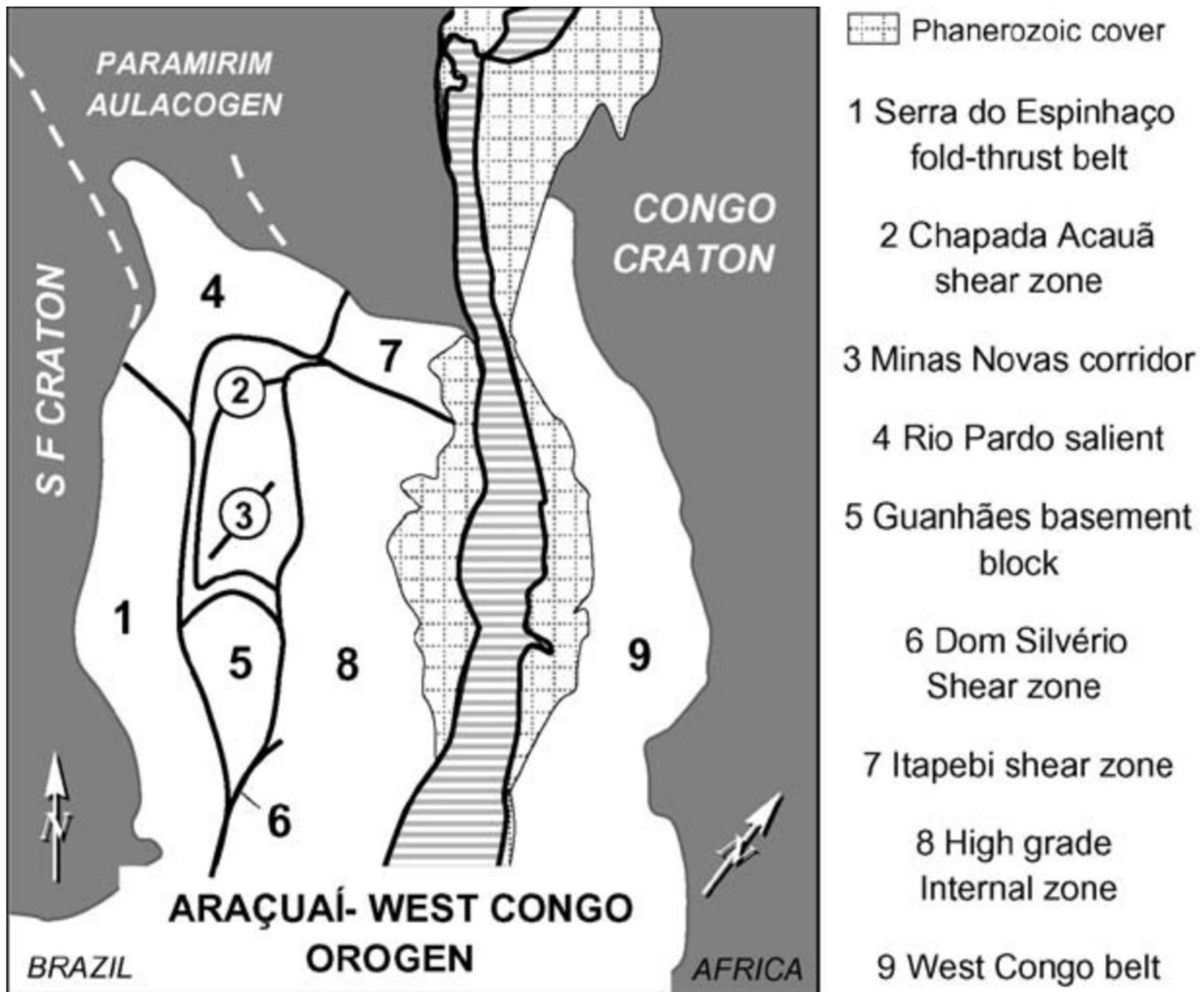


Figure 2.3: Structural domains of the Araçuaí-West Congo orogen (From Alkmim *et al.*, 2006).

2.3 OVERVIEW ON THE STRATIGRAPHY OF THE ARAÇUAÍ OROGEN

2.3.1 The Basement of the Araçuaí orogen

Following the criteria proposed by Almeida *et al.* (1981) and subsequently adopted by Alkmim *et al.* (2006), in this section only the rocks older than 1.8 Ga will be described.

The basement crops out in the Araçuaí belt and Crystalline core (Fig. 2.2). In the former domain, basement is mainly composed of Archean tonalite-trondhjemite-granodiorite (TTG) gneisses and the remnants of greenstone belts. Paleoproterozoic rocks supracrustal and granitoid intrusions that record reworking processes during the Trans-Amazonian and the Brasiliano orogenic periods (Pedrosa-Soares & Wiedemann-Leonardos, 2000; Pedrosa-Soares *et al.*, 2001; Alkmim *et al.*, 2017 and references therein). In the Crystalline core, the Archean and Paleoproterozoic complexes crop out mainly south and to the east of the city of Conselheiro Pena (S of 19°S). These complexes are composed of upper amphibolite- to granulite facies gneisses. Paleoproterozoic ages characterize the Juiz de Fora and Pocrane complexes (Pedrosa-Soares *et al.*, 2001; Novo 2013; Gonçalves *et al.*, 2014, 2018). Archean-Paleoproterozoic rocks are also present in the northern sector of the Araçuaí belt (Itabuna Complex). These rocks represent the Paleoproterozoic linkage between the São Francisco and Congo Cratons through the Bahia-Gabon bridge (e.g. Heilbron *et al.*, 2004), occurred during the Trans-Amazonian Orogeny (see Fig. 2.1).

2.3.2 Late Paleoproterozoic to Mesoproterozoic sequences

In the Araçuaí orogenic belt, this time interval is almost totally represented by the Espinhaço Supergroup (Figs. 2.2 and 2.4). This Supergroup subdivided in nine Formations, represent a package of 6000 m made up of metasediments, metaconglomerates, metapelites with subordinate occurrence of carbonates and metavolcanics, all of which experienced up to greenschist facies metamorphism (Danderfer *et al.*, 2009; Chemale *et al.*, 2012; Alkmim *et al.*, 2017). These formations record mainly tectonic rifting events. Evidence of the first rifting event, the so-called “Espinhaço rift event” is preserved mainly in the Bandeirinha and São João da Chapada formations that comprise sandstones, pelites, conglomerates (Uhlein *et al.*, 1998; Pedrosa-Soares *et al.*, 2001; Alkmim *et al.*, 2006; Pedrosa-Soares and Alkmim, 2011; Chemale *et al.*, 2012 and references therein) and bimodal volcanic rocks and granites with ages between 1.75 – 1.70 Ga (Machado *et al.*, 1989; Dussin & Dussin, 1995). The second extensional stage is preserved mainly at the northern part of the Espinhaço Range located roughly between the margin of the São Francisco Craton and the Paramirim Corridor (Fig. 2.2). This rift is characterized through the extrusion of alkaline to peralkaline trachyte at ca. 1.57 Ga (Danderfer *et al.*, 2009). The third rifting Stage (see Alkmim *et al.*, 2006 and reference therein), is recorded by a sedimentary sequence with alternating sandstones, pelites and carbonates (Uhlein *et al.*, 1998; Pedrosa-Soares *et al.*, 2000; Pedrosa-Soares and Alkmim, 2011) and by the presence of mafic dyke swarms cutting the older Espinhaço Formations. These basaltic dykes have tholeiitic affinities (De Min *et al.*, 2005) and crystallization ages between ca. 1.1 to 0.85 Ga (Machado *et al.*, 1989; Danderfer *et al.*, 2009) are found mainly along the eastern

border of the São Francisco Craton and represent the separation between the São Francisco Craton and the Congo Craton. At the same time (ca. 875 ± 9 Ma) emplacement of A-Type granites of the Salto da Divisa suite occurred. Consequently, south of 18°S , this rift stage culminated with the Macaúbas rifting phase which created a narrow ocean basin, the so-called Macaúbas basin, filled by volcano-glacio-sedimentary material (i.e. Macaúbas Group) (e.g. Alkmim *et al.*, 2006; Kuchenbecker *et al.*, 2015; Alkmim *et al.*, 2017).

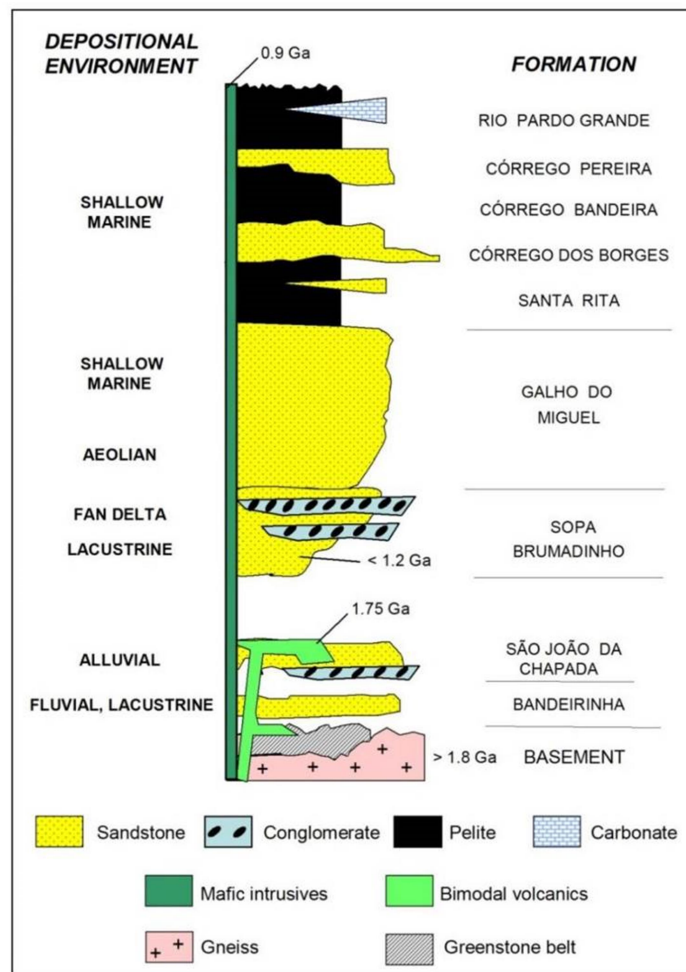


Figure 2.4: Stratigraphic column for the Espinhaço Supergroup in the Araçuaí belt (From Pedrosa-Soares & Alkmim, 2011).

2.3.3 Neoproterozoic rift-related rocks successions

The Macaúbas Group (Fig. 2.2 and 2.5) is a rock succession (up to 10 km thick) characterizing the external portion of the Araçuaí orogen (i.e. Araçuaí belt). It shows proximal deposits containing both non-glacial and glacial deposits, with minor occurrence of basic volcanics all of which have been metamorphosed at greenschist facies (Pedrosa-Soares *et al.*, 2001; Alkmim *et al.*, 2006; Pedrosa-Soares & Alkmim, 2011). This group it is divided in three major succession

(Fig. 7): 1) non-glacial succession comprising the Matão, Duas Barras, Capelinha, Planalto de Minas and Rio Peixe Bravo Formations, 2) the glacial-bearing diamictite-rich rocks of the Serra do Catuni, Nova Aurora and Lower Chapada Acauã Formations and 3) the post-glacial diamictite-bearing Upper Chapada Acauã and the Ribeirão da Folha formation (Kuchenbecker *et al.*, 2015; Souza *et al.*, 2017 and references therein). The Chapada Acauã Formation consists of the Rio Preto, Mato Grande and Posses Member (c.f. Pedrosa-Soares & Alkmim, 2011). Notably, the Ribeirão da Folha formation hosts slices of oceanic meta-mafic and meta-ultramafic rocks representing a tectonically dismembered ophiolite complex (Pedrosa-Soares *et al.*, 1992, 1998, 2001, Queiroga *et al.*, 2007; Pedrosa-Soares and Alkmim, 2006). A U-Pb zircon age from one of these ophiolites gave an age of ca. 600 Ma (LA-ICP-MS U-Pb age on zircon Queiroga 2010) while an associated plagiogranite yielded an age of 660 ± 29 Ma (LA-ICP-MS U-Pb age on zircon; Queiroga *et al.*, 2007). These data are interpreted as the evidence of ocean spreading between 660 to 600 Ma.

Recently, Kuchenbecker *et al.*, (2015) contributed in understanding the initial and final depositional history of the Macaúbas Group. The history of this group would start around 930 Ma to conclude at ca. 630 - 600 Ma with the closure of the basin occurred around 580 – 545 Ma.

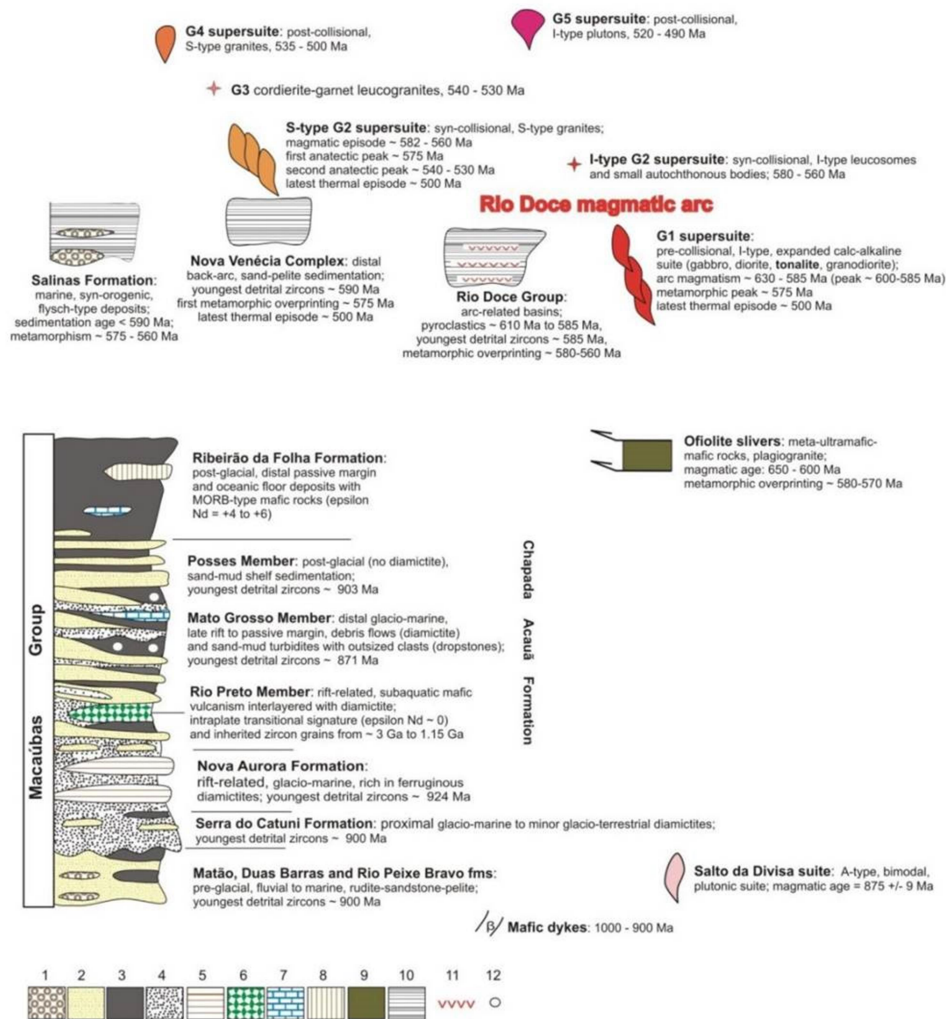


Figure 2.5: Stratigraphic succession for the Neoproterozoic rift-related, pre-and orogenic-related rocks units. For the Macaúbas Group: 1) rift-related mafic volcanic rocks; 2, conglomerates; 3, diamicites; 4, sandstones; 5, pelites; 6, carbonate rocks; 7, glaciogenic iron formation; 8, sulphide-bearing cherts and diopsidites with massive sulphide bodies, and banded iron formations (volcanic-exhalative rocks); 9, mafic and ultramafic rocks of ophiolite slivers; 10, greywacke–pelite association; 11, detrital iron formation; 12, dropstones. (From Pedrosa-Soares & Alkmim, 2011, modified).

2.3.4 Neoproterozoic pre-and orogenic-related rocks units

The so-called Rio Doce Arc, located in the internal part of the Araçuaí orogen (Pedrosa-Soares *et al.*, 2008) comprises igneous, volcanic and metasedimentary rocks representing the four main orogenic stages named pre-collisional (c. 630 – 585 Ma), syn-collisional (c. 585 – 560 Ma), late-collisional (c. 560 – 530 Ma) and finally post-collisional (c. 530 – 480 Ma), are those identifying igneous rocks represented by granitoid stocks and batholiths with I- and S-type affinity were emplaced (Fig. 2.2 and 2.5) between the late Neoproterozoic and the end of Cambrian covering an area of approximately 450 km long and 250 km wide (e.g. Pedrosa-Soares *et al.*, 2011). This long lasting granitoid magmatism has been divided into five Supersuites (from G1 to G5). According to Pedrosa-Soares *et al.* (2001; 2008; 2011) the I-type G1 Supersuite formed during the

pre-collisional, oceanic subduction-related phase, whereas the S-type granite-dominated G2 Supersuite (cf. Pedrosa-Soares & Alkmim, 2011; Gardim *et al.*, 2015; Melo *et al.*, 2017a; 2017b) is assigned to the syn-collisional stages. The S-type G3 granitoids formed during the transition between the syn-collisional and late-collisional periods (ca. 545 – 525 Ma) (when the orogenic collapse took place). The S-type G4 and I-type G5 Supersuite are interpreted as being post-collisional, related to the gravitational collapse of the orogen (Pedrosa-Soares *et al.*, 2011; De Campos *et al.*, 2016).

2.3.4.1 The Rio Doce mesedimentary Group

Since this project is aimed to gain a better understanding of the pre-collisional I-type granitoids of the G1 Supersuite, a detailed description and state of the art of these rocks will be presented in Chapter 3.

Contemporaneous to the pre-collisional granitic magmatism, arc-related volcano-sedimentary material of the Rio Doce Group was deposited in an active margin setting (Fig. 2.2 and 2.5; Pedrosa-Soares *et al.*, 2001, 2008; Vieira, 2007). From structural and stratigraphic work in the Rio Doce Valley coupled with petrographic and geochronology studies, Vieira (2007) has subdivided this Group into four formations: the Tumiritinga, Palmital do Sul, São Tomé and João Pinto Formations. The first two formations are thought to be contemporaneous, while the last one is interpreted to be the youngest (Vieira, 2007). All these formations have experienced low to middle amphibolite facies metamorphism, except for the Tumiritinga formation which underwent upper amphibolite facies metamorphism ($T = 638 \pm 76 \text{ }^\circ\text{C}$; $P = 0.45 \pm 0.1 \text{ GPa}$ Casteñada *et al.*, 2009, in Vieira, 2007). Starting from the two older formations, the Tumiritinga rocks are shistose, sometimes of gneissic aspect and are intercalated with calc-silicate rocks. Field evidence suggests that the contact with the G1 granitoids is primary (i.e. intrusive) and tectonic (i.e. shear zone). Within these metasedimentary rocks localized partial melts are found in the form of quartzo-feldspathic veins, and foliated metavolcanic rock are observed (Vieira, 2007). The metamorphic banding reflects variation in quartz and feldspar in relation to biotite. The primary felsic mineralogical assemblage, allowed Vieira (2007) to classify this rock as a dacite, while accessory minerals are represented by rare poikiloblastic garnet, muscovite, zircon as well as opaques. The contemporaneous Palmital do Sul Formation differ from the Tumiritinga Formation on the basis of intercalations of arkosic micaceous-quartzites that overly directly over the Paleoproterozoic Pocrane Complex (Vieira, 2007). Volcanic rocks in the form of a fragment of a volcanic bomb have been found here as well. From petrographic studies this magmatic rock has been interpret as a dacitic tuff with having primary red biotite identified as Ti-rich biotite. Accessory minerals are zircon, titanite, allanite and opaques. The

São Tomé formation lies stratigraphically above these two formations. This is made of schists, with variable proportions of quartz, mica and plagioclase. Garnet, cordierite and sillimanite are also present (Vieira, 2007). The youngest formation, the João Pinto Formation consists of quartzites with rare intercalations of mica-quartz schist and calc-silicates. The protoliths are considered as being granodiorites, tonalities and diorite on the basis of abundant plagioclase, in this latter the source is thought to be a quartz-sandstone and silt-sandstone.

Geochemical studies of the two metavolcanic Formations (Palmital do Sul and Tumiritinga) have confirmed the petrographic classification and have allowed determine the volcanic source. Vieira (2007) interpret this silicic magmatism as produced from a mantle source with the interplay of lower crust-related melts. Steep REE patterns and high $(La/Yb)_N$ (up to 18.53) suggest that either restitic garnet remained in the source region or precipitated in the deepest part of a magma chamber. Contribution from the G1 granitoids is also taken in consideration in order to explain some felsic chemical signatures. The Tumiritinga and São Tomé Formations indicate that the tectonic environment was a continental active margin and deposition occurred in a basin related to a magmatic arc. U-Pb geochronology of zircons from the meta-sedimentary rocks of the Rio Doce Group overlap with the magmatic activity registered by the granitoid rocks of the G1 Supersuite (630 – 575 Ma; Nalini, 1997; Nalini *et al.*, 2005; Pedrosa-Soares *et al.*, 2001; Pedrosa-Soares & Alkmim, 2011; Mondou *et al.*, 2012). In fact, magmatic zircons found in volcanoclastic rocks give U-Pb (TIMS and U-Pb LA-ICP-MS) crystallization ages of 585 ± 4 Ma, whereas the youngest detrital zircon age from a turbiditic meta-sandstone is 594 ± 3 Ma (Vieira, 2007). Contribution from Paleoproterozoic basement is evident from the presence of detrital zircons from the São Tomé formation giving U-Pb ages (SHRIMP) between 2050 and 2200 Ma. Following the above statements, Vieira (2007) characterized the Rio Doce Group as a supracrustal sequence, consisting of metavolcanics and metasedimentary assemblages belonging to a magmatic arc, related to pre-collisional stages of the Araçuaí orogen. The Tumiritinga and Palmital do Sul Formations were deposited in a fore-arc (basin?) settings, while the São Tomé rocks were deposited in a back-arc basin. Moreover, the complex field-geochronological relationship found between the lower formations of the Rio Doce Group and the intruding G1 Galiléia granitoids were explained as different granitic pulses emplaced in different parts of the Rio Doce Group, which underwent deformation and erosion (Vieira 2007).

2.3.4.2 The Jequitinhonha and Nova Venecia complexes

The Jequitinhonha and Nova Venecia complexes are high-grade metasediments whose protoliths are interpreted as deposited in an arc-related setting. The former is located on the northeastern margin of the orogenic belt (Fig. 2.2), and is characterized by kinzigitic assemblages (mainly migmatized biotite gneiss) with protoliths that may reflect sediments deposited in the northern gulf linked to the Macaúbas basin during marine transgression, contemporaneous to the oceanic spreading of the basin (Pedrosa-Soares & Wiedemann-Leonardos, 2000; Pedrosa-Soares *et al.* 2001, 2008). Recently, Richter *et al.* (2015) gave a better understanding of the Nova Venecia complex. This complex represented by migmatites, granulites and granites records high grade metamorphism with the production, extraction and emplacement of peraluminous granitic magmas. The main rocks studied are biotite-garnet-cordierite or orthopyroxene metagreywacke (metatexites), garnet-bearing peraluminous granites and cordierite-garnet bearing felsic granulites. The history of this complex starts with sedimentation at 606 Ma (maximum depositional age), burial event around 602 Ma (P-T-t modelling; LA-ICP-MS zircon and monazite U-Pb ages; Melo *et al.*, 2017a) and the synchronous intrusion at ca. 593 Ma of granitoids belonging to the G1 and G2 supersuite. The metamorphic peak of the Nova Venecia complex happened from 575 – to 560 Ma and has been estimated between 0.45 to 0.75 GPa in a range of temperature of 750 to 850°C. A high temperature retrograde metamorphism (0.45 – 0.6 GPa, 640 – 800 °C) followed the previous event. This study also shows that metamorphic, as well as magmatic zircons and monazites record that two main heat pulses occurred between ca. 593 – 560 Ma and between ca. 523 – 495 Ma, although previous works infer a long-lasting heating since ca. 640 till ca. 480 Ma. The second heating event is in agreement with the intrusion of norite bodies at 520 up to 480 Ma. Importantly, Richter *et al.* (2015) showed that the crystallization of the G1 and G2 granitoids, previously considered as separate events following the pre and syn-collisional model of Pedrosa-Soares *et al.* (2001, 2011), is contemporaneous and lasted for at least 15 My, that is, between 595 – 570 Ma.

2.4 GEODYNAMIC EVOLUTION OF THE ARAÇUAÍ OROGENIC BELT

The Araçuaí-West Congo orogen was formed during the Brasiliano/Pan-African orogeny in response to the amalgamation of West Gondwana. The occurrence of oceanic mafic-ultramafic slivers within the Riberão da Folha formation (Macaúbas Group; Pedrosa-Soares *et al.*, 1992, 1998, 2001, 2008, 2011) as well as the I-type signature of G1 granitoids have been interpreted by many authors (Peixoto *et al.*, 2013 and reference therein) as lines of evidence supporting subduction of the Macaúbas oceanic slab below the Congolian Neoproterozoic belt in the early stage of evolution

of the Belt (630 to 580 Ma). This subduction predates the main collisional event that started at around 575 Ma, and is characterized by the emplacement of voluminous S-type granites and coeval high-grade metamorphism. In the next sub-section I will present this well-established model (the so-called Nutcracker model) following the reconstruction proposed by Alkmim *et al.* (2006, 2017)

Alternative models will be presented in the last sub-sections of this chapter. This set of models, proposed by Trompette *et al.* (1992), Trompette, (1994, 1997), Vauchez *et al.* (2007), Mondou *et al.* (2012), Petitgirard *et al.* (2012) and more recently by Fossen *et al.*, (2017), regard the Araçuaí orogen as a collisional belt in which subduction of a pre-existing oceanic crust was minor or absent.

2.4.1 The Nutcracker model

Stage I: The Espinhaço rift and the Macaúbas basin

Between ca. 1100 to 850 Ma (Fig. 2.6a; Machado *et al.*, 1989; Uhlein *et al.*, 1998; Almeida *et al.*, 2000; De Min *et al.*, 2005; Rosset *et al.*, 2007; Silva *et al.*, 2008; Danderfer *et al.*, 2009; Kuchenbecker *et al.*, 2015; Souza *et al.*, 2017 and references therein) the extensional movement reactivated along paleo-extensional structures where magmatism occurred previously at 1750 Ma (Uhlein *et al.*, 1998; Alkmim *et al.*, 2006) and ca. 1570 Ma (Danderfer *et al.*, 2009). This reactivation of an older rift systems led to the opening of the Macaúbas basin between the actual São Francisco and Congo Craton; this basin S of 18°S (present time), turned into a narrow oceanic basin (Pedrosa-Soares *et al.*, 1992, 2001, 2007). Evidence of this spreading event is represented by the occurrence of amphibolites interpreted as ocean-floor basalts dated at 816 ± 72 Ma (Sm/Nd whole rock isochron; e.g. Pedrosa-Soares *et al.*, 1998) and plagiogranites at 660 ± 29 Ma (LA-ICP-MS U-Pb age on zircon; Quieroga *et al.*, 2007).

Stage II: Initial closure of the Macaúbas basin

At approximately around 625 - 600 Ma (Fig. 2.6b; Pedrosa-Soares and Wideramann-Leonardos, 2000) the São Francisco-Congo, Paranapanema, and Kalahari Cratons start colliding, with the São Francisco-Congo Craton rotating counter-clockwise (Alkmim *et al.*, 2006). The resulting compressional strain led to the Macaúbas basin closure establishing an east-dipping oceanic crust subduction (e.g. Pedrosa-Soares *et al.*, 1998). This event was the engine for the building up the Rio Doce Magmatic Arc, and the generation of the G1 arc-related I-type granitoids (Pedrosa-Soares *et al.*, 2001). Alkmim *et al.* (2006) defined this orogen as “forced”, meaning that

external collisions were more efficient in producing crustal thickening and continuous magmatism, than a slab-pull force.

Stage III: The collisional stage and the end of the Macaúbas basin

The construction of the calc-alkaline magmatic arc ended around 585 Ma (Pedrosa-Soares & Widemann-Leonardos, 2000) and the nutcracker-like system continued its closure action producing north, west and east verging fold-thrust belts over the Paramirim aulacogen, São Francisco and West Congo Craton, respectively (Fig. 2.6c). The compressional event reached the metamorphic peak between 585 and 560 Ma, coeval with the emplacement of the G2 S-type granitoids (Pedrosa-Soares *et al.*, 2001, 2008, 2011).

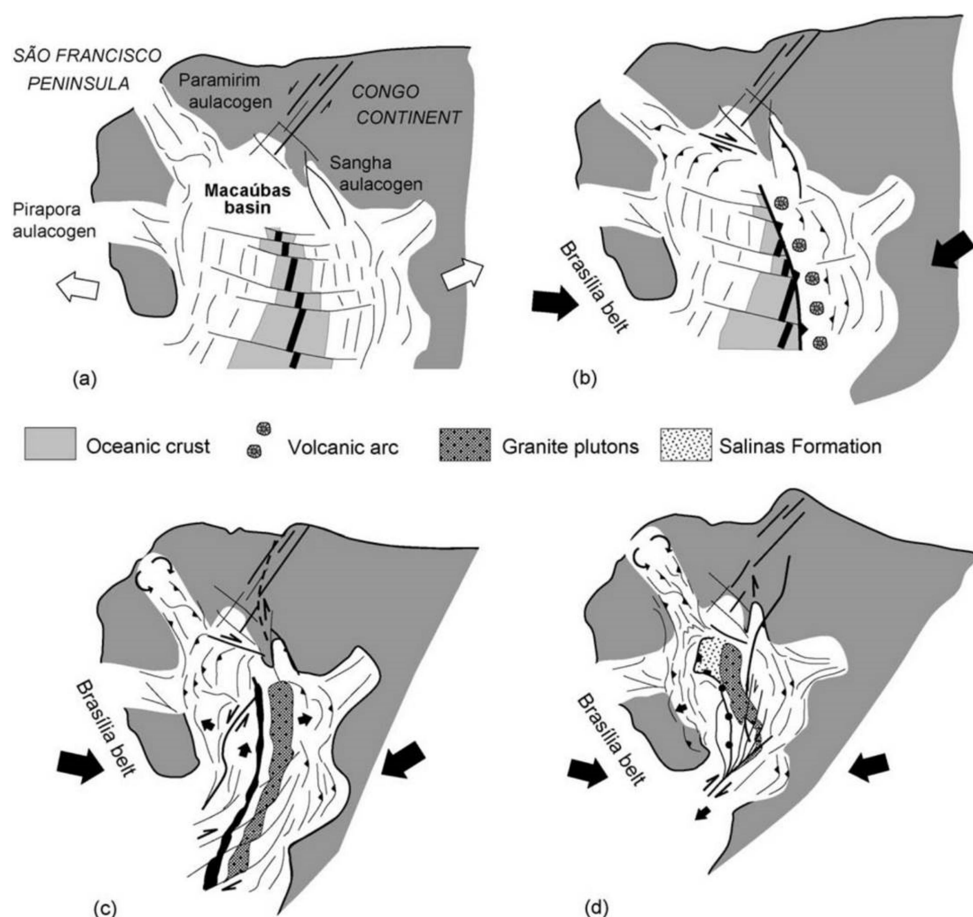


Figure 2.6: Palinspastic reconstruction of the Nutcracker model for the AWC orogen: a) stage I: The Espinhaço rift and the Macaúbas basin; b) stage II: Stage II: Initial closure of the Macaúbas basin; c) stage III: Stage III: The collisional stage and end of the Macaúbas basin; d) stage IV to V: Southwestern AWC orogen escapement and its collapse. Cartoon modified from Alkmim *et al.* (2011).

Stage IV to V: Southwestern AWC orogen escapement and its collapse

During the fourth stage (560-535 Ma) the Kalahari Craton collided with the southernmost portion of the Congo Craton. During this time the southern branches of the Brasiliano/Pan-African orogenic system formed, (Fig. 2.6d) creating the space problem, that is stress arrangements in its southern portion. The solution to the space problem proposed by Alkmim *et al.* (2006), is the lateral escape of material occurred by a system of shear zone consisting of northeast-trending dextral strike-slip faults, which bent around the southern Archean-Paleoproterozoic lobe of the São Francisco Craton. The last period of tectonic activity occurred between 520 to 419 Ma. In this time the thickened crust in the northern half of the orogen collapsed, exposing the lowest part of the Araçuaí orogen. According to Alkmim *et al.* (2006) this collapse causes decompression and related partial melting of rocks belonging to the middle-lower section of the crust, triggering the G4 and G5 granitoid magmatism. The large volume of felsic magma produced during the inferred extensional collapse led Alkmim *et al.* (2006) to speculate on the role of mantle in supplying heat. These authors proposed two possible options that could account for the relatively voluminous post-collisional magmatism in the Araçuaí Belt. Whereas the first model suggests delamination and sinking of the lithospheric mantle as the process that heated the crust up, the second model considers the interaction between the rise of asthenospheric material due to extensional collapse episode, and the previously (?) subducted Macaúbas oceanic ridge (see also Gardim *et al.*, 2014).

2.4.2: The Araçuaí ensialic belt

Trompette (1997) geochronological and geotectonic data identify two categories of Brasiliano/Pan-African belts. The first were tectonically active since 1.0 – 0.9 Ga and ended around 600 Ma, having therefore an old long-lived (O-LL) cycle. The second one have a young short-lived cycle (Y-SL), starting around 600 Ma and concluded in Early Cambrian times (ca. 520 Ma). The same author recognize that the Araçuaí-West Congo belt has had an intracratonic O-LL orogenic cycle, marked by an oceanisation stage (cf. Pedrosa-Soares *et al.*, 1992, 1998), probably of limited width (cf. Trompette, 1997). Trompette (1994) argue against a rifted ocean and indicates the possibility of widespread fragments of cratonic nuclei between the São Francisco and Congo Craton. Trompette (1997) proposes that the tectonic evolution of the Araçuaí orogen could be seen as an intracontinental belt, with deep faults parallel to the axis belt and reaching the mantle in its internal part. An implication of this scenario, is that the Riberão da Folha ultramafic rocks would not be ophiolitic sequences, but just deep ultramafic oceanic-related slivers, dredged to the surface during the shortening events. Eventually, in the geodynamic reconstruction, Trompette (1997)

suggests a continent-continent interaction as a mechanism for the construction of the Araçuaí-West Congo orogen in which all the stresses (Trompette *et al.*, 1992) would have been accommodated by the deformations in the Brasiliano Espinhaço branch. According to Alkmim *et al.* (2006), this interpretation would not explain most of the geometric and kinematic aspects of the AWC orogen.

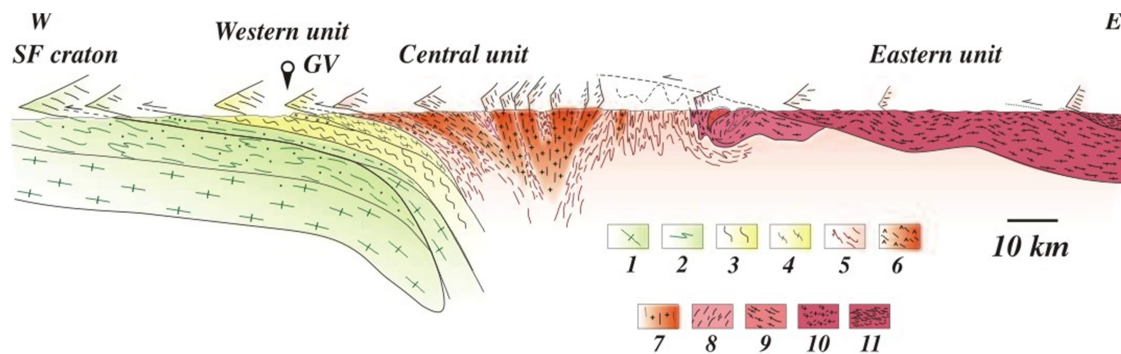


Figure 2.7: E-W schematic cross section of the Araçuaí belt in which are shown the three domains. From Vauchez *et al.* (2007): 1) granulites and 2) metasediments of the São Francisco Craton, 3) metasediments and 4) tonalitic mylonites of the western domain, 5) metasediments and the granitoids of the 6) São Vitor and 7) Galiléia Plutons belonging to the Central domain, and finally the Eastern domain made of 8) anatexites, 9) syn- to late collisional granitoids, and 10) kinzigitic mylonites. GV: Governador Valadares

2.4.3: The Araçuaí Hot orogen: deformation of a pervasively molten middle crust?

An alternative interpretation similar to that of Trompette (1997), was given by Vauchez *et al.* (2007) who consider the Araçuaí orogen as a “Hot Orogen”. These authors envisage similar features between the AWC orogen, the Tibetan Plateau and the Central Andean one. Geophysical surveys have demonstrated that both these two last belts are characterized by a middle crust having low seismic velocities, high attenuation and high electrical conductivity (e.g. Vauchez *et al.*, 2007). In numerical terms, the Tibetan middle crust (at ca. 15-18 km) has a temperature range of ~ 550 to ~ 700°C, with a geotherm of 37°C/km. In the Central Andean belt, the middle crust at ca. 20 km, is characterized by a temperature of ca. 650°, with a geotherm of 32°C/km. These data are quite similar and support the evidence that the middle and lower crust underlying the Tibetan and the Central Andean belt contain a thick (> 10 km) partially molten layer, i.e. contain large amounts of melt, in the form of anatexites and/or partially molten plutons (Vauchez *et al.* 2007). In these situations where the lithosphere is hot, its rheology change completely (Vauchez *et al.*, 2007 and reference therein). A quantity of melt less than of 7% (Rosemberg & Handly, 2005) coupled with a high temperature conditions, weakens the lithosphere strength implying that the strains are not

anymore localized, but are homogeneously distributed. This means that the rocks deform coherently and faults deformation is accommodated over weakkilometre scale shear zones (e.g. Vauchez *et al.*, 2007). These conditions are observed in many Archean to Proterozoic belts hosting TTG, migmatites and greenstone assemblages and also in other Phanerozoic active margins (Cagnard *et al.*, 2006). Using field, petrographic, anisotropy of magnetic susceptibility (AMS) and geochronological studies, Vauchez *et al.* (2007), Petitgirard *et al.* (2009), Mondou *et al.* (2012), Cavalcante *et al.* (2013) and lately Fossen *et al.*, (2017) recognize that the Araçuaí orogen, in the same time that it was experiencing HT-LP ($> 700\text{ }^{\circ}\text{C}$, 0.6 GPa), was also subjected to pervasive partial melting and widespread magmatism, developing a $\sim 300\text{ km}$ long, 50-100 km wide and $> 10\text{ km}$ thick anatectic domain.

2.4.3.1: The partially molten Araçuaí Crystalline Core

According to Vauchez *et al.* (2007), Petitgirard *et al.* (2009), Mondou *et al.* (2012) and Cavalcante *et al.* (2013) the Crystalline Core can be subdivided in three domains (western, central and eastern domain) (Fig. 2.7 and 2.8). All of them display similar and coherent deformation histories (i.e. strain distributed homogeneously), without strain localization along their contacts. Evidence for large volume of crust was deformed at high temperature subjected to a similar HT syn-kinematic conditions are given by similar U-Pb SHRIMP ages (Vauchez *et al.*, 2007) between the central domain composed of pre-collisional G1 granitoids ($576 \pm 5 - 594 \pm 6\text{ Ma}$; Noce *et al.*, 2000 and Nalini, 1997, respectively) and the western one, represented by the syn-collisional G2 rocks ($574.9 \pm 3.3\text{ Ma}$; Vauchez *et al.*, 2007). According to Vauchez *et al.* (2007) this evidence suggests the Crystalline Core had a weak lithosphere constituted by a pervasively molten-middle crust with a high geotherm of $30\text{-}35^{\circ}\text{C}/\text{km}$ and a slow cooling rate ($<5\text{ }^{\circ}\text{C}/\text{Ma}$; Petitgirard *et al.*, 2009). This is quite similar to the values reported above for the Tibetan and Andean Hot orogens, meaning that at the time of its formation, the Araçuaí orogen had a hot and weak lithosphere, behaving thus like an “Hot orogen”.

2.4.3.2: The Central Plutonic Unit

The studies of Mondou *et al.* (2012) and Fossen *et al.*, (2017) supports this model and especially they focus on the central magmatic (or plutonic) unit, which is also the subject of this PhD project. Mondou *et al.* (2012), performing AMS and field observations (Fig. 10), further subdivide the central magmatic unit in four sectors (Fig. 2.8a and 2.9), which show different magmatic flows (Fig. 2.8). The western part (sector 1) displays eastward dipping orogen-parallel

magmatic foliation probably related to the westward thrust over the São Francisco Craton, whereas to the east, although an orogen-parallel foliation still remains, sector 2 displays steeply dipping character coupled by rapid changes in horizontal to vertical lineation. This is interpreted as a zone of crustal thickening and transpression (lateral escape). Sector 3 may represent horizontal lateral escape flow, since it shows flat-lying foliations with ~ NS-trending lineation. A zone of sinistral transcurrent oblique with respect to the trend of the belt has been identified in the central domain, and constitutes the fourth sector (Mondou *et al.*, 2012). Furthermore, nine LA-ICP-MS U-Pb zircon ages in the central domain, shed light on the homogeneity of the obtained ages within the fourth sectors ($587 \pm 5 - 579 \pm 8$ Ma), even though they have different magmatic fabrics (Mondou *et al.*, 2012). Given that the deformation began around 580 Ma and lasted for tens of My, with a very slow cooling rates (<5 °C/My; Petitgirard *et al.*, 2009), this plutonic unit, emplaced by multiple granitic batches at the time of the orogenic events, suffered deformation before complete crystallization, which occurred more than 20 Ma later (Mondou *et al.*, 2012). This observation is also supported by thin section studies, which show that neither quartz nor feldspars show solid-state deformation, like undulate extinction or recrystallized grains.

2.4.3.3: An almost ensialic Neoproterozoic orogen

Mondou *et al.* (2012) explain that the reported data joined to those highlighted by Vauchez *et al.* (2007) corroborate the hypothesis of a Hot orogen character for the Araçuaí orogen, and argue against a pre-collisional character for G1 Granitic rocks (Pedrosa-Soares *et al.*, 2001). A similar explanation for the anatectic eastern domain of the Araçuaí belt, is given by Calvalcante *et al.* (2013). Such ideas lately culminated with the new model of Fossen *et al.* (2017). These authors speculate against a long-lived arc system (640 – 580 Ma) suggested by Pedrosa-Soares *et al.* (2011) and Gonçalves *et al.* (2016). According to Fossen *et al.* (2017) such long-lived arc system would have been produced at least 1000 km of subducted oceanic crust below the Congo Craton. In order to allow this convergence the Gabon bridge should have been broken up already one time before the Cretaceous. Consequently Fossen *et al.* (2017) propose that the subduction was limited and that after 625 Ma the Araçuaí orogen behaved as an ensialic, partially molten middle crust orogenic system.

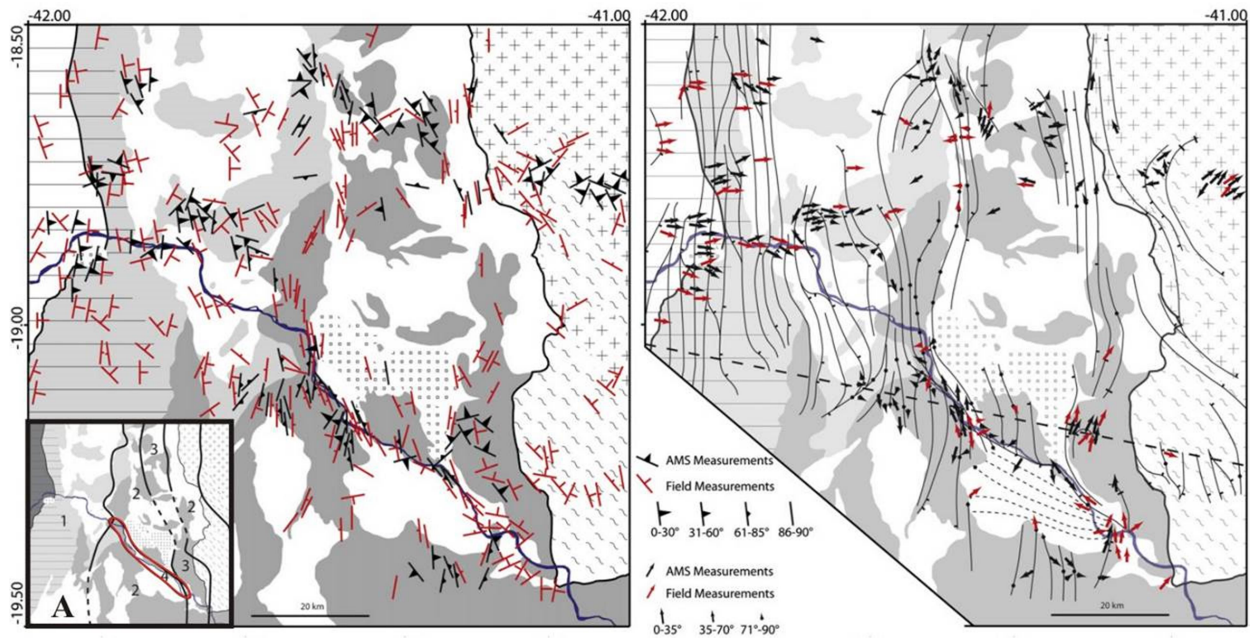


Figure 2.8: Map showing structural (left) and AMS (right) measurements within the central plutonic unit. Fig. A inset shows the subdivision of the central plutonic unit in 4 sections. The heavy red line identify the section 4. (From Mondou *et al.*, 2012, modified)

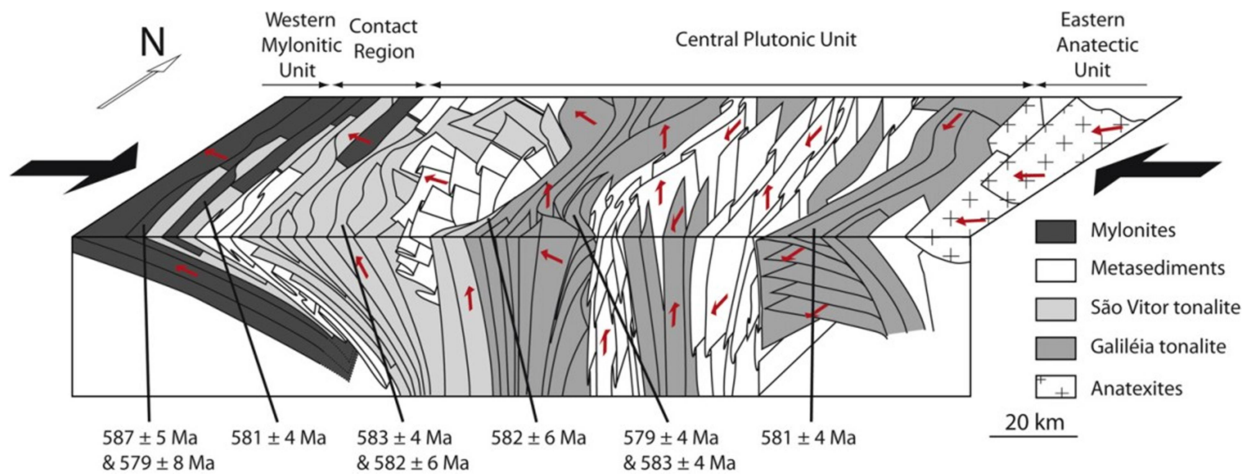


Figure 2.9: 3D diagram showing the structural interpretation of the central plutonic unit. Red arrows indicate the main flow directions, the big black arrows indicate the main strain direction, while the numbers identify the carried out ages. The image is not in scale while the dips at depth have been extrapolated. (From Mondou *et al.*, 2012, modified).

References

- Alkmim F.F., Kuchenbecker M., Reis H.L.S., Pedrosa-Soares A.C. 2017. The Araçuaí Belt. In: Heilbron M., Cordani U.G., Alkmim F.F. (Eds.) São Francisco Craton, Eastern Brazil, Tectonic Genealogy of a Miniature Continent, *Regional Geology Reviews, Springer International Publishing Switzerland*, p. 255-276
- Alkmim F.F., Marshak S., Pedrosa-Soares A.C., Peres G.G., Cruz S.C.P., Whittington A. 2006. Kinematic evolution of the Araçuaí-West Congo Orogen in Brazil and Africa: Nutcracker tectonics during the Neoproterozoic assembly of Gondwana. *Precambrian Research*, **149**:46-63.
- Almeida F.F.M., Brito Neves B.B., Carneiro C.D.R. 2000. Origin and evolution of the South American Platform. *Earth-Sciences Review*, **50**:77-111.
- Almeida F.F.M., Hasui Y., Brito-Neves B.B., Fuck R.A. 1981. Brazilian Structural provinces: An introduction. *Earth-Sciences Review*, **17**:1-29.
- Brito-Neves B.B., Campos Neto M.C., Fuck R. 1999. From Rodinia to Western Gondwana: an approach to the Brasiliano/Pan-African cycle and orogenic collage. *Episodes*, **22**:155-199.
- Brueckner H.K., Cunnigham., W.D., Alkmim F.F., Marshak S. 2000. Tectonic implications of Precambrian Sm-Nd dates from the southern São Francisco Craton and adjacent Araçuaí and Ribeira belts, Brazil. *Precambrian Research*, **99**:255-269.
- Cagnard F., Durrien N., Gapais D., Brun J.P. Ehlers C. 2006. Crustal thickening and lateral flow during compression of hot lithospheres, with particular reference to Precambrian Times. *Terra Nova*, **18**:72-78.
- Chemale F., Dussin I.A, Martins M.S., Alkmim F.F., Quiroga G. 2010. The Espinhaço Supergroup in Minas Gerais: A Stenian Basin? In *7th South American Symposium on Isotope Geology – VII SSAGI*, Brasília. Universidade de Brasília, p. 552-555.
- Cruz S.C.P. & Alkmim F.F. 2006. The tectonic interaction between the Paramirim Aulacogen and the Araçuaí belt, São Francisco Craton Region, Eastern Brazil. *Anais da Academia Brasileira de Ciências*, **78**:151-173.
- Cunningham W.D., Alkmim F.F., Marshak S. 1998. A structural transect across the coastal mobile belt in Brazilian Highlands (latitude 20°S): the roots of a Precambrian transpressional orogen. *Precambrian Research*, **92**:251-275.

Cunningham W.D., Marshak S., Alkmim F.F. 1996. Structural style of basin inversion at mid-crustal levels: two transects in the internal zone of the Brasiliano Araçuaí Belt, Minas Gerais, Brazil. *Precambrian Research*, **77**:1-15.

da Silva L.C., McNaughton N.J., Armstrong R., Hartmann L.A., Fletcher I.R. 2005. The Neoproterozoic Mantiqueira Province and its African connections: a zircon-based U-Pb geochronological subdivision for the Brasiliano/Pan-African systems of orogens. *Precambrian Research*, **136**:203-240

Danderfer A., De Waele B., Pedreira A.J., Nalini H.A. 2009. New geochronological constraints on the geological evolution of the Espinhaço basin within the São Francisco Craton-Brazil. *Precambrian Research*, **170**:116-128

De Campos C.P., de Madeiros S.R., Mendes J.C., Pedrosa-Soares A.C., Dussin I., Ludka I.P., Dantas E.L. 2016: Cambro-Ordovician magmatism in the Araçuaí Belt (SE Brazil): Snapshot from a post-collisional event. *Journal of South American Earth Sciences*, **68**:248-268

De Min A., Rosset A., Marques L.S., Chaves A., Piccirillo E.M. 2005. Widespread Late Mesoproterozoic Tholeiitic Magmatism of the São Francisco Craton (Brazil): Petrology, geochemistry and geotectonic settings. *Russian Geology and Geophysics*, **49**:981-992.

de Souza M.E.S., Sousa Martins M., Resende Madeira M., Queiroga G.N., Barbosa M.S.C. 2017. Interação tectônica entre bacias successoras no domínio externo do Orógeno Araçuaí: estudo de caso da região de Planalto de Minas, Minas Gerais. *Geologia USP, Série Científica*, **17**:143-156

Dias Gonçalves T., Caxito A.F., Pedrosa-Soares A.C., Stevenson R., Dussin I., da Silva L.C., Alkmim F., Pimentel M. 2016. Age, provenance and tectonic setting of the high-grade Jequitinhonha Complex, Araçuaí Orogen, eastern Brazil. *Brazilian Journal of Geology*, **46**:199-219

Dussin I.A., Dussin T.D. 1995. Supergrupo Espinhaço: Modelo de evolução geodinâmica. *Geonomos*, **3**:19-26.

Fischel D.P., Pimentel M.M., Fuck R.A., Costa A.G. Rosière C.A. 1998. Geology and Sm-Nd isotopic data for the Mantiqueira and Juiz de Fora complexes (Coastal Mobile belt) in the Abre Campo region, Minas Gerais, Brazil. In: *International Conference on Precambrian and Craton Tectonics*, Universidade Federal de Ouro Preto, Ouro Preto, Brazil, p. 21-23 (abstracts).

Fossen H., Cavalcante G.C., de Almeida R.P. 2017. Hot Versus Cold Orogenic Behaviour: Comparing the Araçuaí-West Congo and the Caledonian Orogens. *Tectonics*, **36**:2159-2178

Gonçalves L., Alkmim F.F., Pedrosa-Soares A., Gonçalves C.C., Vieira V. 2018: From the plutonic root to the volcanic roof of a continental magmatic arc: a review of the Neoproterozoic Araçuaí orogen, southeastern Brazil. *International Journal of Earth –Science*, **107**:337-358

Gonçalves L.E., Alkmim F.F., Pedrosa-Soares C.A., Dussin I.A., Valeriano, C.d.M., Nalini Jr.H.A. Lana C., Tedeschi M. 2016. Granites of the intracontinental termination of a magmatic arc: an example from the Ediacaran Araçuaí orogen, southeastern Brazil. *Gondwana Research*, **36**:439-458

Gonçalves L.E., Farina F., Lana C., Pedrosa-Soares C.A., Alkmim F.F., Nalini Jr.H.A. 2014. New U-Pb ages and lithochemical attributes of the Ediacaran Rio Doce Magmatic Arc, Araçuaí confined orogen, southeastern Brazil. *Journal of South American Earth Sciences*, **52**:1-20.

Heilbron M., Pedrosa-Soares A.C., Neto M., Da Silva L., Trouw R., Janasi V. 2004. Brasiliano Orogens in Southeast and South Brazil. In: Wienberg R., Trouw R., Hackspacher P. (Eds.), The 750-550 Ma Brasiliano Event of South America. *Journal of Virtual Explorer*. Electronic Edition, **17**:1-51

Kuchenbecker M., Pedrosa-Soares A.C., Babinski M., Fanning M. 2015. Detrital zircon age patterns and provenance assessment for pre-glacial to post-glacial successions of the Neoproterozoic Macaúnas Group, Araçuaí orogen, Brazil. *Precambrian Research*, **266**:12-26

Machado N., Schrank A., Abreu F.R., Knauer L.G., Almeida-Abreu P.A. 1989. Resultados preliminares da geocronologia U-Pb na Serra do Espinhaço Meridional. *Boletim do Núcleo Minas Gerais – Sociedade Brasileira de Geologia*, **10**:171-174.

Marshak S., Alkmim F.F., Whittington A., Pedrosa-Soares A.C. 2006. Extensional collapse in the Neoproterozoic Araçuaí orogen, eastern Brazil: a setting for reactivation of asymmetric crenulation cleavage. *Journal of Structural Geology*, **28**:129-147.

Melo M.G., Lana C., Stevens G., Pedrosa-Soares A.C., Gerdes A., Alkmim L.A., Nalini Jr. H.A., Alkmim F.F. 2017a. Assessing the isotopic evolution of S-type granites in the Carols Chagas Batholith: clues from U-Pb, Hf isotopes, Ti geothermometry and trace element composition of zircon. *Lithos*, **284-284**:730-750

Mondou M., Egydio-Silva M., Vauchez A., Raposo M.I.B., Bruiguiet O., Oliveira A.F. 2012. Complex, 3D strain patterns in a synkinematic tonalite batholith from the Araçuaí Neoproterozoic orogen (Eastern Brazil): Evidence from combined magnetic and isotopic chronology studies. *Journal of Structural Geology*, **39**:158-179.

Noce M.C., Noce M.C., Pedrosa-Soares A.C., da Silva L.C., Armstrong R., Alkmim F.F. 2007a. Evolution of a polycyclic basement complexes in the Araçuaí Orogen, based on U-Pb SHRIMP data: Implication for the Brazil-Africa links in the Paleoproterozoic time. *Precambrian Research*, **159**:60-78

Noce M.C., Pedrosa-Soares A.C., da Silva L.C., Alkmim F.F. 2007b. O embasamento Arqueano e Paleoproterozoico do Orógeno Araçuaí. *Geonomos*, **15**:17-23

Novo T.A. 2013. *Caracterização do Complexo Pocrane, Magmatismo Básico Mesoproterozóico e Unidades Neoproterozóicas do Sistema Araçuaí-Ribeira, com ênfase em Geocronologia U-Pb (SHRIMP e LA-ICP-MS)*. Ph.D Thesis. UFMG, Belo Horizonte, Brazil, pp. 193.

Pedrosa-Soares A.C. & Alkmim F.F. 2011. *The Brazilian Counterpart of The Araçuaí-West Congo Orogen*. Field Trip Guide. Rio de Janeiro, Brazil. pp. 44.

Pedrosa-Soares A.C. & Wiedemann-Leonardos, C.M. 2000. Evolution of the Araçuaí belt and its connection to the Ribeira Belt, Eastern Brazil. In: Cordani, U.G., Milani, E.J., Thomaz Filho, A., Campos, D.A. (Eds.), Tectonic Evolution of South America. *International Geological Congress*, Rio de Janeiro, pp. 265–285.

Pedrosa-Soares A.C., Alkmim F.F., Tack L., Noce C.M., Babinski M., Silva L.C., Martins-Neto M. 2008. Similarities and differences between the Brazilian and African counterparts of the Neoproterozoic Araçuaí-West Congo Orogen. In: Pankhurst J.R., Trouw R.A.J., Brito Neves B.B., De Wit M.J. (Eds.) West Gondwana: Pre-Cenozoic Correlations across the South Atlantic Region. *Geological Society of London, Special Publications*, **294**:153-172.

Pedrosa-Soares A.C., De Campos C., Noce C.M., Silva L.C., Novo T., Roncato J., Medeiros S., Castañeda C., Queiroga G., Dantas E., Dussin I., Alkmim F.F. 2011. Late Neoproterozoic–Cambrian granitic magmatism in the Araçuaí Orogen (Brazil), the Eastern Brazilian Pegmatite Province and related mineral resources. *Geological Society London Special Publications*, **350**:25-51.

Pedrosa-Soares A.C., Noce C.M., Vidal P., Monteiro R., Leonardos O.H. 1992. Toward a new tectonic model for the Late Proterozoic Araçuaí (SE Brazil) - West Congolian (SW Africa) Belt. *Journal of South American Earth Sciences*, **6**:33-47.

Pedrosa-Soares A.C., Noce C.M., Wiedemann-Leonardos C.M., Pinto C.P. 2001. The Araçuaí-West Congo Orogen in Brazil: an overview of a confined orogen formed during Gondwanaland assembly. *Precambrian Research*, **110**:307–323.

Pedrosa-Soares A.C., Vidal P., Leonardos O.H., Brito-Neves B.B. 1998. Neoproterozoic oceanic remnants in eastern Brazil: Further evidence and refutation of an exclusively ensialic evolution for the Araçuaí-West Congo orogen. *Geology*, **26**:519-522.

Peixoto E., Pedrosa-Soares A.C., Alkmim F.F., Dussin I.A. 2013. A suture-related accretionary wedge formed in the Neoproterozoic Araçuaí orogen (SE Brazil) during Western Gondwanaland assembly. *Gondwana Research*, **27**:878-896

Peres G.G., Alkmim F.F., Jordt-Evangelista H., 2004. The southern Araçuaí belt and the Dom Silvério Group: geologic architecture and tectonic significance. *Anais da Academia Brasileira de Ciências*, **76**:771–790.

Petitgirard S., Vauchez A., Egydio-Silva M., Bruguier O., Campos P., Monié P., Babinski M., Mondou M. 2009. Conflicting structural and geochronological data from the Ibituruna quartz-syenite (SE Brazil): effect of protracted “hot” orogeny and slow cooling rate? *Tectonophysics*, **477**:174-196.

Porada H. 1989. Pan-African rifting and orogenesis in southern to equatorial Africa and Eastern Brazil. *Precambrian Research*, **44**:103–136.

Queiroga G.N. 2010. *Caracterização de restos de litosfera oceânica do Orógeno Araçuaí entre os paralelos 17° e 21° S.* (PhD thesis). Universidade Federal de Minas Gerais.

Queiroga G.N., Pedrosa-Soares A.C., Noce C.M., Alkmim F.F., Pimentel M.M., Dantas E., Martins M., Castañeda C., Suita M.T.F., Prichard H. 2007. First dating of a plagiogranite found in Brazil: The U-Pb Zircon Age of the Ribeirão da Folha ophiolite, Araçuaí Orogen. *Geonomos*, **15**:61-65.

Richter F., Lana, C, Stevens G., Buick I., Pedrosa-Soares A.C., Alkmim F.F., Cutts K. 2015. Sedimentation, metamorphism and granite generation in a back-arc region: Records from the Ediacaran Nova Venécia Complex (Araçuaí Orogen, Southeastern Brazil). *Precambrian Research*, **272**:78-100

Rosenberg C.L. & Handy M.R. 2005. Experimental deformation of partially melted granite revisited: implication for the continental crust. *Journal of Metamorphic geology*, **23**:19-28.

Rosset A., De Min A., Marques L.S., Macambira M.J.B., Ernesto M., Renne P.R., Piccirillo E.M. 2005. Genesis and geodynamic significance of Mesoproterozoic and Early Cretaceous tholeiitic dyke swarms from the São Francisco Craton (Brazil). *Journal of South American Earth Sciences*, **24**:69-92.

Silva L.C., Pedrosa-Soares A.C., Teixeira L.R. 2008. Tonian rift-related, A-type continental plutonism in the Araçuaí orogen, Eastern Brazil: new evidences for the breakup stage of the São Francisco–Congo Palecontinent. *Gondwana Research*, **13**:527–537.

Tack L., Wingate M.T.D., Liégeois J.-P., Fernandez-Alonso M., Deblond A. 2001. Early Neoproterozoic magmatism (1000–910 Ma) of the Zadinian and Mayumbian Groups (Bas-Congo): onset of Rodinian rifting at the western edge of the Congo Craton. *Precambrian Research*, **110**:277–306.

Tedeschi M., Novo T., Pedrosa-Soares A.C., Dussin I., Tassinari C., Silva L.C., Gonçalves L., Alkmim F.F., Lana C., Figueiredo C., Dantas E., Medeiros S., De Campos C., Corrales F., Heilbron M. 2016. The Ediacaran Rio Doce magmatic arc revisited (Araçuaí-Ribeira orogenic system, SE Brazil). *Journal of South American Earth Science*, **68**:167-186

Torsvik T.H., Rouse S., Labails C., Smethurst M.A. 2009. A new scheme for the opening of the South Atlantic Ocean and the dissection of an Aptian salt basin. *Geophysical Journal International*, **177**:1315-1333.

Trompette R. 1994. Geology of Western Gondwana (2000–500 Ma). In: *Pan-African/Brasiliano aggregation of South America and Africa*. A.A. Balkema, Rotterdam, pp. 350.

Trompette R. 1997. Neoproterozoic (≈600 Ma) aggregation of Western Gondwana: a tentative scenario. *Precambrian Research*. **82**: 101–112.

Trompette R. 2000. Gondwana evolution; its assembly at around 600 Ma. *Comptes Rendus Academie Science Paris*, **330**:305-315.

Trompette R., Uhlein A., Egydio-Silva M.E., Karmann I. 1992. The Brasiliano São Francisco Craton revisited (central Brazil). *Journal of South American Earth Science*, **6**:49-57.

Uhlein A., Trompette R.R., Egydio-Silva M. 1998. Proterozoic rifting and closure, SE border of the São Francisco Craton, Brazil. *Journal of South American of Earth Science*, **11**:191–203.

Vauchez A., Egydio-Silva M., Babinski M., Tommasi A., Uhlein A., Liu D. 2007. Deformation of a pervasively molten middle crust: insights from the Neoproterozoic Ribeira-Araçuaí orogen (SE Brazil). *Terra Nova*, **19**:278-286.

Vieira V.S. 2007. *Significado do Grupo Rio Doce no Contexto do Orógeno Araçuaí*. Ph.D Thesis. IGC-UFMG, Belo Horizonte, Brasil, pp. 117.

CHAPTER 3

THE GRANITOIDS OF THE G1 SUPERSUITE – A STATE OF THE ART

3.1 GENERALITIES

The granitic bodies that constitute the G1 silicic suite are batholiths and stocks, named Brasilândia, Derribadinha, Divino, Estrela-Muniz Freire, Cuiete Velho, Muriaé, Manhuaçu, Mascarenhas-Baixo Gandu, Teófilo Otoni, Chapada do Bueno, São Vitor, and Galiléia (e.g. Pedrosa-Soares *et al.*, 2011; Gonçalves *et al.*, 2018 and reference therein). On the basis of field, textural and geochemical features Gonçalves *et al.* (2014) have subdivided these granitoids in three groups: 1) the Orthopyroxene-bearing rocks (i.e. charnokites), 2) the enclave-rich tonalite-granodiorite (ETG) and 3) enclave-poor granite to tonalite (GT).

The opx-bearing rocks are mainly constituted by the Derribadinha tonalite, a N-S elongated body located in the western part of the area investigated by Gonçalves *et al.* (2014). This intrusion lies between the Paleoproterozoic Juiz de Fora and Pocrane complexes. This batholith has an overall gneissic structure showing locally migmatitic and mylonitic features. The intrusion varies compositionally from tonalite to granite but locally, small bodies of enderbites as well as Opx-bearing diorities and gabbros have been described (e.g. Gonçalves *et al.*, 2014). The mafic mineral assemblage is represented by ortho and clinopyroxene, hornblende and biotite, with these minerals reaching up to 30 vol.% of the area (Gonçalves *et al.*, 2014).

The enclave-rich tonalite-granodiorite (ETG) and enclave-poor granite to tonalite (GT) groups characterize the São Vitor, Galiléia and Cuieté Velho batholiths (Fig. 3.1). Altogether they form a roughly N-S elongated body cropping out in the between the cities of Teófilo Otoni and Juiz de Fora, extending for an area of ca. > 15,000 km² (Vauchez *et al.*, 2007). These granitoid rocks consist mainly of tonalites and granodiorites and to a lesser extent of granites. Scarce mafic members (i.e. gabbros?) are also present. Moreover the granitoids host a variable but generally high volume of magmatic enclaves.

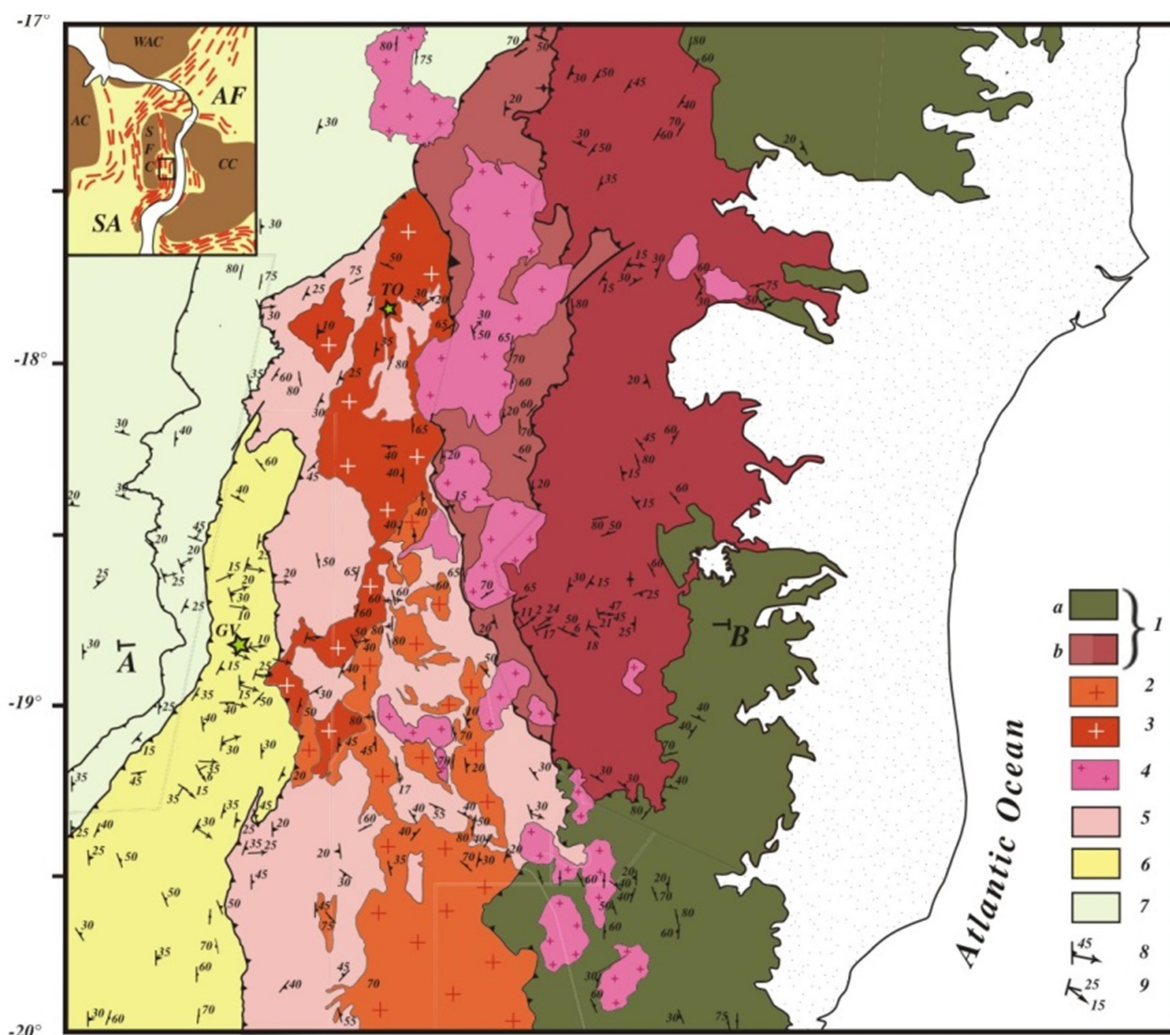


Figure 3.1: simplified map of the Araçuaí orogen. 1) a) diatexite, anatectic granites and migmatitic kinzigites and b) pre- to syn-collisional magmatism; 2) Galiléia and 3) São Vitor Plutons; 4) post- to late-collisional magmatism; 5) high temperature metasediments; 6) metasediments and meta-igneous mylonites thrust over the 7) São Francisco Craton. Also shown are 8) foliation and lineation measured in field and 9) AMS measurements. GV: Governador Valadares and TO: Teófilo Otoni cities. Inset, AWCO before the opening of the South Atlantic Ocean: AF and SA, Africa and South America Continents, respectively, while AC, SFC, CC and WAC are Amazonian, São Francisco, Congo and West African Cratons, respectively. From Vauchez *et al.* (2007), modified. The geological section A – B is the same showed in Fig. 2.7.

The granitoids forming the G1 suite are medium- to high-potassic calc-alkaline rocks of metaluminous composition (Nalini, 1997; Pedrosa-Soares *et al.*, 2001; 2011; Gonçalves *et al.*, 2014, 2016; 2018; Tedeschi *et al.*, 2016). Their position, composition and age, predating the main collisional event marked by the emplacement of voluminous S-type granitoids, has generated widespread consensus in interpreting the G1 Supersuite as representing the roots of a magmatic arc (Pedrosa-Soares *et al.*, 1998, 2001, 2008, 2011; Alkmim *et al.*, 2006; Gonçalves *et al.*, 2014, 2016; 2018; Tedeschi *et al.*, 2016)

One of the aims of this thesis is to investigate the petrographic, geochemical and geochronological variability characterizing the granitoids belonging to the G1 Supersuite. In particular, it will focus on the São Vitor and Galiléia batholiths, cropping out in the area delimited by the cities of Governador Valadares, São Vitor, Galiléia, Conselheiro Pena and Resplendor (Fig. 2.2). This area that have been mapped at 1:100.000 (Feboli, 2000; Feboli & Paes, 2000; Oliveira, 2000), are generally well-exposed with numerous road-cuts, river-beds and inactive quarries providing access to fresh outcrops.

In the following paragraphs, an overview on São Vitor and Galiléia granitoids will be proposed highlighting the following points:

- Age of the intrusions
- Main features recognized in the field
- Petrographic information and mineral chemistry
- Whole rock geochemistry

In the second part of this section the composition of the G1 (Galiléia) granitoids, that are interpreted by many authors as formed in a continental arc-related scenario will be compared with the composition of well-studied Cordilleran- and I-type granitoids. Moreover, the composition of the Galiléia granitoids will also be compared with that of the Bushy Point granitoids belonging to the Coast Mountain Batholith, Alaska. These Early Cretaceous subduction-related granodiorite to tonalite intrusions display similar textural and petrographic features with the rocks of the G1 suite, and for this reason deserve to be considered (Nalini 1997).

Finally, I will review the two main petrogenetic models for Cordilleran-type granitoid petrogenesis plus that suggested by Nalini (1997).

3.2 THE GALILEIA AND SÃO VITOR PLUTONS

3.2.1 Brief geochronological review

Geochronological data for the São Vitor pluton are scarce. Two LA-ICP-MS U-Pb zircon ages obtained from tonalites and two leucocratic intrusions (Mondou, 2010; Mondou *et al.*, 2012) range from 579 ± 8 and 587 ± 5 Ma. Brueckner *et al.* (2000) obtained a Sm-Nd isochrone of 563 ± 6 Ma from a foliated granodiorite.

In contrast to the São Vitor pluton, a robust age dataset exist for the Galiléia granitoids. Nalini (1997) and Gonçalves (2009) from a quarry close to the city of Conselheiro Pena, report two different ages, that is 594 ± 6 Ma (TIMS U-Pb zircon age) and 579 ± 8 Ma (LA-ICP-MS U-Pb zircon age), respectively. Zircon crystals belonging to a diorite enclave hosted within the granodiorite give a weighted mean age of 581 ± 3 Ma (LA-ICP-MS U-Pb zircon age; Gonçalves *et al.*, 2014), with one of the grain showing an inherited core of 2117 ± 9 Ma. Similar LA-ICP-MS U-Pb zircon ages falling between 579 ± 4 and 585 ± 4 Ma are obtained by Mondou *et al.* (2012) from Galiléia tonalities. A summary of all the ages for this central area of the Galiléia batholith is reported in table 3.1. Samples with poor geographical site location are ecluded.

Reference	Sample	E	S	Lithology	U-Pb Zircon Age (Ma)	Methodology
Mondou <i>et al.</i> (2010)	AR-264	190724	7906278	Contact tonalite	581 ± 4	LA-ICP-MS
Mondou <i>et al.</i> (2010)	AR-1057	198724	7900156	São Vitor tonalite	583 ± 4	LA-ICP-MS
Mondou <i>et al.</i> (2010)	AR-940	200318	7912478	Leucocratic intrusion	587 ± 5	LA-ICP-MS
Mondou <i>et al.</i> (2010)	AR-87-1	200523	7912814	Leucocratic intrusion	580 ± 8	LA-ICP-MS
Mondou <i>et al.</i> (2010)	AR-800	221388	7885889	São Vitor tonalite	582 ± 6	LA-ICP-MS
Mondou <i>et al.</i> (2010)	AR-787	231450	7881829	Galiléia tonalite	582 ± 6	LA-ICP-MS
Gonçalves (2009)	L003	239888	7880586	Galiléia granodiorite	579 ± 8	LA-ICP-MS
Gonçalves <i>et al.</i> (2014)	L003	239888	7880586	Galiléia diorite enclve	581 ± 3	LA-ICP-MS
Nalini (1997)	MD03	240143	7880577	Galiléia granodiorite	594 ± 6	TIMS
Mondou <i>et al.</i> (2010)	AR-705	240565	7877419	Galiléia tonalite	579 ± 4	LA-ICP-MS
Mondou <i>et al.</i> (2010)	AR-815	246171	7875394	Galiléia tonalite	583 ± 4	LA-ICP-MS
Mondou <i>et al.</i> (2010)	AR-717	263079	7877724	Galiléia tonalite	581 ± 4	LA-ICP-MS

Table 3.1: Table showing the name, location (UTM coordinates) and granitoid ages for the central area of the Galiléia Batholith and methodology implied. The ages are reported in column from W to E.

Recently, Tedeschi *et al.* (2016) reviewed the geochronological data for the Galiléia batholith. Analyzed samples now cover the whole batholith from north to the south. The work of Tedeschi

and co-workers allowed them to suggest that the Galiléia batholith is represented by three main intervals of magmatic crystallization with relative peak ages (Fig. 3.2):

- 1) The oldest magmatic activity, mainly recognized in the eastern and central zone of the batholith, ranges from 632 to 605 Ma with a peak at 625 – 615 Ma;
- 2) The second interval, widespread through the whole batholith, spans from 605 – 585 Ma and registered a peak of activity around 600 – 590 Ma;
- 3) The third and final period of metaluminous granitic magmatism seems to be more intense from the centre towards the western part of the batholith; here the peak is at 585 – 575 Ma, bracketed for an older and younger age of 585 to 570 Ma, respectively.

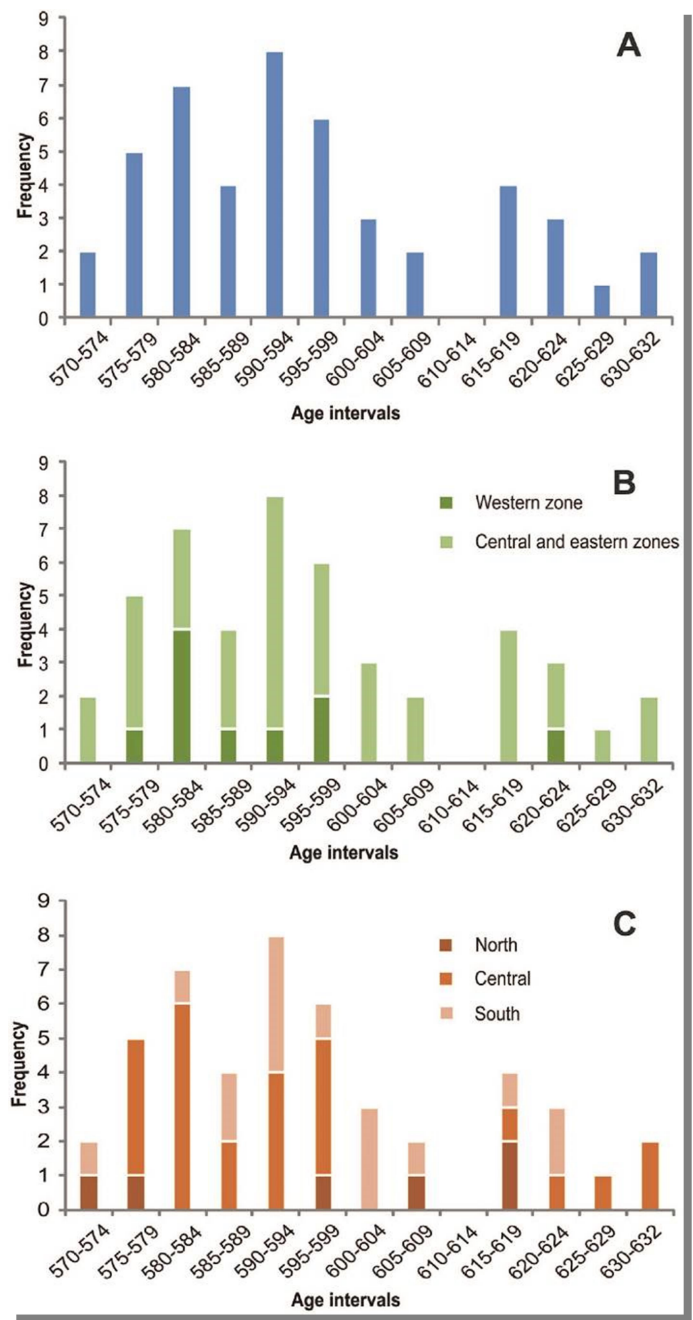


Figure 3.2.: U-Pb ages distribution histograms for the Rio Doce Arc. a: general diagram; b: ages from the western, central and eastern batholith; c: ages from the northern, central and southern part of the batholith. (Modified from Tedeschi *et al.*, 2016).

3.2.2 São Vitor and Galiléia Plutons: field relationships.

The best exposures of the São Vitor granitoids are along the main roads BR-259 and BR-381. The outcrops have mainly lens-shape in map view (Fig. 3.3a and Feboli, 2000). In general the rocks are coarse- to medium-grained garnet-hornblende-biotite grey gneiss (Fig. 3.3b; Feboli, 2000; Mondou *et al.*, 2012). Feboli (2000) and Mondou *et al.* (2012) agree that the São Vitor pluton hosts both magmatic enclaves and xenoliths (Fig. 3.3c). The granitoids have well-defined foliation that vary locally mylonitic to protomylonitic character (Feboli, 2001). Mondou *et al.* (2012) recognize that the foliation is alternately given by the alignment of, either hornblende or biotite, or in other locations by the long axes of the enclaves. The contact between São Vitor and Galileia Plutons is difficult to locate and/or recognize, even though Feboli (2000) report that the passage is transitional and could be marked by a presence of a whitish granitoid with large feldspar grains (ca. 5 cm). The Galiléia Pluton measures ~ 70 km in length and ca. 30 km wide (Nalini, 1997), has a NNW-SSE orientation and outcrops in the middle of the Rio Doce Valley, between the cities of Sapucaia do Norte, Galiléia, Conselheiro Pena, João Pinto (Fig. 3.1).

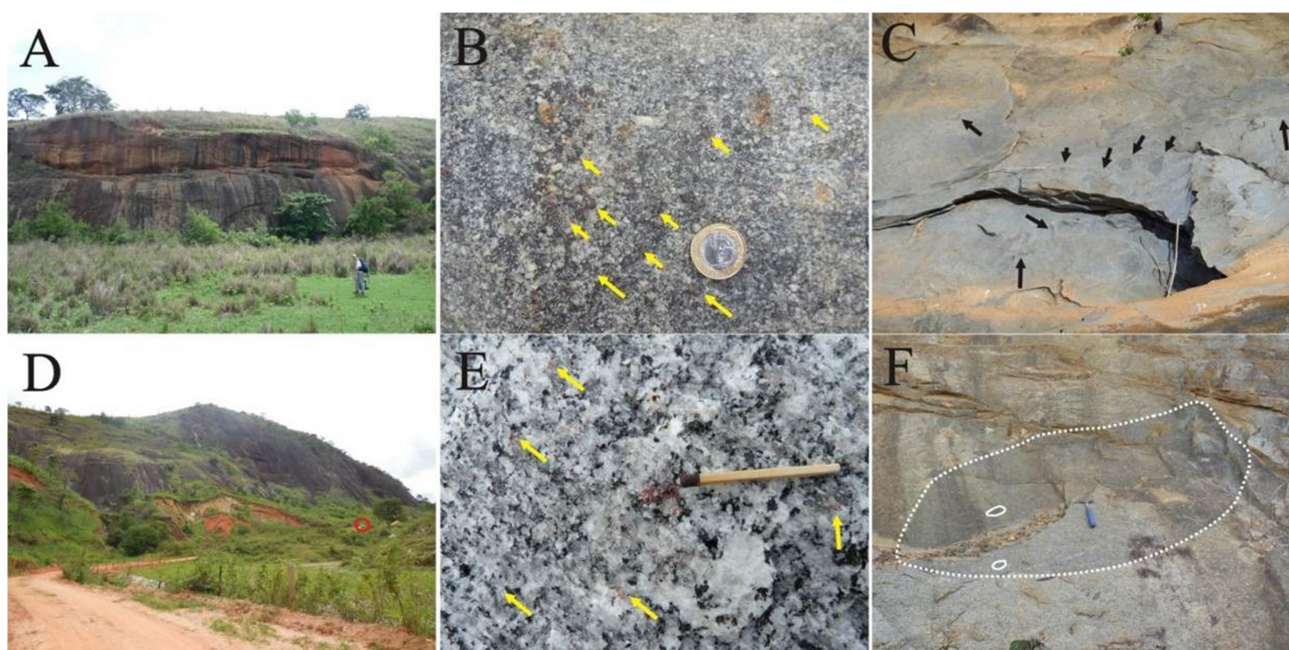


Figure 3.3. Typical appearance of the Galiléia batholiths in the field. a) São Vitor outcrop; b) magmatic texture recognizable in the field; the yellow arrows indicate the presence of garnets; c) outcrop with the presence of enclaves (black arrows); d) Galiléia outcrop; the red circle car; e) magmatic texture of the Galiléia pluton; the match and yellow arrows indicate the garnets; f) Galiléia outcrop crowded by enclaves: note the biggest one > 3 m (dotted white circle) and the smallest one inside it (white circles).

In contrast to São Vitor rocks, the Galiléia pluton it is characterized only by domes that rise quite high with respect to the normal topography (Fig. 3.3d). According to Nalini (1997) and Nalini *et al.* (2000) these rocks are medium- to coarse -grained hornblende-biotite-garnet bearing tonalites, granodiorites, granites (Fig. 3.3e) and a minor amount of micro-granitic dykes. The orientation of biotite (Nalini 1997) and/or hornblende (according Mondou *et al.*, 2012), indicate the foliation, while Nalini *et al.* (2005) interpret the orientation of hornblende, biotite and rarely plagioclase as partial remnants of magmatic foliation. A common feature characterizing the Galiléia pluton is the presence of a high volume of mafic magmatic enclaves. Heterogeneous in dimensions (from less than 3 cm, to > 3 m; Fig. 3.3f) and aligned along the main orientation (NW), mostly of the enclaves are hybridised, with inclusions of feldspars and garnets (Nalini, 1997; Nalini *et al.*, 2005; Vauchez *et al.*, 2007; Mondou *et al.*, 2012). Nalini (1997) and Nalini *et al.* (2008) recognize that the general foliation has an orientation of N20°-30°W, with a dip ranging from 50° to 80° towards NE. Mondou *et al.* (2012) has coupled structural and AMS studies (Anisotropy of Magnetic susceptibility) to investigate and subdivide the area located between Governador Valadares and Aimorés into 4 sections (see Fig. 2.8, Chapter 2). The Galiléia Pluton, falls entirely into the section 2 (Fig. 2.8) and the structural and AMS data presented by these authors is consistent with data reported by Nalini (1997); (for comparison see the above data reported from Nalini (1997) and those reported by Mondou *et al.* (2012) in chapter 2). Mondou *et al.* (2012) (Figure 2.8), recognize section 4 as being a sinistral transcurrent shear zone having N150°E orientation. The interpretation of this zone as a shear zone is in good agreement with the previous studies conducted by Nalini (1997) and Nalini *et al.* (2008). In fact these author called this zone, Galiléia-Resplendor Shear Zone. However, Nalini (1997) and Nalini *et al.* (2008) investigating not only the cinematic of the Galiléia granitic suite, but also that of São Tomé schists and Urucum granitoids (G2 Supersuite), propose that this shear zone has a dextral movement, instead. Moreover these last authors identify that the enclaves present in this transcurrent shear zone as having axis elongation of N30-60°W and N20°-35°W, which is in disagreement with respect to the other measure done in the others Galiléia enclaves that have a dextral component of N30°W.

The São Vitor and Galiléia Plutons are cut by pegmatitic dykes, probably associated with the Urucum suite (e.g. Nalini, 1997 and Mondou *et al.* 2012). Structural data exist just for the Galiléia Pluton (Nalini, 1997). Pegmatites are tabular, cm to meter scale in thickness and zoned. On the basis of field relationships, two different generations have been mapped. The first generation intrude along the schistosity and/or are folded following the deformation São Tomé metasediments. The folded pegmatites show a direction of the fold axes of N10°W up to N50°W, with a dip

between 30° to 50° SE-NW, while those following the schistosity are N20°W/80°NE. The second generations show boudinage shape. These bodies have a boudinage axes sub-parallel with the schistosity of the host rock, i.e. from NS till N50°W, with a dip ranging from N to NW of 20°.

3.2.3 Mafic enclave abundance as a tool for subdividing the Galiléia batholith in different intrusive suites

Gonçalves *et al.* (2014) provide a further subdivision of the Galiléia batholith, separating the enclave-rich granodiorite – tonalites (EGT) located mainly in the central and eastern part of the batholith. Gonçalves *et al.* (2014) recognize the high quantity of cm- to m-sized enclaves with composition spanning from diorites to gabbros. The EGT are mainly medium- to coarse-grained tonalites to granodiorite. Biotite is ubiquitous and is sporadically associated with hornblende; garnet is commonly an accessory phase. The medium to coarse-grained enclave-poor granite-tonalite (GT) rocks are more common in the central and southeaster portion of the Galiléia Pluton and show a more evolved character (e.g. tonalites and granites) than the EGT subtype. In general the authors agree with Nalini (1997) and Nalini *et al.* (2007) concerning the solid-state deformation character highlighted by the EGT and GT rocks, although Gonçalves *et al.* (2014) reported that many parts of the GT show just a magmatic foliation. The peculiarity of this group is its poor enclave content (Gonçalves *et al.*, 2014) that sometime result in extensive enclave-free bodies. The authors have proposed some suggestions as possible explanations for the contemporaneous presence and absence of enclaves between ETG and GT:

- i) plutons constituting the Galiléia batholiths are cut and expose different levels (i.e. erosion driven process)
- ii) upper crustal level: allochthonous plutons emplaced far from magma mixing zones
- iii) plutons, or part of them composed of more evolved magmas formed for fractional crystallization
- iv) plutons or part of them composed by magmas resulting from partial melting of other granitic plutons at the base of the arc and/or from basement sources of adequate composition.

3.2.4 Micro-textural features of the São Vitor and Galielia granitoids

The petrographic characteristics of the São Vitor granitoids have been described by Feboli (2000) while the main contributions describing the micro-textural features of the Galiléia pluton are those of Nalini (1997), Oliveira (2000) and Nalini *et al.* (2005). Instead Mondou *et al.* (2012) and Gonçalves *et al.* (2014) take in account the whole central part of the Galiléia batholith.

The São Vitor tonalites, granodiorites and granites (Feboli, 2000) have hypidiomorphic to granoblastic texture. Aggregates of polygonal and oriented feldspar and quartz associated with “films” of hornblende and biotite define the foliation. Allantite is present as a minor accessory mineral and associated with hornblende and biotite. K-feldspars are associated with myrmekite textures and plagioclase sometimes shows tardive albitization. Contrary to previous author, Mondou *et al.* (2012) report the presence of garnet, zircon, titanite and muscovite. The same authors also point out that the amphiboles and garnet are more abundant in these rocks than in the Galiléia pluton. With respect to the São Vitor pluton, the Galiléia Pluton (Nalini, 1997; Nalini *et al.*, 2005) is crosscut by microgranitic dikes. Igneous rocks vary from medium to coarse-grained and only occasionally porphyritic and protomylonitic. The major rock-forming phase observed are plagioclase, hornblende, biotite, K-feldspar, quartz and garnet (Nalini *et al.*, 2000). Accessory minerals are titanite, zircon, apatite, ilmenite, epidote and allantite. In addition Feboli (2000) describe granular hypidiomorphic to granoblastic texture for this rocks, with less pronounced foliation to possibly isotropic.

There is general agreement between the authors about the enclaves belonging to the São Vitor as well as to the Galiléia Pluton. These mafic rocks show granular, microgranular and ophitic texture, with a primary mineral assemblage consisting of hornblende, biotite, K-feldspar, zoned plagioclase, ortho- and clinopyroxene (Nalini 1997; Feboli 2000; Nalini *et al.*, 2005; Mondou *et al.*, 2012; Gonçalves *et al.*, 2014). Garnet, zircon, titanite, apatite (Gonçalves *et al.*, 2014) and poikiloblastic epidote with amphibole inclusions (Mondou *et al.*, 2012) are also reported as accessory minerals.

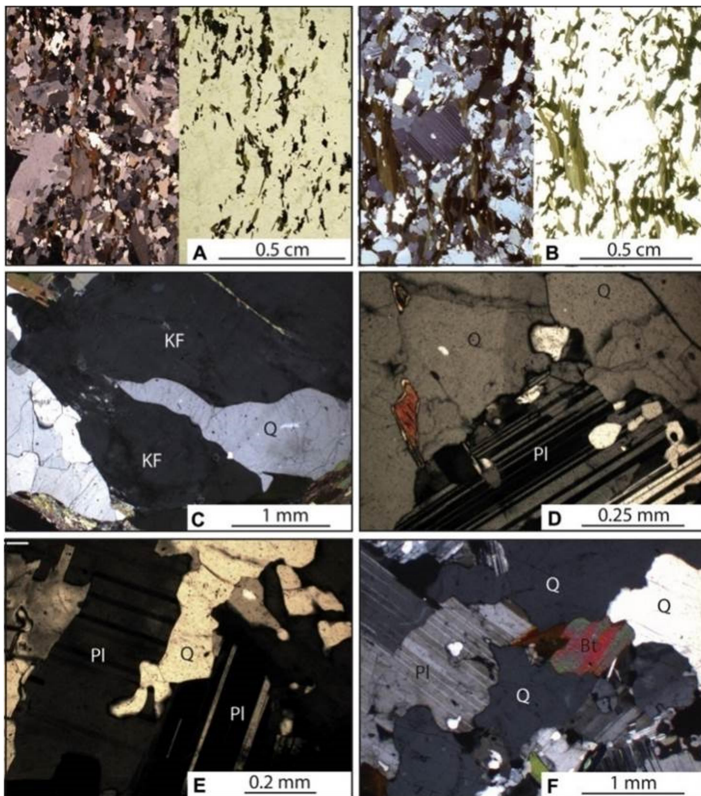


Figure 3.4. Petrographic features of Galiléia and São Vitor granitoids. a) c) and e) Galiléia and b) d) and f) São Vitor rocks. KF: K-feldspar; Q: quartz; Pl: plagioclase; Bt: biotite. In c), d), e) and f) is highlighted as the quartz grains are interstitial and like the k-feldspars, they have curved, lobate and irregular boundaries, witnesses of a magmatic texture. From Mondou *et al.* (2012) modified.

It is worth noting that there is little difference between the petrography of São Vitor and Galiléia granitoids (Fig. 3.4). Instead, there is major disagreement between the various authors about the origin of the pervasive foliation observed for the Galiléia batholiths. In fact, Nalini (1997), Nalini *et al.* (2005), Gonçalves *et al.* (2014) interpret the deformation as formed at solid-state while Mondou *et al.* (2012) consider the deformation to be syn-magmatic. The first hypothesis is supported by petrographic investigation. Gonçalves *et al.* (2014) recognize solid-state deformation in the form of elongated quartz and feldspars grains, as well as in sub-grains or in recrystallized forms, showing undulose extinction, triple junctions, and as in the case of feldspar, mechanically twinning. In contrast Mondou *et al.* (2012) consider a syn-magmatic behaviour for these plutonic rocks since the large quartz grains show irregular shape (Fig. 3.4c, d, e, f), usually preserving their interstitial morphology. Moreover for Mondou *et al.* (2012) another line of evidence against the solid-state deformation is the lack of pressure shadows or recrystallization tails formed around feldspar, which in turn do not show fractures and undulate extinctions, but preserve irregular boundaries like the quartz grains.

3.2.5 Mineral chemical review

The only detailed petrographic investigation coupled with mineral chemistry for the Galiléia pluton was conducted by Nalini (1997). Following Nalini (1997), a brief summary of the main mineral chemical features of the studied rocks is given below.

Quartz can form inclusions in feldspars, biotite, amphibole and garnet. Sub-euhedral and anhedral small grains (0.1 – 0.6 mm) are aligned along plagioclase and mafic minerals edges, displaying signs of recrystallization and undulate extinction. Quartz also forms large crystals (5 – 6 mm) with undulate extinction, sometimes corroding amphibole, feldspar and plagioclase and occasionally stretched parallel to the biotites.

The K-feldspars ($Or_{91} - Or_{93}$) are commonly microcline. They are found in two forms, as large perthitic crystals (0.5 – 2.5 mm) with undulose extinction and edged by quartz and plagioclase; and as interstitial grains (0.2 – 0.7 mm), which are fragmented and deformed, sometimes entering into plagioclase and biotite micro-fractures. Nalini (1997) recognize 3 populations of plagioclase. The first and more diffuse type are big zoned crystals (2 – 15 mm) with calcic cores and sodic rims. The calcic zones show dendritic rings formed by inclusions, probably indicating a re-equilibration or re-melting of a pre-existing mineral. In general these plagioclase ($An_{88} - An_{50}$) are rich in inclusions and are also found within the enclaves ($An_{88} - An_{50}$). The second type is common in more leucocratic samples. They are sub-hedral to anhedral small (0.1 – 1 mm) crystals, more calcic, with little or no zoning, inclusions-free and in contact with ferromagnesian minerals as well as type 1 plagioclase. Some type 2 plagioclase have undulate extinction. The last type is associated with myrmekite in conjunction with K-feldspars, ranging in composition from andesine to oligoclase and from oligoclase to albite.

Biotite is widespread in all the Galiléia granitoids and occurs as mm, euhedral to sub-hedral brown to reddish crystals. Three types of crystals are described by Nalini (1997): 1) those (0.2 – 2 mm) rich in mineral inclusions and generally associated to amphiboles and plagioclase, 2) those marking the rock foliation and associated with sphene, quartz and recrystallized feldspars and 3) small crystals (0.05 – 0.1 mm) included in both plagioclase crystals as well as in microcline crystals. All biotites fall in the annite and siderophyllite field and have Mg# content (i.e. $Mg/(Mg+Fe_{Tot})$) from 0.48 to 0.28 that decrease from tonalite to granites. Biotites in the enclaves have Mg# (ca. 0.43) comparable with those belonging to the more mafic granitoids. Both the K_2O and Al_2O_3 of biotite remain quite constant along the range of composition of the whole rock-suite.

The amphiboles like the other minerals reported so far display a range of different shapes. Within the granitoids there are 3 different type of types amphibole: 1) small grains (< 0.1 to 0.8 mm), sub-hedral to anhedral, green with cleavage, containing many different mineral inclusions such as quartz, plagioclase, apatite, sphene, epidote, zircon, but importantly no garnet. 2) These are the largest amphibole crystals (4 – 5 mm) and are euhedral and anhedral. Inclusions are quartz, ilmenite, and K-feldspars. 3) The third type of amphibole 3), are mm to cm sized and occurs within the enclaves. These amphibole crystals are sub-hedral to anhedral, like those in the granitoids and have mineral inclusions; are associated with zircons and biotites, the latter sometimes forming coronas at the amphibole rims. Nalini (1997) suggest that this texture could be the product of pyroxene destabilization. All the amphiboles analysed by Nalini (1999), are calcic, showing a constant mg# and having chemical evidence of crystallization at high pressure (> 0.8 GPa) and high temperatures.

The Galiléia Pluton (and the enclaves contained therein) is characterized by the widespread presence of euhedral, sub-hedral, anhedral and sometimes skeletal garnets with dimensions between 0.5 to 6 mm. Mineral inclusions such as quartz, plagioclase, biotite, zircon, epidote and rarely amphibole, are seen especially in the core of the areas. Regardless of the grain shape, the garnets are always in contact with biotite and plagioclase, quartz and K-feldspar. Regarding the skeletal shape Nalini (1997) suggest that this could be evidence of garnet disequilibrium with the granitic melts at the time of crystallization. Chemically these garnets are CaO rich (up to 45 mol.% of Grossular), especially those within the granodiorites and enclaves, while in the more silicic sample they are more iron-rich (Almandine of 44 mol.%). Interestingly the more mafic granitoids i.e. the tonalite MD14A, contain the more mafic garnets with an almandine and Pyrope composition of 64% and 21%, respectively. Nalini (1997) pointed out how garnet is extremely rare within I-type metaluminous granitoids.

Prismatic to ovoid zircons (0.03 – 0.1 mm) are associated with biotite, amphibole and rarely plagioclase and quartz.

Another significant characteristic of the Galiléia granitoids is the occurrence of epidote. It occurs in three forms: 1) sub-euhedral and anhedral polygonal crystals reaching up to 1 mm in size. These are generally related to biotite, probably suggesting contemporaneous crystallization; 2) as coronas around allanite; 3) as small anhedral crystals that grow at the expense of plagioclase crystals. The Fe₂O₃ content of epidote is low (6.34 – 7.59 wt.%). The pistacite content ranges from 11% and 21% (Nalini, 1997).

Allanite, are also present, occurring as crystals (0.2 – 0.7 mm) zoned and mantled by epidote. Allanites in granodiorites are enriched in MgO, MnO, MREE, Th and Y and depleted in TiO₂, FeO and CaO, with respect to allanites in the granites. Instead, epidote coronae is characterized by a depletion in LREE and Al₂O₃.

Apatite are acicular (0.1 – 0.7 mm), mostly occurring within the enclaves as inclusions within amphibole, biotite, plagioclase, garnet, quartz and zircon. Prismatic crystals (0.5 – 1.0 mm) associated with biotite, are present within the granitoids. Generally the apatites have F ranging from 2 wt.% and 5 wt.% (Nalini, 1997), with CaO and P₂O₅ (53.6 – 56.3 and 36.6 – 43.0 wt.%, respectively) content typical for granitoids rocks.

Fe-Ti minerals, like ilmenite and titanite are also present. Titanite (0.1 – 0.4 mm) is diffuse in the Galiléia granitoids (Nalini, 1997) especially in tonalites and granodiorites. Titanite crystals have different forms (sub-anhedral, euhedral, acicular and lozenge) with some of them being enclosed in biotite, while others (0.5 – 0.8 mm) occur as inclusions within amphibole, biotite and garnet. Ilmenite (0.3 – 0.6 mm) is mostly present in the matrix as well as included in biotites, amphiboles and garnets of the more mafic granites, and are relatively enriched in MnO (1.20 – 2.03 wt.%).

Secondary accessory minerals are chlorite, sericite and carbonate.

3.2.4 Whole rock geochemistry

In this section a summary of the main geochemical features of the ETG, GT and enclaves constituting the Rio Doce Arc will be described, according to the data presented by Gonçalves *et al.* (2014). The ETG and GT have SiO₂ content between 59.4 - 73.7 wt.% and 60.0 to 76.2 wt.%, respectively (Fig. 3.5a; Gonçalves *et al.*, 2014), while the enclaves have a composition plotting from the granodiorite to the gabbroic field with SiO₂ ranging from 47.3 and 67.1 wt.%. The more mafic enclave have transitional- to alkaline character (K₂O+Na₂O 4.16 – 7.30 wt.%). The gabbroic rocks plot more in the alkaline field and on average are more mafic than the enclaves (SiO₂ 49.6 – 58.3 wt.%). One of them plots in the syenite field. The composition of the gabbros is more widespread than that of the enclaves, with the former from calcic to alkaline, while the latter are mainly calc-alkaline. The EGT plot largely within the calcic field and similar to the Cordilleran I-type granitoids (Frost *et al.*, 2001 and reference therein), they show enrichment in calc-alkaline affinity as silica increases. In the other hand, the GT rocks display a more widespread behaviour falling in three of the four fields of Figure 3.5b. All the rocks considered are mainly magnesian, and

just few of them are ferroan (Fig. 3.5c). In general the granitoids are metaluminous (Fig. 3.5d) and peraluminous (A/CNK 0.76 – 1.39) a feature shown also by the enclaves that with respect the gabbroic rocks (metaluminous, 0.54 – 1.03; $Fe+Mg$ 0.13 – 0.28 a.p.f.u.), show a high maficity ($Fe+Mg$, a.p.f.u.) content (0.35 a.p.f.u.). All the rocks described here (Gonçalves *et al.*, 2014) show a weak positive correlation between K_2O and SiO_2 (Fig. 3.6). Overall, the K_2O content remains quite constant varying only between 1 and 3 wt.% from the gabbros to the EGT. For a given SiO_2 content GT rocks are more enriched in K_2O . The enclaves do not exhibit any correlation between K_2O and SiO_2 . A negative linear correlation is displayed by the enclaves plotted over CaO as well as compatible elements such as V and Ni . In this last case the gabbros are not related with the trend formed by the other rock-types, forming their own trend. Considering the Rb (Fig. 3.6), a slightly positive correlation is showed when plotted against SiO_2 . Two trends are formed by the EGT rock-type in the SiO_2 vs. Sr space (Fig. 3.6). In the first trend the Sr composition of the rocks slightly increase with decreasing SiO_2 content while the slope of the negative correlation between SiO_2 and Sr is steeply dipping. This tendency became clear observing the behaviour of the GT rocks that reach the highest Sr content (886 ppm). Just two GT samples plot within the first trend. The gabbroic rocks are unrelated with the previously described trends. The enclaves are scattered plotting within the gabbroic field as well as along the ETGs having low Sr content. A good negative correlation is shown also considering the MgO content, where the enclaves have the highest content (9.58 wt.% with a $Mg\#$ of 0.70) with some of them being less evolved than the gabbroic rocks. Rare Earth Elements for the EGT show a variable LREE enrichment giving the lowest and the highest $(La/Yb)_N$ content (5.08 and 47.17, respectively; Gonçalves *et al.*, 2014), compared to the GT rocks ($(La/Yb)_N$ 11.47 – 30.55). In contrast, GT rocks have an Eu/Eu^* ratio range (0.41 – 1.20) larger than that shown by the EGTs (0.64 – 1.04).

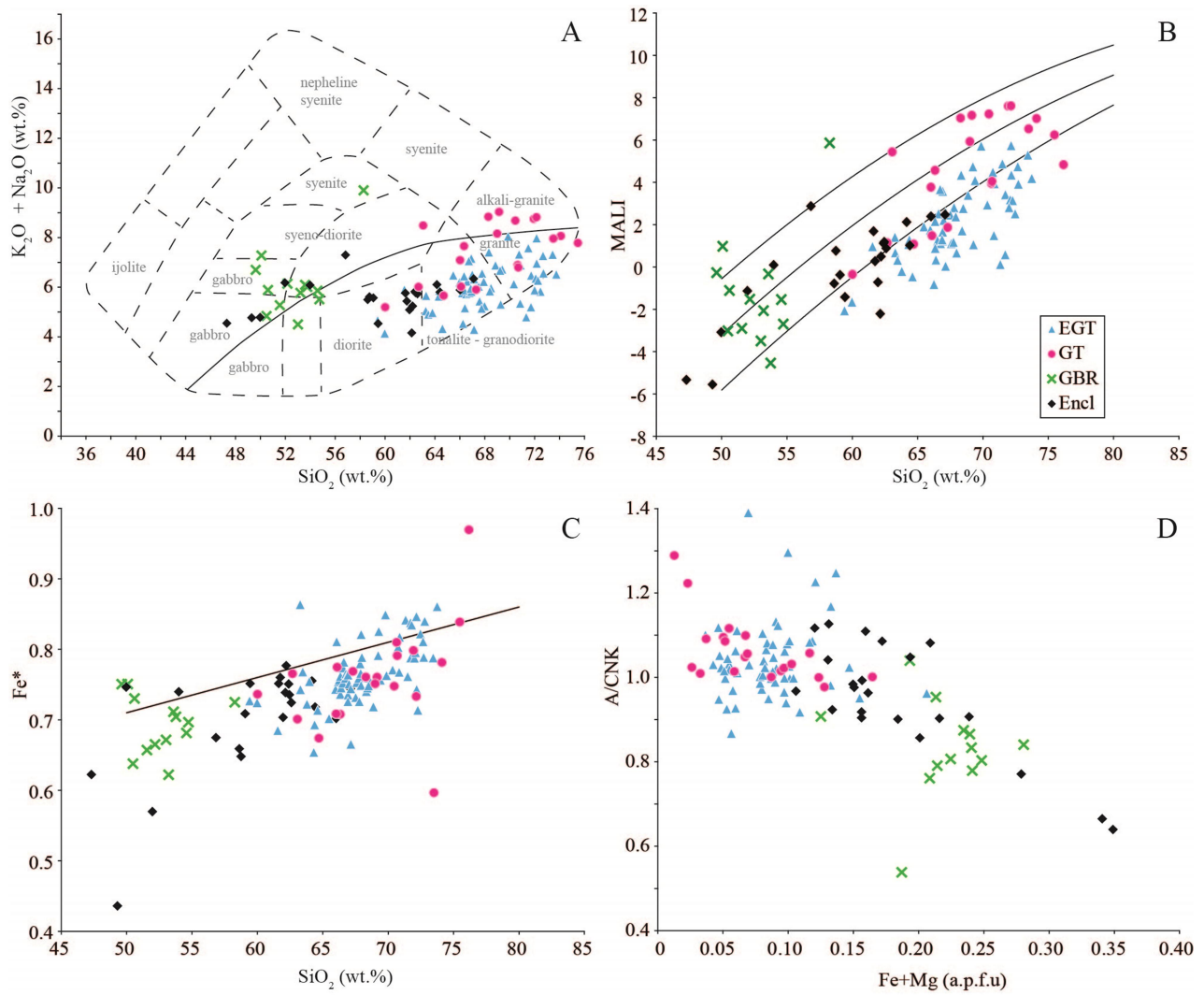


Figure 3.5. Main discrimination diagrams. a) TAS (K_2O+Na_2O vs SiO_2) diagram after Wilson, (1989): EGT: enclave-rich tonalite and granodiorite; GT: enclave-poor granite to tonalite; GBR: gabbros; Encl: enclaves; b) MALI (K_2O+Na_2O-CaO) vs SiO_2 (Frost *et al.*, 2011) diagram separating 1) alkalic, 2) alkali-calcic, 3) calc-alkaline and 4) calcic rocks. c) Fe^* [= $FeO_{tot}/(FeO_{tot}+MgO)$] vs SiO_2 (Frost *et al.*, 2011) subdividing (black curved line) magnesian from ferroan rocks. d) A/CNK (mol.% $Al_2O_3/ CaO+K_2O+Na_2O$) vs. SiO_2 for granitoid rocks. From Gonçalves *et al.* (2014) modified.

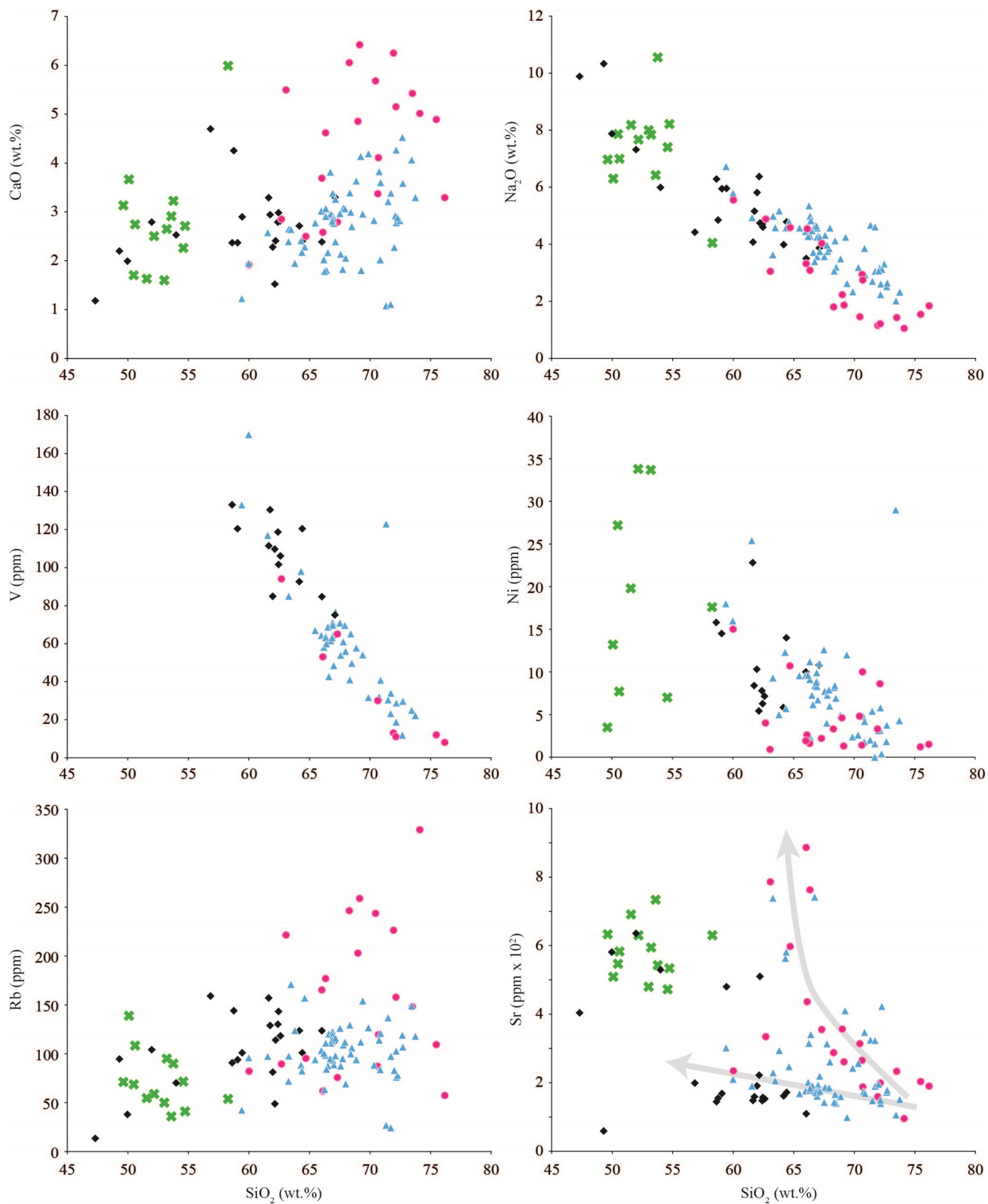


Figure 3.6. Major (K₂O and CaO) and trace elements (V, Ni, Rb and Sr) against SiO₂. In the Sr vs. SiO₂ diagram light grey arrows are reported in order to show the two suggested trends. See the text for major explanations. Symbols as in Fig. 3.5b. Form Gonçalves *et al.* (2014) modified.

The recent works of Gonçalves *et al.*, (2014; 2018) and Tedeschi *et al.* (2016) review the whole rock Sr-Nd isotopic data and Hf isotopes in zircons for the whole Galiléia batholith. Because the negative Nd, Hf and radiogenic Sr_i ($^{87}\text{Sr}/^{86}\text{Sr} > 0.708$) an important contribution from the continental crust rather than from the oceanic one was proposed for the G1 igneous rocks. The crustal contribution is supposed being represented by 2.0 – 1.4 Ga rocks (Archean - Paleoproterozoic basement and anorogenic-related rocks) with possible younger 0.8 – 0.6 Ga rocks. These last rocks series are thought to be mantle-related magmas in the form of mafic enclaves that characterize the Galiléia Batholith. Whether or not the mantle magmas have contributed to create mixing in these granitoids, for sure these mafic magmas gave the heat to partially melt the continental crust that mostly contributed for the Galiléia granitogenesis. Notably, these conclusion are not dissimilar to those reported by Nalini Jr (1997).

3.3. THE SÃO VITOR-GALILEIA GRANITOIDS AND THE CORDILLERAN-TYPE BATHOLITHS.

In this section I will compare the composition of the G1 granitoids with that of well-studied arc granitoids from the Cordilleran margin.

Arc-related I-type batholiths chosen for this purpose are those coming from the South and North Patagonian batholith (Fig. 3.7a), Western and Eastern Peninsular Ranges and Sierra Nevada Batholiths (Fig. 3.7b). As a last case, the Bushy Point granitoids belonging to the Revillagigedo Island, South-eastern Alaska, (Fig. 3.7b) have been considered due to their petrographic similarity to the G1 granitoids.

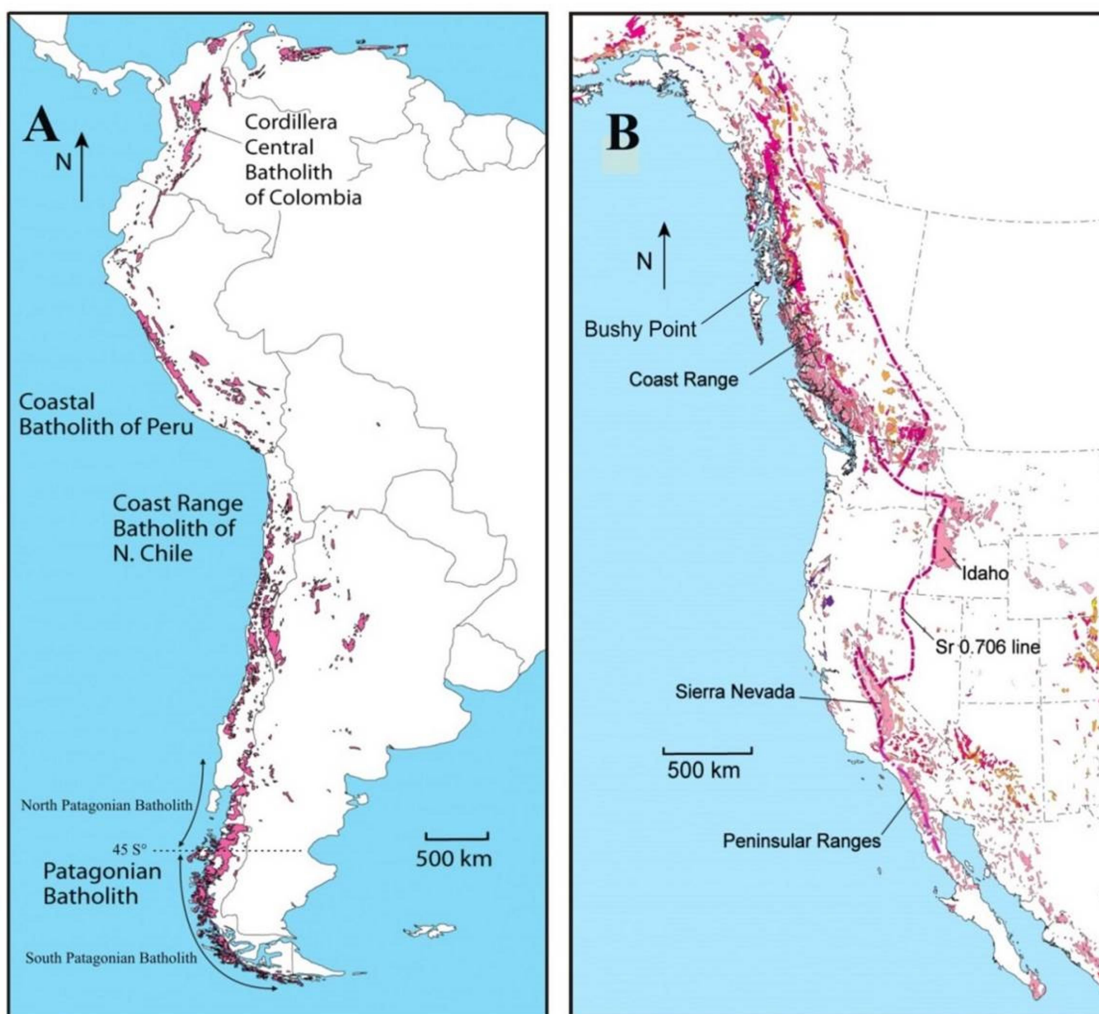


Figure 3.7. Map showing the location of the Cordilleran I-Type Batholiths. a) South Cordilleran batholiths. It is also indicated the location of the North Patagonian and South Patagonian Batholiths; b) map showing the Northern American Batholiths. In it are reported the location of the Peninsular Ranges, Sierra Nevada batholiths and the Bushy Point granitoids. The purple dotted line indicate the $Sr = 0.706$ boundary (Lee *et al.*, 2007) between two different batholithic domains.

Although there are some differences, the here proposed diagrams (Fig. 3.8 to 3.12) show as the G1 granitoids overlap the whole range of the geochemical variability shown by the Cordilleran-I-type granitoids. All the compared suites cover a SiO_2 range (< 40 to 80 wt.%) that is larger than that of the G1 granitoids. The Eastern Peninsular Ranges Batholith (EPRB) granitoids show a gap between the more mafic (SiO_2 ca. 42 – 52 wt.%) and more leucocratic samples (SiO_2 60 – 75 wt.%), while the Bushy Point granitoids, although with less data available in literature, are in general the more silica poor. The Eastern Peninsular Ranges Batholith (EPRB) show a gap at around 60 wt.% of SiO_2 , as well. This gap is also shown by the Patagonian Batholiths, but is more restricted. Comparing SiO_2 against the $\text{K}_2\text{O}/\text{Na}_2\text{O}$ ratio (Fig. 3.8), the enclave-bearing granitoids (EGT) of the Galiléia pluton are mainly transitional ($0.5 < \text{K}_2\text{O}/\text{Na}_2\text{O} < 1.0$) with some samples falling in the sodic field ($\text{K}_2\text{O}/\text{Na}_2\text{O} < 0.5$) and others in the potassic one ($\text{K}_2\text{O}/\text{Na}_2\text{O} > 1$). The enclave-poor granitoids (GT) instead are intermediate, potassic and ultrapotassic. The Cordilleran granitoids cover all the three fields showing that there is a positive correlation between SiO_2 and $\text{K}_2\text{O}/\text{Na}_2\text{O}$ ratio. The G1 granitoids mimic quite well these trend especially those that of the EPRB (Fig. 3.8). Typical of Cordilleran I-type granitoids and of the G1 igneous rocks is the principal slightly peraluminous to metaluminous character as displayed in the (A/CNK) vs. (Fe+Mg; maficity index) diagrams (Fig. 3.9). Some of them with low maficity (Fe+Mg) ca. < 0.10 (a.p.f.u.) show a peraluminous character. In this case some of the EGT granitoids have (A/CNK) >1 with (Fe+Mg) content between 0.10 – 0.15 (a.p.f.u.). In general the Galiléia granitoids (ETG and GT) have a maficity index between 0.01 and 0.12 while the other batholiths in general range from 0.01 and ca. 0.77 (a.p.f.u.; Fig. 3.9). The other considered diagrams (Figs. 3.10, 3.11 and 3.12) do not show other major differences between G1 rocks and the other Cordilleran Batholiths.

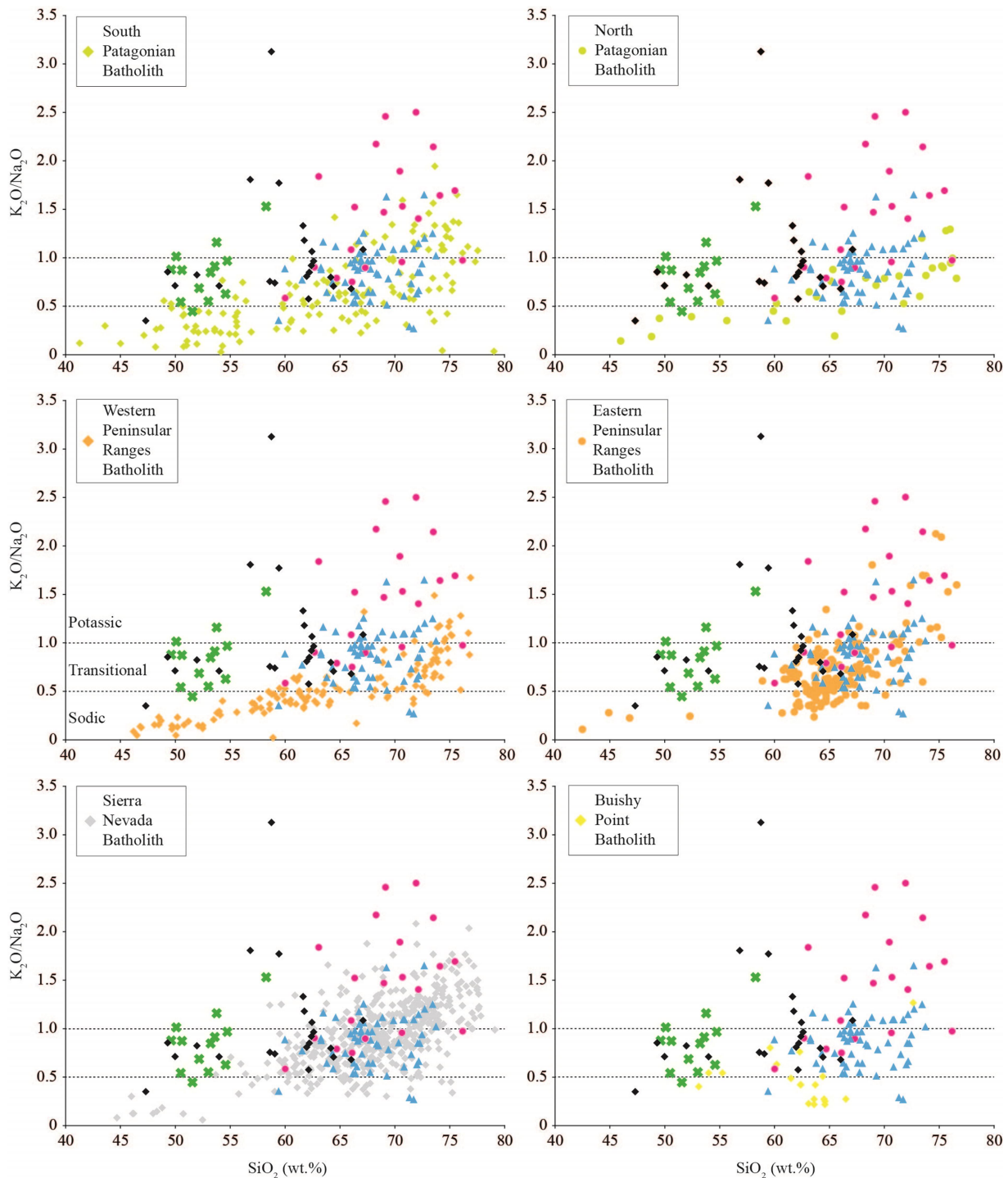


Figure 3.8. K_2O/Na_2O vs SiO_2 . South Patagonian Batholith: Hervé *et al.* (2007); North Patagonian Batholith; Pankhurst *et al.* (1999) and Castro *et al.* (2011); Western Peninsular Ranges Batholith and Eastern Peninsular Ranges Batholith: Lee *et al.* (2007); Sierra Nevada Batholith: Bateman *et al.* (1984) and Cecil *et al.*, 2011; Bushy Point granitoids: Arth *et al.* (1988) and Cook *et al.* (1991) and Crawford *et al.* (2005). Other symbols as in Fig. 3.6b.

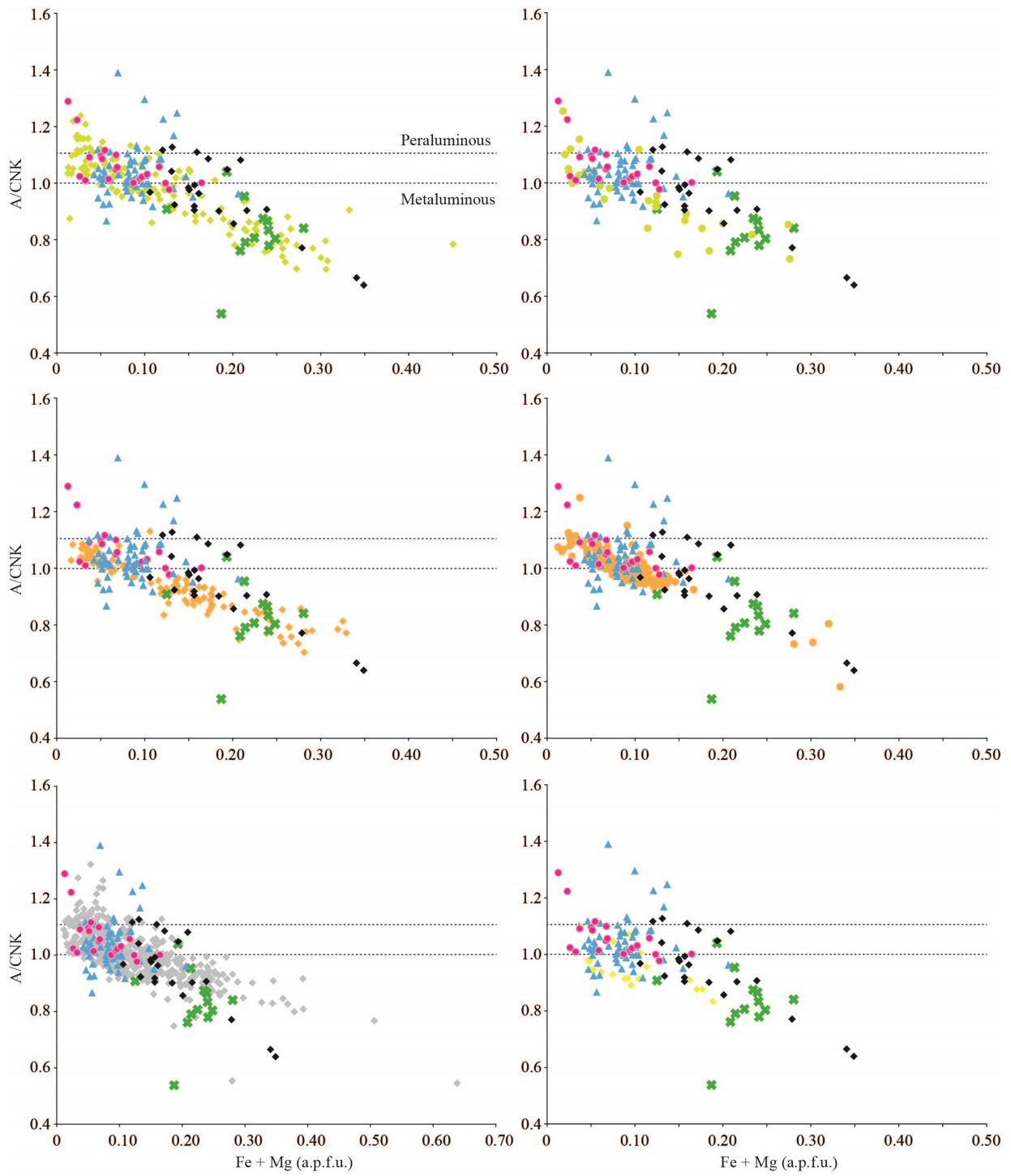


Figure 3.9. (A/CNK) vs maficity index, (Fe+Mg a.p.f.u.). Symbols as in Fig. 3.5b and Fig. 3.8.

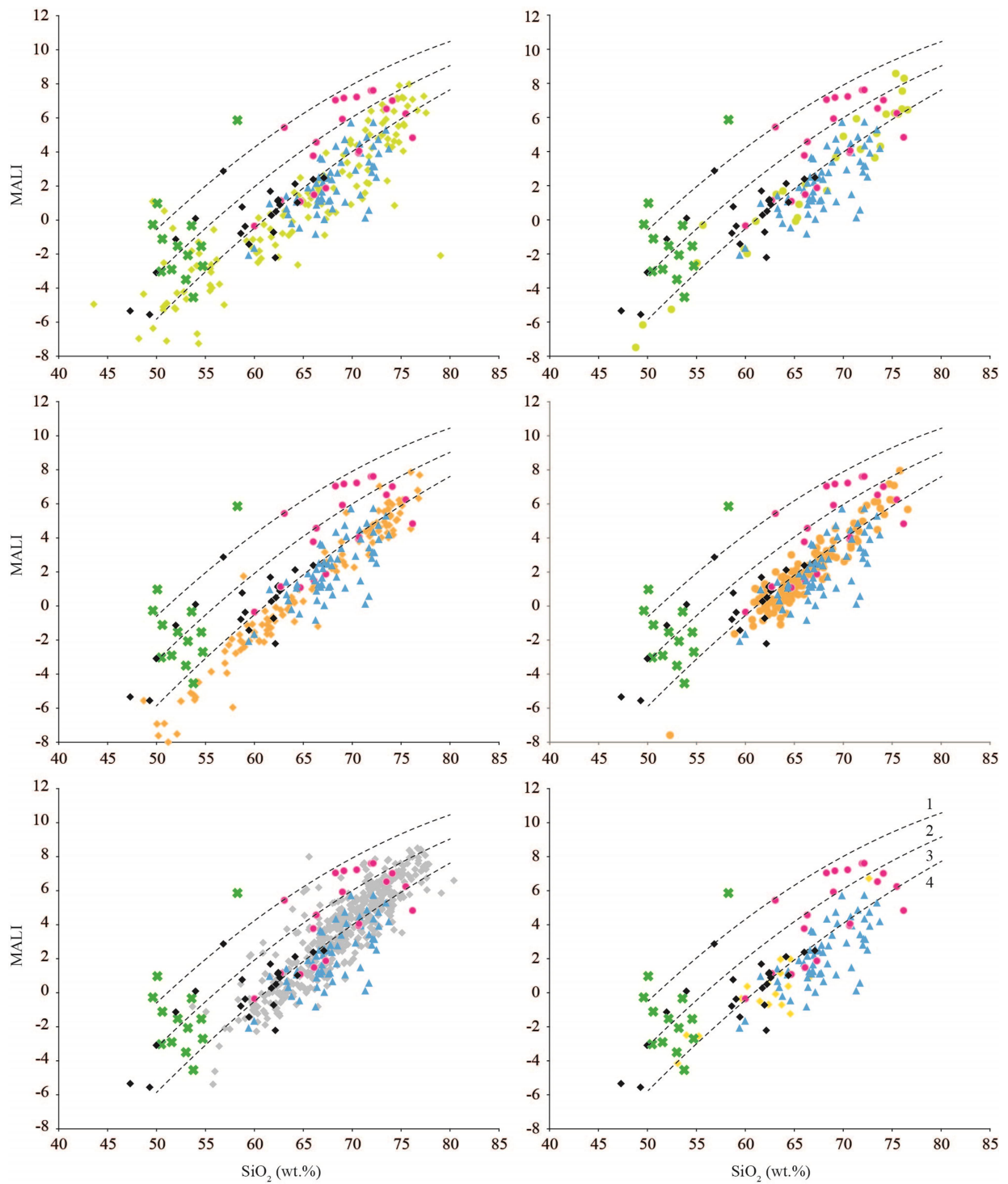


Figure 3.10. MALI vs. SiO₂ for granitoid rocks (Frost *et al.*, 2001). The numbers indicate 1) alkali, 2) alkali-calcic, 3) calc-alkaline and 4) calcic fields. Symbols as in Fig. 3.5b and Fig. 3.8.

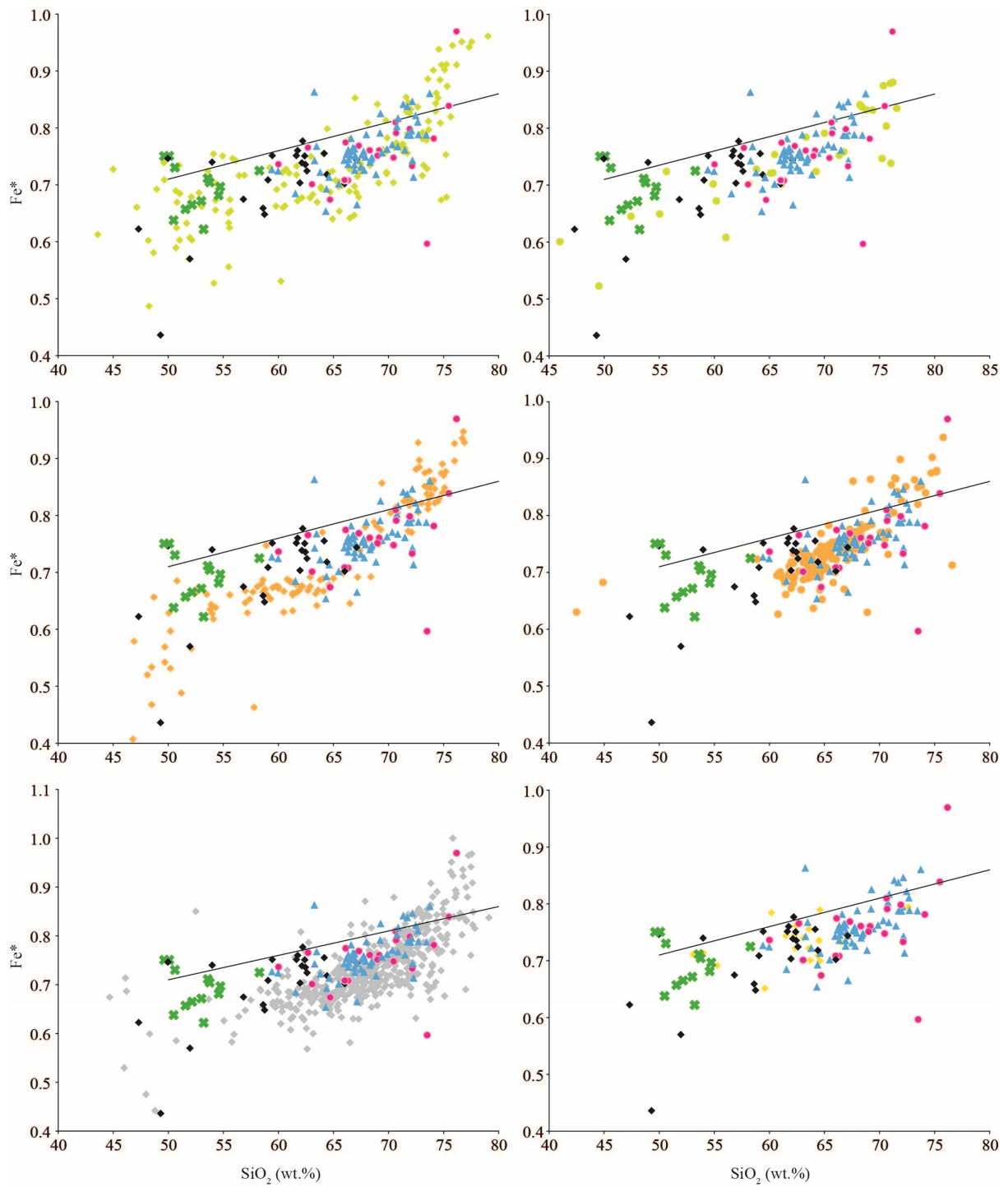


Figure 3.11. Fe^* [$Fe_{Tot}/(FeO_{Tot}+MgO)$] vs. SiO_2 diagram for discriminate ferroan and magnesium granitoids (Frost *et al.*, 2001). Symbols as in Fig. 3.5b and Fig. 3.8.

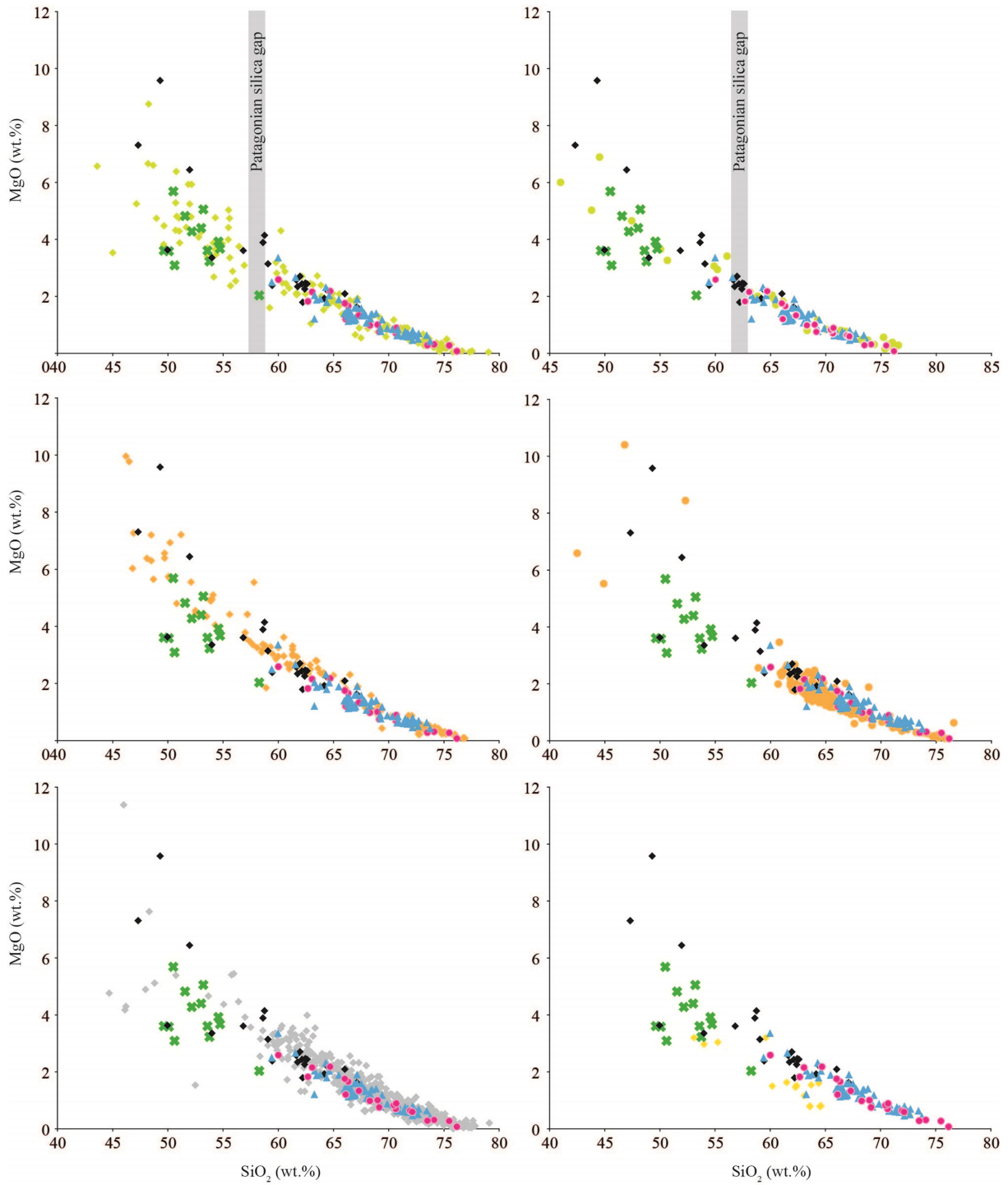


Figure 3.12. MgO vs. SiO₂. For the Southern and Northern Patagonian Batholiths it has been reported the Patagonian silica gap from Castro (2013). Symbols as in Fig. 3.5b and Fig. 3.8.

From a petrographic point of view, the Galiléia Batholith with respect to the here considered Cordilleran granitoids, have a peculiar mineral assemblage, that is, the diffuse ubiquitous presence of garnet and epidote. Even though the latter mineral is present in most of the batholiths (South and North Patagonian Batholith, Western and Eastern Peninsular Ranges Batholith and Sierra Nevada Batholith) only within the Bushy Point granitoids similar petrographic features have been met (garnet + epidote). Also the mineral chemistry seems to be identical (Nalini, 1997). Interestingly Zen & Hammarstrom, (1984a, 1984b), for similar mineralogical assemblage, constrain the granitoids emplacement above 0.8 GPa, with a temperature no less than 700°C.

3.3.1 Petrogenetic models for the G1 plutonic rocks and tectonic implications

Recently, Gonçalves *et al.* (2014) have presented 2 petrogenetic models for the genesis of the G1:

- Melting, assimilation, storage and homogenisation (MASH) model, process in which mantle-derived melts fractionate, assimilate crustal rocks and emplace at shallow levels within the pre-existing crust;
- The second model suggest that I-type granitoids could be the product of partial melting of pre-existing acidic to intermediate biotite and hornblende-rich metasedimentary and/or igneous rocks, coupled with the entrainment of a peritectic minerals, most probably pyroxene and plagioclase (Clemens *et al.* 2011).

The work of Gonçalves *et al.* (2014) is mostly based on a careful review of literature data and although these authors have discussed wisely the models, many question still remain open about how the Galiléia granitogenesis.

The two models differ based upon the role played by mantle-derived magmas in the genesis of the G1 granitoids. Following the first model, mantle-derived magmas are of primary importance for the genesis of these rocks with fractional differentiation playing an important role in shaping the composition of the original mantle-derived component, thus allowing efficient mixing between crust- and mantle-derived end-members. The opposite view, regards the mantle as the primary heat source triggering melting of a heterogeneous source made of biotite and biotite + hornblende sources. In this view, the composition of the granitoids is controlled by the temperature of fluid-absent reaction and by the primary heterogeneity of the crustal sources, and the presence of widespread occurrence of magmatic enclaves could be witnesses of magmatic underplating generating the heat. These models, although to some extent are reconcilable differ mainly in the volume of crustal growth that took place during genesis of G1 granitoids. Both models seem to be

able to account for the major element composition of I-type granitoid as already pointed out by (Clemens & Stevens, 2012).

The model of mixing between mantle- and crust-derived melts is the one adopted to explain the general arc-related intermediate to silicic magmatism. In fact the overall similarity between the rocks of the G1 Supersuite, with the typical arc-related Cordilleran-type granitoids described elsewhere, had led many authors to interpret that these rocks formed in response to subduction processes and crustal thickening (Pedrosa-Soares *et al.*, 1992, 1998, 2001, 2011; Alkmim *et al.*, 2006; Gonçalves *et al.* 2014; 2016; 2018). More specifically Pedrosa-Soares and co-workers suggest that the extensive granitic magmatism that occurred within the Araçuaí Arc, was due to the consumption of a large amount of Neoproterozoic oceanic lithosphere, which produced arc-derived mantle-melts that in turn triggered the melting of the overlying Paleoproterozoic basement, and subsequently mafic and crustal melts mixed together. Explanation for this hybrid signature is the presence of gabbros, mafic enclaves and the crustal signature of the Sr and Nd isotopes. Involvement of Transamazonian crustal rocks is suggested by the inherited Paleoproterozoic ages in zircons and by the Nd T_{DM} model ages (1.2 – 2.1 Ga). Support to this geodynamic model comes also from the presence of ophiolitic slivers with an N-MORB signature (e.g. Pedrosa-Soares, 1998), the fact that the G1 magmatism predate the G2 collisional magmatism (Pedrosa-Soares *et al.*, 2011) and by the presence of arc-related volcano-metasedimentary rocks (Vieira, 2007).

The second model, that basically argues for the recycling of the continental crust, see little or not involvement of oceanic lithosphere subduction (Nalini, 1997). This author suggest that the genesis of the G1 granitoids is a function of a continental collision without participation of a lithospheric subduction. Evidence supporting this model are: 1) the negative ϵNd and high values of $^{87}Sr/^{86}Sr$ suggest essentially the involvement of only crustal-derived melts in the genesis of the Rio Doce granitoids, while the basic magma which produced the enclaves could be derived by the melting of hydrated, basic, lower crustal rocks. In turn these enclaves once interacting with more felsic melts would have undergone isotopic re-equilibration; 2) the Archean to Early Proterozoic model ages obtained for the Galiléia granitoids and enclaves may indicate low mantle contribution, so low juvenile crustal accretion during the Brasiliano Orogeny; 3) the transpressive behaviour of the shear zone characterizing the Araçuaí orogen and all the Brazilian Atlantic coast, seems have reached the deepest part of the lower crust and controlled the emplacement of the granitoids and 4) the lacking of a continuous ophiolitic alignment along the 3000 km of the Atlantic Brazilian Shear zone, although the pieces of slivers up to now investigated suggest a MORB affinity. Support to this

model is also the finding of inherited Paleoproterozoic zircon ages found in the G1 granitoids as well as within their enclaves.

Thus both of the models and the respective tectonic implications have some limitations.

In the first case, the strong crustal signature of the Sr and Nd isotopes implies large amounts of assimilated wall rocks. Unfortunately this is in disagreement with the thermal limitations (see Glazner, 2007) for the incorporation of the crustal rocks within the basaltic magmas. Moreover for this case, the gabbroic rocks should occur at least 3 or 4 times than the contemporaneous granitoids, fact that in the case of the Araçuaí orogen is not subsistent since the gabbroic rocks are not so widespread due to either lack of detailed studies or due to collisional and post-collisional crustal delamination.. Furthermore, neither the fractional crystallization is not able to explain the great chemical variability of these plutonic rocks (Gonçalves *et al.*, 2014). Finally, the nutcracker model (i.e confined orogen with restricted subduction process) seems not compatible with the volume of granitic magma represented by the Galiléia batholith. This would require a long-lived subduction, evidence against the nutcracker model.

The second model that take in consideration the recycling of the basement rocks due to a continent-continent collision, to be applicable, on one hand must explain the presence of ophiolitic slivers, that in recent geological maps, are clearly aligned along the probable subduction suture. In the other hand seems unlikely to generate such volume of melts over a period of > 60 Myrs. In conclusion, the above presented models are both applicable in some ways, but their petrological, thermodynamic and tectonic limitations, make the study of the G1 and the related geodynamic implications, truly challenging. Therefore a more in-depth study must be done, to constrain better the possible geochemical, petrological and tectonic processes involved.

References

- Alkmim F.F., Marshak S., Pedrosa-Soares A.C., Peres G.G., Cruz S.C.P., Whittington A. 2006. Kinematic evolution of the Araçuaí-West Congo Orogen in Brazil and Africa: Nutcracker tectonics during the Neoproterozoic assembly of Gondwana. *Precambrian Research*, **149**:46-63.
- Arth J.G., Backer F., Stern T.W. 1988. Coast Batholith and Taku plutons near Ketchikan, Alaska: Petrography, geochronology, geochemistry, and isotopic character. *American Journal of Sciences*, **288-A**:461-489.
- Bateman P.C., Dodge F.C.W., Bruggman P.E. 1984. Major oxide analyses, CIPW norms, modes, and bulk specific gravities of plutonic rocks from the Mariposa 1 degrees by 2 degrees sheet, central Sierra Nevada, California. *U S Geological Survey OF 84-0162*, 59 pp.
- Brueckner H.K., Cunningam., D., Alkmim F.F., Marshak S. 2000. Tectonic implications of Precambrian Sm-Nd dates from the southern São Francisco Craton and adjacent Araçuaí and Ribeira belts, Brazil. *Precambrian Research*, **99**:255-269.
- Castro A. 2013. Tonalite-granodiorite suite as cotectic system: a review of experimental studies with applications to granitoid petrogenesis. *Earth-Sciences Review*, **124**: 68-95.
- Castro A., Moreno-Ventas I., Fernández C., Vujovich G., Gallastegui G., Heredia N., Martino R.D., Becchio R., Corretgé L.G., Díaz-Alvarado J., García-Arias M., Liu D.-Y. 2011. Petrology and SHRIMP U-Pb zircon geochronology of Cordilleran granitoids of the Bariloche area, Argentina. *Journal of South American Earth Sciences*, **32**:508-530.
- Cecil M.R., Rotberg G.L., Ducea M.N., Saleeby J.B., Gehrels G.E. 2011. Magmatic growth and batholithic root development in the northern Sierra Nevada, California. *Geosphere*, **8**:592-606
- Clemens J.D., Stevens G., Farina F. 2011. The enigmatic sources of I-type granites: the peritectic connexion. *Lithos*, **126**:174-181.
- Cook R.D., Crawford M.L., Omar G.I., Crawford W.A. 1991. Magmatism and deformation, southern Revillagigedo Island, southeastern Alaska. *Geological Society of American Bulletin*, **103**:829-841.
- Crawford M.L., Crawford W.A. Lindline J. 2005. 105 Million years of igneous activity, Wrangell, Alaska, to Prince Rupert, British Columbia. *Canadian Journal of Earth Science*, **42**:097-1116.
- Féboli W.L. & Paes V.C. 2000. *Folha Itanhomi. Projeto Leste*. CPRM-CODEMIG. <http://www.portalgeologia.com.br/mapa/>.

Féboli, W.L., 2000. *Folha Governador Valadares. Projeto Leste*. CPRM-CODEMIG. <http://www.portalgeologia.com.br/mapa/>.

Glazner A.F. 2007. Thermal limitations on incorporation of wall rocks into magma. *Geology*, **35**:319-322.

Gonçalves L., Alkmim F.F., Pedrosa-Soares A., Gonçalves C.C., Vieira V. 2018: From the plutonic root to the volcanic roof of a continental magmatic arc: a review of the Neoproterozoic Araçuaí orogen, southeastern Brazil. *International Journal of Earth Science*, **107**:337-358

Gonçalves L.E. 2009. *Características Gerais e História Deformacional da Suíte Granítica G1, entre Governador Valadares e Ipanema, MG*. Master Thesis. Universidade Federal de Ouro Preto, Ouro Preto, Brasil, p. 112.

Gonçalves L.E., Alkmim F.F., Pedrosa-Soares C.A., Dussin I.A., Valeriano, C.d.M., Nalini Jr.H.A. Lana C., Tedeschi M. 2016. Granites of the intracontinental termination of a magmatic arc: an example from the Ediacaran Araçuaí orogen, southeastern Brazil. *Gondwana Research*, **36**:439-458

Gonçalves L.E., Farina F., Lana C., Pedrosa-Soares C.A., Alkmim F.F., Nalini Jr.H.A. 2014. New U-Pb ages and lithochemical attributes of the Ediacaran Rio Doce Magmatic Arc, Araçuaí confined orogen, southeastern Brazil. *Journal of South American Earth Sciences*, **52**:1-20.

Lee C-T.A., Morton D.M., Kistler R.W., Baird A.K. 2007. Petrology and tectonics of Phanerozoic continent formation: from island arcs to accretion and continental arc magmatism. *Earth and Planetary Science Letters*, **263**:370-387.

Mondou M., Egydio-Silva M., Vauchez A., Raposo M.I.B., Bruiguiet O., Oliveira A.F. 2012. Complex, 3D strain patterns in a synkinematic tonalite batholith from the Araçuaí Neoproterozoic orogen (Eastern Brazil): Evidence from combined magnetic and isotopic chronology studies. *Journal of Structural Geology*, **39**:158-179.

Mondou, M. 2010. *Structural and Thermal Evolution of a Synkinematic Batholith from the Neoproterozoic Araçuaí Hot Orogen (Eastern Brazil)*. PhD Thesis. University of São Paulo and University of Montpellier II, pp.216.

Nalini Jr. H.A. 1997. *Caractérisation des suites magmatiques néoproterozoïques de la région de Conselheiro Pena et Galiléia (Minas Gerais, Brésil): étude géochimique et structurale des suites Galiléia et Urucum et leur relation avec les pegmatites à éléments rares associées*. These Docteur, Ecole Nationale Supérieure des Mines de Paris, pp. 237

Nalini Jr. H.A., Bidal E., Paquette J.L., Machado R. 2000. Geochronologie U-Pb et géochimie isotopique Sr-Nd des granitoides Neoproterozoïques des suites Galileia et Urucum, vallée du Rio Doce, Sud-Est du Brésil. *Comptes Rendus Academie Science Paris*, **331**:459-466.

Nalini Jr. H.A., Machado R., Issamu E., Bidal E. 2008. A importância da tectônica transcorrente no alojamento de granitos pré a sincolisionais na região do vale do médio Rio Doce: o exemplo das suítes graníticas Galiléia e Urucum. *Revista Brasileira da Geociências*, **38**:741-752.

Nalini Jr. H.A., Machado R.M., Bilal E. 2005. Geoquímica e petrogênese da Suíte Galiléia: exemplo de magmatismo tipo I, metaluminoso, pré-colisional, neoproterozóico da região do Médio Vale do Rio Doce. *Revista Brasileira de Geociências*, **35**:23-24.

Oliveira M.J.R. 2000. *Folha Conselheiro Pena. Projeto Leste. CPRM-CODEMIG.* <http://www.portalgeologia.com.br/mapa/>.

Pankhurst R.J., Weaver S.D., Hervé F., Larrondo P. 1999. Mesozoic-Cenozoic evolution of the North Patagonian Batholith in Aysen, southern Chile. *Journal of the Geological Society*, **156**: 673-694.

Pedrosa-Soares A.C., Alkmim F.F., Tack L., Noce C.M., Babinski M., Silva L.C., Martins-Neto M. 2008. Similarities and differences between the Brazilian and African counterparts of the Neoproterozoic Araçuaí-West Congo Orogen. In: Pankhurst J.R., Trouw R.A.J., Brito Neves B.B., De Wit M.J. (Eds.) *West Gondwana: Pre-Cenozoic Correlations across the South Atlantic Region. Geological Society of London, Special Publications*, **294**:153-172.

Pedrosa-Soares A.C., De Campos C., Noce C.M., Silva L.C., Novo T., Roncato J., Medeiros S., Castañeda C., Queiroga G., Dantas E., Dussin I., Alkmim F.F. 2011. Late Neoproterozoic–Cambrian granitic magmatism in the Araçuaí Orogen (Brazil), the Eastern Brazilian Pegmatite Province and related mineral resources. *Geological Society London, Special Publications*, **350**:25-51.

Pedrosa-Soares A.C., Noce C.M., Vidal P., Monteiro R., Leonardos O.H. 1992. Toward a new tectonic model for the Late Proterzoic Araçuaí (SE Brazil) - West Congolian (SW Africa) Belt. *Journal of South American Earth Sciences*, **6**:33-47.

Pedrosa-Soares A.C., Noce C.M., Wiedemann-Leonardos C.M., Pinto C.P. 2001. The Araçuaí-West Congo Orogen in Brazil: an overview of a confined orogen formed during Gondwanaland assembly. *Precambrian Research*, **110**:307–323.

Pedrosa-Soares A.C., Vidal P., Leonardos O.H., Brito-Neves B.B. 1998. Neoproterozoic oceanic remnants in eastern Brazil: Further evidence and refutation of an exclusively ensialic evolution for the Araçuaí-West Congo orogen. *Geology*, **26**:519-522.

Tedeschi M., Novo T., Pedrosa-Soares A.C., Dussin I., Tassinari C., Silva L.C., Gonçalves L., Alkmim F.F., Lana C., Figueiredo C., Dantas E., Medeiros S., De Campos C., Corrales F., Heilbron M. 2016. The Ediacaran Rio Doce magmatic arc revisited (Araçuaí-Ribeira orogenic system, SE Brazil). *Journal of South American Earth Science*, **68**:167-186

Vauchez A., Egydio-Silva M., Babinski M., Tommasi A., Uhlein A., Liu D. 2007. Deformation of a pervasively molten middle crust: insights from the Neoproterozoic Ribeira-Araçuaí orogen (SE Brazil). *Terra Nova*, **19**:278-286.

Zen E-an. & Hammarstrom J.M. 1984a. Magmatic epidote and its petrologic significance. *Geology*, **12**:515-518.

Zen E-an. & Hammarstrom J.M., 1984b. Mineralogy and a petrogenetic model for the tonalite pluton at Bushy Point, Revillagigedo Island, Ketchikan 1° x 2° Quadrangle, South-eastern Alaska. *U.S. Geological Survey, Circular* **939**:118-123.

CHAPTER 4**MAGMATIC GARNET IN CORDILLERAN-TYPE GALILÉIA
GRANITOIDS OF THE ARAÇUAÍ BELT (BRAZIL): EVIDENCE FOR
CRYSTALLIZATION IN THE LOWER CRUST**

PRESENTATION OF THE PUBLICATION

This paper¹, first authored by Francesco Narduzzi has been published in *Lithos* during my PhD. The aspects highlighted in this paper were done independently by Francesco Narduzzi while receiving standard supervision by his supervisor Herminio Harias Nalini Jr., Federico Farina, Gary Stevens, Cristiano Lana. I did the sampling part in the field, I did the petrographic description, acquired the mineral chemical data through SEM equipment and I have prepared the rock powders for XRF geochemical analyses. I did also the literature review and I have written the majority of the scientific paper. Federico Farina contributed to the field work and together with Gary Stevens and Cristiano Lana, have assisted me during the paper writing and some data interpretation.

F. Narduzzi^{a,b*}

F. Farina^{a,c}

G. Stevens^b

C. Lana^a

H.A. Nalini Jr.^a

^aApplied Isotope Research Group, Departamento de Geologia, Escola de Minas, Universidade Federal de Ouro Preto, Campus Universitário Morro do Cruzeiro s/n, 35400-000 Ouro Preto, MG, Brazil

^bCentre for Crustal Petrology, Department of Earth Science, University of Stellenbosch, Private Bag X1, 7602 Stellenbosch, South Africa

^cUniversity of Geneva, Department of Earth Sciences, Rue des Maraîchers 13, 1205 Geneva, Switzerland

¹Narduzzi, F., Farina, F., Stevens, G., Lana, C., Nalini Jr., H.A. 2017. Magmatic garnet in Cordilleran-type Galiléia granitoids of the Araçuaí belt (Brazil): Evidence for crystallization in the lower crust. *Lithos*. 282-283:82-97 DOI: 10.1016/j.lithos.2017.02.017



Magmatic garnet in the Cordilleran-type Galiléia granitoids of the Araçuaí belt (Brazil): Evidence for crystallization in the lower crust



F. Narduzzi^{a,b,*}, F. Farina^{a,c}, G. Stevens^b, C. Lana^a, H.A. Nalini Jr.^a

^a Applied Isotope Research Group, Departamento de Geologia, Escola de Minas, Universidade Federal de Ouro Preto, Campus Universitário Morro do Cruzeiro s/n, 35400-000 Ouro Preto, MG, Brazil

^b Centre for Crustal Petrology, Department of Earth Science, University of Stellenbosch, Private Bag X1, 7602 Stellenbosch, South Africa

^c University of Geneva, Department of Earth Sciences, Rue des Maraîchers 13, 1205 Geneva, Switzerland

ARTICLE INFO

Article history:

Received 9 September 2016

Accepted 25 February 2017

Available online 06 March 2017

Keywords:

Grossular-rich magmatic garnet

Magmatic epidote

High pressure crystallization

Cordilleran-type Galiléia granitoids

Araçuaí Orogen

ABSTRACT

Magmatic garnet, together with epidote, is a rare mineral association in cordilleran-I-type granitoids and of special petrogenetic significance. The metaluminous to slightly peraluminous ($ASI = 0.97\text{--}1.07$) Galiléia batholith (Brazil) is a large (ca. 30,000 km²), Neoproterozoic (ca. 632–570 Ma) weakly foliated calc-alkaline granitoid body, characterized by the widespread occurrence of garnet (grossular 25–43 mol%) and epidote (pistacite 9.3–22.7 mol%). Field, petrographic and mineral chemical evidence indicates that garnet, epidote, biotite as well as white mica crystals (low-Si phengite), are magmatic. There is no difference in bulk rock major and trace element composition between the Galiléia granitoids and other garnet-free cordilleran-type granitoids worldwide. This evidence strongly suggests that the origin of the uncommon garnet + epidote parageneses is related to the conditions of magma crystallization, such as pressure, temperature and water content. Comparison between the mineral assemblages and mineral compositions from this study and those recorded in crystallization experiments on metaluminous calc-alkaline magmas, as well as within garnet-bearing metaluminous volcanic rocks and granitoids, indicates that the supersolidus coexistence of grossular-rich garnet, epidote and white mica is consistent with magma crystallization at pressures greater than 0.8 GPa (above 25 km depth) and at temperatures below 700 °C, i.e. near the water saturated solidus. Furthermore, resorption textures around garnet (plagioclase ± quartz coronas) and epidote suggest that these minerals have been partially consumed prior to complete crystallization. These findings demonstrate that at 630 Ma the crust underneath the Araçuaí Orogen was already at least 25–30 km thick and relatively cool. However, this contrasts with the marked high heat flow registered from the neighbour Carlos Chagas Batholith located 50 km to the east. In fact such granitoids record granulite-facies metamorphism at the same pressure and time (ca. 570 Ma) of Galiléia granitoids crystallization. Thus, a more suitable geodynamic scenario is required in order to explain these two contrasting thermal regimes within the same orogen. Eventually, field, petrographic and mineral chemical analogies with similar garnet-bearing granitoids located in the fore-arc settings of the British Columbia subduction zone, possibly imply that the Galiléia granitoids represent “rare” garnet- and epidote-bearing metaluminous Cordilleran-I-type granites which can only form in a fore-arc setting.

© 2017 Elsevier B.V. All rights reserved.

1. Introduction

Garnet is a common minor component of peraluminous granites formed via partial melting of Al-rich metasedimentary rocks (i.e. S-type granites). In these rocks, garnet has been shown to be commonly peritectic, produced by biotite incongruent melting of the metapelitic source of the S-type magma, or due to partial melting of metasedimentary country rock which the magma intruded (Erdmann et al., 2009; Lackey et al., 2012; Melo et al., 2016). Furthermore, garnet

has also been proposed to represent entrained crystals from the source, that were not involved in the anatexis process (i.e. a restite crystal, Vernon, 2007) or a xenocryst incorporated from the wall rock during the ascent and emplacement of the granitic body (Clarke, 2007). On the other hand, many studies have shown that garnet in S-type granites can also be magmatic in origin (e.g. Allan and Clarke, 1981; Barnes et al., 2012; Dalquist et al., 2007; Harrison, 1988; Lackey et al., 2012; Miller and Stoddard, 1981; Villaros et al., 2009). In addition, when subjected to metamorphism at suitable conditions, granites may develop metamorphic garnet. A good example is reported by Vielzeuf and Schmidt (2001), where Hercynian granitoids subjected to high pressure metamorphism during Alpine orogenesis developed garnet aureoles around biotite and plagioclase.

* Corresponding author at: Applied Isotope Research Group, Departamento de Geologia, Escola de Minas, Universidade Federal de Ouro Preto, Campus Universitário Morro do Cruzeiro s/n, 35400-000 Ouro Preto, MG, Brazil.

E-mail address: narduzzi13@gmail.com (F. Narduzzi).

In metaluminous cordilleran-type granites as well as in metaluminous volcanic rocks, garnet is extremely rare and few natural occurrences have been reported in the literature (e.g. Bach et al., 2012; Barnes and Allen, 2006; Dawes and Evans, 1991; Day et al., 1992; Evans and Vance, 1987; Harangi et al., 2001; Samadi et al., 2014). Crystallization experiments (e.g. Alonso-Perez et al., 2009; Green, 1972, 1977, 1992; Green and Ringwood, 1968; Schmidt, 1993; Schmidt and Thompson, 1996) on metaluminous andesitic and tonalitic to granodioritic compositions show that garnet is stabilized at high pressures and at low temperatures, in magmas that are water-rich (typically in the range of 5–10 wt.% H₂O). The rare occurrence of garnet in such compositions in the plutonic record suggests that these conditions are rarely achieved (or preserved) in nature. Metaluminous granites and volcanic rocks with dacitic–rhyolitic composition can also be characterized by another uncommon magmatic mineral: epidote (Brandon et al., 1996; Schmidt, 1993; Schmidt and Poli, 2004; Schmidt and Thompson, 1996; Zen and Hammarstrom, 1984a, 1984b). More than a decade ago, Schmidt and Poli (2004) reported 19 occurrences worldwide. Since then an increasing number of scientific works reported its presence in other cordilleran-type granitic plutons and batholiths. As with garnet, epidote can be either metamorphic or magmatic. Magmatic epidote is commonly interpreted to indicate crystallization at moderate- to high-pressures (>0.6 GPa), with water saturation of the magma (≥ 10 wt.% of H₂O) (Schmidt and Thompson, 1996). Experimental evidence (Holdaway, 1972; Liou, 1973; Schmidt and Poli, 2004; Schmidt and Thompson, 1996) indicates that epidote stability is dependent on melt composition and f_{O_2} state, with crystallization being favoured in metaluminous granodioritic to tonalitic compositions in a relatively oxidized environment (i.e. NNO oxygen buffer). In addition, epidote appears to crystallize together with garnet only above approximately 1.2 GPa (Schmidt and Thompson, 1996). We combined information on occurrences of magmatic garnet (Samadi et al., 2014) and epidote (Schmidt and Poli, 2004) in metaluminous intrusives and volcanic rocks worldwide and there appear to be only few localities where magmatic garnet and epidote have crystallized together. These include: the garnet–epidote bearing dikes cropping out in the Front Range, Colorado (Dawes and Evans, 1991; Evans and Vance, 1987); the Dehnow pluton, north east Iran (Samadi et al., 2014); the Bushy Point Granites, south eastern Alaska (Arth et al., 1988; Zen and Hammarstrom, 1984a, 1984b); the Jinshan Intrusion associated with the Dabie Orogenic belt, China (e.g. Xu et al., 2013) and the subject of this study, the 30,000 km² Neoproterozoic Cordilleran-type Galiléia Batholith, located within the Araçuaí Orogen, Brazil (Mondou et al., 2012; Nalini, 1997; Nalini et al., 2000, 2005, 2008; Vauchez et al., 2007). Garnet and epidote-bearing assemblages have been reported throughout the Galiléia batholith but the origin of both minerals has not been accurately constrained. Detailed field and petrographic investigations coupled with mineral chemistry, whole rock geochemistry and comparison with the assemblages and mineral compositions produced in high pressure experiments, are used here to shed light on the origin of garnet and epidote in the Galiléia batholith.

2. Geological background

2.1. General background of the Araçuaí Orogenic Belt

The Araçuaí Orogenic Belt, together with its African counterpart (the West Congolian Belt), was formed during the Brasiliano/Pan-African orogeny (ca. 640–520 Ma; e.g. Alkmim et al., 2006). This orogen, located in south-eastern Brazil (Fig. 1a), lies between the Atlantic Ocean and the São Francisco Craton. Different tectono-stratigraphic schemes have been proposed to describe the architecture of this orogen. Pedrosa-Soares et al. (2001) and Pedrosa-Soares and Wiedemann-Leonardos (2000) proposed its subdivision into external, internal and northern domains, while Mondou et al. (2012) and Vauchez et al. (2007) adopted

another subdivision (Fig. 1b) defining a Western Domain (or Western Mylonitic Unit), a Central Domain (or Central Plutonic Unit) and an Eastern Domain (or Anatectic Unit). Each domain is separated through major thrust zones (Fig. 1b; e.g. Vauchez et al., 2007). The Western Domain, which has been thrust over the eastern São Francisco Craton (mostly made up of gneiss and Al-quartzites), consists of high-temperature (~750 °C) and relatively low-pressure (~0.6 GPa) metasedimentary mylonites crosscut by abundant syn-kinematic garnet–cordierite-bearing leucocratic veins (570–580 Ma, LA-ICP-MS U–Pb zircon and monazite ages; Petitgirard et al., 2009). The Central Domain is mainly represented by Neoproterozoic (ca. 632–570 Ma) I-type granitoids which intrude the Paleoproterozoic basement (ca. 2.2–2.0 Ga) represented by the Pocrane gneiss Complex, and by the arc-related Rio Doce metasediments (Fig. 1c) (Gonçalves et al., 2014 and reference therein). According to Pedrosa-Soares et al. (2001) and Pedrosa-Soares et al. (2011) the granitoids and the metasediments are grouped together into the granitic 1 (G1) supersuite and are thought to be related to the pre-collisional stages of the Brasiliano orogeny that build up the Araçuaí orogen (Pedrosa-Soares et al., 2001). The Eastern Domain is subdivided into the Nova Venécia complex composed of migmatites, granulites and granites (e.g. Richter et al., 2015) and into the Carlos Chagas batholith characterized by peraluminous S-type granitoids (e.g. Melo et al., 2016). These rocks, according mainly to their location, ages and geochemistry (Pedrosa-Soares et al., 2001), are subdivided in syn-collisional (G2, 585–560 Ma), late collisional (G3; 560–530 Ma) and post-collisional (G4–G5, 530–480 Ma) supersuites. Small igneous bodies belonging to the G2, G4 and G5 supersuites, intrude into the Central Domain.

2.2. The Galiléia Batholith

The granitoids of the G1 supersuite (Fig. 1b, c) consist of orthopyroxene-rich (i.e. charnockites) and orthopyroxene-free granites and granodiorites, the latter forming the so-called Galiléia Batholith and displaying variable amounts of mafic microgranular enclaves (MME) (e.g. Gonçalves et al., 2014). The batholith extends roughly north–south for ca. 600 km, almost the entire length of the Araçuaí orogen, covering an area of approximately 30,000 km² (Fig. 1a) (Gonçalves et al., 2014; Pedrosa-Soares et al., 2011; Pedrosa-Soares et al., 2001; Vauchez et al., 2007). Based on field evidence, mineral textural studies and geochemical features, Gonçalves et al. (2014) have recently further subdivided the Galiléia batholith into a suite of enclave-rich tonalite–granodiorite rocks and a suite of enclave-poor tonalitic to granitic rocks. These two suites, appear to occur throughout the whole batholith (Fig. 1b and c). Geochemically, the opx-free granitoids resemble medium- to high-K metaluminous Cordilleran-type granitoids, and are interpreted as being produced during the Rio Doce arc-related magmatism; they are suggested to be derived from the partial melting of the Paleoproterozoic basement due to underplating of mantle derived magmas (e.g. Gonçalves et al., 2014). However, assimilation of host rocks, fractional crystallization during the ascent of mantle-derived magmas, or mixing between mantle derived magma with felsic magmas of crustal origin have also been proposed as possible processes that might have shaped the Galiléia igneous rocks (e.g. Gonçalves et al., 2014).

Recently, Tedeschi et al. (2016) presented new ages for the whole G1 granitoid suite and reviewed the age information available from previous studies. The entire age spectrum demonstrates that the G1 granitoids have magmatic zircon crystals indicating intrusion between 632 and 570 Ma. Tedeschi et al. (2016) identify three main intervals of crystallization ages: 632–605 Ma, 600–590 Ma and 585–570 Ma (Fig. 13 in Tedeschi et al., 2016), which have been suggested to represent three main periods of granitogenesis thus corresponding to three main phases of construction of the Rio Doce arc.

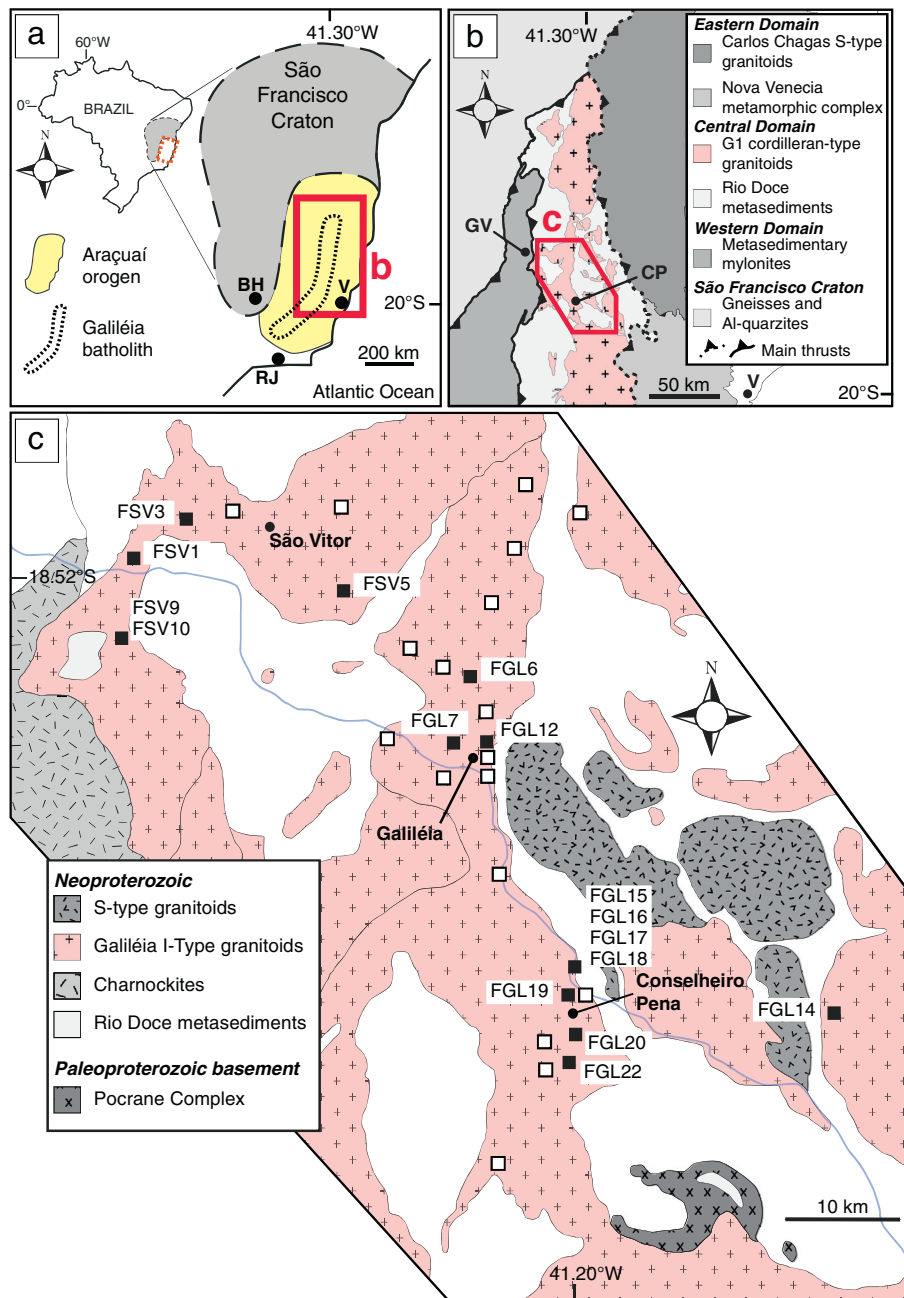


Fig. 1. Schematic geological map of the Araçuaí Orogen and Galiléia granitoids (modified after Vauchez et al., 2007). (a) Location of the Araçuaí Orogen (red rectangles) and Galiléia batholith in Brazil; SFC: São Francisco Craton; (b) Subdivision of the Araçuaí Orogen in Western, Central and Eastern domain while black bold and dotted lines are major thrusts separating each domain (after Vauchez et al., 2007); red polygon indicate the study area; (c) Geological map of the central part of the Galiléia batholith; In (a) and (b): BH: Belo Horizonte; CP: Conselheiro Pena; GV: Governador Valadares; RJ: Rio de Janeiro; V: Vitória. (For interpretation of the references to colour in this figure legend, the reader is referred to the web version of this article.)

2.3. The Rio Doce metasedimentary host rocks

The Rio Doce metasediments are poorly studied. In the studied area an unpublished work (Vieira, 2007) has proposed that these rocks underwent medium pressure amphibolite facies metamorphism with pressure estimates from empirical geobarometry on garnet-bearing rocks of approximately 0.5 GPa. The study was conducted on areas far from the contact with the Galiléia granitoids. Cunningham et al. (1996) and Nalini et al. (2008) report that the Galiléia granitoids have both intrusive and tectonic contacts with the Rio Doce metasediments. Mondou et al. (2012) suggested also that intrusion was contemporaneous with pervasive deformation in the Rio Doce metasediments.

3. Results

This study focuses on the granites belonging to the enclave-rich unit in the central part of the Galiléia batholith (Fig. 1b and c), previously investigated by Gonçalves et al. (2014), Mondou et al. (2012), Nalini (1997), Nalini et al. (2000, 2005, 2008) and Vauchez et al. (2007). The study area covers ca. 4000 km². In this paper we use the name Galiléia granitoids to refer to the enclave-rich granitoids of the Galiléia batholith. A description of the analytical methods used as well as the complete dataset comprehensive of both mineral chemistry data and whole rock compositions are presented in the Online Supplementary Material.

3.1. Field relationships

The studied rocks consist of medium-grained tonalites, granodiorites, and subordinate granites (Fig. 2), that are either equigranular or porphyritic, with the latter texture reflecting the presence of feldspar crystals (≥ 1 cm) larger than the respective matrix minerals. Less commonly, coarse- and fine-grained examples of tonalite and granodiorite also occur. The granitoids are typically weakly deformed showing a foliation that is defined by the orientation of biotite and amphibole crystals and marked by the long axis of stretched mafic enclaves (Fig. 2a and b). The foliation has a dip ranging from 50° to 80° towards NE or SW (see also Nalini et al., 2008). Some outcrops display evidence for the coexistence of slightly different varieties of granite, one more melanocratic and the other more leucocratic (Fig. 2c). Based on petrographic and field observations, major rock-forming minerals are plagioclase

(32–42 vol.%), quartz (15–33 vol.%) and K-feldspar (1.5–14 vol.%). Biotite, amphibole and garnet are the main mafic minerals (see also Gonçalves et al., 2014), with biotite being the most abundant, forming up to 19 vol.%. Hornblende is not ubiquitous and occurs in ca. 80% of the outcrops, sometimes forming crystals of up to 1 cm in size and making up 3–18 vol.% of the rock. Garnet forms a minor component of the rocks up to 2 vol.%. A detailed description of the procedure used for the vol.% estimation is given in Section 3.1.1. Accessory minerals are epidote, allanite, titanite, apatite, zircon, pyrite and pyrrhotite, while oxide minerals such as magnetite and ilmenite are rare.

Tonalites and granodiorites are characterized by different amounts of mafic microgranular enclaves (MME) (Fig. 2a, b, and d). MMEs can be lobate, stretched, lenticular, and sometimes showing bridge structures (Fig. 2a, b, e and f, respectively). In agreement with Nalini et al. (2008) the enclaves are generally stretched along a $N30-60^\circ W$

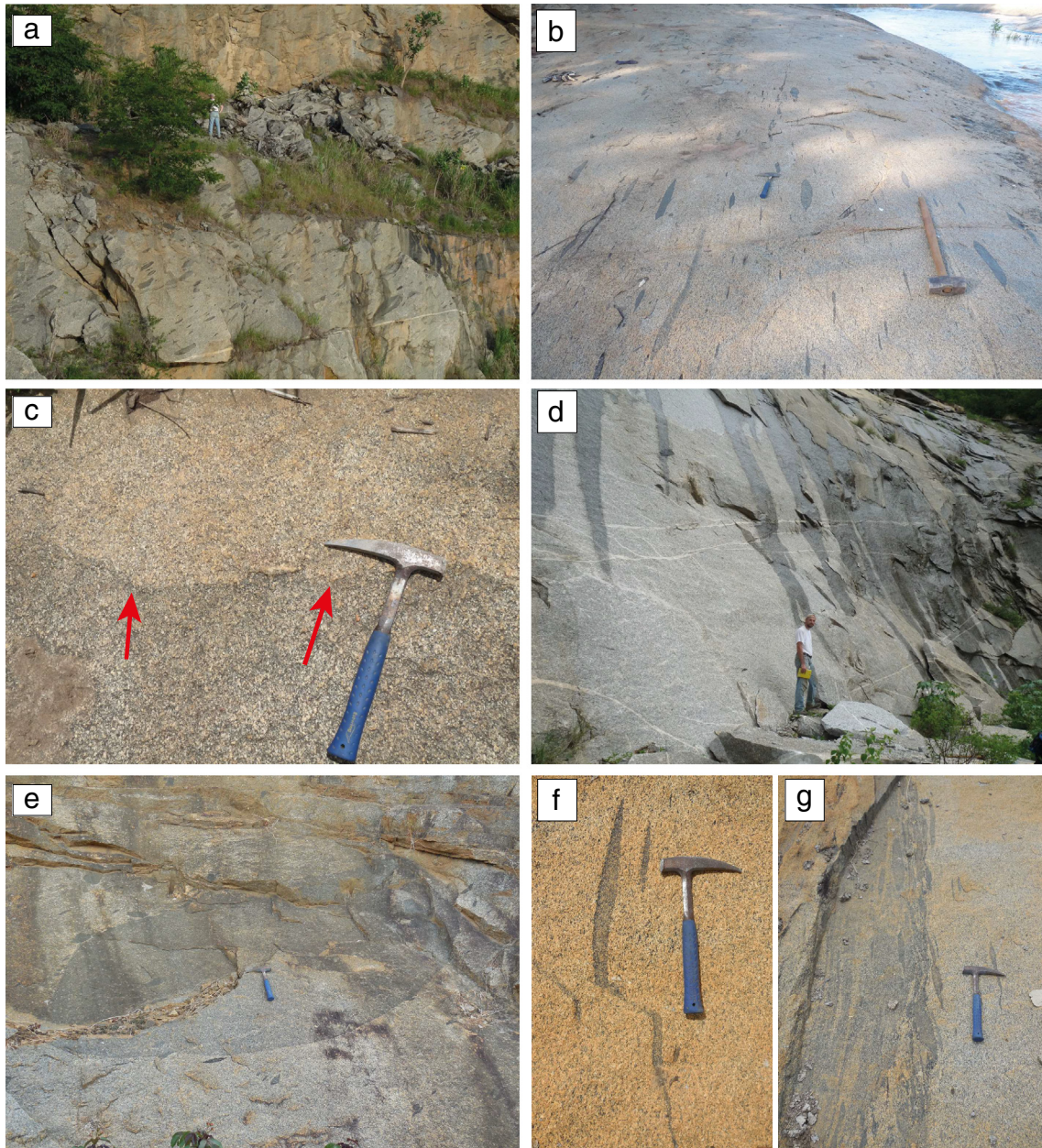


Fig. 2. Field features of the Galiléia granitoids. Typical appearance of a: (a) garnet-bearing enclave-rich granitoids, (b) garnet-free granitoid containing widespread MMEs (≥ 7 MME/m²), (c) coexistence of a melanocratic and leucocratic granitic magmas as indicated by the red arrows, (d) MME-free garnet-bearing granite; (e) rounded composite enclave reaching almost 4 m in width; (f) stretched enclaves. Note the bridge structure, possibly due to deformation in sub-magmatic state; (g) stretched enclaves swarm in a composite dyke. Brown and blue hammer are 60 and 32 cm in length, respectively. (For interpretation of the references to colour in this figure legend, the reader is referred to the web version of this article.)

direction and exhibit variable aspect ratios (length/width = 2:1 to ca. 10:1). The most stretched enclaves occur in outcrops where the granitoids are both strongly and weakly deformed (Fig. 2a and b, respectively). The stretched mafic enclaves in the weakly deformed granites (i.e. Fig. 2b) have aspect ratios that are inconsistent with the weak fabrics in the matrix around the enclaves, confirming that they represent a strong magmatic state lineation produced by magma flow (e.g. Paterson et al., 1998). In the least deformed outcrops, MMEs have also variable sizes reaching occasionally up to 4 m in length (Fig. 2e), while in other areas they are small (<2 cm) and can easily be misinterpreted as biotite clots. In order to quantify their abundance, MME counting (MME/m², Fig. 3a) was performed using an area of 5 × 5 m, for a total of 30 outcrops. Where possible, more than one area was analysed for each outcrop. In the counting procedure, only those MMEs that were at least for three-quarters of their area inside the grid were counted.

MME counts range between 0 and 7 MME/m², with values between 1.70 and 3.30 MME/m² being typical (Fig. 2a, c, d).

3.1.1. Garnet abundance and distribution

Garnet is widespread in the Galiléia Batholith and garnet counting (garnet crystals/m², Fig. 3b) was performed in order to describe the variation in the number of macroscopically visible crystals per m²; a grid area of 10 × 20 cm was used. Counting was conducted for 30 outcrops. In this case, up to five areas were counted per each outcrop, with the grids randomly distributed on the surface of the outcrop and separated by distances of more than 1 m in order to avoid counting bias. Within individual outcrop the garnet crystal/m² counts do not vary significantly. Consequently, the average values calculated are assumed to be representative for each outcrop.

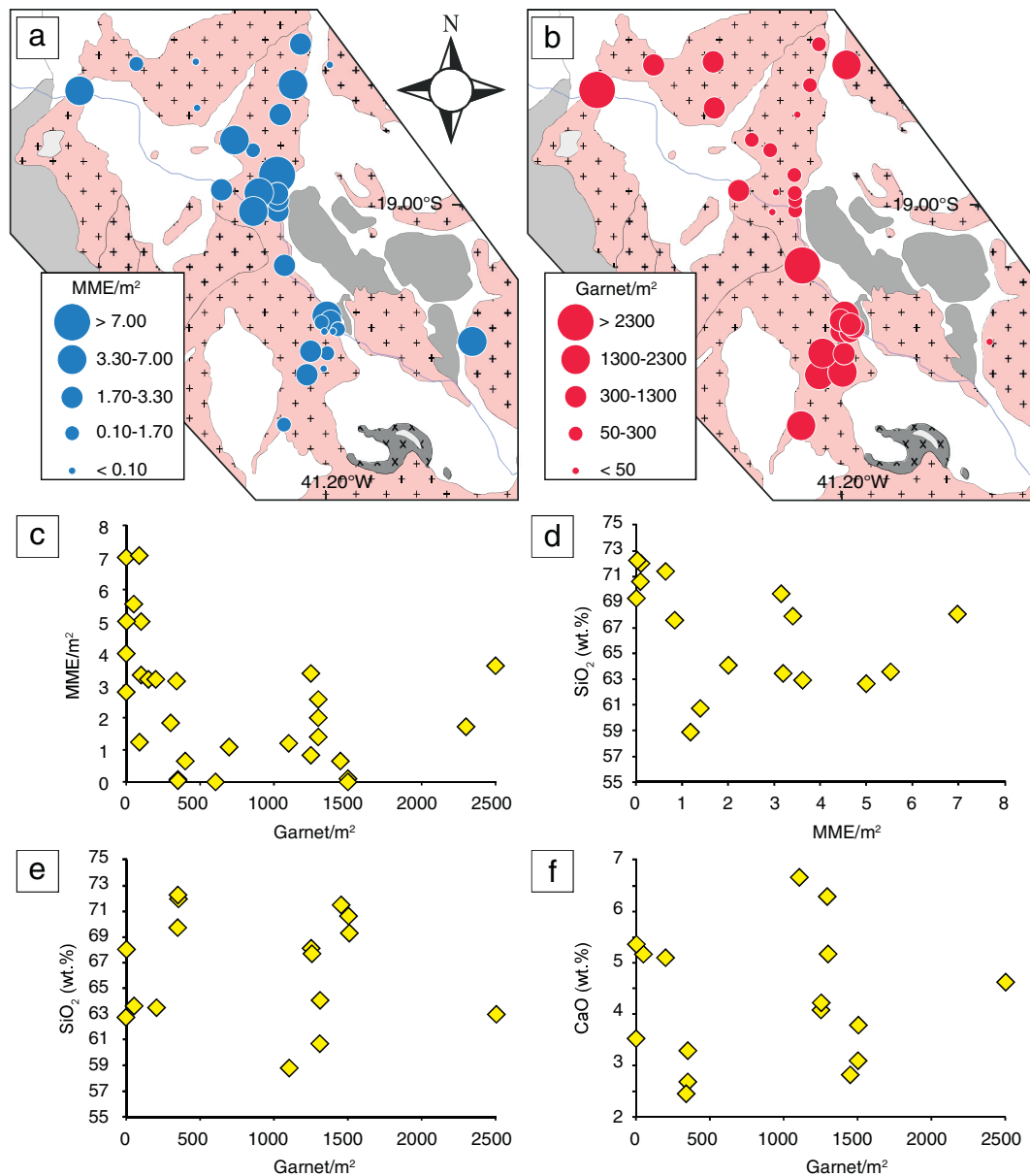


Fig. 3. Garnet and mafic enclave counting. MME (a) and garnet (b); counts for 30 outcrops. The grids used for counting were 25 m² (5 × 5 m) for MMEs and 200 cm² (10 × 20 cm) for garnets (later converted in m²). The lowest garnet counts (Grt/m² < 50) represent 0 vol.%, while the highest reach almost 2 vol.% of the outcrop. Note that the area is the same as in Fig. 1c and this counting procedure covered all the entire area, that is ca. 4000 km²; (c) Average garnet vs. MME counts; (d) and (e) MME/m² and Grt/m² are plotted against granitoid SiO₂ content; in (f) the Grt/m² is plotted against the CaO (see the text for more explanation). Note that for some of the samples here plotted, the chemical analyses will be reported elsewhere.

The number of garnet crystals per m^2 varies from 0 to a maximum of 2500. This equates to a variation from 0 up to ca. 2 vol.%. Nevertheless, most of the batholith has a garnet crystal abundance between 300 and 1300 crystals/ m^2 . There is no relationship between garnet abundance and degree of rock deformation. Moreover, there is no relationship between the abundance of garnet crystals and proximity to contacts with the country rocks (Fig. 3b), nor with the presence of country rock xenoliths. Additionally, there is also no relationship between the number of garnet crystals and the abundance of mafic enclaves (Fig. 3c) or with the geochemistry of the rocks. In fact the MME and garnet abundance results in a scattered behaviour when compared with bulk rock SiO_2 and CaO concentrations (Fig. 3d, e and f). Garnet is found mostly in granodiorites with the exception of the only tonalite sampled. Garnet ranges in size from 1 to 6 mm with an average of less than 2 mm (Figs. 4 and 5). Crystals typically have a dark red core surrounded by an orange rim. In the field, garnet exhibits a range of habits that occur with different associations, irrespective of the degree of matrix deformation. These are: 1) anhedral to subhedral crystals mantled by or included in subhedral feldspars in porphyritic weakly deformed to non-deformed granitoids (Fig. 4a and b, respectively); 2) skeletal crystals showing evidence of resorption associated with plagioclase and biotite in textures that suggest that these minerals have replaced garnet (Fig. 4c) and 3) euhedral garnets in amphibole-bearing granitoids (Fig. 4d). Moreover garnet appears to also have been transferred from the granite to the MMEs during mingling between the felsic and intermediate to mafic magmas. This occurred directly as dispersed single crystals as well as after being included in subhedral feldspar (Fig. 4e).

3.2. Petrography

The Galiléia granitoids display four different ferromagnesian mineral associations which are reported in order of abundance: 1) biotite + garnet (Bt + Grt), 2) biotite + amphibole + garnet (Bt + Amp + Grt), 3) biotite + amphibole (Bt + Amp), and 4) biotite (Bt), with epidote ubiquitous in all these rocks.

3.2.1. Major and minor rock-forming phases

Biotite (Figs. 5 and 6) varies in colour from dark brown to reddish, with euhedral and subeuhedral habitus, rarely exceeding 2 mm; apatite, zircon and epidote are common inclusions. Biotite is also found as inclusions within garnet, amphibole and plagioclase. The colour of biotite inclusions is identical to the matrix biotite and these crystals are always smaller than 1 mm. In the MMEs, biotite always appears to be in textural equilibrium with the other minerals, and as in the granites, biotite defines the foliation.

The rocks contain several different types of plagioclase. The most common type is represented by subhedral crystals that vary in size from less than 1 mm up to 5 mm (Figs. 4, 5 and 6). These crystals are slightly zoned and show undulose extinction. Plagioclase (\pm quartz) coronas around garnet, as well as plagioclase inclusions within garnet, share these characteristics. Plagioclase also occurs as larger (10 to 15 mm) crystals that have euhedral to subhedral An-rich cores surrounded by more sodic rims (Fig. 6j); these crystals are also found within the MMEs (Fig. 6k). Cracked and zoned epidote can be found as inclusions within the plagioclase (Fig. 6c). The presence of plagioclase showing intragranular fractures filled by late magmatic minerals such as quartz and K-feldspar is also recognized. This possibly represents microfractures developed in the presence of late stage melt (Fig. 6l). Alkali-feldspars occur either as larger (0.5 to 5 mm) perthitic microcline or smaller interstitial (0.2–0.7 mm) crystals, showing undulate extinction and weak deformation, respectively. They are also included in garnets.

Amphibole is present in the granitoids as well as within MMEs, and always occurs with lower modal abundance than biotite. Amphiboles are euhedral to subhedral with sizes comprising between ca. 0.1 and 0.8 mm, although larger amphibole (> 1 cm) also occurs. Inclusions in amphibole comprise biotite, plagioclase, apatite, zircon, titanite, ilmenite, primary sulphides, quartz and occasional epidote. Amphibole in the mafic enclaves displays a slightly more resorbed aspect relative to that in the granite, resulting in subhedral to anhedral habitus. Their colour and size are however comparable to those of the granitoids.

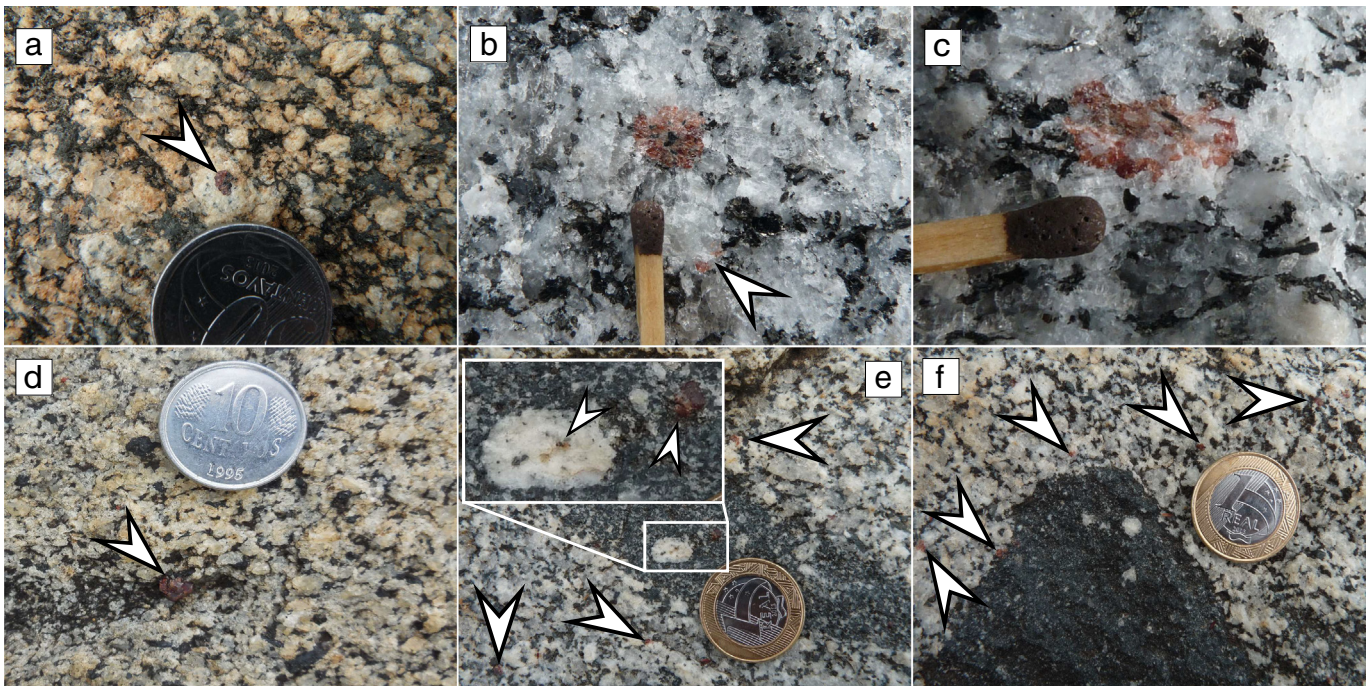


Fig. 4. Garnet field relationships. Garnets are indicated with arrows. Sizes are between 1 and 6 mm with an average of 3 mm; (a) anhedral garnet included in subhedral feldspar in weakly deformed granites; (b) subhedral radial garnet included in feldspar with evident biotite inclusion; (c) garnet in net disequilibrium and texturally associated with plagioclase feldspar and biotite; (d) euhedral garnet in amphibole bearing weakly deformed granite; (e) MME containing garnets occurring both as single crystals and included in subhedral feldspar; note the stretched character of the enclave hosted in weakly deformed granite; (f) garnet-free MME in garnet-bearing granites. The match head is 5 mm while grey and yellow coins are 2 and 2.5 cm, respectively. (For interpretation of the references to colour in this figure legend, the reader is referred to the web version of this article.)

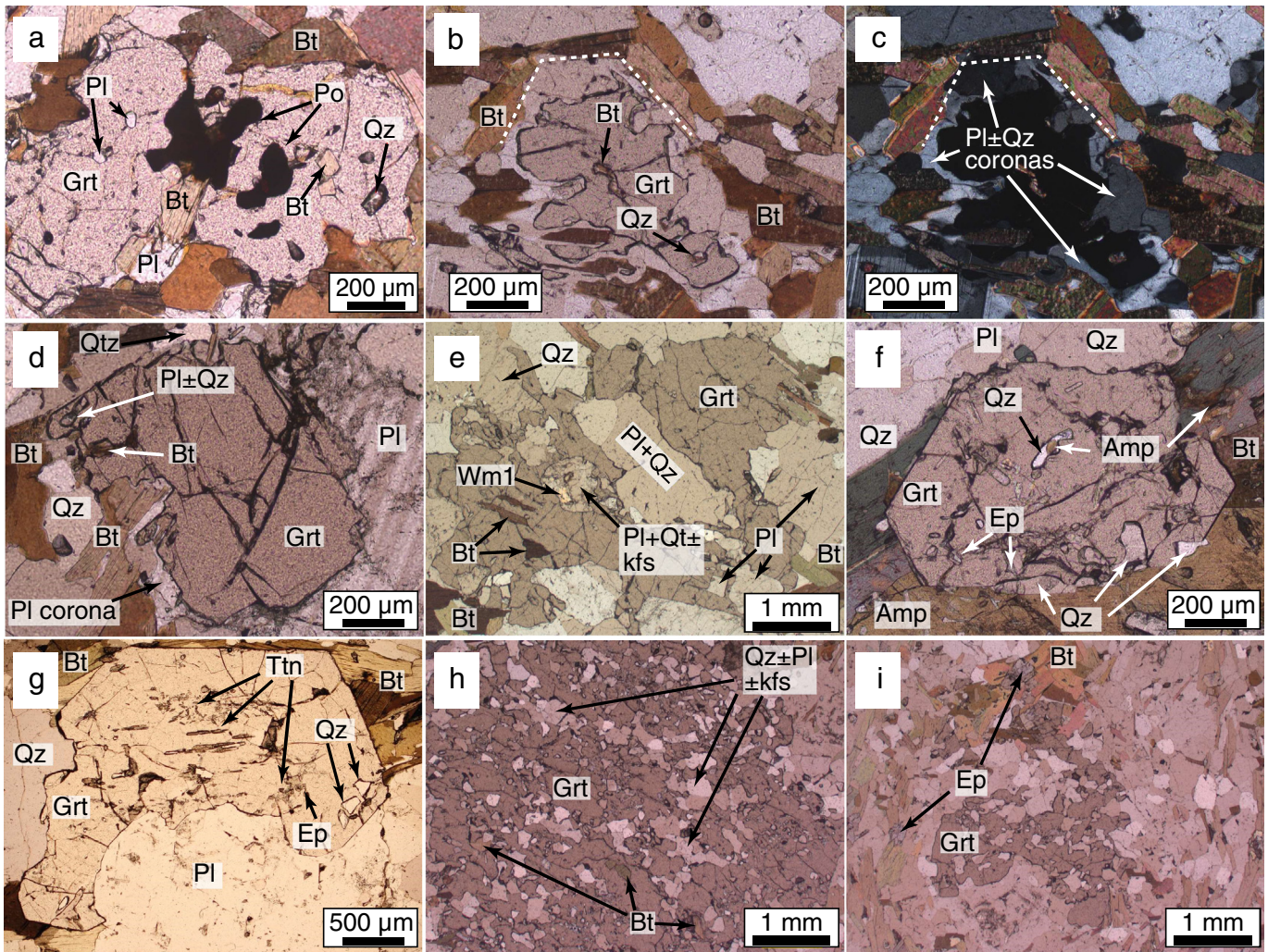


Fig. 5. Garnet petrography: (a) to (e) garnet in Bt + Grt granitoids; (f) and (g) garnets in Bt + Amp + Grt granitoids; (h) and (i) garnets in MMEs; (a) to (d) anhedral to subhedral garnets within the same thin section belonging to a slightly deformed granitoids; (a) inclusion-rich anhedral garnet having resorbed rims, mostly surrounded by biotites; note the random distribution of the inclusions; (b) and (c) inclusion-poor anhedral garnet with well-developed plagioclase \pm quartz and biotite coronas pseudomorphosing previous garnet shape; (c) is at crossed nicols; (d) inclusion-poor subhedral garnets showing different levels of rims resorption and plagioclase coronas; inclusions are localized only at the top left coupled with the increasing in grossular content (cf. Fig. 7b); (e) anhedral-skeletal garnet within weakly deformed granites (cf. Fig. 4c) with inclusion of primary white mica (Wm1) replacing magmatic plagioclase (cf. Fig. 6f); (f) randomly-distributed inclusion-rich euhedral garnet showing weakly resorption as also highlighted in Fig. 7a; (g) inclusion-rich subhedral garnet in weakly deformed granitoids with evident plagioclase resorption; (h) garnet having spongy-like texture probably as a consequence of geochemical disequilibrium with respect the host MME; this texture is not evident for the garnets hosted in the granitoids; the mineral inclusions assemblage in this garnet (cf. Fig. 7c) as well as those from (a) to (g) matches the mineral matrix assemblage of the host granitoids; (i) garnet crystal in MMEs almost completely resorbed; eventually, despite belonging to weakly deformed granitoids, none of the garnets crystal show any pressure shadows or recrystallization front around their resorbed rims; Other explanations in the text. Mineral abbreviations as in Whitney and Evans (2010).

Garnet crystals are commonly cracked and as already evidenced from field observations, they exhibit different textures. Following their shapes, garnet crystals have been subdivided in two types: anhedral/skeletal and subhedral/euhedral. Except for a single rock (Fig. 5a–d), all the samples contain only one garnet type. It is noteworthy that no correlation between crystal shape and mineral assemblage of the granitoid has been observed (i.e. amphibole-bearing or amphibole-free granitoids) (cf. Fig. 5a–g). Additionally, and regardless of their shape, garnet crystals may or not contain inclusions. A subset of subhedral crystal garnets exhibit weakly to pronounced resorbed rims without any recrystallization or surrounding pressure shadow texture (Fig. 5a–g). Garnet is commonly mantled by plagioclase \pm quartz coronas, which occasionally are surrounded by an external biotite corona, which in some cases pseudomorphs the original crystal, suggesting complex garnet replacement reactions (Fig. 5b, c). Inclusion assemblages within garnets comprise mostly quartz (30–36%), plagioclase (19–20%), titanite (15–16%), epidote (10–12%) and biotite (9–11%). White mica, apatite, zircon, and in rare cases amphibole, K-feldspar, primary sulphides and zoisite are also recognized (10–12%). The inclusions

are randomly distributed within the garnet crystals and, with the exception of zoisite (Fig. 6f), the inclusion assemblage corresponds to the mineral association constituting the matrix of the granitoids (Figs. 5 and 7a, b). Garnet within the mafic enclaves displays spongy-like textures resulting from intense resorption of both rims and cores (Fig. 5h), thus suggesting that garnet crystals originally formed in the granite were transferred into the enclave. In this latter, in a more mafic and probably hotter magma, garnet was in strong disequilibrium (Fig. 5i). The few well-preserved garnet crystals within the MMEs host abundant inclusions of biotite, plagioclase, titanite, epidote and quartz (Figs. 5h, i and 7c), with these inclusions matching the mineralogical assemblage of the hosting granitoid rather than that of the MME. In particular, the amphibole crystals that form a significant fraction of the MMEs are never observed as inclusions in the garnets.

3.2.2. Main accessory phases

Epidote crystals are small (≤ 1 mm), with euhedral to subhedral shapes (Fig. 6a, b and c). In the granitoids and in the MMEs epidote appears in the matrix and as inclusions in biotite, plagioclase, garnet and

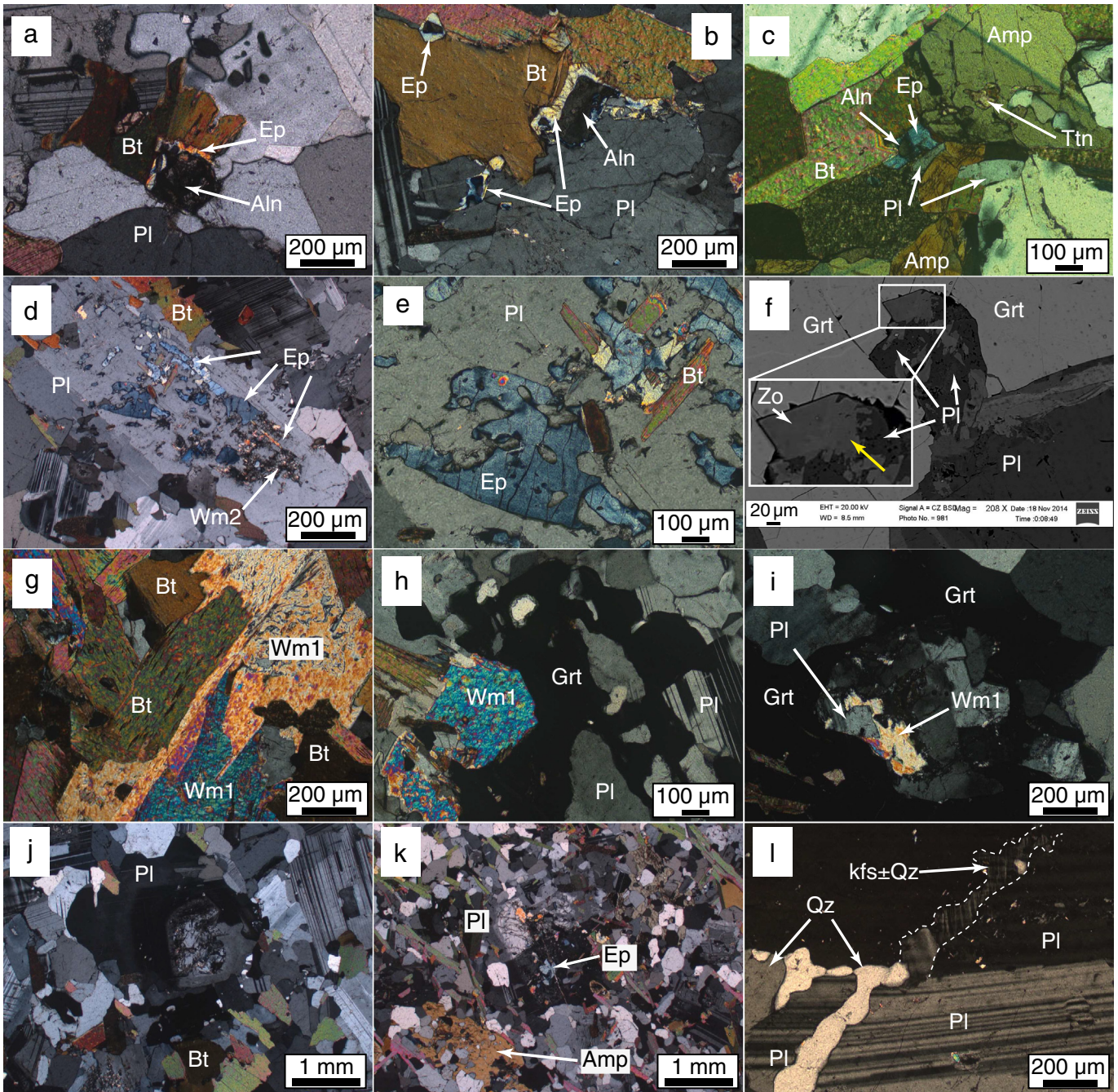


Fig. 6. General petrography. (a) and (b) Epidote in matrix crystallized between biotite and plagioclase while in (c) also between amphibole; note in (b) top left the well preserved epidote inclusion in biotite with evident allanite core; in the matrix epidote rim surrounding allanitic cores are preserved because mantled by biotite and absent due to plagioclase resorption; (d) and (e) epidote inclusions in plagioclase; these inclusions are skeletal/ragged, cracked, zoned and mostly have corroded rims; secondary white micas (Wm2) are sericitic micas; (f) zoisite inclusion in garnet, the latter being replaced by a plagioclase corona; zoisite in contact with garnet has a darker colour than the part of the crystal in contact with plagioclase; (g) primary white mica (Wm1) in matrix is replacing magmatic biotite; in (h) Wm1 is armoured by garnet; (i) Wm1 included in garnet while is replacing plagioclase; (j) and (k) plagioclase with An-rich cores surrounded by more sodic rims in granitoids and MME, respectively; (l) micro-fractured plagioclase filled by late stage quartz and K-feldspar. Except (f), all the other figures are in crossed nicols.

only rarely in amphibole. In the matrix, epidote rims surrounding allanite cores are generally zoned, and are located between amphibole, plagioclase and biotite and/or plagioclase and biotite (Fig. 6a, b and c, respectively). Epidote, like garnet, shows resorption textures, especially when in contact with plagioclase (Fig. 6a, b). Epidote inclusions (≤ 0.1 mm) (Fig. 6b top left) occasionally display allanite cores, and when hosted in biotite or hornblende, they usually show subhedral habitus. In plagioclase, epidotes are ragged with corroded, curvilinear sharp rims and cracks, which are not observed in the surrounding plagioclase (Fig. 6d and e). The latter features have been previously reported by

Chang and Andronicos (2009) and Zen and Hammarstrom (1984a, 1984b) whose proposed contrasting interpretation. The epidote crystals are only rarely in between biotite and quartz in the Bt-free garnet granodiorite.

White mica is widespread within Bt + Grt bearing rocks. It is observed with a subhedral magmatic habitus forming crystals of up to ca. 1 mm in size (Fig. 6g) and as inclusions in garnet (Fig. 6f). Relatively large crystals of white mica are commonly associated with biotite (Fig. 6g) while small crystals (< 0.3 mm) are often included in garnet or being armoured by it. This is evident by the sharp contact between

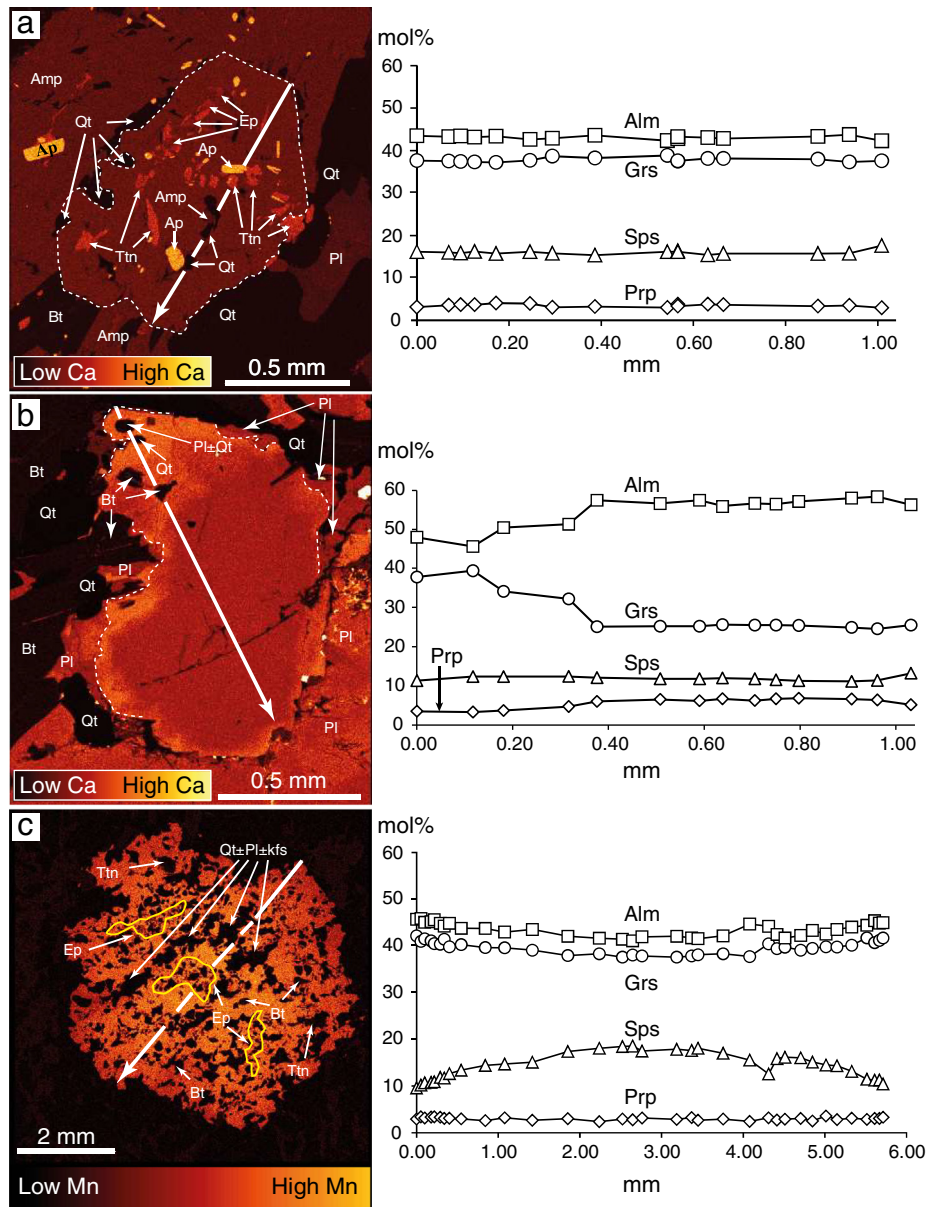


Fig. 7. Garnet chemical maps and profiles. (a) Garnet from Bt + Amp + Grt granitoids (same crystal shown in Fig. 5f); (b) garnet from Bt + Grt granitoids (same crystal shown in Fig. 5d); (c) garnet in MME (same in crystal shown in Fig. 5h); white dashed lines in (a) and (b) show garnet boundaries; for each map thick white arrows indicate the sense of the section analysed; the relative rim to rim zonation patterns are given in the diagram in the left. The maps also indicate the inclusions. More traverses are available at Table OSM1 and Fig. 1 in OSM 2.

these two minerals (Fig. 6h and f). Sericite, formed as a partial replacement after some plagioclase crystals, and very minor replacement after minerals by chlorite, are the only secondary minerals recognized in the rocks.

3.3. Mineral chemistry

All garnets represent almandine–grossular–spessartine solid solutions with ubiquitously low pyrope content (<7 mol%). Grossular (X_{Grs}) and spessartine (X_{Sps}) contents are relatively high, ranging from 24.1 to 43.4 (with 85% > 35 mol%) and from 9.4 to 18.8 mol%, respectively (Table 1 and Table OSM1). The significance of this is discussed in Section 4.2. In more detail, garnets belonging to the Bt + Grt assemblage have compositions within the range $Alm_{41.7-58.5}Grs_{24.1-40.1}Sps_{9.4-18.8}Prp_{1.9-6.9}$. Within the Bt + Amp + Grt granitoids and MMEs, the crystals display a more restricted range of compositions, that is $Alm_{40.1-43.5}Grs_{37.3-43.4}Sps_{13.8-17.2}Prp_{2.7-3.7}$ and $Alm_{40.9-45.7}Grs_{37.4-42.0}Sps_{9.6-18.5}Prp_{2.4-3.6}$, respectively. The great majority (ca. 95%) of the analysed

garnets despite having different textures are unzoned (Fig. 7a and 1a in OSM 2). In a few cases where garnets have been found having grossular reverse bell-shape-like profiles (Figs. 7b and 1b in OSM 2), the

Table 1

Summary of the grossular, pyrope, almandine and spessartine content in mol% of magmatic garnets in metaluminous to slightly peraluminous natural granitoids and experimental melts.

Garnet	Grossular	Pyrope	Almandine	Spessartine
Galiléia granitoids ^a	24.1–43.4	1.9–6.9	40.1–58.5	9.4–18.8
Bushy Point Granitoids ^b	33–46	2–6	41–52	10–11
Experimental garnets ^c	20.4–31.5	13.5–35.2	40.7–58.5	0.7–6.8
Worldwide natural garnets ^d	11.8–28.4	1.5–43.8	37.1–72.7	1.4–19.5

^a This study.

^b Zen and Hammarstrom (1984a).

^c Alonso-Perez et al. (2009); Green (1992); Schmidt (1993); Schmidt and Thompson (1996).

^d Bach et al. (2012); Barnes and Allen (2006); Day et al. (1992); Dawes and Evans (1991); Harangi et al. (2001); Owen and Marr (1990); Samadi et al. (2014).

grossular content increases from core to rim from ca. 25 mol% up to almost 40 mol%. Pyrope and spessartine patterns appear broadly flat. Other zonation is seen in garnet hosted in the MMEs where, a decrease in X_{SpS} from core to rim, from 17.42 to 9.57 mol% is associated by an increase in X_{Grs} and X_{Alm} (from 37.68 to 41.55 mol% and from 41.76 to 44.76 mol%, respectively) (Fig. 7c). It is important to note that the X_{Prp} in all the garnets is constantly low, and Mg# always <0.10. These observations are in agreement with Nalini (1997) who performed the firsts and only mineral chemistry analyses of garnets from the Galiléia.

Analyses of epidotes from the matrix of the granitoids and MMEs show pistacite contents [Ps = (Fe³⁺/Fe³⁺ + Al) * 100] in the range of 14.6–22.7 mol% and 13.9–17.8 mol%, respectively (Fig. 8a and Table OSM3). The Ps content of epidote inclusions within garnets, biotite, plagioclase and amphibole from the granites (9.3–22.2 mol%) and from the MMEs (11.6–17.3 mol%) is slightly wider but overall similar to that of the epidote in the relevant rock matrix. Rare zoisite inclusions in garnet have FeO_{Total} below 2 wt.% and Ps = 3.8–4.2 mol%.

Biotite in Bt + Grt granitoids (Fig. 8b and Table OSM4) exhibits higher Fe# [Fe/(Fe + Mg); 0.63–0.70] than biotite in other assemblages and MMEs, which display Fe# ~ 0.58–0.62. The TiO₂ contents of biotites do not show any significant difference between the different granitoid assemblages and the MMEs, ranging from 1.47 to 3.04 wt.%. The composition of biotite inclusions in garnets is similar to that of biotite in the matrix. Biotite inclusions in garnets from the MMEs have a very narrow range of Fe# and higher titanium contents (1.90–3.00 wt.%) with respect to those in the MMEs matrix (1.10–2.03 wt.%).

Primary white mica crystals have Si contents (3.14–3.22 a.p.f.u.) similar to some low-Si phengites in metamorphosed granitoids (Fig. 8c and Table OSM4) (Evans and Patrik, 1987), although Al_{Tot} (2.62–2.53 a.p.f.u.) and Mg + Fe_{Tot} (0.26–0.37 a.p.f.u.) differ slightly (Fig. 8d). These crystals are also similar in composition to primary muscovite from peraluminous granitoids (Huang et al., 2015; Liu et al., 2014; Miller et al., 1981), but are compositionally distinct from sericitic

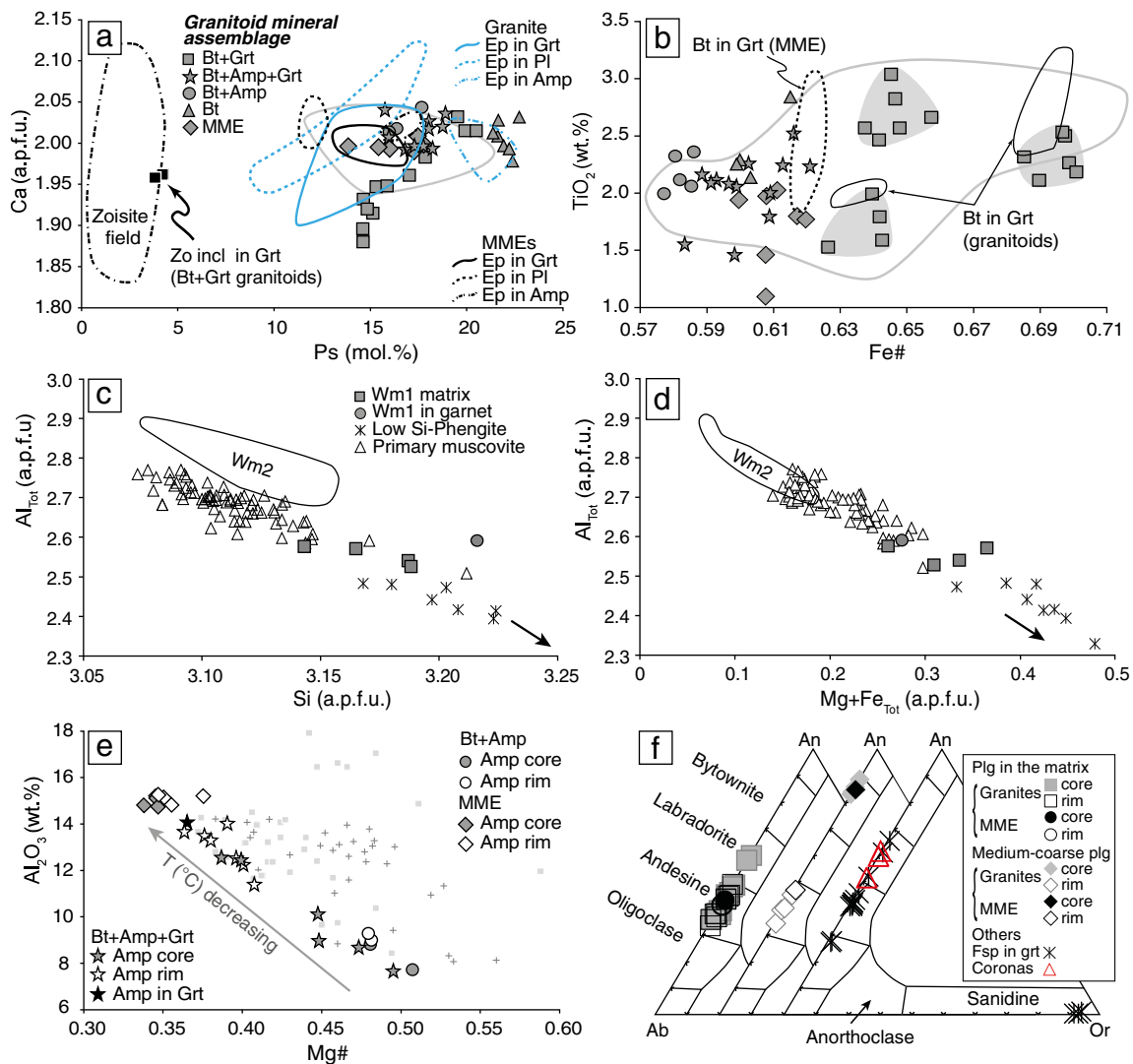


Fig. 8. Mineral chemistry. (a) Epidote composition plotted in a Ca (a.p.f.u.) against their pistacite content [Ps = (Fe³⁺/Fe³⁺ + Al) * 100]; black squares in the grey field are compositions from the inclusion shown in Fig. 6f; zoisite field from high pressure experiments (up to 3.2 GPa) from Patiño-Douce (2005) and Skjerlie and Patiño-Douce (2002); (b) Fe# [Fe/(Fe + Mg)] vs. TiO₂ (wt.%) for biotites; in (a) and (b) thick grey line indicates epidote and biotite analyses performed by Nalini (1997), respectively; (c) and (d) primary and secondary white micas composition are plotted in Si (a.p.f.u.) and Mg + Fe_{Tot} (a.p.f.u.) against Al_{Tot}; other primary muscovites are from peraluminous granitoids (Huang et al., 2015; Liu et al., 2014; Miller et al., 1981) while metamorphic low-Si phengites are from Evans and Patrik (1987); black arrows indicate that some analyses from the latter authors plot below Al_{Tot} = 2.3 (a.p.f.u.) and above Si = 3.25 and Mg + Fe_{Tot} 0.5 (a.p.f.u.); (e) amphibole composition plotted in the Mg# against Al₂O₃ (wt.%) ; grey squares and grey crosses are analyses from Nalini (1997) on amphiboles from Galiléia granitoids and MMEs, respectively; grey arrow indicates the decreasing of temperature as the Mg# decreases (i.e. Alonso-Perez et al., 2009); (f) Ternary An-Ab-Or feldspar classification diagram (after Deer et al., 1992).

products (low Si and higher Al_{Tot}) within plagioclase crystals from granitoids and MMEs.

Using *Locock's* (2014) amphibole spread sheet classification after the IMA 2012 report of *Hawthorne et al.* (2012) (Table OSM5), amphiboles are classified as follows: amphiboles from Bt + Amp-granitoids are unzoned and compositionally similar to the ferro-hornblende cores of the amphiboles from Bt + Amp-Grt-granitoids, which instead have rims classified as ferro-pargasite, as is the case for the core of the rare amphibole inclusion in garnet (Fig. 8e). There is a marked variation in Mg# and Al_2O_3 content between the cores and the respective rims of amphiboles from the Bt + Amp + Grt assemblage (Fig. 8e). Mg# in the cores varies between 0.50 and 0.39, while Mg# from the rims have a lower and more restricted range of values (0.36–0.41). As described by *Alonso-Perez et al.* (2009), this decrease in Mg# is related to decreasing temperature during magma crystallization. In contrast, Al_2O_3 is depleted in the cores (7.68–12.58 wt.%) compared with the respective rims (11.41–14.02 wt.%). The composition of amphibole cores and rims is identical in the MMEs, with a lower Mg# and Al_2O_3 content than amphibole in the granitoids. Note that the mineralogy of these rocks renders them unsuitable for the application of the Al in hornblende geobarometer, e.g. *Hammarstrom and Zen* (1986) and *Mutch et al.* (2016).

Euhedral and subhedral plagioclase crystals together with plagioclase coronas over garnet and inclusions in garnets share the same normal zonation, with labradorite cores and andesine rims (An_{60} to An_{36} ; Fig. 8f and Table OSM6). The texturally distinct cores from 10 to 15 mm sized plagioclase found in the Galiléia granites as well as in mafic enclaves have very high An contents (from An_{83} to An_{89}), differing completely from their rims (An_{35} to An_{47}).

3.4. Whole rock geochemistry

Whole rock compositions from Galiléia igneous rocks and mafic enclaves have been previously analysed by *Gonçalves et al.* (2014), *Nalini* (1997) and *Nalini et al.* (2005). Our major and trace element data agree (Table OSM7) with those reported by these authors (Fig. 9). The granitoids here studied are granodiorites with only one tonalite (Fig. 9a). K_2O content (1.76–3.8 wt.%) shows a positive correlation with SiO_2 (62.21–72.04 wt.%) (Fig. 9b) and as expected for I-type granitoids (e.g. *Clemens et al.*, 2011; *Farina et al.*, 2012), A/CNK (0.97–1.07) and CaO (2.82–6.09 wt.%) are negatively and positively correlated with $FeO_{Tot} + MgO$ (2.96–8.29 wt.%) (Fig. 9c and d, respectively). A negative correlation is also seen with respect to MnO (0.04–0.17 wt.%) (Fig. 9e). Overall, major and trace element composition of the Galiléia granitoids,

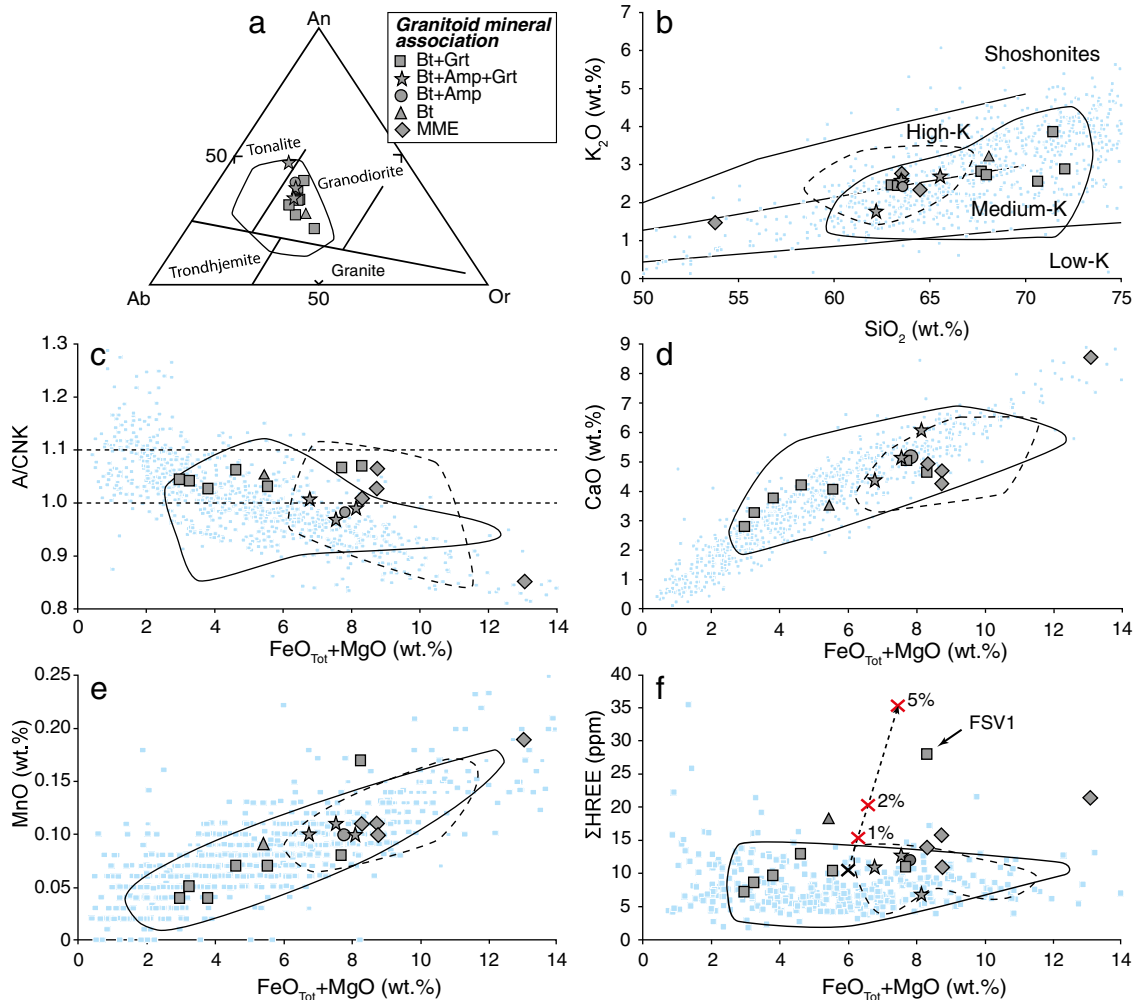


Fig. 9. Whole rock geochemistry. (a) Normative An-Ab-Or diagram (after *Barker*, 1979) for the Galiléia granitoids; (b) SiO_2 against K_2O ; (c), (d), (e) and (f) $FeO_{Tot} + MgO$ is plotted against A/CNK [molar $Al/(2Ca + Na + K)$], CaO, MnO and $\Sigma HREE$, respectively. Plain lines and dotted lines represent compositional fields for granitoids and mafic enclave analyses from *Gonçalves et al.* (2014) and *Nalini* (1997), respectively. Light blue squares are metaluminous cordilleran-type I-type granitoids from North and South Patagonian Batholith (*Castro et al.*, 2011; *Hervé et al.*, 2007; *Pankhurst et al.*, 1999), Western and Eastern Peninsular Ranges (*Lee et al.*, 2007), Sierra Nevada Batholith (*Bateman et al.*, 1984; *Cecil et al.*, 2011; *Dodge et al.*, 1982) and Lachlan Fold Belt (*Clemens et al.*, 2011); (e), black dotted arrow indicates the incremental trend in maficity and $\Sigma HREE$ of a typical cordilleran-type granitoids similar to one of the Galiléia granitoids at which has been added from 1 to 5 vol.% of garnet. Except for one sample (FSV1), the $\Sigma HREE$ content for the Galiléia granitoids is similar to the cordilleran-type granitoids; see text for further explanation. (For interpretation of the references to colour in this figure legend, the reader is referred to the web version of this article.)

match well with those of Cordilleran-type granites worldwide (Fig. 9). Garnet-bearing enclaves have Mg# values ranging between 0.36 and 0.40, whereas the only garnet-free enclave which was analysed and classified as a gabbro displays the highest Mg# (0.46), $\text{FeO}_{\text{Tot}} + \text{MgO}$ (13.07 wt.%) and $\sum \text{HREE}$ (10.07 ppm).

4. Discussion

The widespread occurrence of garnet and epidote is the most striking and petrologically interesting characteristic of the Galiléia Batholith. To our knowledge, only one previous study reports magmatic garnet compositions matching those described in this study, that is the Bushy Point granites in south eastern Alaska (Zen and Hammarstrom, 1984a) (Table 1).

4.1. Magmatic garnet, epidote and white mica in the Galiléia batholith

Several lines of field, petrographic and chemical evidence indicate that the garnet crystals in the Galiléia granitoids are magmatic. Firstly, garnet crystals occur in weakly deformed granitoids showing no evidence of metamorphism. Garnet abundance does not correlate with the degree of deformation in the granite and garnet crystals occur as inclusions in large euhedral alkali-feldspar crystals in granites showing porphyritic textures (Fig. 4a). Secondly, garnet abundance does not increase in the proximity of the contact with the Rio Doce metasediments and garnet crystals in the batholith have different compositions from garnet in the metapelites, the former being higher in CaO (Fig. 10). Further simple chemical arguments confirm that garnets in the Galiléia granitoids are neither entrained from the country rocks nor inherited from the source. In fact, the inclusion of 1 to 5 vol.% of source rock garnet in a typical cordilleran-type granite would discernibly increase both the $\text{FeO}_{\text{Tot}} + \text{MgO}$ and $\sum \text{HREE}$ of the rock as illustrated in Fig. 9e; this behaviour is not observed for the garnet-bearing samples of the Galiléia batholith. Moreover, the abundance of garnet does not correlate with the SiO_2 and CaO content of the granitoids and their presence is reported from the least ($\text{SiO}_2 = 58.8$ wt.%), to the most evolved ($\text{SiO}_2 = 72.2$ wt.%) garnet-bearing Galiléia granitoid. Furthermore, the garnet-bearing Galiléia granitoids are geochemically identical to many other garnet-free Cordilleran-type granites worldwide.

Finally, the minerals hosted as inclusions within the garnet crystals are the same, both in terms of assemblage and composition, as those constituting the matrix of the granitoids. It is also worth noting that garnet occurrence and/or abundance are not related to the abundance of MMEs in the outcrop, suggesting that garnet did not form in the

enclaves as also confirmed by the disequilibrium features acquired by garnet crystals hosted in the enclaves.

Collectively, this evidence demonstrates that garnet in the studied rocks is magmatic. Therefore, we conclude that the presence/absence of this garnet depends on variables other than the rock composition.

In the Galiléia batholith there are two other coexisting minor phases that appear to be magmatic and may be important in understanding the conditions of magma crystallization: epidote and white mica. In agreement with textural observations on magmatic epidotes reported by Schmidt and Poli (2004), Schmidt and Thompson (1996) and Zen and Hammarstrom (1984b), the presence of epidote crystals rimming allanite cores, and their common occurrence in the interstitial sites between the rock forming minerals (amphibole, plagioclase and biotite) point towards a magmatic origin for epidote (e.g. Nalini, 1997). Furthermore, the Ps content of matrix epidote crystals (14.6–22.7 mol%) is very similar to epidote inclusions hosted within rock-forming phases (Ps = 9.3–22.2 mol%), supporting a magmatic origin for both textural varieties of epidote. Based on textural observation we exclude that epidotes (Ps = 9.3–17.4 mol%) included in plagioclase (Fig. 6c) are derived from the alteration of this mineral. In fact, epidote inclusions are ragged, cracked, and commonly zoned showing corroded and/or resorbed rims. Following Chang and Andronicos (2009) and Dawes and Evans (1991), we interpret these inclusions as early magmatic crystals followed by re-sorption before plagioclase overgrowth during successive magmatic stages. Epidote crystals within the MMEs share similar textural and compositional (Ps = 11.8–17.3 mol%) features with those in the granites, thus they are also interpreted as being magmatic. Finally, despite the fact that the occurrence of white mica overgrowing magmatic biotite and plagioclase could suggest a secondary origin, the presence of white mica as inclusion in the garnet points towards a magmatic origin. Its primary origin is also supported by its chemical composition which is similar to other low-Si phengites and primary muscovites from the literature, but quite different from sericitic products (i.e. late secondary white mica) (Fig. 8c, d).

4.2. Pressure–temperature conditions

4.2.1. Pressure of crystallization

Crystallization experiments and studies on natural metaluminous igneous rocks have shown that garnet with CaO contents above 4 wt.% (and in general with Grs > 10 mol%) records crystallization at pressures above approximately >0.8 GPa (Alonso-Perez et al., 2009; Bach et al., 2012; Barnes and Allen, 2006; Dawes and Evans, 1991; Day et al., 1992; Green, 1972, 1977, 1992; Green and Ringwood, 1968; Green, 1972; Harangi et al., 2001; Samadi et al., 2014 and others). Schmidt and Thompson (1996) investigated garnet stability within a granodiorite and established that the garnet-in reaction is located at a pressure as high as 1.3 GPa and around 800 °C. Garnet stability within granitoid magmas varies as a function of composition as well as pressure and temperature (see also Vielzeuf and Schmidt, 2001). Although no crystallization experiments have produced garnet with grossular contents as high as those observed in the Galiléia garnets (Table 1), similarities between experimental and natural rock studies are in good agreement in indicating that the presence of grossular-rich magmatic garnet within the Galiléia granitoids can be regarded as evidence of crystallization at a pressure above at least 0.8 GPa.

This conclusion is also supported by the occurrence of phengitic white mica and epidote in the Galiléia granitoids. According to Schmidt and Poli (2004) and Schmidt and Thompson (1996), the appearance of epidote in the crystallization sequence of a cooling magma is pressure dependent. These authors demonstrated that epidote is stable above 0.6 GPa, and that its temperature of first crystallization in a cooling magma increases with increasing pressure. In the Galiléia granitoids, epidote is found as a common inclusion in biotite and plagioclase, as a rare inclusion in garnet, and in the matrix between amphibole, plagioclase and biotite. Based on the experiments of

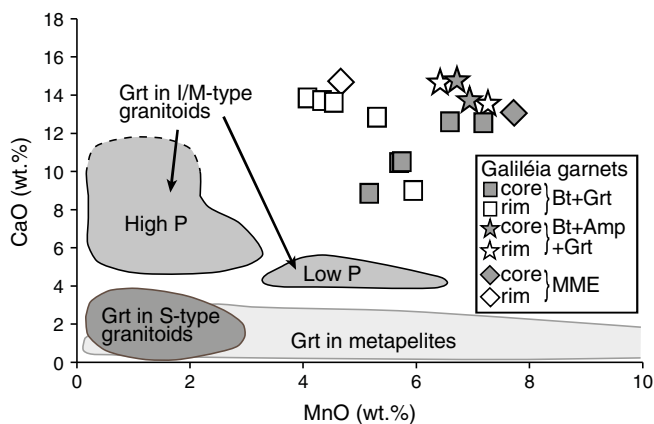


Fig. 10. CaO against MnO wt.% (after Harangi et al., 2001 and Samadi et al., 2014). Note that the upper limit of the area representing the CaO rich-garnets has not been defined, yet. Here and in Fig. 11 only the more representative (core and rim) analyses for the Galiléia garnets are reported.

Schmidt and Thompson (1996), this textural information is consistent with pressure conditions in the range of 0.8–1.0 GPa. Thus the experiments of Alonso-Perez et al. (2009), Green (1992), and Schmidt and Thompson (1996), constrain the stability of garnet + epidote within the Galiléia granitoids to pressures between ca. 0.8 and 1.0 GPa, corresponding to depths of approximately 25–30 km in the lower crust.

4.2.2. The geochemical diversity of the Galiléia garnets

The most striking characteristic of the Galiléia magmatic garnets is their extremely high grossular and spessartine contents reaching 45 mol% and 20 mol%, respectively and constantly low pyrope content (<7 mol%). (Figs. 10 and 11). We compared the chemistry of these crystals with: 1) garnet from crystallization experiments at high pressure (>0.8 GPa) using metaluminous to weakly peraluminous starting materials that were similar in composition to the Galiléia granitoids (Alonso-Perez et al., 2009; Green, 1992; Schmidt, 1993; Schmidt and Thompson, 1996) (Fig. 12), and 2) magmatic garnet from natural metaluminous to weakly peraluminous felsic igneous rocks (Bach et al., 2012; Barnes and Allen, 2006; Dawes and Evans, 1991; Day et al., 1992; Harangi et al., 2001; Owen and Marr, 1990; Samadi et al., 2014; Zen and Hammarstrom, 1984a). We observe that the Galiléia garnets are more grossular-rich and pyrope-poor ($\text{Gr}_{24.1-43.4}\text{Prp}_{1.9-6.9}\text{Alm}_{40.1-58.5}\text{Sps}_{9.4-18.8}$) than both experimental ($\text{Gr}_{20.4-31.5}\text{Prp}_{13.5-35.2}\text{Alm}_{40.7-58.5}\text{Sps}_{0.7-6.8}$) and natural crystals ($\text{Gr}_{11.8-28.4}\text{Prp}_{1.5-43.8}\text{Alm}_{137.1-72.7}\text{Sps}_{1.4-19.5}$) (Table 1). However, the Galiléia garnets are compositionally identical to the magmatic garnet crystals ($\text{Gr}_{33-46}\text{Prp}_{6-6}\text{Alm}_{41-52}\text{Sps}_{10-11}$) from the metaluminous

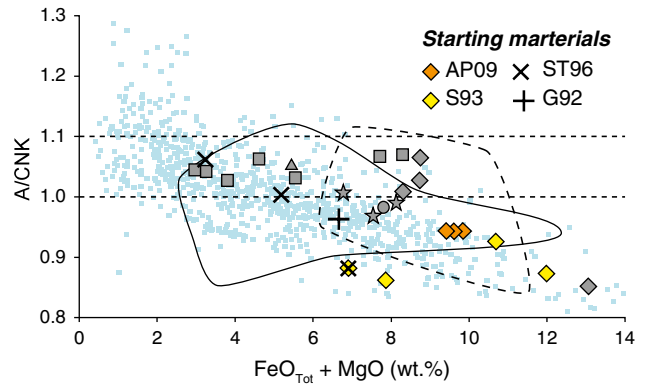


Fig. 12. A/CNK vs $\text{FeO}_{\text{Tot}} + \text{MgO}$ diagram. Comparison between Galiléia granitoids, Cordilleran-type granites and starting materials used in high pressure crystallization experiments. AP09: Alonso-Perez et al. (2009); G92: Green (1992); S93: Schmidt (1993); ST96: Schmidt and Thompson (1996). Other symbols are as in Fig. 9.

Bushy Point Granitoids (A/CNK 0.91–1.10; SiO_2 59.6–72.6 wt.%; CaO 1.3–6.2 wt.%) (Zen and Hammarstrom, 1984a). From Fig. 11a and b, it appears that only the garnet which crystallized in experiments at a temperature of 650 °C and at high water contents (≥ 10 wt.%) has compositions close to those of some of the Galiléia garnets.

In the experimental garnet, the pyrope content decreases at decreasing temperatures while the almandine contents show the opposite

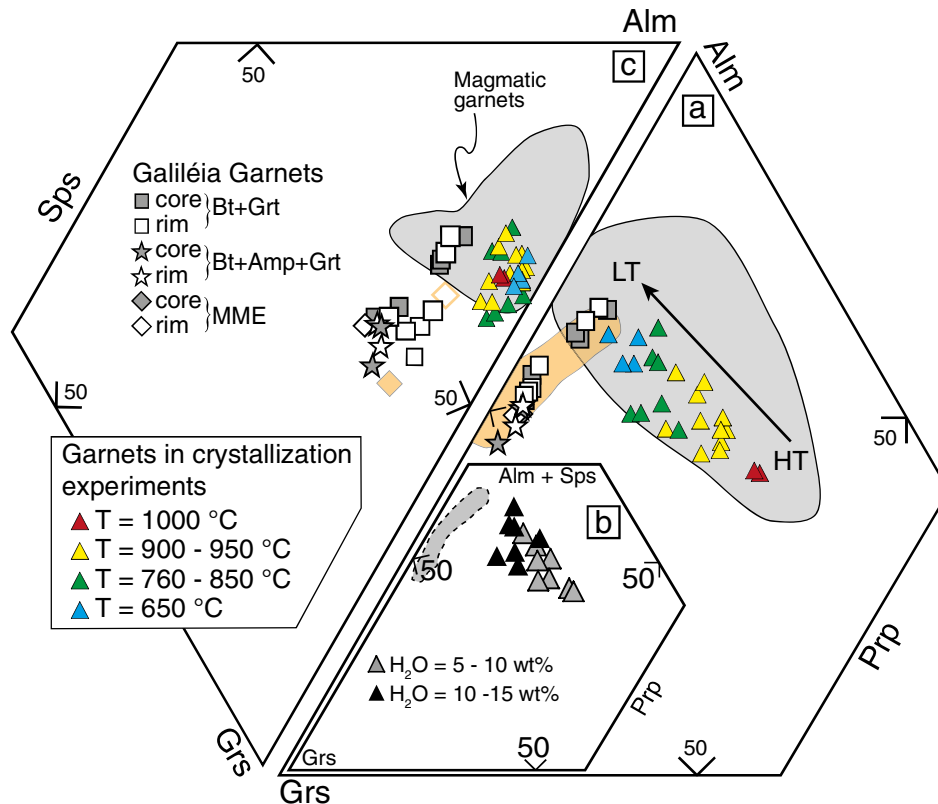


Fig. 11. Comparison between Galiléia, experimental and natural magmatic garnets. (a) Almandine-grossular-pyrope classification diagrams. Experimental garnets (coloured triangles) are those in equilibrium with the metaluminous and slightly peraluminous experimental melts. These garnets are reported according to their crystallization temperature. Grey field: magmatic garnets in volcanic as well as granitic metaluminous to weakly peraluminous rocks (Bach et al., 2012; Barnes and Allen, 2006; Dawes and Evans, 1991; Day et al., 1992; Harangi et al., 2001; Owen and Marr, 1990; Samadi et al., 2014). Light orange field: Bushy Point garnets from Bushy Point Granitoids, Alaska (Zen and Hammarstrom, 1984a). Note that for these garnets the grossular field was redrawn from Fig. 70 of Zen and Hammarstrom (1984a). Grey arrow indicates the trend from high (HT) to low (LT) temperature garnets. (b) Alm + Sps–Grs–Prp diagram. The same experimental garnets used in (a), here are plotted considering the water content of the experimental melt. Grey dotted area represents the part of the diagram covered by the Galiléia granitoids. Note that for the garnets of Green (1992) and those at 650 °C of Schmidt (1993) there is no data relative to the water of the melt. (c) Almandine–grossular–spessartine diagram. Symbols as in a). Note that only for one Bushy point garnet the spessartine content has been reported (filled and empty light orange diamonds are core and rim, respectively). (For interpretation of the references to colour in this figure legend, the reader is referred to the web version of this article.)

behaviour, being negatively correlated with temperature (Fig. 11a, b and c). These relationships might account for the low pyrope content exhibited by the Galiléia garnet, but data retrieved from experimental studies do not explain the origin of the high spessartine and especially high grossular content observed in the garnet of the Galiléia batholith. The only experiments that seem to suggest a negative correlation between the grossular content and temperature are those performed by Alonso-Perez et al. (2009) at 1.2 GPa. These authors observed an increase of grossular content from 20.7 to 31.5 mol% as a consequence of a decrease in temperature from 1000 to 850 °C and to an increase of the water content of the melt from 5.4 to 11.0 wt%. Nevertheless, any clear correlation is observed considering the spessartine content.

A possible explanation for the high grossular content of the Galiléia garnet might come from Schmidt and Thompson (1996). They observed that in metaluminous granitic systems, quartz and epidote start crystallizing at temperature around 655 and 700 °C, respectively, with epidote stable in water saturated melts (≥ 10 wt.%). Thus the high grossular content of garnet crystals together with their epidote and quartz inclusions, might suggest that these garnets were produced by a process of dissolution and recrystallization in which garnet was continuously reacting and re-equilibrating with a melt that was evolving towards low temperature (<650–700 °C) and high water contents (>10 wt.%). The same explanation could also apply for the spessartine content, which increases as the magma evolves (Miller and Stoddard, 1981).

4.3. Geotectonic implications: a new tectonic model for the Araçuaí Orogen?

It is worth remarking that garnet is widespread in the Galiléia batholith characterizing outcrops that are in many cases more than 10 km apart. This simple observation indicates that similar high-pressure conditions were attained in the whole batholith.

Since little is known about the P–T–t history of the host Rio Doce metasediments, any attempts to understand its relationships with the Galiléia granitoids remain quite speculative. Nevertheless, some observations can be made.

So far it has been highlighted that the Galiléia granitoids record high pressure (>0.8 GPa) crystallization and emplacement in the lower crust. This implies that since 630 Ma the crust underneath this portion of the Araçuaí Orogen was already at least 25–30 km thick and relatively cool. This is in contrast with the hot thermal regime registered from the neighbour Carlos Chagas Batholith, located 50 km to the east, within the eastern domain (Fig. 1b; Melo et al., 2016). In fact, this batholith records granulite-facies metamorphism (0.9–1.0 GPa and 790–820 °C) at 570 Ma, age at which: 1) the Galiléia granitoids were already crystallized (632–570 Ma; Tedeschi et al., 2016) and 2) the Araçuaí Orogen was experiencing syn-collisional tectonics (Pedrosa-Soares et al., 2011). Overall, this would imply that the Galiléia high pressure granitoids should also record granulite-facies metamorphism. Instead, these rocks are weakly deformed and do not show any evidence of metamorphic overprinting. This has two possible and different tectonic implications: either the Galiléia granitoids at 570 Ma were already exhumed at shallower crustal levels, which prevented them from undergoing granulite facies metamorphism, or alternatively these garnet-bearing granitoids and the Carlos Chagas batholith belonged to different lithospheric domains joined together after 570 Ma. The last hypothesis is supported by the presence of a poorly-studied major thrust separating the central and eastern domains (see black bold dotted line in Fig. 1b; e.g. Vauchez et al., 2007).

Eventually, the same field, petrographic and chemical features so far reported for the garnet-bearing Galiléia granitoids have been also described for the garnet-bearing Bushy point granites (Zen and Hammarstrom, 1984a). Noteworthy these granitoids are located presumably within the accretionary prism and/or fore-arc settings of the north-coastal British Columbia subduction zone, south eastern Alaska. In such settings, high pressure, low temperature (Brown, 2006) and water-rich magmas are readily achievable. Notably, some of these

conditions are those suggested by this work. It is then possible that both the garnet-bearing Galiléia and Bush Point granitoids represent “rare” garnet- and epidote-bearing metaluminous Cordilleran-I-type granites which can only form in a fore-arc setting.

5. Conclusions, remarks and open questions

The presence of magmatic garnet crystals together with the presence of magmatic epidotes indicates a high-pressure crystallization environment probably between 0.8 and 1.0 GPa, corresponding to depths of approximately 25–30 km. These findings would also imply that at 630 Ma the crust below the Araçuaí orogen was already over-thickened and cool. High grossular and spessartine content in garnet together with its epidote and quartz inclusions might be due to reaction between the crystal and the evolving granitic magma towards low temperature and high water content. Some resorption textures also indicate that these minerals were consumed before complete crystallization. Eventually, what has been highlighted throughout this work has opened new challenging questions like: 1) why no experiments so far were able to reproduce the composition of the Galiléia garnets? 2) How much water was present in the melt from which the grossular- and spessartine-rich Galiléia garnets crystallized? 3) How much melt (vol.%) was still present during garnet crystallization at high-pressure and temperature of ca. 650–700 °C? And eventually, despite there is a clear connection between the garnet-bearing Galiléia granitoids and the fore-arc related garnet-bearing Bushy Point and, 4) what is the most reliable geodynamic scenario for having within the same orogenic system, at the same pressure condition and at the same geological time, two contrasting thermal regimes? More studies must be done in order to answer to all of the above questions.

Supplementary data to this article can be found online at <http://dx.doi.org/10.1016/j.lithos.2017.02.017>.

Acknowledgements

The authors wish to acknowledge funding from CNPq (401334/2012-0, 302058/2015-0, 402852/2012-5) and FAPEMIG (APQ03943, RPQ-0067-10-RDP 00063-10) grants and Edital UFOP Auxílio a pesquisador 2015. FN thanks Conselho Nacional de Desenvolvimento Científico e Tecnológico for the financial support (CNPq 164000/2013-5). G. Stevens gratefully acknowledges National Research Funding support through the SARChI programme. Careful and constructive reviews from Ramin Samadi and Patrizia Fiannacca have stimulated and strongly improved the quality of the manuscript. We also thank Editor Nelson Eby for the editorial handling. C. Albert, C. Aguilar, C. Martinez, G. Gonçalves and M. Melo are kindly acknowledged for their technical and moral support. L. Ziberna and M. Casanova are also thanked for their scientific and friendly support. This work is part of the first author's doctorate project.

References

- Alkmim, F.F., Marshak, S., Pedrosa-Soares, A.C., Peres, G.G., Cruz, S.P.C., Whittington, A., 2006. Kinematic evolution of the Araçuaí-West Congo orogen in Brazil and Africa: nutcracker tectonics during the Neoproterozoic assembly of Gondwana. *Precambrian Research* 149, 43–64.
- Allan, B.D., Clarke, D.B., 1981. Occurrence and origin of garnets in the South Mountain Batholith, Nova Scotia. *The Canadian Mineralogist* 19, 19–24.
- Alonso-Perez, R., Müntener, O., Ulmer, P., 2009. Igneous garnet and amphibole fractionation in the roots of island arcs: experimental constraints on andesitic liquids. *Contributions to Mineralogy and Petrology* 157, 541–558.
- Arth, J.G., Barker, F., Stern, T.W., 1988. Coast Batholith and Taku Plutons near Ketchikan, Alaska: petrography, geochronology, geochemistry, and isotopic character. *American Journal of Science* 288-A, 461–489.
- Bach, P., Smith, I.E.M., Malpas, J.G., 2012. The origin of garnets in andesitic rocks from the Northland Arc, New Zealand, and their implication for sub-arc processes. *Journal of Petrology* 53, 1169–1195.
- Barker, F., 1979. Trondjemites: definition, environment and hypotheses of origin. In: Barker, F. (Ed.), *Trondjemites, Dacites and Related Rocks*. Elsevier, Amsterdam, pp. 1–12.

- Barnes, C.G., Allen, C.M., 2006. In: Snoke, A.W., Baren, C.G. (Eds.), *Depth of Origin of Late Middle Jurassic Garnet Andesite, Southern Klamath Mountains, California*. Geological Studies in the Klamath Mountains Province, California and Oregon: A volume in honour of William P. Irwin Geological Society of American Special Papers 410, pp. 269–286.
- Barnes, C.G., Frost, C.D., Nordgulen, Ø., Prestvik, T., 2012. Magma hybridization in the lower crust: possible consequences for deep-crustal magma mixing. *Geosphere* 8, 518–533.
- Bateman, P.C., Dodge, F.C.W., Bruggman, P.E., 1984. Major oxide analyses, CIPW norms, modes, and bulk specific gravities of plutonic rocks from the Mariposa 1 x 2 degrees sheet, central Sierra Nevada, California. United State Geological Survey OF 84-0162 (59 pp.).
- Brandon, A.D., Creaser, R.A., Chacko, T., 1996. Constraints on rates of granitic magma transport from epidote dissolution kinetics. *Science* 271, 1845–1848.
- Brown, M., 2006. Duality of thermal regimes is the distinctive characteristics of plate tectonics since the Neoproterozoic. *Geology* 34, 961–964.
- Castro, A., Moreno-Ventas, I., Fernández, C., Vujovich, G., Gallastegui, G., Heredia, N., Martino, R.D., Becchio, R., Corretgé, L.G., Díaz-Alvarado, J., Garcías-Arias, M., Liu, D.-Y., 2011. Petrology and SHRIMP U-Pb zircon geochronology of Cordilleran granitoids of the Bariloche area, Argentina. *Journal of South American Earth Sciences* 32, 508–530.
- Cecil, M.R., Rotberg, G.L., Ducea, M.N., Saleeby, J.B., Gehrels, G.E., 2011. Magmatic growth and batholithic root development in the northern Sierra Nevada, California. *Geosphere* 8, 592–606.
- Chang, J.M., Andronico, C.L., 2009. Constraints on the depth of generation and emplacement of a magmatic epidote-bearing quartz diorite pluton in the Coast Plutonic Complex, British Columbia. *Terra Nova* 21, 480–488.
- Clarke, B.D., 2007. Assimilation of xenocrysts in granitic magmas: principles, processes, proxies, and problems. *The Canadian Mineralogist* 45, 5–30.
- Clemens, J.D., Stevens, G., Farina, F., 2011. The enigmatic sources of I-type granites: the peritectic connexion. *Lithos* 126, 174–181.
- Cunningham, W.D., Marshak, S., Alkmim, F.F., 1996. Structural style of basin inversion at mid-crustal levels: two transects in the internal zone of the Brasileiro Araçuaí Belt, Minas Gerais, Brazil. *Precambrian Research* 77, 1–15.
- Dalquist, J.A., Galindo, C., Pankhurst, R.J., Rapela, C.W., Alasino, P.H., Saavedra, J., Fanning, C.M., 2007. Magmatic evolution of the Peñón Rosado granite: petrogenesis of garnet-bearing granitoids. *Lithos* 95, 177–207.
- Dawes, R.L., Evans, B.W., 1991. Mineralogy and geothermobarometry of magmatic epidote-bearing dyke, Front Range, Colorado. *Geological Society of America Bulletin* 103, 1017–1031.
- Day, R.A., Green, T.H., Smith, I.E.M., 1992. The origin and significance of garnet phenocryst and garnet-bearing xenoliths in Miocene calc-alkaline volcanics from Northland, New Zealand. *Journal of Petrology* 33, 125–161.
- Deer, W.A., Howie, R.A., Zussman, J., 1992. *An Introduction to the Rock-forming Minerals*. 2nd eds. Longman, Harlow.
- Dodge, F.C.W., Millard Jr., H.T., Helsing, H.N., 1982. Compositional variations and abundances of selected elements in granitoid rocks and constituent minerals, Central Sierra Nevada, Batholith, California. Geological Survey Professional Paper. 1248, p. 29.
- Erdmann, S., Jamieson, R.A., Macdonald, M.A., 2009. Evaluating the origin of garnet, cordierite and biotite in granitic rocks: a case study from the South Mountain Batholith, Nova Scotia. *Journal of Petrology* 50, 1477–1503.
- Evans, B.W., Patrik, B.E., 1987. Phengite-3T in high pressure metamorphosed granitic orthogneisses, Seaward Peninsula, Alaska. *The Canadian Mineralogist* 25, 141–158.
- Evans, B.W., Vance, J.A., 1987. Epidote phenocrysts in dacitic dikes, Boulder Country, Colorado. Contributions to Mineralogy and Petrology 96, 178–185.
- Farina, F., Stevens, G., Dini, A., Rocchi, S., 2012. Peritectic phase entrainment and magma mixing in the late Miocene Elba Island laccolith-pluton-dyke complex (Italy). *Lithos* 153, 243–260.
- Gonçalves, L., Farina, F., Lana, C., Pedrosa-Soares, A.C., Alkmim, F.F., Nalini Jr., H.A., 2014. New U-Pb ages and lithochemical attributes of the Ediacaran Rio Doce magmatic arc, Araçuaí confined orogen, southeastern Brazil. *Journal of South American Earth Sciences* 52, 1–20.
- Green, T.H., 1972. Crystallization of calc-alkaline andesite under controlled high-pressure hydrous condition. Contributions to Mineralogy and Petrology 34, 150–166.
- Green, T.H., 1977. Garnet in silicic liquids and its possible use as a P-T indicator. Contributions to Mineralogy and Petrology 65, 59–67.
- Green, T.H., 1992. Experimental phase equilibrium studies of garnet-bearing I-type volcanics and high-level intrusives from Northland, New Zealand. Transactions of the Royal Society of Edinburgh: Earth Sciences 83, 429–438.
- Green, T.H., Ringwood, A.E., 1968. Origin of garnet phenocryst in calc-alkaline rocks. Contributions to Mineralogy and Petrology 18, 163–174.
- Hammarstrom, J.M., Zen, E-na, 1986. Aluminum in hornblende: an empirical igneous geobarometer. *American Mineralogist* 71, 1297–1313.
- Harangi, S.Z., Downes, H., Kosa, L., Szabo, C.S., Thirlwall, M.F., Mason, P.R.D., Matthey, D.P., 2001. Almandine garnet in calc-alkaline volcanic rocks of the Northern Pannonian basin (Eastern-Central Europe): geochemistry, petrogenesis and geodynamic implications. *Journal of Petrology* 42, 1813–1843.
- Harrison, T.N., 1988. Magmatic garnets in the Cairngorm granite, Scotland. *Mineralogical Magazine* 52, 659–667.
- Hawthorne, F.C., Oberti, R., Harlow, G.E., Maresh, W.V., Martin, R.F., Schumacher, J.C., Welch, M.D., 2012. IMA report, nomenclature of the amphibole supergroup. *American Mineralogist* 91, 2031–2048.
- Hervé, F., Pankhurst, R.J., Fanning, C.M., Calderón, M., Yaxely, G.M., 2007. The south Patagonian batholith: 150 my of granite magmatism on a plate margin. *Lithos* 97, 373–394.
- Holdaway, M.J., 1972. Thermal stability of Al-Fe epidote as a function of f_{O_2} and Fe content. Contributions to Mineralogy and Petrology 37, 307–340.
- Huang, H.-Q., Li, X.-H., Li, Z.-X., Li, W.-X., 2015. Formation of Jurassic South China Large Granitic Province: insights from the genesis of the Jiufeng pluton. *Chemical Geology* 401, 43–58.
- Lackey, J.S., Romero, G.A., Bouvier, A.-S., Valley, J.W., 2012. Dynamic growth of garnet in granitic magmas. *Geology* 40, 171–174.
- Lee, C.T.A., Morton, D.M., Kistler, R.W., Barid, A.K., 2007. Petrology and tectonics of Phanerozoic continent formation: from island arc to accretion and continental arc magmatism. *Earth and Planetary Science Letters* 263, 370–387.
- Liou, J.G., 1973. Synthesis and stability relations of epidote, $Ca_2Al_2FeSi_3O_{12}(OH)$. *Journal of Petrology* 14, 381–413.
- Liu, Z.-C., Wu, F.-Y., Ji, W.-Q., Wang, J.-G., Liu, C.-Z., 2014. Petrogenesis of the Ramba leucogranite in the Tethyan Himalaya and constraints on the channel flow model. *Lithos* 208–209, 118–136.
- Locock, A.J., 2014. An Excel spreadsheet to classify chemical analyses of amphiboles following the IMA 2012 recommendations. *Computers and Geosciences* 62, 1–11.
- Melo, M.G., Stevens, G., Lana, C., Pedrosa-Soares, A.C., Frei, D., Alkmim, F.F., Alkmim, L.A., 2016. Repeated partial melting events in the Araçuaí orogen (southeastern Brazil): evidence from the polymetamorphic Carlos Chagas batholith. *Lithos* DOI: j.lithos.2016.10.012 (in press).
- Miller, C.F., Stoddard, E.F., 1981. The role of manganese in the paragenesis of magmatic garnet: an example from the Old Woman-Piute Range, California. *The Journal of Geology* 89, 233–246.
- Miller, C.F., Stoddard, E.F., Bradfish, L.J., Dollase, W.A., 1981. Composition of plutonic muscovite: genetic implications. *The Canadian Mineralogist* 19, 25–34.
- Mondou, M., Eglydio-Silva, M., Vauchez, A., Raposo, M.I.B., Bruguier, O., Oliveira, A.F., 2012. Complex, 3D strain patterns in a synkinematic tonalite batholith from the Araçuaí Neoproterozoic orogen (Eastern Brazil): evidence from combined magnetic and isotopic chronology studies. *Journal of Structural Geology* 39, 158–179.
- Mutch, E.J.F., Blundy, J.D., Tattitch, B.C., Cooper, F.J., Brooker, R.A., 2016. An experimentally study of amphibole stability in low-pressure granitic magmas and a revised Al-in-hornblende geobarometer. Contributions to Mineralogy and Petrology 171, 85.
- Nalini Jr., H.A., 1997. Caractérisation de suites magmatiques néoproterozoïques de la région de Conselheiro Pena et Galiléia (Minas Gerais, Brésil). Etude géochimique et structurale des suites Galiléia et Urucum et relation avec les pegmatites à éléments rares associées. Ecole National Supérieure de Mines de Paris et de Saint Etienne, St Etienne, p. 237 (PhD thesis).
- Nalini Jr., H.A., Bilal, E., Paquette, J.-L., Pin, C., Machado, R., 2000. Géochronologie U-Pb et géochimie isotopique Sr-Nd des granitoïdes néoproterozoïques des Suites Galiléia et Urucum, vallée du Rio Doce, Sud Est du Brésil. *Comptes Rendus* 331, 459–466.
- Nalini Jr., H.A., Machado, R., Bilal, E., 2005. Geoquímica e petrogênese da suíte Galiléia: exemplo de magmatismo tipo-I metaluminoso pre-colisional Neoproterozoico da região do médio do Vale de Rio Doce (MG). *Revista Brasileira de Geociências* 35, 23–34.
- Nalini Jr., H.A., Machado, R., Endo, I., Bilal, E., 2008. A importância da tectônica transcorrente no alojamento de granitos pré a sincolisional na região do vale do médio Rio Doce: o exemplo da suíte granítica Galiléia e Urucum. *Revista Brasileira de Geociências* 38, 741–752.
- Owen, J.V., Marr, R.A., 1990. Contrasting garnet parageneses in a composite Grenvillian granitoid pluton, Newfoundland. *Mineralogical Magazine* 54, 367–380.
- Pankhurst, R.J., Weaver, S.D., Hervé, F., Larrondo, P., 1999. Mesozoic–Cenozoic evolution of the North Patagonian Batholith in Aysén, southern Chile. *Journal of the Geological Society of London* 156, 673–694.
- Paterson, S.R., Fowler Jr., K.T., Schmidt, K.L., Yoshinobu, A.S., Yuan, E.S., Miller, R.B., 1998. Interpreting magmatic fabric in plutons. *Lithos* 44, 53–82.
- Patiño-Douce, A.E., 2005. Vapour absent melting of tonalite at 15–32 kbar. *Journal of Petrology* 46, 275–296.
- Pedrosa-Soares, A.C., De Campos, C.P., Noce, C., Silva, L.C., Novo, T., Roncato, J., Medeiros, S., Castañeda, C., Queiroga, G., Dantas, E., Dussin, I., Alkmim, F.F., 2011. Late Neoproterozoic–Cambrian granitic magmatism in the Araçuaí Orogen (Brazil), the Eastern Brazilian Pegmatite Province and related mineral resources. *Geological Society of London Special Publication* 350, 25–51.
- Pedrosa-Soares, A.C., Noce, C.M., Wiedemann-Leonardos, C.M., Pinto, C.P., 2001. The Araçuaí-West Congo Orogen in Brazil: an overview of a confined Orogen formed during Gondwanaland assembly. *Precambrian Research* 110, 307–323.
- Pedrosa-Soares, A.C., Wiedemann-Leonardos, C.M., 2000. Evolution of the Araçuaí belt and its connection to the Ribeira Belt, Eastern Brazil. In: Cordani, U.G., Milani, E.J., Tomaz, Filho A., Campos, D.A. (Eds.), *Tectonic Evolution of South America*, International Geological Congress, Rio de Janeiro, pp. 265–285.
- Petitgirard, S., Vauchez, A., Eglydio-Silva, M., Bruguier, O., Camps, P., Monié, P., Babinski, M., Mondou, M., 2009. Conflicting structural and geochronological data from the Ibituruna quartz-syenite (SE Brazil): effect of protracted orogeny and slow cooling rate? In: Chardon, D., Ray, P. (Eds.), *Hot Orogens Special Issue Tectonophysics* 477, pp. 174–196.
- Richter, F., Lana, C., Stevens, G., Buick, I., Pedrosa-Soares, A.C., Alkmim, F.F., Cutts, K., 2015. Sedimentation, metamorphism and granite generation in a back-arc region: record from the Ediacaran Nova Venécia Complex (Araçuaí Orogen, Southeastern Brazil). *Precambrian Research* 272, 78–100.
- Samadi, R., Mirnejad, H., Kawabata, H., Harris, C., Valizadeh, M.V., Gazel, E., 2014. Magmatic garnet in the Triassic (215 Ma) Dehnow pluton of NE Iran and its petrogenetic significance. *International Geology Review* 56, 596–621.
- Schmidt, M.W., 1993. Phase relations and compositions in the tonalite as a functions of pressure: an experimental study at 650°C. *American Journal of Science* 293, 1011–1060.
- Schmidt, M.W., Poli, S., 2004. Magmatic epidote. *Reviews in Mineralogy and Geochemistry* 56, 399–430.

- Schmidt, M.W., Thompson, A.B., 1996. Epidote in calc-alkaline magmas: an experimental study of stability, phase relationships, and the role of epidote in magmatic evolution. *American Mineralogist* 81, 462–474.
- Skjerlie, K.P., Patiño-Douce, A.E., 2002. The fluid-absent partial melting of zoisite-bearing quartz eclogite from 1.0 to 3.2 GPa; implications for the melting in thickened continental crust and for subduction-zone processes. *Journal of Petrology* 43, 291–314.
- Tedeschi, M., Novo, T., Pedrosa-Soares, A., Dussin, I., Tassinari, C., Silva, L.C., Gonçalves, L., Alkmim, F., Lana, C., Figueiredo, C., Dantas, E., Medeiros, S., De Campos, C., Corrales, F., Heilbron, M., 2016. The Ediacaran Rio Doce magmatic arc revisited (Araçuaí-Ribeira orogenic system, SE Brazil). *Journal of South American Earth Sciences* 68, 167–186.
- Vaucher, A., Egydio-Silva, E., Babinski, M., Tommasi, A., Uhlein, A., Liu, D., 2007. Deformation of a pervasively molten middle crust: insights from the Neoproterozoic Ribeira-Araçuaí orogen (SE Brazil). *Terra Nova* 19, 278–286.
- Vernon, R.H., 2007. Problems in identifying restite in S-type granites in southeastern Australia, with speculation on source of magma and enclaves. *The Canadian Mineralogist* 45, 147–178.
- Vieira, V.S., 2007. Significado do grupo do Rio Doce no context do Orógeno Araçuaí. (PhD Thesis). Universidade Federal de Minas Gerais, Belo Horizonte, p. 117.
- Vielzeuf, D., Schmidt, M.W., 2001. Melting relations in hydrous systems revisited: application to metapelites, metagreywakes and metabasalts. *Contributions to Mineralogy and Petrology* 141, 251–267.
- Villars, A., Stevens, G., Buick, I.S., 2009. Tracking S-type granite from source to emplacement: clues from garnet in Cape Granite suite. *Lithos* 112, 217–235.
- Whitney, D.L., Evans, B.W., 2010. Abbreviations for names of rock-forming minerals. *American Mineralogist* 95, 185–187.
- Xu, L., Xiao, Y., Wu, F., Li, S., Simon, K., Wörner, G., 2013. Anatomy of garnets in a Jurassic granite from the south-eastern margin of the North China Craton: magma sources and tectonic implication. *Journal of Asian Earth Science* 78, 198–221.
- Zen, E-an, Hammarstrom, J.M., 1984a. Mineralogy and petrogenetic model for the tonalite pluton at Bushy Point, Revillagigedo Island, Ketchikan 1° × 2° quadrangle, southeastern Alaska. *United State Geological Survey* 939, 118–123.
- Zen, E-an, Hammarstrom, J.M., 1984b. Magmatic epidote and its petrologic significance. *Geology* 12, 515–518.

CHAPTER 5

EXTREME U-Pb AGE VARIABILITY IN A NEOPROTEROZOIC, LOWER-CRUSTAL BATHOLITH: IMPLICATIONS FOR MAGMA STORAGE IN AN ACCRETIONARY PRISM

PRESENTATION OF THE PUBLICATION

This paper¹, first authored by Francesco Narduzzi is in preparation for submission to Earth and Planetary Science Letters. The aspects highlighted in this paper were done independently by Francesco Narduzzi while receiving standard supervision by his supervisor Herminio Harias Nalini Jr., Federico Farina, Gary Stevens, Cristiano Lana. I did: zircon separation for U-Pb geochronology, zircon imaging by SEM, zircon U-Pb LA-SF-ICP-MS and LA-MC-ICP-MS analyses, zircon trace elements (LA-SF-ICP-MS) and analyses the zircon Lu-Hf isotopes (LA-MC-ICP-MS). I did also the literature review and I have written the majority of the scientific paper. Ana Alkmim reduced the zircon Lu-Hf LA-MC-ICP-MS data.

F. Narduzzi^{a*}

C. Lana^a

F. Farina^b

G. Stevens^c

A. Alkmim^a

H.A. Nalini Jr.^a

^aApplied Isotope Research Group, Departamento de Geologia, Escola de Minas, Universidade Federal de Ouro Preto, Campus Universitário Morro do Cruzeiro s/n, 35400-000 Ouro Preto, MG, Brazil

^bUniversity of Geneva, Department of Earth Sciences, Rue des Maraîchers 13, 1205 Geneva, Switzerland

^cCentre for Crustal Petrology, Department of Earth Science, University of Stellenbosch, Private Bag X1, 7602 Stellenbosch, South Africa

¹Narduzzi, F., Lana, C., Farina, F., Stevens, G., Alkmim, A., Nalini Jr., H.A. Extreme U-Pb age variability in a Neoproterozoic, lower crustal batholith. Implications for magma storage in an accretionary prism.

Extreme U-Pb age variability in a Neoproterozoic, lower crustal batholith. Implications for magma storage in an accretionary prism.F. Narduzzi^a., C. Lana^a., F. Farina^b., G. Stevens^c., A. Alkmim^a. H.A. Nalini Jr^a.^aApplied Isotope Research Group, Departamento de Geologia, Escola de Minas, Universidade Federal de Ouro Preto, Campus Universitário Morro do Cruzeiro s/n, 35400-000 Ouro Preto, MG, Brazil^bUniversity of Geneva, Department of Earth Sciences, Rue des Maraîchers 13, 1205 Geneva, Switzerland^cCentre for Crustal Petrology, Department of Earth Science, University of Stellenbosch, Private Bag X1, 7602 Stellenbosch, South Africa**ABSTRACT**

Exhumed mid- to lower-crustal batholiths are key natural laboratories for studying the histories of magma reservoirs and their role in the evolution of the Earth's lithosphere and atmosphere. Some batholiths record details of the internal structure of magma chambers and provide insights into the thermal and chemical evolution in the crystal mush. However, the lifetime of reservoirs and the duration of magmatic activity in them remains a puzzle. While U-Pb geochronology of young, exhumed plutons and related volcanic rocks suggest very short lifespans for magma activity, large and relatively old batholiths seem to have lived for tens of millions of years. Here we investigate the lifetime of a giant 15,000 km² batholith, in SE Brazil. The batholith itself was assembled in the lower crust during the accretionary/collisional stages of the Neoproterozoic Aracuaí Orogeny. While reasonably homogeneous (in terms of mineralogy/texture and major/trace elements), all samples from the main part of the batholith (8 samples) record extreme variability in magmatic U-Pb dates from ca. 630 to 555 Ma. Trace element geochemistry and Hf isotopes from the igneous zircons – here interpreted as autocrysts (ca. 555 – 560 Ma) and antecrysts (> 560 Ma) – are all consistent storage of magma in a highly active, long-lived magma reservoir, rather than a simple cooling following fractional crystallization at the level of magma emplacement. Based on regional constraints and available petrographic information for our samples, we interpret that such continuous injections of magma took place in the lower crust, at temperatures that kept the system above its solidus through the 80 Ma of zircon crystallization. Unradiogenic ¹⁷⁶Hf/¹⁷⁷Hf and ¹⁴³Nd/¹⁴⁴Nd isotope chemistry indicate no direct mixing with mantle-derived magmas, which is in agreement with the scarcity of mafic products in the region, and supports previous suggestions of emplacement in an evolving accretionary prism. We suggest that

the magmas originated from partial melting of fertile volcanoclastic sediments in the accretionary prism, and that the prism itself was continuously fed by material eroded off the magmatic arc.

Key words: U-Pb zircon LA-MC-ICP-MS geochronology; lower crustal batholith; accretionary prism, long-lived magmatism, Araçuaí orogen; Neoproterozoic Galiléia batholith

1. INTRODUCTION

The development of magma reservoirs is an essential process in coupling the evolution of the continental lithosphere with Earth's atmosphere. The reservoirs themselves are a link in the process of crustal differentiation, potentially feeding upper crustal felsic magmas whilst accommodating the crystal mush from which the melts segregated within the lower- to mid-crust (Bachmann & Bergantz, 2008; Barboni *et al.*, 2016; Cashman *et al.*, 2017; Cooper, 2017; Cooper & Kent, 2014; Deering *et al.*, 2017; Rubin *et al.*, 2017). Some felsic magmas which intrude the upper crust will cataclastically discharge into the atmosphere, thus contributing to the energy/mass balance between crust and atmosphere (e.g., Karakas *et al.*, 2017). The flux of supereruptions is demonstrably conditional to the volume of magma erupted and, consequently, it depends on the duration of magma production within the source. However, because active magma reservoirs are not directly observable, their existence is only established by lines of evidence such as geophysical data, fossil magma chambers (plutons/batholiths), or long-lived supereruptions (Bachmann & Bergantz, 2008). It follows that modelling the development and duration of magma reservoirs at different stages of Earth's evolution requires a full understanding of the crystallization ages of the crystal mushes and related volcanic systems (e.g., Deering *et al.*, 2017).

Recent high-precision U-Pb geochronology of young plutonic/magmatic systems suggest that substantial volumes of evolved magma accumulate over time-scales of hundreds of thousands of years (Farina *et al.*, 2010; Fiannacca *et al.*, 2017; Leuthold *et al.*, 2012; Samperton *et al.*, 2015; Schaltegger *et al.*, 2009; Schoene *et al.*, 2012). In modern (or recent) continental arc settings, voluminous upper-crustal granitic magmatism and volcanic eruptions are constructed in time scales ranging from less than 10^5 up to 10^7 years (e.g., Fig. 1) (Cashman *et al.*, 2017; Cooper, 2017; Coleman *et al.*, 2004; Lipmann & Bachmann, 2015). Such magmas are thought to be produced in the upper or middle crust by Melting Assimilation Storage and Homogenisation (MASH) or Deep Crustal Hot zones (DCH) (Annen *et al.*, 2006 and references therein). In contrast, some Precambrian exhumed mid- to lower crustal batholiths, representing either post-collisional magmatism or partial melting events of volcanic arc-derived immature sediments (within accretionary prisms, and fore/back-arc settings) can record vast and long-lived magmatic histories,

spanning over 10 million years (Fig. 1) (Cai *et al.*, 2011; Clemens *et al.*, 2017a; Clemens & Stevens, 2016; Foster & Goscombe, 2013; Jeon *et al.*, 2012; Jiang *et al.*, 2016; Melo *et al.*, 2017a, 2017b; Romano *et al.*, 2013; Sharkov 2010; Shoene & Bowring, 2010). Judging that all magmatic systems seem to follow similar incremental evolution – marked by intervals of high melt flux and periods of magmatic quiescence - a puzzle remains that some older magmatic systems, especially those related to accretionary prisms and fore/back arc settings seem to record more extended periods of magmatic activity.

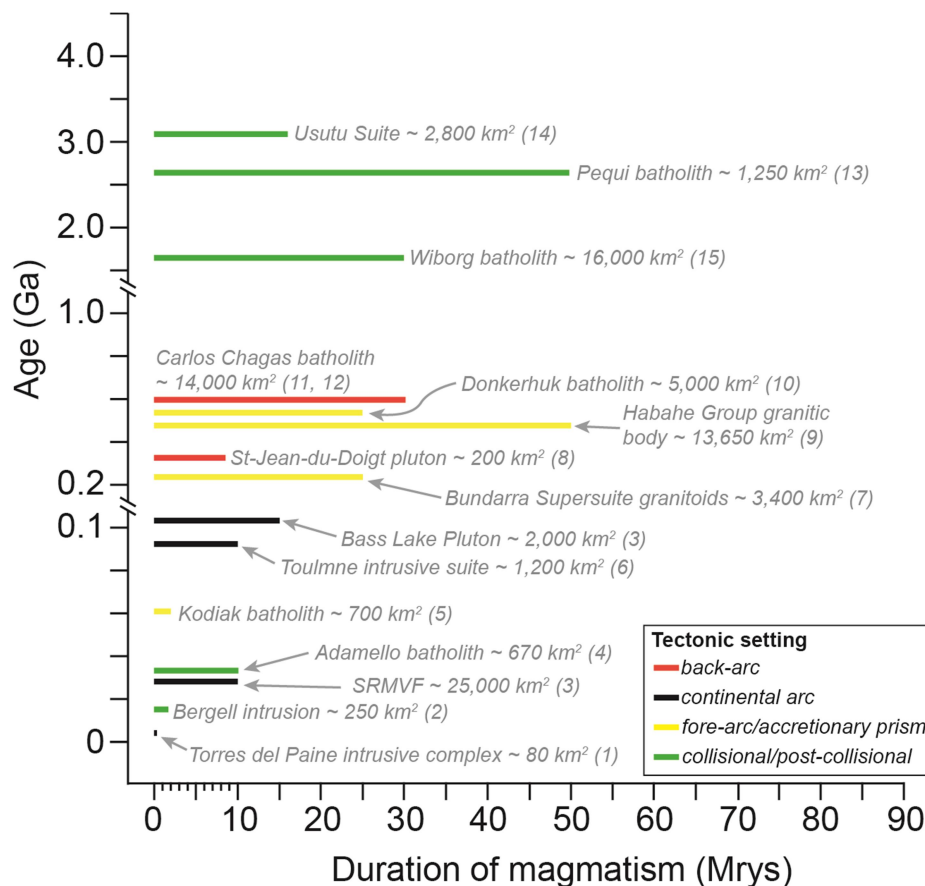


Figure 1. Comparison of duration of magmatism from different ages and tectonic settings. (1) Leuthold *et al.* (2012); (2) Samperton *et al.* (2015); (3) (SRMFV - Southern Rocky Mountain Volcanic Field) Lipmann & Bachmann, (2015); (4) Schaltegger *et al.* (2009); (5) Farris (2010); (6) Coleman *et al.* (2004); (7) Jeon *et al.* (2012); (8) Barboni *et al.* (2013); (9) Jiang *et al.* (2016); (10) Clemens *et al.* (2017); (11) Melo *et al.* (2017a); (12) Melo *et al.* (2017b); (13) Romano *et al.* (2013); (14) Schoene & Bowring, (2010); (15) Sharkov (2010).

Despite some exceptions, such as the back-arc-related St-Jean-Du-Doigt pluton (Barboni *et al.*, 2013) and the accretionary-prism-related Kodiak batholith (Farris 2010), what arises from this simple comparison (e.g., Fig. 1) is that larger, deeply exhumed batholiths record long-lived magmatic activity than their younger shallow level counterparts. This dichotomy may simply be a

sample bias in the geological record (e.g., introduced by the level of exposure) or indicate the fact that long-lived magma chambers can only survive in the mid- to lower crust because of the higher background T. Thus, more data on duration of magmatism of different ages and from different settings are needed to constrain processes of magma production and crystallization in magma reservoir.

Here the lifetime of a giant granitic batholith is investigated through high-precision U-Pb geochronology, coupled with Hf and trace elements in zircons from the well preserved Neoproterozoic Galiléia batholith, of the Araçuaí orogen (SE Brazil). The Galiléia batholith is probably one of the largest batholiths in South America, encompassing an area over 15000 km². It crystallized from metaluminous magmas that were incrementally assembled in the lower crust (> 0.8 GPa) (Narduzzi *et al.*, 2017) during the initial stages of the Araçuaí Orogeny (Pedrosa-Soares *et al.*, 2011). All studied samples from this batholith record extremely variable magmatic zircon ages, testifying a large and extremely protracted magmatic activity. We explore evidence recorded in these magmatic zircons to investigate whether the Galiléia Batholith is an eroded remnant of a lower crustal magma chamber.

2. GEOLOGICAL BACKGROUND

The Galiléia batholith crops out in the Araçuaí orogen over an area of more than 15,000 km² (> 300 km length and > 50 km wide) (Fig. 2a) (e.g., Pedrosa-Soares *et al.*, 2011). The granitoids forming the batholith (hereafter Galiléia granitoids) intrude, (1) medium- to high-grade (amphibolite/granulite facies) arc-related metasediments of the so-called Rio Doce Group, and (2) the juvenile ($\epsilon\text{Nd} \geq 0$) Paleoproterozoic gneisses of the Pocrane Complex (Gonçalves *et al.*, 2018; Mondou *et al.*, 2012; Narduzzi *et al.*, 2017) (Figs. 2b and c). The metasediments and Galiléia granitoids together form the Rio Doce magmatic arc (Pedrosa-Soares *et al.*, 2011). The granitoids are weakly deformed and record widespread high-pressure magmatic minerals such as grossular-rich garnet, epidote and primary low-Si phengite-like white mica (Narduzzi *et al.*, 2017). They are mainly represented by medium- to high K (1.01 to 6.25 wt.%), metaluminous to slightly peraluminous [A/CNK ($\text{Al}/\text{Ca}+\text{N}+\text{K}$ mol.%) = 0.86 to 1.11], medium-grained tonalites and granodiorites, whereas granites are less abundant. Silica content ranges between 59 and 76 wt.% while $\text{FeO}_{\text{Tot}}+\text{MgO}$ correlate positively with A/CNK and negatively with CaO, indicating an overall I-type affinity (Fig. 3) (Clemens *et al.*, 2011; Farina *et al.*, 2012; Narduzzi *et al.*, 2017). Magmatic garnet, epidote and primary low-Si phengite in these granites suggest emplacement and crystallization in the lower crust (> 0.8 GPa; ca. 25 – 30 Km) (Narduzzi *et al.*, 2017). Moreover,

the Galiléia granitoids markedly contrast with the geochemistry of the Rio Doce metasediments (Fig. 3), which are marked by a slightly to strongly peraluminous ($1.1 < A/CNK < 2.2$) character.

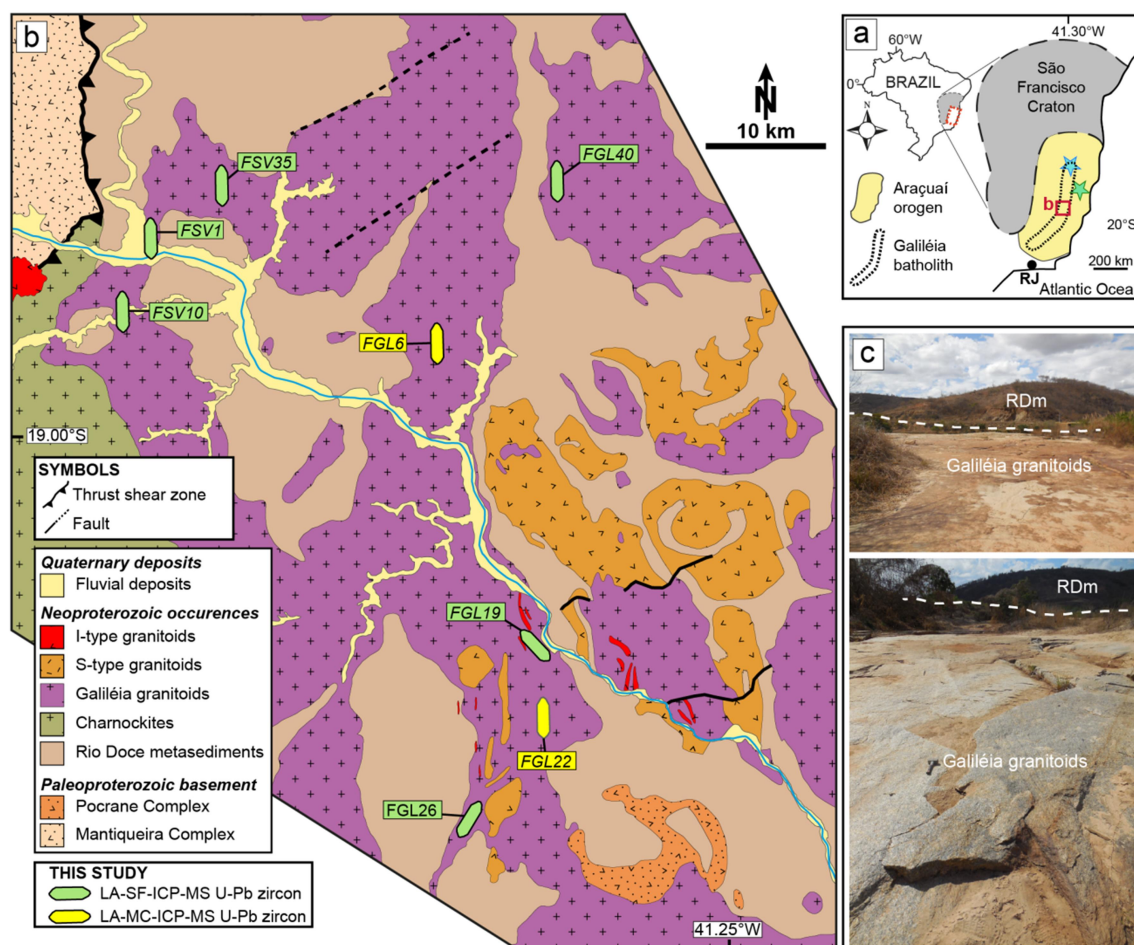


Fig. 2. The Araçuaí Orogen and Galiléia granitoids. (a) Localization of the Araçuaí Orogen and Galiléia Batholith in SE Brazil. Note as the Galiléia batholith extents almost for the same length of the orogen; RJ: Rio de Janeiro; blue star northern part of the Galiléia batholith (Gonçalves *et al.*, 2018); green star Carlo Chagas Batholith (Melo *et al.*, 2017a, 2017b). (b) Geological map of the central part (ca. 4,000 km²) of the batholith with the localization of the studied samples; (c) Galiléia granitoids in contact with the Rio Doce metasediments (RDm). White dotted line indicate the contact.

More mafic members of the Galiléia Batholith (e.g., diorites and gabbros) are scarce, but mafic micro-granular enclaves are commonplace, showing different degrees of hybridization by their host (Fig. 3). The occurrence of mafic-intermediate microgranular enclaves together with the Nb, Ta, Ti and Sr negative anomalies exhibited by the Galiléia granitoids and their strong isotopic crustal signature (whole rock $\epsilon_{Nd} = -6.7$ to -13.8 ; zircon $\epsilon_{Hf} = -5.2$ to -11.7) have all been interpreted as evidence of MASH-related silicic magmatism (Gonçalves *et al.*, 2018 and references therein). According to this model, dehydration of the subducting oceanic slab produced metasomatism of the mantle wedge and ensuing mafic magmas that rose through the continental crust. Upon intrusion, the mafic magmas partially melted the continental crust and generated the

Galiléia granitoids through assimilation, mixing and fractional crystallization (Gonçalves *et al.*, 2018; Pedrosa-Soares *et al.*, 2011; Tedeschi *et al.*, 2016). However these studies seem not to consider the thermodynamic limitations of this process during assimilation of large volumes of continental crust (Glazner, 2007), evidence already discussed in Gonçalves *et al.* (2014). Indeed if the thermodynamics of this process is considered, then the amount of crustal material required to reproduce the geochemical and isotopic variability of these rocks would be too extensive (see discussion). The continental crust is thought to be Paleoproterozoic due to the Nd and Hf_{TDM} ages ranging between 1.39 to 2.26 Ga and rare inherited zircon cores at ca. 2.0 Ga.

Some authors (Mondou *et al.*, 2012; Pétitgirard *et al.*, 2009; Vauchez *et al.*, 2007) suggest that the main magmatic event for the Galiléia batholith took place around 580 to 570 Ma. By contrast, three main crystallization intervals (at 632 – 605 Ma, 600 – 590 Ma and 585 – 570 Ma) have been proposed recently after a compilation of all the published zircon U-Pb ages (47 U-Pb dated samples) (Tedeschi *et al.*, 2016). Significantly, a close examination of the published U-Pb data shows a wide variation of magmatic ages within individual sample (e.g., Table 2 and Fig. 6 of Pedrosa-Soares *et al.*, 2011).

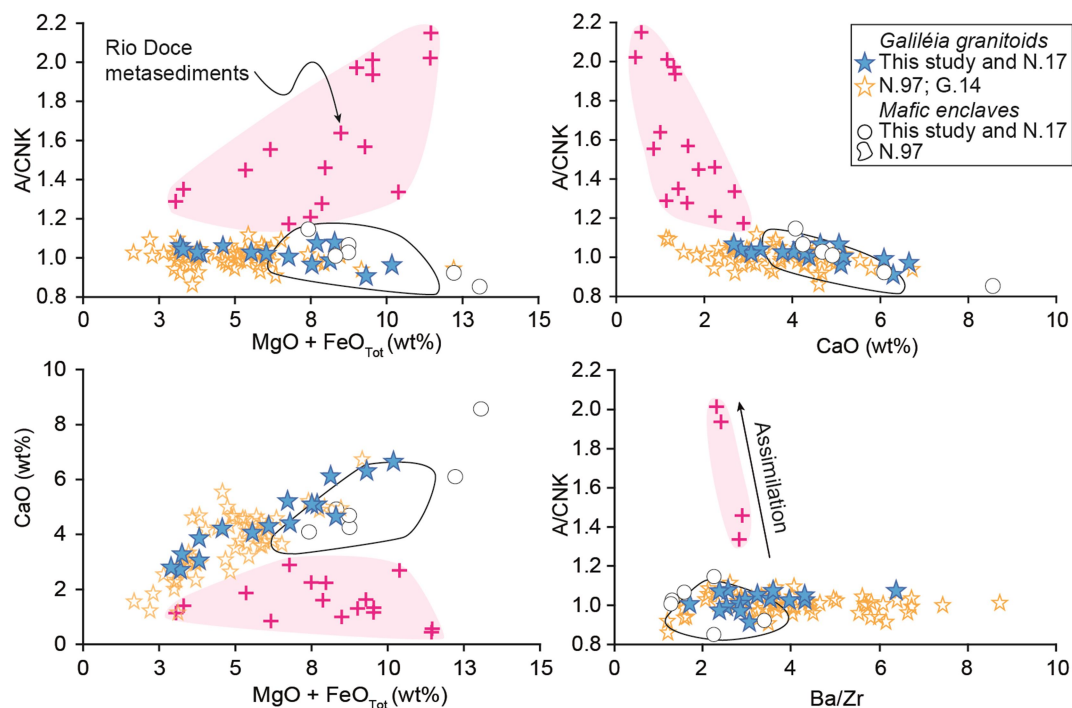


Fig. 3. Hacker diagrams. N.17: Narduzzi *et al.* (2017); N.97: Nalini Jr. (1997); G.14: Gonçalves *et al.* (2014). Rio Doce Metasediments geochemistry is from Vieira, (2007) and Novo, (2013). Granitic samples which location was uncertain were not used.

3. METHODS

To investigate the causes of this age variability in the Galiléia granitoids, we have sampled eight granitoids from the central part of the batholith (Fig. 2b). For each of the rock sampled at least 100 transparent and fracture-free zircons grains were handpicked, mounted in epoxy resin and imaged by cathodoluminescence (CL). These grains were dated via in-situ laser ablation-sector field-inductively coupled plasma-mass spectrometry (LA-SF-ICP-MS), and the Hf isotopic composition was determined by LA- multi-collector (MC) -ICP-MS on the same textural domain previously dated (See the supplementary material SM1 and SM2 for details).

A further refinement of the U-Pb age dating was done for two of these samples via LA-MC-ICP-MS (Lana *et al.*, 2017; Santos *et al.*, 2017) to achieve a precision on individual $^{206}\text{Pb}/^{238}\text{U}$ spot dates down to 0.5%. For this, the zircon grains and fragments of reference material were mounted on the same epoxy disc, within two squares of ca. 3 x 3 mm each (Fig. SM3-1) and distance of 5 mm from each other. Primary and secondary standards were mounted close to the unknown. Finally, trace elements were also measured by LA-SF-ICP-MS (see methods in Supplementary material).

Analyses were carried out using a Thermo-Finnigan Neptune Plus Multicollector ICP-MS coupled to a Photon-Machines 193 nm laser system at Universidade Federal de Ouro Preto, Brazil. Laser conditions were 20 μm spot size, 6 Hz repetition rate, and 3 mJ intensity. The ablated material was carried by Ar (ca. 1.1 L/min) and He (ca. 0.5 L/min). Individual spot analyses lasted 45 seconds, comprising of 15-seconds background and 30 seconds of signal + background. Corrections include background, down-hole fractionation, instrumental mass bias drift and common Pb (Lana *et al.*, 2017). All ages were then calculated using Isoplot/Ex4 program (Ludwig, 2003). BB9 (560 ± 0.4 Ma; Santos *et al.*, 2017) was used as primary standards, while Temora (416 ± 0.24 Ma; Black *et al.*, 2003), Plešovice (337.3 ± 0.4 ; Sláma *et al.*, 2008) and in-house P3 (600 Ma; Lana *et al.*, 2017) were chosen as secondary standards. BB9, Temora and P3 gave concordia ages of 561 ± 1 Ma [2S; $n = 20$; $\text{MSWD}_{\text{C+E}} 1.14$), 337 ± 4 Ma [2S; $n = 24$; $\text{MSWD}_{\text{C+E}} 0.79$), 414 ± 1 Ma [2S; $n = 7$; $\text{MSWD}_{\text{C+E}} 0.26$) and 601 ± 2 Ma [2S; $n = 4$; $\text{MSWD}_{\text{C+E}} 0.51$), respectively. Although Temora has a slightly lower age than the accepted values, the others are well within the ID-TIMS published ages (Fig. SM3-2).

Trace elements in zircons were acquired at the UFOP using a Thermo-Fisher Element II SF-ICP-MS linked to a Photon Machines 193 nm ArF Excimer laser. Ablation was done in a 0.7 l/min He gas stream using a 25 μm laser spot size and mixed with Ar before entering the ICP-MS.

Repetition rate was set to 6 Hz with laser energy density of 0.7 J/cm². ²⁴⁰UO/²³⁸U was below 1% and measurements were carried out with 15s background and 30s data acquisition. ²⁹Si, ⁴⁴Ca, ⁸⁹Y, ⁴⁵Sc, ⁹³Nb, ¹⁴⁰Ce, ¹⁴¹Pr, ¹⁴⁶Nd, ¹⁴⁷Sm, ¹⁵³Eu, ¹⁵⁷Gd, ¹⁵⁹Tb, ¹⁶³Dy, ¹⁶⁵Ho, ¹⁶⁶Er, ¹⁶⁹Tm, ¹⁷²Yb, ¹⁷⁵Lu, ¹⁷⁸Hf, ²⁰⁶Pb, ²⁰⁸Pb, ²³²Th, and ²³⁸U were analysed. GLITTER (Van Achterbergh *et al.*, 2001) was used for data reduction using stoichiometric ²⁹Si for internal standardization. NIST 612 glass was used as the primary standard. NIST 610 standard glass and BCR and BHVO-1 basaltic glasses were used as secondary standards.

All zircon data, standard analyses and a new set of whole rock geochemistry are reported in the supplementary material. Major and trace element whole rock analytical procedures are described in Narduzzi *et al.* (2017) and appendix A for further details.

4. RESULTS

4.1 Zircon textures

The selected zircons are subhedral to euhedral, typically stubby and prismatic with sizes between 80 and 450 µm and length-width ratios from 2:1 up to 4:1. Under CL (Figs. 4a, 4b and SM3-3) grains are fracture-free, many show core-to-rim oscillatory zoning and are commonly characterized by thin (<20 µm), dark rims. As shown in Fig. 4b, some of the crystals show centres that can be either (i) dark grey sub-idiomorphic and oscillatory zoned or (ii) light grey rounded and structureless. Both these centre-types are surrounded by overgrowths (i.e. magmatic edges in Figs. 4a and b). A subset of the zircon centers displays resorption surfaces and are truncated by outer magmatic zoned domains. These are interpreted as resorbed inherited cores. Most of the grains record no inherited cores, but rather a continuous magmatic zoning from centre to rim. None of the CL images showed appreciable metamictization textures suggesting re-equilibration of zircons within aqueous fluids or melts



Fig. 4. Cathodoluminescence images of the Galiléia zircons. a) and b) representative images of the zircons analysed by LA-SF-ICP-MS (Figs. 5.4 and 5.6) and high-precision multicollector LA-ICP-MS (Fig. 5.5 and 6.6), respectively. In a) and b) the numbers in white correspond to the $^{206}\text{Pb}/^{235}\text{U}$ spots. Accordingly these are reported in the weighted plots of Figs. 5.4 and 5.5, respectively. b) White arrows indicate resorption features, whereas black arrows indicate oscillatory zoning textures.

4.2 U-Pb age dating

Of the two hundred and three spots, one hundred and fifty-five U-Pb dates were concordant to subconcordant (>95 % concordant). In each of the sample analyzed, U-Pb dates spread along the concordia line with $^{206}\text{Pb}/^{238}\text{U}$ dates spanning from 630 ± 10 to 549 ± 9 Ma (Figs. 5 and SM3-3). It is worth noting that, even when the resorbed cores are excluded the difference between oldest and youngest grain per hand sample (Δt_h) span from 33 to 63 Myrs. Spot analyses on resorbed and inherited cores ($n = 8$) comprise dates between 586 ± 10 to 714 ± 15 Ma.

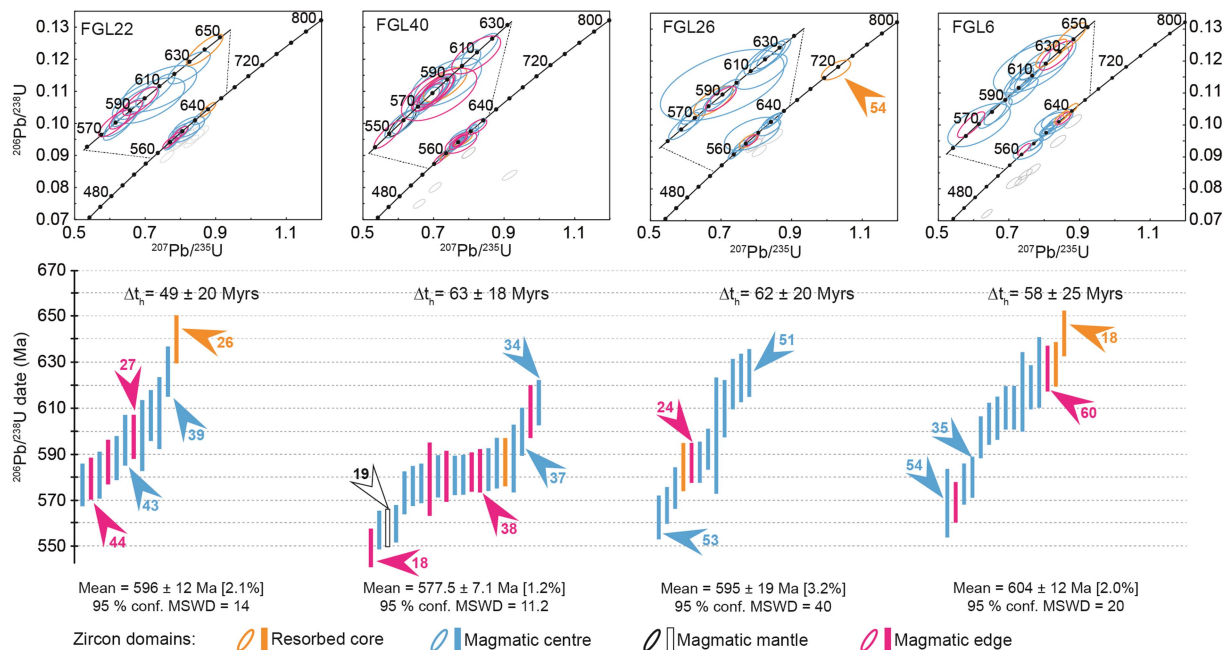


Fig. 5. Concordia diagrams and weighted mean plots of LA-SF-ICP-MS dating. For each hand sample, Δt_n is the difference between the oldest and youngest magmatic dates. Ellipses and error bars are 2s. Others samples are reported in Fig. E3 Appendix E. Numbers close to the error bars are according to the spot numbers in Fig. 6.3a

Results of high-precision LA-MC-ICP-MS (Lana *et al.*, 2017) analyses gave concordant dates between 99 to 100%. Weighted mean plots (Fig. 6) confirm previous LA-SF-ICP-MS analyses with dates plotting along the concordia line (Figs. 7a) with dates spanning from 633 ± 4 to 552 ± 4 Ma. Each of the two individual hand sample exhibits significant date dispersion: sample FGL22 from 631 ± 4 to 552 ± 5 Ma, sample FGL6 from 633 ± 4 to 554 ± 4 Ma. Additionally: i) both samples display a net decrease in the number of resorbed domains younger than 610 – 600 Ma, ii) resorbed cores have dates spanning from ca. 675 to 575 Ma while the oscillatory zoned cores and magmatic edges span from 640 down to 550 Ma (Figs. 6, 7a and b) and iii) between the oldest and youngest magmatic grain there is a difference of up to 80 Myrs. Notably, from a total of 274 concordant spots (SF + MC), none of them returned a Paleoproterozoic date.

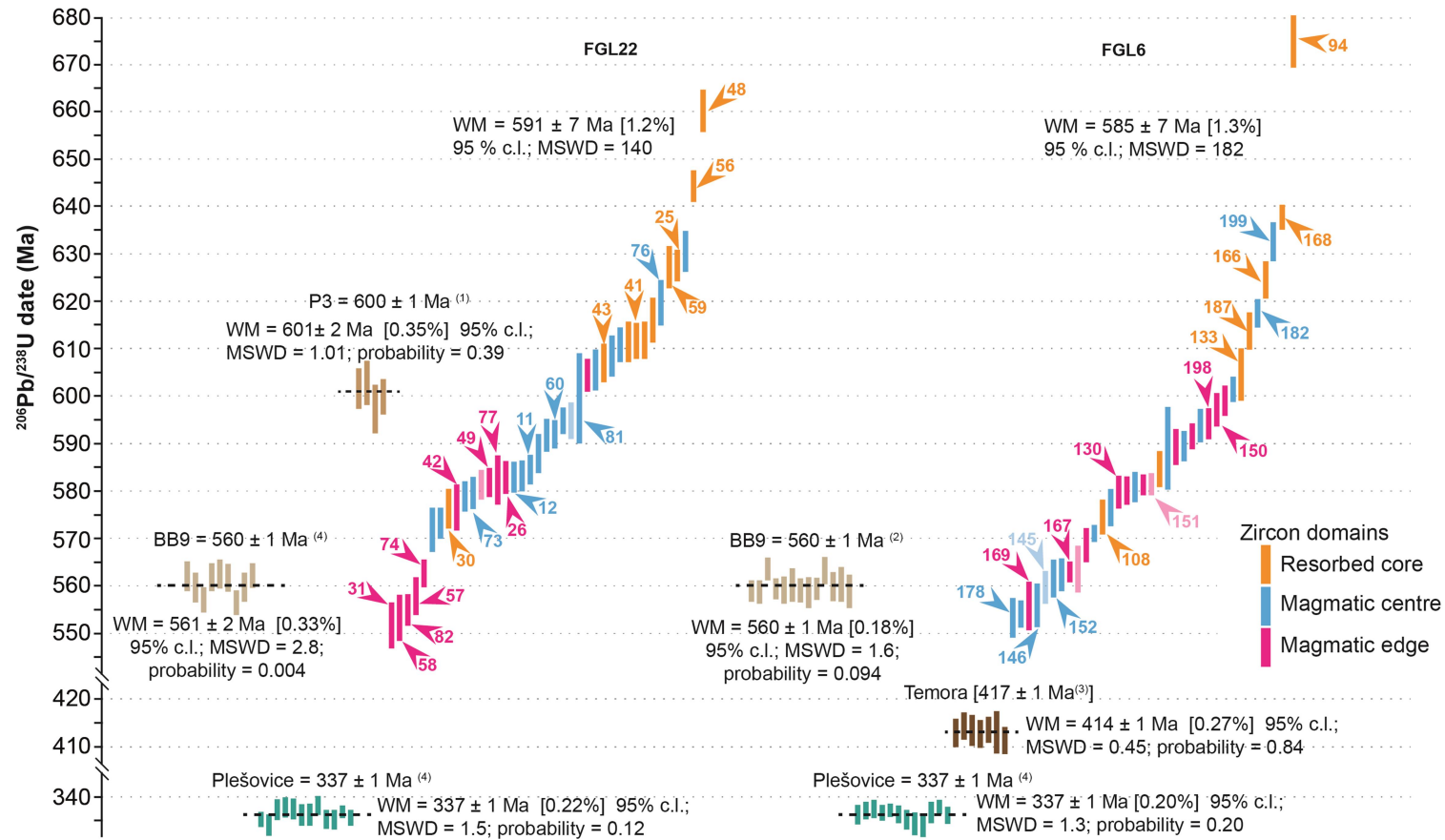


Fig. 6. Zircon images and weighted mean plots for the two high-precision multi collector dated samples. Note the date variation of the two samples despite the homogeneous ages obtained from the standards. Transparent error bars refer to those dates which have not been further used in the interpretation (see appendix D). Error bars are 2s. Numbers close to the error bars are according to the spot numbers in Fig. 5.4b. Superscript numbers close to standard ages are: 1) Lana *et al.* (2017); 2) Santos *et al.* (2017); 3) Black *et al.* (2003); 4) Sláma *et al.* (2008).

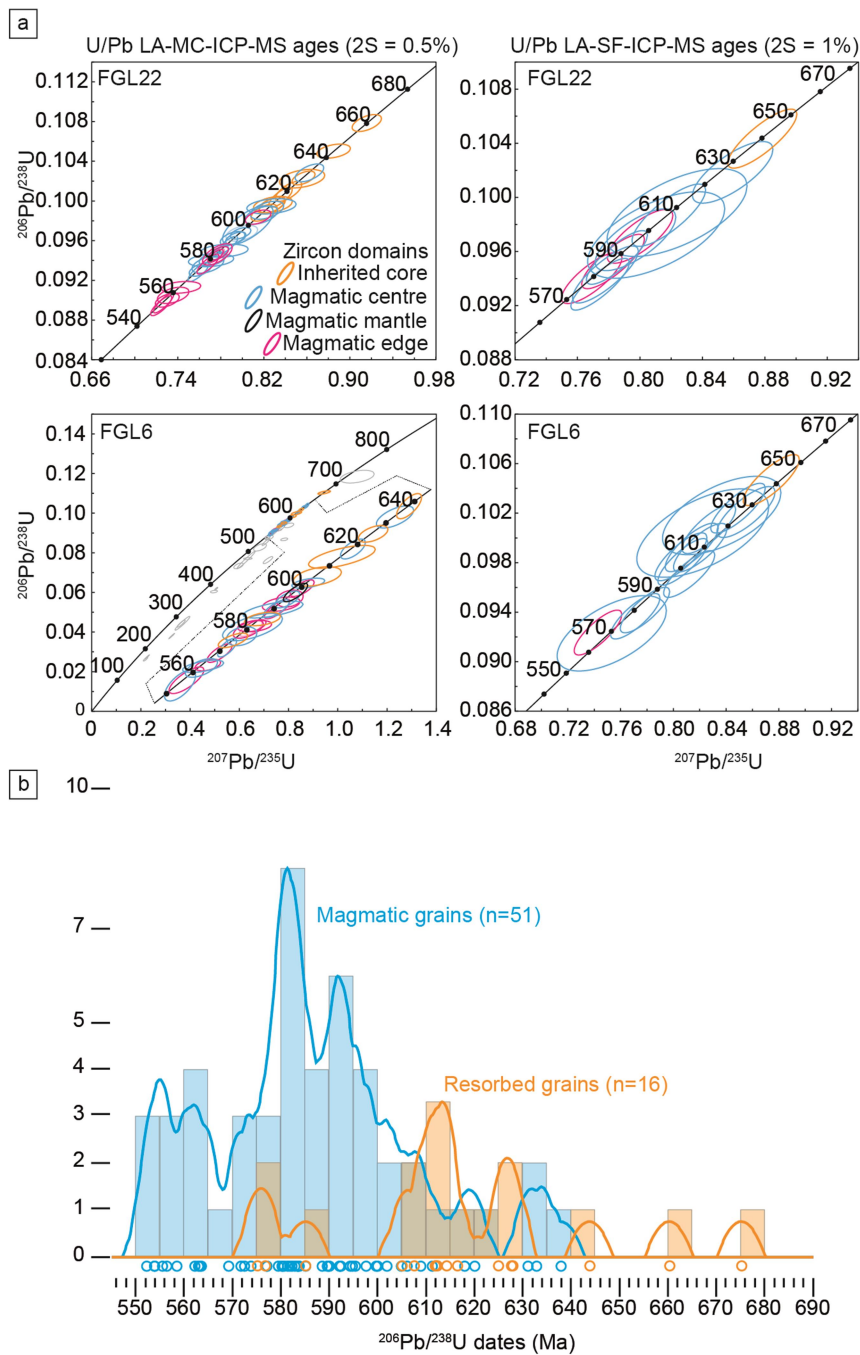


Fig. 7. a) Comparison between concordia diagrams from high-precision and LA-SC-ICP-MS date. **b)** Density plot diagram showing for the MC dates. This was generated using Vermeesch, (2012) density plot. Note that magmatic grains encompass the ante and autocrystic zircons.

4.3 Hf data and trace elements

The zircon $^{177}\text{Hf}/^{176}\text{Hf}_{(t)}$ composition varies from 0.282020 to 0.282343, with $\epsilon\text{Hf}_{(t)}$ from -6.0 to -14.2 (mean -9.0 ± 0.31 2S) (Fig. 8) with no systematic difference between the Hf isotopic composition of magmatic centres and rims. Zircon crystals from individual samples are characterized by a spread in $^{176}\text{Hf}/^{177}\text{Hf}$ of up to 0.0003 corresponding to ca. 8 epsilon units. Resorbed cores have $^{177}\text{Hf}/^{176}\text{Hf}_t$ composition overlapping ($0.281957 \div 0.282211$; $\epsilon\text{Hf}_{(t)}$ -6.2 to -14.6; mean 8.5 ± 1.91 2S) with that of magmatic overgrowth and core-to-rim oscillatory zoned crystals. Zircon crystals from the central portion of the Galileia batholith display a wider variability and a clear crustal character than those from rocks sampled in the northern portion of the batholith ($\epsilon\text{Hf}_{(t)} = -5.2$ to -9.3 ; Gonçalves *et al.*, 2016) and, to the east, in the Carlos Chagas batholith (CCB) ($\epsilon\text{Hf}_{(t)} = -1.8$ to -8.2 ; Melo *et al.*, 2017b) (blue and green star in Fig. 2a, respectively). Likewise, the Galiléia resorbed zircon are significantly more crustal than the similar inherited crystals from the CCB ($\epsilon\text{Hf}_{(t)} = -1.9$ to -7.4 ; Melo *et al.*, 2017b).

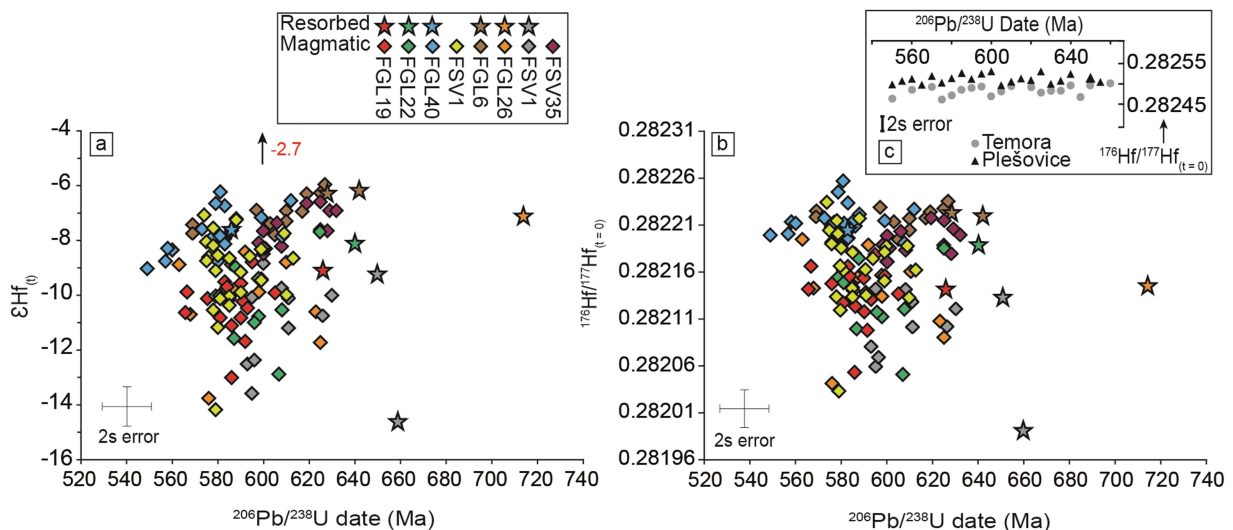


Fig. 8. Hf isotopes analyses vs. SF $^{206}\text{Pb}/^{238}\text{U}$ dates. a) ϵHf_t vs. $^{206}\text{Pb}/^{238}\text{U}$ dates; b) $^{176}\text{Hf}/^{177}\text{Hf}$ at present time (i.e. $t = 0$) against the relative zircon date; c) measured $^{176}\text{Hf}/^{177}\text{Hf}_{(t=0)}$ of the two standards used during our Hf analyses and plotted against a range of Pb-loss-derived dates. Note that the chosen range of dates is the same found for the Galiléia magmatic zircons. See text and Appendix E for further explanations.

Rare Earth Elements (REEs) and incompatible elements (IEs) from resorbed cores, magmatic centers and edges have broadly similar patterns without significant difference between each domain. All zircon domains are enriched in non-stoichiometric Ca and Ba with values up to 1823 and 4.78 ppm, respectively (data tables in the supplementary material). These, together with other elemental ratios such as Yb/Gd, Th/U, Sc/Th and Eu/Eu* do not correlate with the relative age (Fig. 9). The $(\text{Ce}/\text{Nd})_N$ ratio [here used to approximate (Chelle-Michou *et al.*, 2014) the Ce/Ce*

anomaly $[=(D_{Ce}^{zrc/melt} / \sqrt{D_{La}^{zrc/melt} \times D_{Pr}^{zrc/melt}})]$ (Trail *et al.*, 2012)] for magmatic zircons is rather scattered (0.32 ÷ 7.15) when compared to that of resorbed domains (0.32 ÷ 2.44). The values for $(Ce/Nd)_N$ in the resorbed cores are inversely correlated with age. Notably, $(Ce/Nd)_N$ ratios for both zircon domains are well below the reported range values from continental arc granitoids-derived zircons (11 ÷ 37; Grimes *et al.*, 2015). Instead, they are similar to zircons crystallized from gabbrodiorites (2 ÷ 9) (Chelle-Michou *et al.*, 2014) suggesting low oxygen fugacities (i.e. fO_2) typical of mafic systems. Additionally, there is a slight decrease in Zr/Hf ratio from resorbed cores towards younger magmatic domains.

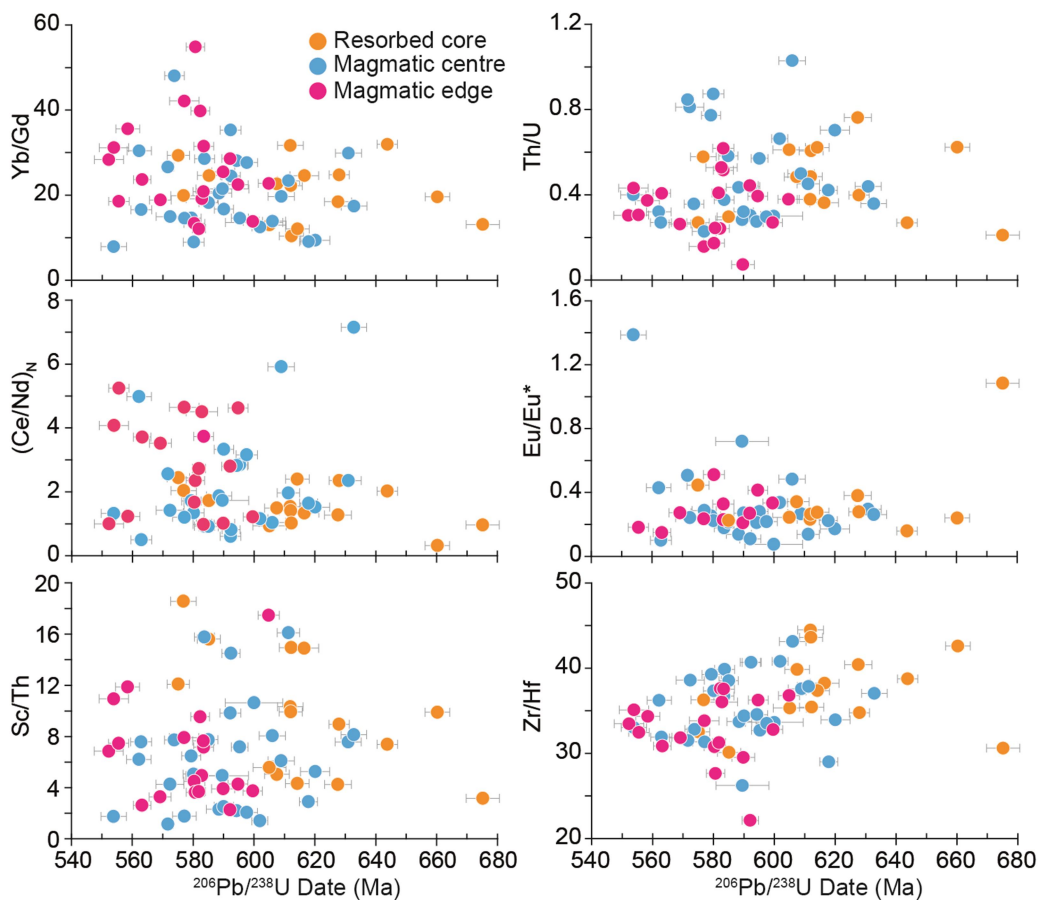


Fig. 9. Zircon trace elements vs. high-precision multi collector dates. Errors are 2s. Normalization uses the Chondrite after McDonough & Suns, (1995).

5. DISCUSSION

5.1 Extreme U-Pb age variability: Pb Loss, inheritance, or multiple events of crystallization in a warm magma chamber?

In-situ U-Pb zircon dates determined by conventional LA-SF-ICP-MS and high precision LA-MC-ICP-MS returned identical results, revealing extreme U-Pb age variability in magmatic zircons of the Galiléia Batholith (Figs. 5, 6 and 7). Most samples of the batholith record concordant U-Pb zircon dates from 630 Ma to 550 Ma, implying either multiple events of early Pb loss, inheritance from the sedimentary rocks from the Rio Doce, or a natural preservation of magmatic zircon in a long-lived reservoir.

Multiple events of early Pb-loss are rare in nature, being observed only in clearly high-grade, sector zoned metamorphic zircons (e.g., Ashwall *et al.*, 1999; Wang *et al.*, 2011), whereas conventional Pb-loss should define a discordia line between the crystallization at 630 Ma and the timing of Pb-loss at 550 Ma. Data from high precision LA-MC-ICP-MS were however highly concordant, spreading along the concordia from 630 to 550 Ma. Conventional Pb-loss seems unlikely given the identical age range from each rock sample studied here. These samples were collected at least 10 km apart from each other and had petrographic and geochemical features similar to those from other parts of the body (Gonçalves *et al.*, 2018; Pedrosa-Soares *et al.*, 2011; Tedeschi *et al.*, 2016). Furthermore, a close investigation of the relation between apparent trace elements, alpha dose, magmatic age dates and $^{176}\text{Hf}/^{177}\text{Hf}$ variation precludes any possibility of early Pb loss (SM4). Especially, the measured values of $^{176}\text{Hf}/^{177}\text{Hf}_{t=0}$ against the relative zircon date are not linear (Fig. 8b) as expected and documented for zircons that have experienced Pb loss (e.g., c.f. Fig. 2 in Vervoort & Kemp, 2016). In fact, if Pb-loss would have occurred in the Galiléia samples, it would have created an invariant linear trend for $^{176}\text{Hf}/^{177}\text{Hf}_{t=0}$ with varying $^{206}\text{Pb}/^{238}\text{U}$ dates. This is well explained in Fig. 5.8c, which models the $^{176}\text{Hf}/^{177}\text{Hf}_{t=0}$ of the primary and secondary reference material measured during the analyses with a hypothetical range of dates derived from Pb-loss.

The studied zircons record identical magmatic, oscillatory zoned textures, and similar trace element geochemistry, suggesting that they were not assimilated from the country rocks - the Rio Doce metasediments. This is strongly supported by recent studies (Degler *et al.*, 2017; Schannor *et al.*, 2018) showing that zircon populations belonging to the Rio Doce metasediments may record Paleoproterozoic ages, whereas other Mesoproterozoic zircon record a positive $\varepsilon\text{Hf}_{(t \geq 614 \text{ Ma})}$, thus very different from those documented here.

In summary, our new geochronological dataset suggests a long-lived (ca. 80 Myrs), uninterrupted granitic magmatism, from ca. 630 to 555 Ma. The magmatic zircons are interpreted as autocrysts (ca. 555 – 560 Ma) and antecrysts (> 560 Ma), implying a long-lived injection of magma batches within the magma reservoir (i.e., where the Galiléia batholith was incrementally assembled). Zircon trace element geochemistry indicates an open-system behavior rather than a simple cooling and fractional crystallization at the level of magma emplacement. Notably, the contemporaneous crystallization of magmatic epidote (i.e. LREE-rich accessory mineral; Bea, 1996) might have lowered the $(\text{Ce}/\text{Nd})_{\text{N}}$ in the magmatic zircon and thus explaining the apparent contrasting low $f\text{O}_2$ s shown by the Galiléia zircons.

The similar variability in trace element geochemistry and Hf isotopes between autocrysts and antecrysts imply that magma batches were geochemically similar. Many grains were entrapped in mafic minerals (i.e. biotite and amphiboles) which were not dissolved at each new magma injection, thus preserving the zircons from resorption. We believe that the continuous injection of compositionally similar magmas (and ensuing magma stirring and overturning within the chamber) could have erased former geochemical heterogeneities and redistributed zircon (autocrysts and antecrysts) throughout the batholith (Burgisser & Bergantz, 2015; Huber *et al.*, 2009). This uninterrupted melt arrival in a lower crustal crystal mush would also be responsible for keeping the system continuously above its solidus (Annen *et al.*, 2006; Chashman *et al.*, 2017). Moreover, latent heat buffering (i.e., mushification; Huber *et al.*, 2009) might have contributed in extending the partially molten state of the mushy reservoir and lowered additional heterogeneities due to crystal-liquid separation.

We could not use Ti-in-Zr thermometer because Ti buffering mineral phases were lacking (see also Kent & Cooper, 2017), but P-T-t studies from various middle to lower crustal rocks (ca. 0.5 GPa – 1.1 GPa) exposed within the Araçuaí orogen (Mondou *et al.*, 2012; Melo *et al.*, 2017a; Richter *et al.*, 2015, Peixoto *et al.*, 2017; Shannor *et al.*, 2018) indicate depth of emplacement between 20 and 30 km and a regional geothermal gradient of ca. 30 °C/km. This is consistent with the occurrence of the high-pressure garnet-epidote-phengite mineral assemblage described by Narduzzi *et al.* (2017) for the Galiléia granites. Even when this low-medium geothermal gradient of 30 °C/km is considered, this corresponds to a room temperature > 600 °C. Such a high temperature contributes to keep the magmatic system partially molten for tens of millions of years.

We conclude that the Galiléia batholith is an eroded remnant of a Neoproterozoic magma chamber, which was assembled and stored within the lower crust, and kept warm (e.g. Barboni *et*

al., 2016) for approximately 80 Ma, at temperatures likely fluctuating between 650 to 750°C. Notably, similar age variation is found in another granitic body belonging to the Habahe Group in the Chinese Altai. This granite was assembled in an accretionary-prism between 440 – 370 Ma, at mid- to lower crustal levels (Jiang *et al.*, 2016). Each individual sample collected from different parts of this granite (possibly > 10 km apart), records an age variability of more than 50 Myrs (magmatic zircon ages) (Cai *et al.*, 2011). Like for the Galiléia samples, such age variability seems to encompass almost the entire life span of the whole granitic body.

5.2 Nature of the source: mantle wedge or accretionary prisms?

The scarcity of mafic products associated with the lower crustal Galiléia batholith and the relatively unradiogenic $^{176}\text{Hf}/^{177}\text{Hf}$ and $^{143}\text{Nd}/^{144}\text{Nd}$ isotope chemistry of the Galiléia samples indicate that these rocks mostly formed by partial melting of the lower continental crust with only minor involvement of mantle-derived magmas during the assembly and growth of the Galiléia batholith. Moreover as already pointed out in Gonçalves *et al.* (2014) MASH processes would require a massive amount of crust to explain the geochemical and isotopic variability so far discussed. Such large crustal assimilation is energetically limited by the system as shown by Glazner (2007). Several samples with $\text{SiO}_2 < 55$ wt.% have unradiogenic whole rock $^{143}\text{Nd}/^{144}\text{Nd}$ - ϵNd range between -7 and -14 (Gonçalves *et al.*, 2016, 2018; Tedeschi *et al.*, 2016) which are consistent with the ϵHf obtained in this study. These crustal isotopic values might suggest that the microgranular enclaves are not produced by mixing between mantle- and crustally-derived magma but through high-T partial melting of mafic-derived source such as gabbros or diorites (Clemens *et al.*, 2017) and by hybridization of these magmas with their host.

Considering a simple process of a basaltic underplating at 5 mm/yr in the lower crust (e.g., similar to that used to reproduce a silicic magmatism having time scales consistent with geochronological observations - Annen *et al.*, 2006), after 80 Myrs of the Galiléia granitic magmatism, this would leave behind an unreasonable mafic crust thick ca. 400 km and distributed below the 15,000 km² area of the batholith.

In our previous study, we suggested that the Galiléia batholith share more similarities with those assembled in the accretionary wedge rather than those found in continental arcs settings (Narduzzi *et al.* 2017). Voluminous granitic plutons such as the Galiléia are mostly found in accretionary wedge, fore-arc and back-arc basin settings (Clemens *et al.*, 2017; Clemens & Stevens 2016; Jiang *et al.*, 2016; Jeol *et al.*, 2012; Melo *et al.*, 2017a, 2017b; Foster & Goscombe, 2013) far from MASH/DCH zones, which are commonly linked to subduction settings. According to

Clemens *et al.*, (2011) and Clemens and Stevens, (2016) andesitic, volcanoclastic and immature sedimentary material accumulated within these tectonic settings are common and fertile sources for granitic magmatism. If these sources are continuously added into the deepest part of the accretionary prism (for melting) they will produce magmas of similar composition, which explains the long-lived and yet homogenous bulk rock chemistry of the Galiléia batholith.

We propose that a long-lived erosion of an on-going (> 714 Ma this study) andesitic Rio Doce volcanic arc (e.g., Pedrosa-Soares *et al.*, 2011), would allow volcanoclastic sediments into the accretionary prism (Fig. 10). The continuous additions of these fertile sediments at the source melting level would not only explain the bulk rock homogeneity, but also it seems a viable way to have magmatic zircons with disparate U-Pb dates but with a constant geochemistry and isotope composition. This interpretation also applies to the resorbed cores which are relatively older than auto- and antecrystic zircons and have $(\text{Ce}/\text{Nd})_{\text{N}}$ values that suggest derivation from a more mafic system (i.e., andesitic-like; Chelle-Michou *et al.*, 2011). We interpret such cores as inherited from a source, compositionally andesitic-like, and slightly older than the Galiléia granitoids. Considering the lower crustal character (25 – 30 km) of the garnet-bearing Galiléia granitoids (Narduzzi *et al.*, 2017), their source should have been at least located above 30 km.

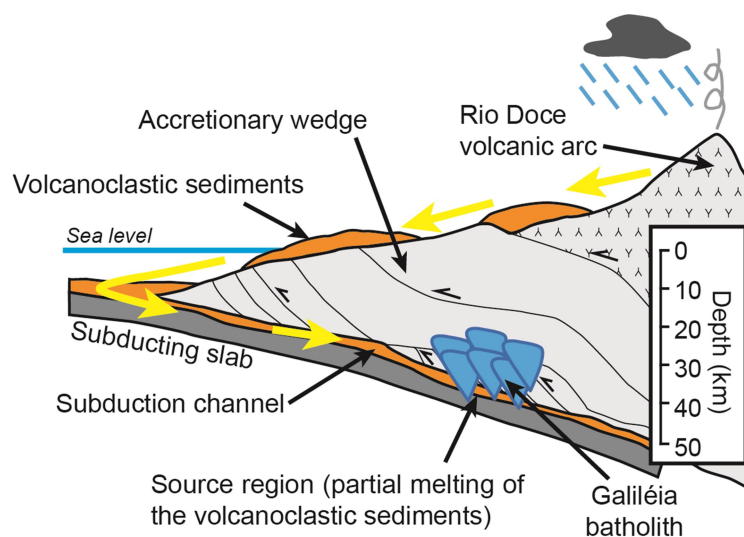


Fig. 10. Accretionary prisms evolutionary model for the Galiléia granitoids (not in scale).

Similar processes where the anatexis reworking of accretionary-related immature sediments caused protracted and voluminous granitic magmatism have been already recognized from similar

geotectonic settings belonging to young (Barker *et al.*, 1992; Farris *et al.*, 2010; Jiang *et al.*, 2016) as well as older accretionary systems (Clemens & Stevens, 2016; Clemens *et al.*, 2017; Foster *et al.*, 2013; Jeol *et al.*, 2012). Such processes must have been more important for the amalgamation of Gondwana Supercontinent when fertile sediments continuously fed many of these accretionary systems. Such fertile sediments were in turn derived from the erosion of exposed Neoproterozoic or older continental and arc-related lithologies (Genade de Araujo *et al.*, 2014; Foster *et al.*, 2013; Melo *et al.*, 2017a, 2017b; Peixoto *et al.*, 2013; Richter *et al.*, 2015).

6 CONCLUSION

The lower crustal (25 – 30 km) Galiléia batholith, one of the largest (15,000 km²) granitic bodies in South America, records up to 80 Myrs of long-lived and uninterrupted granitic magmatism. The Galiléia and many other granitoids show that batholiths and plutons can be assembled over long times (>> 10 Myrs). There are no sufficient field, geochemical and isotopic evidence to call for MASH or DCH zones. Instead, whole rock geochemistry, zircon MC/SF dates, trace elements and Hf isotopes indicate recycling of crustal source likely derived from the erosion of an on-going andesitic Rio Doce volcanic arc from which fertile eroded material was constantly dragged down and partially melted within the deepest parts (> 30 km) of an accretionary wedge. Likewise younger examples (e.g., Jiang *et al.*, 2016), Neoproterozoic accretionary prisms, fore- and back-arc basins intruded by vast and voluminous silicic magmatism were commonplaces for the stabilization and differentiation of the continental crust.

Acknowledgements

The authors wish to acknowledge funding from CNPq (401334/2012-0, 302058/2015-0, 402852/2012-5) and FAPEMIG (APQ03943, RPQ-0067-10-RDP 00063-10) grants and Edital UFOP Auxilio a pesquisador 2015. FN thanks Conselho Nacional de Desenvolvimento Científico e Tecnológico for the financial support (CNPq 164000/2013-5). G. Stevens gratefully acknowledges National Research Founding support through the SARChI programme. Microanalysis Laboratory of the Universidade Federal de Ouro Preto, a member of the Microscopy and Microanalysis Network of Minas Gerais State/Brazil/FAPEMIG is also thanked for its technical support during the cathodoluminescence imaging. FN is in debt with Coralie Siégel, Axel Gerdes and Joshua Davies for their priceless help in solving the Pb-loss problem of the Galiléia zircons. This paper benefited also from discussions with Samuel Bersan, Gulierme Gonçalves, Luca Ziberna and Marilane Gonzaga Melo. This scientific contribution is part of the first author's doctorate project.

References

- Annen C., Blundy J.D., Sparks R.S.J. 2006. The genesis of intermediate and silicic magmas in deep crustal hot zones. *Journal of Petrology*, **47**:505-539.
- Ashwal L.D., Tucker R.D., Zinner E.K. 1999. Slow cooling of deep crustal granulites and Pb-loss in zircon. *Geochimica et Cosmochimica Acta* **63**:2839–2851
- Bachmann O. & Bergantz G., 2008. The Magma Reservoirs That Feed Supereruptions. *Elements*, **4**:17–21.
- Barboni M., Boehnke P., Schmitt A.K., Harrison T.M., Shane P., Bouvier A.-S., Baumgartner L., 2016. Warm storage for arc magmas. *Proceedings of Natural Academy of Science*, **113**:13959–13964
- Barboni M., Schoene B., Ovtcharova M., Bussy F., Schaltegger U., Gerdes A. 2013. Timing of incremental pluton construction and magmatic activity in a back-arc basin setting revealed by ID-TIMS U/Pb and Hf isotopes on complex zircon grains. *Chemical Geology*, **340**:76-93
- Barker F., Farmer G.L., Ayuso R.A., Plafker G., Lull, J.S., 1992. The 50 Ma granodiorite of the eastern Gulf of Alaska: Melting in an accretionary prism in the forearc. *Journal of Geophysical Research*, **97**:6757
- Black L.P., Kamo S.L., Allen C.M., Aleinikoff J.N., Davis D.W., Korsch R.J., Foudoulis C., 2003. TEMORA 1: A new zircon standard for Phanerozoic U-Pb geochronology. *Chemical Geology*, **200**:155–170
- Burgisser A. & Bergantz G.W., 2011. A rapid mechanism to remobilize and homogenize highly crystalline magma bodies. *Nature*, **471**:212–215.
- Cai K., Sun M., Yuan C., Zhao G., Xiao W., Long X., Wu F. 2011. Prolonged magmatism, juvenile nature and tectonic evolution of the Chinese Altai, NW China: evidence from zircon U-Pb and Hf isotopic study of Paleozoic granitoids. *Journal of Asian Earth Science*, **42**:949-968
- Cashman K. V., Sparks R.S.J., Blundy J.D. 2017. Vertically extensive and unstable magmatic systems: A unified view of igneous processes. *Science*, **80**:355
- Chelle-Michou C., Chiaradia M., Ovtcharova M., Ulianov A., Wotzlaw J.-F. 2014. Zircon petrochronology reveals the temporal link between porphyry systems and the magmatic evolution of their hidden plutonic roots (the Eocene Corocohuayco deposit, Peru). *Lithos*, **198–199**:129–140

Clemens J.D., Buick I.S., Kisters A.F.M., Frei D. 2017a. Petrogenesis of the granitic Donkerhuk batholith in the Damara Belt of Namibia: protracted, syntectonic, short-range, crustal magma transfer. *Contribution to Mineralogy and Petrology*, **172**:50

Clemens J.D., Elburg M.A., Harris C. 2017b. Origins of igneous microgranular enclaves in granites: the example of Central Victoria, Australia. *Contributions to Mineralogy and Petrology*, **172**:88

Clemens J.D. & Stevens G. 2016. Melt segregation and magma injections during crustal melting: Breaking out of the matrix. *Earth-Science Reviews*, **160**:333-349

Clemens J.D., Stevens G., Farina F. 2011. The enigmatic sources of I-type granites: the peritectic connexion. *Lithos*, **126**:174-181.

Coleman D.S., Gray W., Glazner A.F. 2004. Rethinking the emplacement and evolution of zoned plutons: Geochronologic evidence for incremental assembly of the Tuolumne Intrusive Suite, California. *Geology*, **32**:433-436

Cooper K.M. 2017. What does a magma reservoir look like? The “crystal’s-eye” view. *Elements*, **13**:23–28.

Cooper K.M. & Kent A.J.R., 2014. Rapid remobilization of magmatic crystals kept in cold storage. *Nature*, **506**:480-483

Deering C.D., Keller B., Schoene B., Bachmann O., Beane R., Ovtcharova M. 2016. Zircon record of the plutonic-volcanic connection and protracted rhyolite melt evolution. *Geology*, **44**: 267–270

Degler R., Pedrosa-Soares A., Dussin I., Queiroga G., Schulz B. 2017. Contrasting provenance and timing of metamorphism from paragneisses of the Araçuaí-Ribeira orogenic system, Brazil: Hints for Western Gondwana assembly. *Gondwana Research*, **51**:30–50

Farina F., Dini A., Innocenti F., Rocchi S., Westerman D.S. 2010. Rapid incremental assembly of the Monte Capanne pluton (Elba Island, Tuscany) by downward stacking of magma sheets. *Geological Society of American Bulletin*, **122**:1463–1479.

Farina F., Stevens G., Dini A., Rocchi S. 2012. Peritectic phase entrainment and magma mixing in the late Miocene Elba Island laccolith-pluton-dyke complex (Italy). *Lithos*, **153**:243–260

Farris D.W. 2010. Tectonic and petrologic evolution of the Kodiak batholith and the trenchward belt, Kodiak Island, AK: Contact fault juxtaposition? *Journal of Geophysical Research Solid Earth*, **115**:1–29

Fiannacca P., Williams I.S., Cirrincione R. 2017. Timescales and mechanisms of batholith construction: Constraints from zircon oxygen isotopes and geochronology of the late Variscan Serre Batholith (Calabria, southern Italy). *Lithos*, **277**:302–314.

Foster D. & Goscombe B., 2013. Continental Growth and Recycling in Convergent Orogens with Large Turbidite Fans on Oceanic Crust. *Geosciences*, **3**:354–388

Ganade de Araujo C.E., Rubatto D., Hermann J., Cordani U.G., Caby R., Basei M.A.S. 2014. Ediacaran 2,500-km-long synchronous deep continental subduction in the West Gondwana Orogen. *Nature Communications*, **5**:5198

Glazner A.F. 2007. Thermal limitations on incorporation of wall rocks into magma. *Geology*, **35**:319-322.

Gonçalves L., Alkmim F.F., Pedrosa-Soares A., Gonçalves C.C., Vieira V. 2018: From the plutonic root to the volcanic roof of a continental magmatic arc: a review of the Neoproterozoic Araçuaí orogen, southeastern Brazil. *International Journal of Earth Science*, **107**:337-358

Gonçalves L.E., Alkmim F.F., Pedrosa-Soares C.A., Dussin I.A., Valeriano, C.d.M., Nalini Jr.H.A. Lana C., Tedeschi M. 2016. Granites of the intracontinental termination of a magmatic arc: an example from the Ediacaran Araçuaí orogen, southeastern Brazil. *Gondwana Research*, **36**:439-458

Gonçalves L.E., Farina F., Lana C., Pedrosa-Soares C.A., Alkmim F.F., Nalini Jr.H.A. 2014. New U-Pb ages and lithochemical attributes of the Ediacaran Rio Doce Magmatic Arc, Araçuaí confined orogen, southeastern Brazil. *Journal of South American Earth Sciences*, **52**:1-20.

Huber C., Bachmann O., Manga M. 2009. Homogenization processes in silicic magma chambers by stirring and mushification (latent heat buffering). *Earth and Planetary Science Letters*, **283**:38–47

Jeon H., Williams I.S., Chappell B.W. 2012. Magma to mud to magma: Rapid crustal recycling by Permian granite magmatism near the eastern Gondwana margin. *Earth and Planetary Science Letters*, **319–320**:104–117.

Jiang Y.D., Schulmann K., Sun M., Štípská P., Guy A., Janoušek V., Lexa O., Yuan C. 2016. Anatexis of accretionary wedge, Pacific-type magmatism, and formation of vertically stratified continental crust in the Altai Orogenic Belt. *Tectonics*, **35**:3095–3118

Karakas O., Degruyter W., Bachmann O., Dufek J. 2017. Lifetime and size of shallow magma bodies controlled by crustal-scale magmatism. *Nature Geoscience*, **10**:446–450

Kent A.J.R. & Cooper K.M. 2018. How well do zircons record the thermal evolution of magmatic systems? *Geology*, **46**:1–4

Lana C., Farina F., Gerdes A., Alkmim A., Gonçalves G.O. Jardim A.C. 2017. Characterization of zircon reference materials via high precision U–Pb LA-MC-ICP-MS. *Journal of Analytical Atomic Spectrometry*, **32**:2011–2023.

Leuthold J., Müntener O., Baumgartner L.P., Putlitz B., Ovtcharova M., Schaltegger U. 2012. Time resolved construction of a bimodal laccolith (Torres del Paine, Patagonia). *Earth and Planetary Science Letters*, **325-326**:85-92

Lipman P.W. & Bachmann O. 2015. Ignimbrites to batholiths: Integrating perspectives from geological, geophysical, and geochronological data. *Geosphere*, **11**:705–743

Ludwig K.R. 2003 *Isoplot/EX Version 3.00: A Geochronological Toolkit for Microsoft Excel*. Berkeley Geochronology Center, Berkeley, CA.

McDonouht W.F. & Suns S.S. 1995. The composition of the Earth. *Chemical Geology*, **67**:1050-1056

Melo M.G., Lana C., Stevens G., Pedrosa-Soares A.C., Gerdes A., Alkmim L.A., Nalini Jr. H.A., Alkmim F.F. 2017b. Assessing the isotopic evolution of S-type granites in the Carols Chagas Batholith: clues from U-Pb, Hf isotopes, Ti geothermometry and trace element composition of zircon. *Lithos*, **284-284**:730-750

Melo M.G., Stevens G., Lana., Pderosa-Soares A.C., Frei D., Alkmim F.F., Alkmin L.A. 2017a. Two cryptic anatectic events within the syn-collisional granitoid from the Araçuaí orogen (southeastern Brazil): Evidence from the polymetamorphic Carlos Chagas batholith. *Lithos*, **277**:51-71

Mondou M., Egydio-Silva M., Vauchez A., Raposo M.I.B., Bruiguiet O., Oliveira A.F. 2012. Complex, 3D strain patterns in a synkinematic tonalite batholith from the Araçuaí Neoproterozoic orogen (Eastern Brazil): Evidence from combined magnetic and isotopic chronology studies. *Journal of Structural Geology*, **39**:158-179.

Nalini Jr.H.A. 1997. *Caractérisation des suites magmatiques néoprotérozoïques de la région de Conselheiro Pena et Galiléia (Minas Gerais, Brésil): étude géochimique et structurale des suites Galiléia et Urucum et leur relation avec les pegmatites à éléments rares associées*. These Docteur, Ecole Nationale Supérieure des Mines de Paris, pp. 237

Narduzzi F., Farina F., Stevens G., Lana C., Nalini H.A. 2017. Magmatic garnet in the Cordilleran-type Galiléia granitoids of the Araçuaí belt (Brazil): Evidence for crystallization in the lower crust. *Lithos*, **282–283**:82–97.

Novo T.A. 2013. *Caracterização do Complexo Pocrane, Magmatismo Básico Mesoproterozóico e Unidades Neoproterozóicas do Sistema Araçuaí-Ribeira, com ênfase em Geocronologia U-Pb (SHRIMP e LA-ICP-MS)*. Ph.D Thesis. UFMG, Belo Horizonte, Brazil, pp. 193.

Pedrosa-Soares A.C., De Campos C., Noce C.M., Silva L.C., Novo T., Roncato J., Medeiros S., Castañeda C., Queiroga G., Dantas E., Dussin I., Alkmim F.F. 2011. Late Neoproterozoic–Cambrian granitic magmatism in the Araçuaí Orogen (Brazil), the Eastern Brazilian Pegmatite Province and related mineral resources. *Geological Society London Special Publications*, **350**:25–51.

Peixoto E., Pedrosa-Soares A.C., Alkmim F.F., Dussin I.A. 2013. A suture-related accretionary wedge formed in the Neoproterozoic Araçuaí orogen (SE Brazil) during Western Gondwanaland assembly. *Gondwana Research*, **27**:878–896

Peixoto, E., Alkmim, F.F., Pedrosa-Soares, A., Lana, C., Chaves, A.O., 2017. Metamorphic record of collision and collapse in the Ediacaran-Cambrian Araçuaí orogen, SE-Brazil: Insights from P-T pseudosections and monazite dating. *Journal of Metamorphic Geology*, DOI: 10.1111/jmg.12287

Petitgirard S., Vauchez A., Egydio-Silva M., Bruguier O., Campos P., Monié P., Babinski M., Mondou M. 2009. Conflicting structural and geochronological data from the Ibituruna quartz-syenite (SE Brazil): effect of protracted “hot” orogeny and slow cooling rate? *Tectonophysics*, **477**:174–196.

Richter F., Lana, C, Stevens G., Buick I., Pedrosa-Soares A.C., Alkmim F.F., Cutts K. 2015. Sedimentation, metamorphism and granite generation in a back-arc region: Records from the Ediacaran Nova Venécia Complex (Araçuaí Orogen, Southeastern Brazil). *Precambrian Research*, **272**:78–100

Romano R., Lana C., Alkmim F.F., Stevens G., Armstrong R. 2013. Stabilization of the southern portion of the São Francisco craton, SE Brazil, through a long-lived period of potassic magmatism. *Precambrian Research*, **224**:143–159.

Rubin A.E., Cooper K.M., Till C.B., Kent A.J.R., Costa F., Bose M., Gravley D., Deering C., Cole J., 2017. Rapid cooling and cold storage in a silicic magma reservoir recorded in individual crystals. *Science*, **356**:1154–1156.

Samperton K.M., Schoene B., Cottle J.M., Brenhin Keller C., Crowley J.L., Schmitz M.D. 2015. Magma emplacement, differentiation and cooling in the middle crust: Integrated zircon geochronological–geochemical constraints from the Bergell Intrusion, Central Alps. *Chemical Geology*, **417**:322–340

Santos M.M., Lana C., Scholz R., Buick I., Schmitz M.D., Kamo S.L., Gerdes A., Corfu F., Tapster S., Lancaster P., Storey C.D., Basei M.A.S., Tohver E., Alkmim A., Nalini H., Krambrock K., Fantini C., Wiedenbeck M., 2017. A New Appraisal of Sri Lankan BB Zircon as a Reference Material for LA-ICP-MS U-Pb Geochronology and Lu-Hf Isotope Tracing. *Geostandard. Geoanalytical Research*, **41**:335–358

Schaltegger U., Brack P., Ovtcharova M., Peytcheva I., Schoene B., Stracke A., Marocchi M., Bargossi G.M. 2009. Zircon and titanite recording 1.5 million years of magma accretion, crystallization and initial cooling in a composite pluton (southern Adamello batholith, northern Italy). *Earth and Planetary Science Letters*, **286**:208–218.

Schoene B. & Bowring S.A. 2010. Rates and mechanism of Mesozoic magmatic arc construction, eastern Kaapvaal craton, Swaziland. *Geological Society of American Bulletin*, **122**:408-429

Schoene B., Schaltegger U., Brack P., Latkoczy C., Stracke A., Günther D., 2012. Rates of magma differentiation and emplacement in a ballooning pluton recorded by U-Pb TIMS-TEA, Adamello batholith, Italy. *Earth and Planetary Science Letters*, **355–356**:162–173

Schannor M., Lana C., Fonseca M.A., 2018. São Francisco – Congo craton break-up delimited by U-Pb-Hf isotopes and trace-elements of zircon from metasediments of the Araçuaí belt. *Geoscience Frontiers*, DOI: 10.1016/j.gsf.2018.02.011.

Sharkov E.V., 2010. Middle-proterozoic anorthosite-rapakivi granite complexes: an example of within-plate magmatism in abnormally thick crust: evidence from east European Craton. *Precambrian Research*, **183**:689-700

Sláma J., Košler J., Condon D.J., Crowley J.L., Gerdes A., Hancher J.M., Horstwood M.S.A., Morris G.A., Nasdala L., Norberg N., Schaltegger U., Schoene B., Tubrett M.N.,

Whitehouse M.J., 2008. Plešovice zircon - A new natural reference material for U-Pb and Hf isotopic microanalysis. *Chemical Geology*, **249**:1–35

Tedeschi M., Novo T., Pedrosa-Soares A.C., Dussin I., Tassinari C., Silva L.C., Gonçalves L., Alkmim F.F., Lana C., Figueiredo C., Dantas E., Medeiros S., De Campos C., Corrales F., Heilbron M. 2016. The Ediacaran Rio Doce magmatic arc revisited (Araçuaí-Ribeira orogenic system, SE Brazil). *Journal of South American Earth Science*, **68**:167-186

Trail D., Bruce Watson E., Tailby N.D., 2012. Ce and Eu anomalies in zircon as proxies for the oxidation state of magmas. *Geochimica et Cosmochimica Acta*, **97**:70–87

Van Achterbergh E., Ryan C.G., Jackson S.E., Griffin W.L., 2001. Data reduction software for LA-ICP-MS: appendix. In: Sylvester, P.J. (Ed.), *Laser Ablation-ICP Mass Spectrometry in the Earth Sciences: Principles and Applications*, vol. 29. *Mineralogical Association of Canada (MAC) Short Course Series*, Ottawa, Ontario, Canada, pp. 239–243.

Vauchez A., Egydio-Silva M., Babinski M., Tommasi A., Uhlein A., Liu D. 2007. Deformation of a pervasively molten middle crust: insights from the Neoproterozoic Ribeira-Araçuaí orogen (SE Brazil). *Terra Nova*, **19**:278-286.

Vermeesch P., 2012. On the visualisation of detrital age distributions. *Chemical Geology*, **312–313**:190–194.

Vieira V.S. 2007. *Significado do Grupo Rio Doce no Contexto do Orógeno Araçuaí*. Ph.D Thesis. IGC-UFMG, Belo Horizonte, Brasil, pp. 117.

Wang Y., Liu D., Dong C., Liu S., Wang S., Yang E. 2011. U–Th–Pb behavior of zircons under high-grade metamorphic conditions: A case study of zircon dating of meta-diorite near Qixia, eastern Shandong. *Geoscience Frontiers*, **2**:137–146.

CHAPTER 6

CONCLUSIONS

6.1 GENESIS AND EVOLUTION OF A NEOPROTEROZOIC MAGMATIC ARC: THE CORDILLERAN-TYPE GRANITOIDS OF THE ARAÇUAÍ BELT, BRAZIL

1. The large Galiléia batholith (ca. 15,000 km²) outcropping in the central part of the Araçuaí orogen (SE Brazil), is a metaluminous to slightly metaluminous (ASI = 0.97–1.07) Neoproterozoic (ca. 632–550 Ma; Pedrosa-Soares *et al.*, 2011; Mondou *et al.*, 2012) weakly foliated calc-alkaline granitoid body characterized by the widespread occurrence of grossular-rich magmatic garnet and magmatic epidote (Narduzzi *et al.*, 2017).
2. Field, petrographic and mineral chemical evidence indicate that garnet, epidote, biotite and white mica (low-Si phengite) are magmatic (Narduzzi *et al.*, 2017).
3. Comparison with experimental (Alonso-Perez *et al.*, 2009; Green 1992) and natural data (Bach *et al.*, 2012; Barnes & Allen, 2006; Day *et al.*, 1992; Dawes & Evans, 1991; Harangi *et al.*, 2001) indicate that the uncommon magmatic garnet+epidote±white mica assemblage in the Galiléia granitoids (Narduzzi *et al.*, 2017) is consistent with granitic magma crystallization at pressures greater than 0.8 GPa (above 25 km depth)
4. This suggest that the that the Galiléia batholith was assembled in the lower crust during the accretionary/collisional stages of the Neoproterozoic Brasiliano Orogeny (Pedrosa-Soares *et al.*, 2011; Narduzzi *et al.*, 2017)
5. All the granitic samples collected from the central part of the Galiléia batholith together with previously published data, record extreme variability in U-Pb zircon magmatic ages from ca. 630 to 555 Ma, indicating a long-lived and uninterrupted injection of magmas (80 Myrs) during the assembling of this batholith.
6. Trace element geochemistry and Hf isotopes from the igneous zircons points to an open-system crystallization, rather than a simple cooling following fractional crystallization at the level of magma emplacement. Moreover these data point towards a rather similar composition between the various batches of melts that constructed the body.
7. Unradiogenic ¹⁷⁶Hf/¹⁷⁷Hf and ¹⁴³Nd/¹⁴⁴Nd isotope chemistry of the Galiléia samples indicate strong crustal recycling without the involvement of mantle-derived magmas.
8. These textural, geochronological and isotopic data are more akin to younger and older granitic plutons assembled within accretionary settings (Clemens *et al.*, 2017; Farris, 2010; Jiang *et al.*, 2016).

9. It is proposed that the giant Galiléia batholith was assembled in an accretionary prism during the Brasiliano Orogeny (Narduzzi et al., 2017).
10. During the Brasiliano/Pan-African Orogeny, accretionary prism / fore- and back–arc settings probably represented important geological areas of voluminous silicic magma production, continental crust differentiation and stabilization (e.g. Foster & Goscombe 2013).

References

Alonso-Perez R., Müntener O., Ulmer P. 2009. Igneous garnet and amphibole fractionation in the roots of island arcs: experimental constraints on andesitic liquids. *Contribution to Mineralogy and Petrology*, **57**:541-558

Bach P., Smith I.E.M. Malpas J.G. 2012. The Origin of Garnets in Andesitic Rocks from the Northland Arc, New Zealand, and their Implication for Sub-arc Processes. *Journal of Petrology*, **53**:1169-1195.

Barnes C.G. & Allen C.M. 2006. Depth of origin of late Middle Jurassic garnet andesite, Southern Klamath Mountains, California. In: Snoke AW, Barends CG (eds) Geological studies in the Klamath Mountains Province, California and Oregon. *Geological Society of American Special Paper*, **410**:269-286

Clemens J.D., Buick I.S., Kisters A.F.M., Frei D. 2017. Petrogenesis of the granitic Donkerhuk batholith in the Damara Belt of Namibia: protracted, syntectonic, short-range, crustal magma transfer. *Contribution to Mineralogy and Petrology*, **172**:50

Dawes R.L. & Evans B.W., 1991. Mineralogy and geothermobarometry of magmatic epidote-bearing dyke, Front Range, Colorado. *Geological Society of American Bulletin*, **103**:1017-1031

Day RA, Green T.H., Smith I.E.M. 1992. The origin and significance of garnet phenocrysts and garnet-bearing xenoliths in Miocene calc-alkaline volcanics from Northland, New Zealand. *Journal of Petrology*, **33**:125-161

Farris D.W. 2010. Tectonic and petrologic evolution of the Kodiak batholith and the trenchward belt, Kodiak Island, AK: Contact fault juxtaposition? *Journal of Geophysical Research - Solid Earth*, **115**:1–29

Foster D. & Goscombe B., 2013. Continental Growth and Recycling in Convergent Orogens with Large Turbidite Fans on Oceanic Crust. *Geosciences*, **3**:354–388

Green T.H. 1992. Experimental phase equilibrium studies of garnet-bearing I-type volcanics and high-level intrusive from Northland, New Zealand. *Transactions of the Royal Society of Edinburgh: Earth Sciences*, **83**:429-438.

Harangi S.Z., Downes H., Kósa L., Szabo C.S., Thirlwall M.F., Mason P.R.D., Matthey D. 2001. Almandine Garnet in Calc-alkaline Volcanic Rocks of the Northern Pannonian Basin

(Eastern-Central Europe): Geochemistry and Geodynamic Implications. *Journal of Petrology*, **42**:1813-1843.

Jiang Y.D., Schulmann K., Sun M., Štípská P., Guy A., Janoušek V., Lexa O., Yuan C. 2016. Anatexis of accretionary wedge, Pacific-type magmatism, and formation of vertically stratified continental crust in the Altai Orogenic Belt. *Tectonics*, **35**:3095–3118

Mondou M., Egydio-Silva M., Vauchez A., Raposo M.I.B., Bruiguiet O., Oliveira A.F. 2012. Complex, 3D strain patterns in a synkinematic tonalite batholith from the Araçuaí Neoproterozoic orogen (Eastern Brazil): Evidence from combined magnetic and isotopic chronology studies. *Journal of Structural Geology*, **39**:158-179.

Narduzzi F., Farina F., Stevens G., Lana C., Nalini H.A. 2017. Magmatic garnet in the Cordilleran-type Galiléia granitoids of the Araçuaí belt (Brazil): Evidence for crystallization in the lower crust. *Lithos*, **282–283**:82–97.

Pedrosa-Soares A.C., De Campos C., Noce C.M., Silva L.C., Novo T., Roncato J., Medeiros S., Castañeda C., Queiroga G., Dantas E., Dussin I., Alkmim F.F. 2011. Late Neoproterozoic–Cambrian granitic magmatism in the Araçuaí Orogen (Brazil), the Eastern Brazilian Pegmatite Province and related mineral resources. *Geological Society London Special Publications*, **350**:25-51.

APPENDICES

APPENDIX A

Supplementary material of the manuscript presented in the chapter 4

A1: Mineral chemistry

For this study mineral chemistry analyses have been performed using using a Leo® 1430VP Scanning Electron Microscope at the Department of Earth Sciences, Stellenbosch University, South Africa. Thin sections were sputter-coated with carbon before imaging and analyses. Textures were studied in backscattered electron (BSE) mode and mineral compositions quantified by EDX (Energy Dispersive X-ray) analysis using an Oxford Instruments ® 133 keV ED X-ray detector and Oxford INCA software. During the quantitative analyses, beam conditions were 20 KV accelerating voltage and 1.5 A probe current, with a working distance of 8.5 mm. Specimen beam current of -20.0 nA. X-ray counts were typically ~7000 cps with counting time at 50s live-time. Analyses were quantified using natural mineral standards. Especially for garnets with high MnO, Rhodonite was chosen for normalization. Mineral chemical compositions were recalculated to mineral stoichiometries to obtain mineral structural formulae. Equation of Droop (1987) was used for the estimative of Fe³⁺ concentration.

A2: XRF analyses

A total of 40 samples were collected during different sampling activities; ca. 10 kg were collected for each sample and ca. 5 kg for each of 16 samples selected for this study were reduced in powder for whole-rock chemistry analysis. Analyses were performed at the Department of Earth Sciences, Stellenbosch University, South Africa. Calculation of the loss on ignition was done by placing powdered samples in an oven at 1000°C for 1 hour. Major element compositions were analysed by X-ray fluorescence spectrometry (XRF) on glass beads prepared with La-free flux. The internal standards were basalt BHVO-1 and granite NIM-G. For the granite, calculated uncertainties (twice the measured deviations for the granite standard expressed in wt.%) are: 0.35 for SiO₂, 0.02 for TiO₂, 0.12 for Al₂O₃, 0.15 for FeO_{Tot}, 0.01 for MnO, 0.02 for MgO, 0.07 for CaO, 0.10 for Na₂O, 0.02 for K₂O and 0.01 for P₂O₅. Results are plotted after normalization to 100 wt.% volatile-free. The same fused beads used for major element determination were used to obtain trace element compositions by applying the method described by Eggins (2003) and analysed using an Agilent 7500 ICP-MS coupled with a Nd-YAG 223 nm New Wave LASER ablation (LA) system operating at a 12 Hz frequency with a mixed He-Ar carrier gas. Three analyses (each comprising a 30 s blank followed by data collection for 60 s) on each whole rock fused disc were obtained using a 100 µm diameter aperture, and the results averaged. After every three samples (i.e. every 10th analysis)

NIST612 (Pearce *et al.* 1997) glass bead was analysed as a calibration standard, in addition to fused discs of NIM-G (granite) and BHVO-1 (basalt) that were analysed as secondary standards. Data were collected in time-resolved mode and were reduced using the SiO₂ content measured by XRF as the internal standard. For each element, the reproducibility of replicate analyses of the samples, and deviation from the certified values of the secondary standards are less than 10%, and mostly less than 5 % relative.

A3: OSM2 - Garnet major element profile

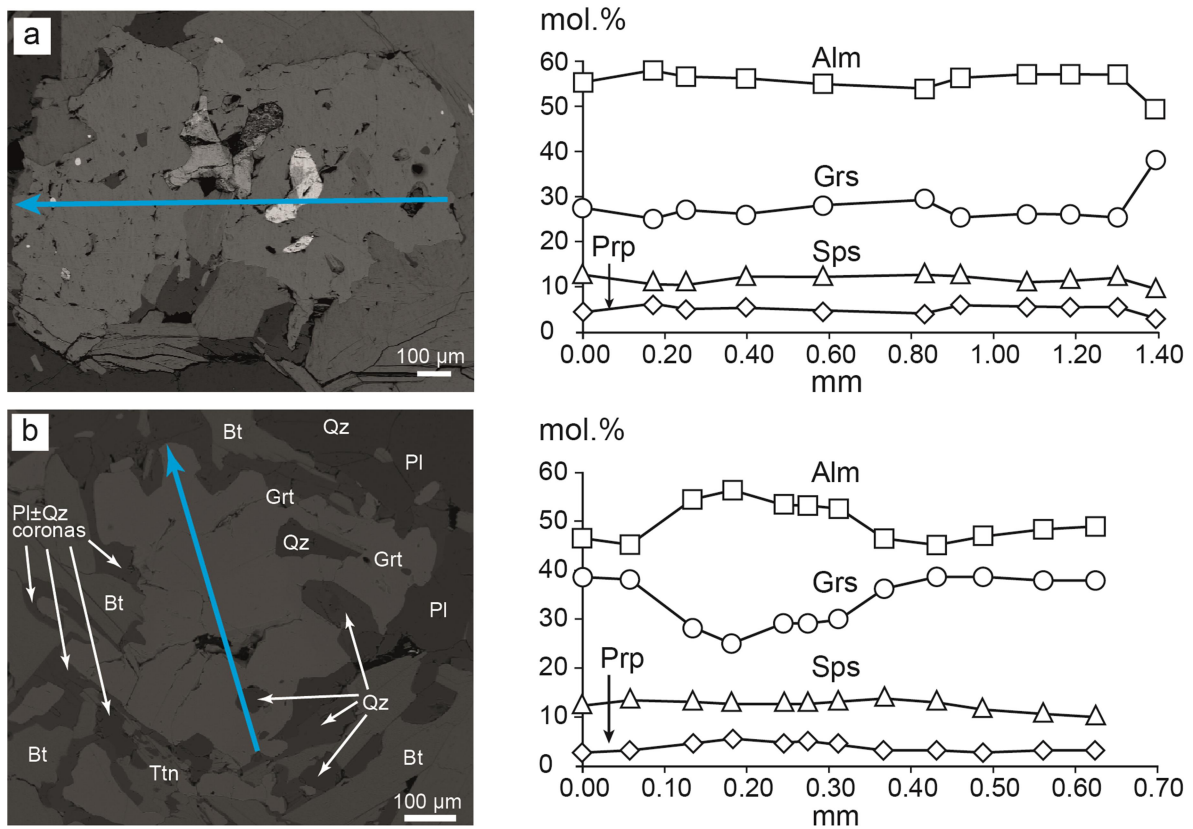


Figure 1: major element profiles for the other garnets in Bt+Grt-bearing granitoids showing: (a) flat profiles and (b) grossular reverse bell-shaped. In (a) the garnet is the same of Fig. 5.5a.

References

Droop G.R.T. 1987. A general equation for estimating Fe³⁺ concentrations in ferromagnesian silicates and oxides from microprobe analyses, using stoichiometric criteria. *Mineralogical Magazine*, **51**:431-435.

Eggins S. 2003. Laser Ablation ICP-MS analysis of geological materials prepared as lithium borate glasses. *Geostandard and Geoanalytical Research*, **27**:147-162.

Pearce N.J.G., Perkins W.T., Westgate J.A., Gorton M.P., Jackson S.E., Meal C.R., Chenery S.P. 1997. A compilation of new and published major and trace element data for NIST SRM 610 and NIST SRM 612 glass reference materials. *Geostandards Newsletters*, **21**:115-144.

Table OSM1: Major element traverses on Galiléia garnets; analyses were done from rim to rim; (1) major elements are reported in wt.%; (2) bdl: below detection limit; (3) Mg# = $Mg/(Mg+Fe^{2+})$

Sample No.	FSV3 – tonalite – Bt+Grt - grt1													
mm	0.00	0.12	0.18	0.32	0.38	0.51	0.59	0.64	0.71	0.75	0.80	0.91	0.96	1.03
SiO ₂ ⁽¹⁾	38.10	38.13	37.46	37.83	37.57	37.93	37.80	37.98	38.01	37.90	37.07	37.18	37.93	37.64
TiO ₂	bdl ⁽²⁾	bdl	bdl	bdl	bdl	bdl	bdl	bdl	bdl	bdl	bdl	bdl	bdl	bdl
Al ₂ O ₃	21.28	21.44	21.47	21.27	21.37	21.49	21.57	21.15	21.60	21.50	20.99	21.00	21.39	21.32
FeO _{Tot}	22.16	21.31	22.80	23.58	26.08	26.07	26.09	25.89	25.98	26.05	25.69	25.93	26.98	25.86
MnO	5.01	5.57	5.44	5.56	5.33	5.21	5.19	5.38	5.18	5.08	4.85	4.75	5.04	5.93
MgO	0.77	0.71	0.82	1.13	1.50	1.67	1.56	1.74	1.57	1.72	1.73	1.66	1.64	1.27
CaO	13.63	14.21	12.07	11.46	8.80	8.90	8.85	9.14	9.00	9.06	8.84	8.58	8.70	9.00
Total	100.95	101.37	100.06	100.81	100.66	101.28	101.05	101.27	101.33	101.32	99.18	99.10	101.68	101.02
Mg# ⁽³⁾	0.06	0.06	0.06	0.08	0.09	0.10	0.10	0.11	0.10	0.11	0.11	0.10	0.10	0.08
Alm	48.10	45.91	50.40	51.38	57.40	57.00	57.40	56.10	57.03	56.79	57.06	58.03	58.46	56.63
Prp	2.98	2.72	3.23	4.37	5.90	6.52	6.11	6.71	6.16	6.70	6.86	6.61	6.35	4.94
Grs	37.91	39.22	34.18	31.99	24.82	24.94	24.93	25.39	25.31	25.29	25.16	24.59	24.15	25.27
Sps	11.01	12.16	12.18	12.26	11.87	11.54	11.56	11.80	11.51	11.22	10.92	10.76	11.05	13.16

Continuation Table OSM1

Sample No.	FSV3 – tonalite – Bt+Grt - grt2											
mm	0.00	0.06	0.13	0.18	0.24	0.27	0.31	0.37	0.43	0.49	0.56	0.62
SiO ₂	38.27	38.50	37.98	38.13	37.54	37.82	38.22	38.09	38.49	38.18	38.29	38.42
TiO ₂	bdl	bdl	bdl	bdl	bdl	bdl	bdl	bdl	bdl	bdl	bdl	bdl
Al ₂ O ₃	21.54	21.48	21.53	21.51	21.35	21.13	21.73	21.37	21.66	21.51	21.48	21.64
FeO _{Tot}	21.37	21.01	24.73	25.46	24.07	24.25	24.08	21.63	21.07	21.59	22.21	22.60
MnO	5.59	6.16	5.88	5.73	5.75	5.71	5.90	6.38	5.90	5.26	4.82	4.48
MgO	0.68	0.81	1.16	1.41	1.20	1.25	1.12	0.81	0.81	0.71	0.77	0.83
CaO	13.88	13.83	9.96	8.88	10.22	10.40	10.71	13.17	14.01	13.92	13.58	13.61
Total	101.32	101.79	101.24	101.13	100.13	100.57	101.76	101.44	101.95	101.17	101.14	101.59
Mg#	0.05	0.07	0.08	0.09	0.08	0.09	0.08	0.06	0.07	0.06	0.06	0.06
Alm	46.42	45.28	54.34	56.37	53.32	53.19	52.62	46.61	45.37	46.91	48.42	49.07
Prp	2.64	3.09	4.56	5.58	4.75	4.89	4.35	3.10	3.11	2.74	3.01	3.22
Grs	38.63	38.19	28.02	25.19	29.02	29.24	29.98	36.36	38.65	38.75	37.93	37.86
Sps	12.31	13.43	13.08	12.85	12.91	12.68	13.05	13.93	12.87	11.59	10.65	9.86

Sample No.	FSV3 – tonalite – Bt+Grt - grt3											
mm	0.00	0.17	0.25	0.40	0.58	0.83	0.92	1.08	1.19	1.30	1.39	
SiO ₂	37.44	38.19	38.37	38.01	37.89	37.57	37.67	37.56	37.80	38.07	38.65	
TiO ₂	bdl	bdl	bdl	bdl	bdl	bdl	bdl	bdl	bdl	bdl	bdl	
Al ₂ O ₃	20.94	21.45	21.57	21.24	21.45	21.29	21.09	21.25	21.50	21.13	21.59	
FeO _{Tot}	25.01	26.83	25.91	25.57	25.23	24.75	25.69	26.18	26.15	26.10	22.69	
MnO	5.66	4.84	5.09	5.52	5.54	5.74	5.57	5.01	5.14	5.42	4.34	
MgO	1.12	1.63	1.31	1.36	1.23	1.06	1.52	1.45	1.42	1.43	0.79	
CaO	9.72	9.07	9.66	9.28	10.07	10.48	9.04	9.37	9.32	9.06	13.69	
Total	99.87	102.01	101.92	100.99	101.42	100.90	100.58	100.83	101.33	101.20	101.76	
Mg#	0.07	0.10	0.08	0.09	0.08	0.07	0.10	0.09	0.09	0.09	0.06	
Alm	55.35	58.01	56.59	56.22	54.92	53.95	56.31	57.09	57.06	57.05	49.28	
Prp	4.40	6.28	5.10	5.35	4.77	4.12	5.94	5.65	5.53	5.58	3.07	
Grs	27.56	25.12	27.04	26.15	28.10	29.26	25.38	26.19	26.05	25.38	38.10	
Sps	12.69	10.59	11.27	12.28	12.21	12.67	12.37	11.06	11.36	11.99	9.54	

Continuation Table OSM1

Sample No.	FGL6 – granodiorite – Bt+Amp+Grt															
mm	0.00	0.07	0.09	0.13	0.17	0.25	0.29	0.39	0.54	0.57	0.57	0.63	0.67	0.87	0.94	1.01
SiO ₂	37.69	37.77	37.73	37.82	37.87	37.76	37.71	37.94	37.17	36.50	38.12	38.59	38.29	38.63	37.85	38.80
TiO ₂	bdl	bdl	bdl	0.13	bdl	bdl	0.14	bdl	bdl	bdl	bdl	bdl	bdl	bdl	bdl	bdl
Al ₂ O ₃	21.05	21.13	20.97	20.89	21.21	20.98	21.12	20.93	20.71	20.44	21.09	21.68	21.27	21.56	21.39	21.58
FeO _{Tot}	19.87	19.92	19.83	19.72	19.92	19.53	19.75	19.89	18.93	19.67	20.06	20.22	19.65	20.10	20.29	19.51
MnO	7.28	7.28	7.16	7.28	7.15	7.27	7.18	6.96	7.10	7.38	7.37	7.17	7.12	7.22	7.25	7.86
MgO	0.76	0.86	0.87	0.88	0.97	0.94	0.75	0.79	0.72	0.91	0.82	0.93	0.88	0.82	0.86	0.73
CaO	13.50	13.56	13.43	13.38	13.41	13.51	13.89	13.66	13.51	13.49	13.67	13.99	13.65	13.79	13.61	13.55
Total	100.14	100.52	99.98	100.11	100.52	99.98	100.53	100.16	98.13	98.38	101.13	102.58	100.87	102.12	101.26	102.04
Mg#	0.07	0.08	0.08	0.08	0.08	0.08	0.07	0.07	0.06	0.09	0.07	0.08	0.07	0.07	0.08	0.06
Alm	43.30	43.11	43.26	43.05	43.23	42.58	42.79	43.39	42.34	42.72	43.14	42.96	42.78	43.19	43.54	42.29
Prp	2.95	3.32	3.40	3.42	3.74	3.63	2.91	3.06	2.86	3.51	3.15	3.50	3.43	3.15	3.30	2.83
Grs	37.68	37.62	37.52	37.42	37.31	37.73	38.55	38.18	38.71	37.54	37.66	38.10	38.09	37.95	37.40	37.63
Sps	16.06	15.96	15.82	16.11	15.72	16.06	15.75	15.37	16.08	16.24	16.06	15.43	15.71	15.71	15.76	17.25
Sample No.	FGL22 – granodiorite – Bt+Grt															
mm	0.00	0.41	0.83	1.54	2.62	2.95	3.55	3.93	4.39							
SiO ₂	38.07	37.99	37.71	37.47	37.64	37.68	37.41	37.55	37.38							
TiO ₂	bdl	bdl	bdl	bdl	0.13	bdl	0.20	bdl	0.19							
Al ₂ O ₃	21.64	21.82	21.19	21.11	21.32	21.28	20.92	21.32	21.28							
FeO _{Tot}	23.29	23.44	23.01	22.22	21.61	21.87	21.76	22.40	22.16							
MnO	4.74	5.39	5.73	6.24	6.61	6.31	6.12	5.70	5.32							
MgO	0.63	0.57	0.59	0.53	0.53	0.47	0.51	0.54	0.52							
CaO	12.80	12.59	12.01	12.16	12.58	12.67	12.75	12.64	12.84							
Total	101.17	101.79	100.25	99.74	100.42	100.27	99.66	100.15	99.69							
Mg#	0.05	0.04	0.04	0.04	0.04	0.04	0.04	0.04	0.04							
Alm	51.07	50.91	50.84	49.30	47.65	48.24	48.14	49.42	49.32							
Prp	2.44	2.19	2.32	2.10	2.07	1.87	2.01	2.14	2.07							
Grs	35.96	35.03	34.01	34.56	35.53	35.80	36.14	35.17	36.62							
Sps	10.53	11.86	12.83	14.03	14.76	14.09	13.71	12.74	11.99							

Continuation Table OSM1

Sample No.	FGL12 – granodiorite – Bt+Amp+Grt															
mm	0.00	0.21	0.31	0.40	0.52	0.64	0.72	0.83	0.97	1.04	1.13	1.24	1.33	1.40	1.45	1.51
SiO ₂	37.56	37.68	37.07	37.96	37.50	37.24	37.28	37.62	37.68	37.41	37.89	37.70	37.97	37.60	38.01	37.97
TiO ₂	bdl	0.18	bdl	bdl	0.20	bdl	bdl	0.16	0.17	bdl	0.13	0.40	bdl	0.17	bdl	0.18
Al ₂ O ₃	21.08	21.06	20.88	21.19	21.25	21.01	20.83	20.93	20.90	21.10	21.09	21.18	21.30	20.82	21.07	21.05
FeO _{Tot}	19.40	19.10	18.63	18.99	18.75	18.99	19.12	18.88	18.68	19.10	18.82	18.31	19.07	18.54	18.79	18.96
MnO	6.45	6.60	6.37	6.75	6.89	6.70	6.60	6.64	6.82	6.76	6.61	6.25	6.70	6.69	6.63	6.66
MgO	0.86	0.78	0.77	0.80	0.75	0.79	0.74	0.74	0.74	0.73	0.71	0.68	0.81	0.72	0.73	0.73
CaO	14.64	14.86	14.90	14.88	14.77	14.53	14.98	15.31	15.12	15.14	15.16	15.49	14.72	15.27	15.50	15.26
Total	99.99	100.27	98.63	100.57	100.12	99.25	99.55	100.27	100.11	100.24	100.40	100.02	100.57	99.80	100.72	100.82
Mg#	0.08	0.07	0.07	0.07	0.07	0.07	0.07	0.07	0.07	0.07	0.07	0.06	0.07	0.07	0.07	0.07
Alm	41.97	41.32	40.90	41.00	40.79	41.47	41.28	40.58	40.37	40.95	40.74	40.06	41.32	40.16	40.27	40.71
Prp	3.33	3.02	3.01	3.08	2.90	3.06	2.83	2.83	2.84	2.80	2.74	2.33	3.12	2.77	2.77	2.80
Grs	40.57	41.20	41.91	41.17	41.15	40.64	41.45	42.14	41.87	41.57	42.03	43.43	40.85	42.39	42.58	41.99
Sps	14.12	14.46	14.17	14.75	15.17	14.83	14.44	14.45	14.92	14.68	14.49	13.85	14.70	14.68	14.38	14.49

Sample No.	FGL12 – granodiorite – Bt+Amp+Grt (continued)									
mm	1.62	1.71	1.98	2.14	2.25	2.41	2.49	2.57	2.72	
SiO ₂	37.87	37.62	37.79	37.99	37.96	37.36	37.92	37.75	37.62	
TiO ₂	0.34	0.20	bdl	bdl	bdl	bdl	bdl	0.22	bdl	
Al ₂ O ₃	21.03	21.22	21.22	21.12	21.10	21.19	21.18	21.14	21.08	
FeO _{Tot}	19.05	18.71	18.98	19.61	19.30	19.40	19.51	19.33	19.73	
MnO	6.59	6.60	6.62	6.53	6.41	6.39	6.44	6.72	6.84	
MgO	0.77	0.79	0.84	0.96	0.86	0.87	0.80	0.96	0.83	
CaO	15.10	15.19	14.59	14.38	15.62	15.63	14.34	14.49	14.15	
Total	100.75	100.34	100.02	100.58	100.25	99.84	100.19	100.60	100.25	
Mg#	0.07	0.07	0.08	0.08	0.08	0.08	0.07	0.09	0.07	
Alm	41.02	40.44	41.39	42.31	41.90	42.03	42.58	41.65	42.66	
Prp	2.96	3.05	3.25	3.71	3.33	3.35	3.10	3.70	3.19	
Grs	41.66	42.06	40.75	39.73	40.68	40.60	40.09	39.99	39.18	
Sps	14.36	14.45	14.61	14.26	14.10	14.02	14.23	14.66	14.97	

Continuation Table OSM1

Sample No.	FGL15 – granodiorite – Bt+Grt															
mm	0.00	0.05	0.11	0.16	0.22	0.27	0.34	0.50	0.58	0.71	0.77	0.85	0.93	1.00	1.09	1.09
SiO ₂	38.53	38.40	38.23	38.05	38.32	38.57	38.71	38.54	38.12	38.57	38.72	38.92	38.92	38.24	38.52	38.55
TiO ₂	bdl	0.21	bdl	0.17	bdl	bdl	0.13	0.20	0.19	0.20	0.19	bdl	0.25	0.13	0.16	bdl
Al ₂ O ₃	21.54	21.66	21.27	21.71	21.63	21.64	21.90	21.46	21.41	21.84	21.63	21.72	21.53	21.65	22.05	21.73
FeO _{Tot}	20.51	19.74	19.39	19.24	19.36	19.39	19.38	18.51	18.29	18.67	18.92	19.73	19.07	19.47	20.09	19.89
MnO	6.78	6.71	7.20	7.42	7.56	7.89	7.89	8.14	7.89	8.17	8.23	7.61	7.77	7.39	7.19	7.08
MgO	0.71	0.56	0.62	0.54	0.65	0.53	0.61	0.57	0.58	0.59	0.50	0.67	0.63	0.69	0.58	0.58
CaO	12.90	13.08	12.98	12.96	12.92	12.73	13.03	13.01	12.90	12.80	12.63	12.71	12.93	12.79	12.54	12.51
Total	100.96	100.38	99.70	100.09	100.44	100.74	101.66	100.43	99.38	100.38	100.83	101.36	101.10	100.36	101.13	100.34
Mg#	0.06	0.05	0.05	0.05	0.05	0.05	0.05	0.05	0.05	0.05	0.05	0.06	0.06	0.06	0.05	0.05
Alm	45.42	44.52	43.65	43.40	43.28	43.43	42.92	41.66	41.72	42.07	42.67	43.94	42.74	43.68	45.17	45.07
Prp	2.79	2.35	2.50	2.18	2.57	2.12	2.39	2.27	2.36	2.37	2.03	2.65	2.52	2.77	2.32	2.36
Grs	36.59	37.80	37.42	37.46	37.02	36.55	36.99	37.51	37.70	36.93	36.51	36.25	37.11	36.76	36.14	36.31
Sps	15.20	15.33	16.42	16.95	17.12	17.90	17.69	18.56	18.22	18.63	18.80	17.16	17.62	16.80	16.37	16.26

Sample No.	FGL15 – granodiorite – Bt+Grt (continued)													
mm	1.19	1.29	1.38	1.45	1.49	1.56	1.60	1.68	1.76	1.82	1.87	1.92	1.95	1.99
SiO ₂	38.52	38.36	38.52	38.71	38.51	38.55	39.02	38.73	38.80	38.86	38.34	39.22	39.20	38.89
TiO ₂	0.13	bdl	0.21	bdl	bdl	bdl	bdl	bdl	bdl	bdl	bdl	bdl	bdl	bdl
Al ₂ O ₃	21.61	21.89	21.59	21.73	21.60	21.94	21.92	21.94	21.99	21.70	21.53	21.85	22.02	21.67
FeO _{Tot}	19.88	20.54	20.80	20.82	20.56	19.99	20.16	20.41	20.42	20.89	21.08	21.37	21.67	20.91
MnO	7.42	6.61	6.45	6.00	6.43	6.83	6.68	6.35	6.01	5.76	5.51	5.13	4.79	4.10
MgO	0.69	0.71	0.63	0.77	0.67	0.71	0.68	0.60	0.68	0.74	0.74	0.73	0.71	0.85
CaO	12.26	12.46	12.71	13.14	12.82	12.50	12.91	12.91	12.93	12.91	13.12	13.22	13.33	13.88
Total	100.49	100.58	100.90	101.16	100.58	100.52	101.37	100.94	100.84	100.87	100.33	101.51	101.71	100.29
Mg#	0.06	0.06	0.05	0.06	0.05	0.06	0.06	0.05	0.06	0.06	0.06	0.06	0.06	0.07
Alm	44.84	46.18	46.49	46.16	46.00	45.23	45.13	45.92	46.11	46.85	47.05	47.71	48.30	47.14
Prp	2.76	2.86	2.50	3.05	2.66	2.86	2.70	2.41	2.74	2.95	2.95	2.89	2.84	3.42
Grs	35.45	35.90	36.40	37.32	36.76	36.25	37.03	37.20	37.41	37.11	37.54	37.81	38.06	40.09
Sps	16.95	15.06	14.61	13.47	14.58	15.66	15.14	14.47	13.74	13.09	12.47	11.60	10.81	9.36

Continuation Table OSM1

Sample No.	FGL16 – enclave															
mm	0.00	0.06	0.10	0.18	0.22	0.29	0.34	0.40	0.55	0.84	1.08	1.42	1.85	2.24	2.52	2.65
SiO ₂	38.50	38.25	38.42	38.09	38.00	38.20	38.19	38.17	37.58	38.52	38.64	38.28	38.25	37.62	38.14	37.66
TiO ₂	0.14	bdl	bdl	bdl	bdl	bdl	0.19	bdl	bdl	bdl	0.16	0.14	bdl	0.22	bdl	0.21
Al ₂ O ₃	21.46	21.30	21.43	21.44	21.31	21.43	21.62	21.73	21.33	21.62	22.40	21.45	21.39	21.35	21.52	21.12
FeO _{Tot}	20.65	20.92	20.45	20.46	20.73	20.34	19.93	20.65	19.82	20.25	19.84	19.69	19.02	18.70	18.76	18.46
MnO	4.29	4.59	4.79	4.82	4.90	5.32	5.22	5.76	5.98	6.60	6.70	6.76	7.77	8.02	8.25	8.23
MgO	0.75	0.88	0.81	0.86	0.87	0.88	0.78	0.81	0.76	0.68	0.83	0.68	0.77	0.60	0.75	0.70
CaO	14.87	14.58	14.70	15.52	14.37	14.29	14.56	14.30	14.22	14.32	14.26	13.81	13.39	13.43	13.28	13.34
Total	100.65	100.51	100.61	100.18	100.18	100.43	100.50	101.42	99.70	102.00	102.83	100.82	100.59	99.94	100.71	99.71
Mg#	0.06	0.07	0.07	0.08	0.07	0.07	0.07	0.07	0.07	0.06	0.07	0.06	0.07	0.05	0.07	0.06
Alm	45.51	45.67	44.87	44.99	45.40	44.66	44.03	44.64	43.60	43.56	42.78	43.33	41.87	41.46	41.26	40.90
Prp	2.94	3.41	3.16	3.37	3.42	3.32	3.07	3.12	2.99	2.60	3.17	2.68	3.03	2.37	2.95	2.77
Grs	41.98	40.77	41.32	40.90	40.32	40.20	41.22	39.62	40.08	39.46	39.40	38.92	37.78	38.15	37.42	37.87
Sps	9.57	10.15	10.65	10.74	10.87	11.83	11.68	12.61	13.33	14.38	14.64	15.06	17.32	18.01	18.38	18.46

Sample No.	FGL16 – enclave (continued)																	
mm	2.76	3.19	3.37	3.45	3.75	4.08	4.31	4.41	4.51	4.70	4.85	5.01	5.15	5.33	5.51	5.61	5.67	5.71
SiO ₂	37.97	37.89	38.05	37.21	37.78	37.90	38.18	38.40	38.33	38.16	37.85	38.33	38.15	37.72	38.25	38.32	38.04	37.55
TiO ₂	0.13	bdl	0.16	0.29	0.15	bdl	bdl	bdl	bdl	bdl	0.15	0.22	bdl	0.16	bdl	bdl	bdl	bdl
Al ₂ O ₃	21.11	21.03	21.17	21.31	21.15	21.49	21.74	21.59	21.45	21.45	21.15	21.31	21.54	21.30	20.94	21.59	21.22	21.31
FeO _{Tot}	18.76	18.93	18.82	18.81	19.01	19.86	20.21	19.15	19.08	19.13	19.61	19.39	19.93	20.04	19.53	20.52	20.10	20.33
MnO	7.73	7.94	7.85	8.09	7.59	6.84	5.69	7.07	7.30	7.19	6.77	6.53	6.47	5.90	4.99	5.04	5.01	4.67
MgO	0.79	0.73	0.82	0.68	0.75	0.61	0.83	0.69	0.74	0.79	0.65	0.92	0.72	0.80	0.70	0.78	0.77	0.84
CaO	13.21	13.20	13.31	13.45	13.49	13.09	14.41	13.88	14.19	13.82	13.95	14.17	14.21	14.26	14.33	14.36	14.40	14.72
Total	99.70	99.72	100.19	99.84	99.92	99.79	101.08	100.77	101.10	100.52	100.12	100.87	101.02	100.18	98.74	100.61	99.54	99.43
Mg#	0.07	0.06	0.07	0.06	0.07	0.05	0.07	0.06	0.07	0.07	0.06	0.08	0.06	0.07	0.06	0.06	0.06	0.07
Alm	41.76	41.89	41.56	41.39	41.97	44.49	43.99	42.25	41.50	42.04	43.10	42.34	43.34	43.84	44.20	45.50	44.67	44.76
Prp	3.14	2.87	3.22	2.68	2.95	2.44	3.21	2.72	2.88	3.08	2.53	3.56	2.80	3.10	2.83	3.05	3.06	3.31
Grs	37.68	37.44	37.66	37.91	38.13	37.56	40.27	39.24	39.53	38.89	39.28	39.65	39.60	39.97	41.53	40.51	40.99	41.51
Sps	17.42	17.80	17.57	18.02	16.95	15.51	12.54	15.79	16.09	15.99	15.08	14.45	14.26	13.08	11.43	11.24	11.28	10.42

Table OSM3: Epidote mineral chemistry: (1) major elements are reported in wt.%; (2) bdl: below detection limit; (3) Ps = $(\text{Fe}^{3+} / \text{Fe}^{3+} + \text{Al}) * 100$

Sample No.	FSV3 – tonalite – Bt+Grt					
	Ep1		Ep2		Ep3	
	Matrix		Matrix		Matrix	
SiO ₂ ⁽¹⁾	40.13		38.76		38.60	38.38
TiO ₂	0.22		0.40		0.19	0.23
Al ₂ O ₃	26.55		26.76		26.46	26.51
FeO _{Tot}	6.89		6.46		6.65	6.40
MnO	bdl ⁽²⁾		bdl		bdl	bdl
CaO	20.62		22.06		22.39	22.52
Total	94.40		94.44		94.28	94.04
Ps ⁽³⁾	15.50		14.60		15.10	14.60

Sample No.	FGL6 – granodiorite - Bt+Amp+Grt					
	Ep1		Ep2		Ep	
	Matrix		Matrix		Inclusion in garnet	
SiO ₂	37.99	38.88	38.48	38.91	38.03	38.42
TiO ₂	0.21	0.14	0.30	0.22	0.19	0.17
Al ₂ O ₃	25.56	26.00	25.58	25.68	26.24	26.71
FeO _{Tot}	7.94	7.66	7.79	8.08	7.03	7.47
MnO	0.17	bdl	0.15	0.16	0.27	0.27
CaO	23.76	23.71	23.52	23.71	23.06	23.84
Total	95.62	96.39	95.82	96.77	94.82	96.89
Ps	18.00	17.30	17.80	18.20	16.00	16.60

Continuation Table OSM3

Sample No.	FGL7 – granodiorite – Bt+Amp				
	Ep1		Ep2		Ep
	Matrix		Matrix		Inclusion in amphibole
SiO ₂	38.58	37.99	39.22	38.23	38.51
TiO ₂	0.15	0.14	bdl	bdl	bdl
Al ₂ O ₃	26.64	26.03	27.31	25.54	24.94
FeO _{Tot}	7.35	7.88	7.33	9.56	10.01
MnO	0.15	bdl	0.16	0.89	0.49
CaO	24.04	24.09	24.38	23.35	23.72
Total	96.92	96.13	98.39	97.57	95.65
Ps	16.40	17.70	16.00	21.00	22.20

Sample No.	FGL12 – granodiorite - Bt+Amp+Grt								
	Ep1		Ep2				Ep		
	Matrix		Matrix				Inclusion in garnet		
SiO ₂	38.54	38.38	38.12	38.55	37.88	38.97	38.37	38.12	37.65
TiO ₂	bdl	bdl	bdl	0.18	0.18	0.17	0.21	0.23	0.32
Al ₂ O ₃	26.25	25.75	26.04	26.90	26.46	26.67	26.30	27.17	26.80
FeO _{Tot}	8.15	8.38	8.56	7.21	6.98	7.59	7.70	6.01	5.84
MnO	bdl	0.24	bdl	0.26	bdl	bdl	0.17	0.22	0.17
CaO	24.02	23.92	24.15	23.97	23.97	23.88	24.11	23.92	23.42
Total	96.95	96.67	96.88	97.07	95.47	97.29	96.85	95.66	94.21
Ps	18.00	18.80	18.90	16.00	15.80	16.80	17.20	13.60	14.30

Continuation Table OSM3

Sample No.	FGL14 - granodiorite - Bt						
	Ep1		Ep2			Ep3	
	Matrix		Matrix			Matrix	
SiO ₂	38.27	38.15	38.99	38.79	38.66	38.79	38.84
TiO ₂	0.15	0.22	0.24	0.18	0.14	bdl	bdl
Al ₂ O ₃	24.74	24.39	24.86	24.87	24.79	25.23	24.86
FeO _{Tot}	9.62	10.12	10.10	9.84	9.98	9.67	9.68
MnO	0.32	0.24	0.29	0.28	0.20	0.18	0.33
CaO	23.73	24.03	23.72	23.85	23.73	24.08	24.22
Total	96.82	97.15	98.20	97.80	97.50	97.95	97.93
Ps	21.60	22.70	22.40	21.90	22.20	21.40	21.70

Sample No.	FGL15 – granodiorite – Bt+Grt									
	Ep1		Ep		Ep/Zo			Zo		
	Matrix		Inclusions in garnet		Inclusion in plagioclase			Inclusion in garnet		
SiO ₂	38.11	38.15	38.21	38.81	38.70	39.23	38.87	38.60	38.60	38.40
TiO ₂	0.15	0.25	bdl	bdl	bdl	bdl	bdl	bdl	bdl	bdl
Al ₂ O ₃	26.12	25.59	27.60	27.76	28.33	29.01	28.90	30.62	30.64	29.17
FeO _{Tot}	6.95	7.51	5.63	5.12	4.48	4.38	4.16	1.72	1.90	2.75
MnO	0.27	0.19	0.24	0.32	bdl	0.17	0.17	0.41	0.34	0.40
CaO	22.67	22.81	22.76	22.50	23.26	23.36	23.40	23.20	23.29	22.87
Total	94.27	94.40	94.43	94.51	94.77	96.15	95.50	94.54	94.77	93.60
Ps	15.90	17.00	12.60	11.60	10.10	9.70	9.30	3.80	4.80	6.30

Continuation Table OSM3

Sample No.	FGL16 - encalve							
	Ep1		Ep2		Ep3		Ep	
	Matrix		Matrix		Matrix		Inclusion in garnet 1	
SiO ₂	39.01	39.37	38.83	39.01	39.36	38.73	39.06	39.20
TiO ₂	bdl	0.13	0.28	bdl	0.16	0.18	0.15	0.20
Al ₂ O ₃	26.84	27.08	27.44	26.60	26.59	26.57	26.83	26.91
FeO _{Tot}	7.25	7.00	6.25	7.88	7.97	8.04	7.53	7.13
MnO	bdl	0.15	0.18	0.22	bdl	bdl	bdl	bdl
CaO	23.86	24.10	23.91	23.92	24.34	23.88	23.77	24.20
Total	96.96	97.83	96.89	97.63	98.41	97.10	97.34	97.64
Ps	16.10	15.50	13.90	17.40	17.50	17.80	16.60	15.80

Sample No. FGL16 – encalve (continued)

Sample No.	Ep				Ep/Zo						
	Inclusion in garnet 2				Inclusion in amphibole			Inclusion in plagioclase 1			Inclusion in plagioclase 2
SiO ₂	39.22	38.82	39.35	39.08	39.03	38.64	38.36	38.82	39.14	38.69	39.09
TiO ₂	0.20	0.16	0.21	0.14	0.14	bdl	bdl	bdl	0.17	0.14	bdl
Al ₂ O ₃	27.49	27.50	27.67	28.07	26.67	26.15	26.76	28.35	28.08	27.97	28.46
FeO _{Tot}	6.11	5.96	6.44	6.11	7.11	7.70	7.42	5.48	5.41	5.25	5.52
MnO	bdl	bdl	bdl	bdl	bdl	bdl	bdl	bdl	bdl	bdl	bdl
CaO	23.95	24.94	24.33	24.27	24.06	24.10	23.87	24.23	24.68	23.79	24.20
Total	96.96	96.38	98.00	97.67	97.01	96.60	94.41	97.08	97.48	95.84	97.27
Ps	13.60	13.30	14.20	13.40	15.90	17.30	16.40	12.10	12.00	11.80	12.10

Continuation Table OSM3

Sample No. FGL22 - granodiorite - Bt+Grt

	Ep1		Ep2		Ep/Zo					
	Matrix		Matrix		Inclusion in plagioclase 1		Inclusion in plagioclase 2			
SiO ₂	38.15	37.65	37.67	37.76	38.44	38.51	39.11	39.28	38.24	38.20
TiO ₂	0.00	0.18	0.16	0.13	bdl	bdl	bdl	bdl	bdl	bdl
Al ₂ O ₃	25.06	25.09	25.27	24.77	27.16	27.98	27.37	24.48	26.37	26.76
FeO _{Tot}	8.78	8.59	7.74	9.01	6.12	5.39	7.17	7.28	6.96	6.98
MnO	0.14	0.24	0.26	0.21	0.18	bdl	bdl	bdl	bdl	0.14
CaO	23.62	23.72	22.91	23.49	23.83	23.76	24.72	24.87	23.90	24.11
Total	95.75	95.47	94.01	95.36	95.73	95.64	98.37	95.90	95.48	95.18
Ps	19.90	19.50	17.90	20.50	13.80	12.00	15.70	17.40	15.80	15.60

Table OSM4: Micas mineral chemistry: (1) major elements are reported in wt.%; (2) bdl: below detection limit; (3) $Fe\# = (Fe_{Tot} / Fe_{Tot} + Mg) * 100$; (4) note that this parameter has been calculated only for the White micas and not for Biotites. Vice versa for the $Fe\#$

Sample No. FGL6 – granodiorite - Bt+Amp+Grt

	Biotite1	Biotite2			Biotite3		Biotite4
	matrix	matrix	matrix	matrix	matrix	matrix	matrix
SiO ₂	35.27	35.53	35.80	36.81	36.45	36.09	35.95
TiO ₂	2.25	2.00	2.53	2.26	1.80	1.47	2.24
Al ₂ O ₃	16.11	16.29	15.94	16.55	17.04	17.15	16.28
FeO _{Tot}	22.77	22.43	22.54	22.10	22.78	22.90	23.20
MnO	0.29	0.44	0.42	0.38	0.31	0.43	0.36
MgO	8.07	8.08	7.88	8.18	8.21	8.62	7.94
CaO	bdl	bdl	0.10	bdl	bdl	bdl	bdl
Na ₂ O	0.20	0.15	bdl	0.15	0.17	0.00	0.16
K ₂ O	9.57	9.56	9.32	9.50	9.65	9.66	9.61
Total	94.53	94.49	94.53	95.93	96.41	96.33	95.74
Fe#	0.61	0.61	0.62	0.60	0.61	0.60	0.62
Fe _{Tot} +Mg	-	-	-	-	-	-	-

Continuation Table OSM4

Sample No.	FGL14 - granodiorite - Bt			
	Biotite matrix			
SiO ₂	36.28	36.83	35.53	35.38
TiO ₂	2.84	2.29	2.14	2.25
Al ₂ O ₃	17.06	17.60	16.83	16.96
FeO _{Tot}	22.95	22.53	21.63	21.95
MnO	0.48	0.42	0.48	0.38
MgO	8.05	8.43	7.98	8.25
CaO	bdl	bdl	0.11	0.12
Na ₂ O	bdl	bdl	bdl	bdl
K ₂ O	9.76	9.88	9.38	9.59
Total	97.41	97.99	94.07	94.87
Fe#	0.38	0.40	0.40	0.40
Fe _{Tot} +Mg	-	-	-	-

Sample No.	FGL15 – granodiorite – Bt+Grt				Sericite (WM2 secondary white mica)			
	Biotite matrix							
SiO ₂	36.22	36.29	36.07	36.36	46.63	46.72	46.34	47.78
TiO ₂	1.99	1.53	1.59	1.79	0.12	0.12	bdl	bdl
Al ₂ O ₃	17.66	17.91	17.45	17.79	37.14	35.87	36.22	35.47
FeO _{Tot}	22.30	22.19	22.64	22.32	0.61	1.70	0.97	1.35
MnO	0.28	0.22	0.33	0.36	bdl	bdl	bdl	bdl
MgO	7.05	7.42	7.07	6.99	0.38	0.17	0.24	0.46
CaO	bdl	bdl	bdl	0.12	bdl	bdl	bdl	bdl
Na ₂ O	bdl	bdl	bdl	bdl	0.25	0.22	0.16	0.18
K ₂ O	9.45	9.52	9.39	9.44	9.81	10.13	10.35	9.99
Total	94.95	95.08	94.68	95.17	94.94	94.93	94.28	95.22
Fe#	0.64	0.63	0.64	0.64	-	-	-	-
Fe _{Tot} +Mg	-	-	-	-	0.070	0.111	0.078	0.120

Continuation Table OSM4

Sample No.	FGL16 - enclave										
	Biotite1		Biotite2		Biotite3			Biotite1		Biotite2	
	matrix		matrix		matrix			inclusion in garnet 1			
SiO ₂	35.66	36.26	36.20	36.85	35.50	35.93	35.79	35.60	35.57	35.96	35.01
TiO ₂	1.77	1.98	2.03	1.94	1.80	1.10	1.46	1.90	2.19	2.20	2.32
Al ₂ O ₃	17.10	17.35	17.43	17.40	17.29	17.48	17.02	16.01	16.23	16.61	16.39
FeO _{Tot}	22.44	22.08	22.04	21.79	22.20	22.14	21.96	22.86	23.10	22.88	22.71
MnO	0.28	0.28	0.23	0.25	0.38	0.33	0.32	0.29	0.39	0.26	0.38
MgO	7.73	7.99	7.87	8.16	7.73	8.04	7.96	7.93	7.87	7.95	7.75
CaO	0.13	bdl	bdl	0.13	0.29	bdl	bdl	bdl	bdl	bdl	0.12
Na ₂ O	bdl	bdl	bdl	bdl	bdl	0.17	0.20	bdl	bdl	bdl	bdl
K ₂ O	9.57	9.65	9.60	9.61	9.25	9.58	9.66	9.60	9.48	9.68	9.31
Total	94.68	95.59	95.39	96.13	94.59	94.81	94.17	94.19	94.84	95.53	93.99
Fe#	0.62	0.61	0.61	0.60	0.62	0.61	0.61	0.62	0.62	0.62	0.62
Fe _{Tot} +Mg	-	-	-	-	-	-	-	-	-	-	-

Sample No.	FGL16 - enclave (enclave)							
	Biotite3 inclusion in garnet 1			Sericite (WM2 secondary white mica)				
SiO ₂	35.42	34.78	48.67	48.66	48.83	48.72	49.83	
TiO ₂	3.00	2.64	bdl	bdl	0.15	0.05	0.38	
Al ₂ O ₃	16.01	16.33	35.69	36.03	36.42	36.04	34.41	
FeO _{Tot}	22.63	23.17	1.99	2.10	2.17	2.09	2.19	
MnO	0.35	0.40	bdl	bdl	bdl	bdl	bdl	
MgO	7.71	7.86	0.65	0.61	0.55	0.60	1.07	
CaO	bdl	0.14	bdl	bdl	bdl	bdl	0.14	
Na ₂ O	bdl	0.20	0.25	0.22	0.16	0.21	0.17	
K ₂ O	9.46	8.94	10.94	11.15	11.25	11.11	10.00	
Total	94.57	94.45	98.18	98.78	99.53	98.83	98.18	
Fe#	0.62	0.62	-	-	-	-	-	
Fe _{Tot} +Mg	-	-	0.170	0.172	0.168	0.182	0.220	

Continuation Table OSM4

Sample No. FGL22 – granodiorite – Bt+Grt

	Biotite1		Biotite2		Biotite3	
	matrix		matrix		matrix	
SiO ₂	35.47	35.52	35.88	35.86	35.84	35.67
TiO ₂	2.27	2.18	2.11	2.32	2.50	2.53
Al ₂ O ₃	17.48	17.85	17.89	17.82	17.67	17.47
FeO _{Tot}	24.07	24.01	23.28	22.98	23.58	23.56
MnO	0.25	0.19	0.31	0.26		0.28
MgO	5.82	5.75	5.88	5.92	5.74	5.75
CaO	bdl	bdl	0.16	bdl	bdl	bdl
Na ₂ O	bdl	bdl	bdl	bdl	bdl	bdl
K ₂ O	8.92	9.09	9.25	9.29	9.26	9.35
Total	94.28	94.60	94.76	94.42	94.59	94.61
Fe#	0.70	0.70	0.69	0.69	0.70	0.70
Fe _{Tot} +Mg	-	-	-	-	-	-

Sample No. FGL22 – granodiorite – Bt+Grt (continued)

	Biotite				White mica (WM1 primary)		
	inclusion in garnet 1		inclusion in garnet 2		matrix	inclusion in garnet	
SiO ₂	35.77	35.66	35.72	35.31	47.19	47.51	49.28
TiO ₂	2.98	3.21	2.40	2.44	0.26	0.22	0.21
Al ₂ O ₃	17.11	17.10	17.18	17.28	35.52	32.13	33.69
FeO _{Tot}	23.49	23.18	23.87	23.55	3.89	3.53	2.92
MnO	0.18	0.29	0.34	0.43	bdl	bdl	bdl
MgO	5.89	5.65	6.17	5.88	1.47	1.39	1.19
CaO	bdl	bdl	0.13	bdl	bdl	bdl	bdl
Na ₂ O	bdl	0.25	bdl	bdl	0.18	0.23	0.19
K ₂ O	9.21	9.13	9.29	9.38	9.60	10.34	8.96
Total	94.63	94.46	95.10	94.27	95.12	95.34	96.43
Fe#	0.69	0.70	0.68	0.69	-	-	-
Fe _{Tot} +Mg	-	-	-	-	0.365	0.336	0.275

Table OSM5: Amphibole mineral chemistry: (1) major elements are reported in wt.%; (2) Mg# = Mg/(Mg+Fe²⁺)

Sample No. FGL6 - granodiorite - Bt+Amp+Grt

	Amphibole 1			Amphibole 2		Amphibole 3		Amphibole
	matrix			matrix		matrix		inclusion in garnet
	core	rim1	rim2	core	rim	core	rim	
SiO ₂ ⁽¹⁾	45.79	43.39	42.54	47.22	43.44	43.12	41.69	42.45
TiO ₂	0.91	0.77	0.70	0.93	0.70	0.72	0.68	0.61
Al ₂ O ₃	9.00	11.41	13.32	7.68	12.25	12.46	13.68	14.09
FeO _{Tot}	19.99	20.11	20.98	18.45	20.28	20.57	20.98	20.60
MnO	0.67	0.69	0.55	0.64	0.60	0.66	0.64	0.50
MgO	8.33	7.09	6.37	9.39	7.01	6.84	6.06	6.15
CaO	11.93	11.73	11.71	11.71	11.90	11.82	11.71	11.83
Na ₂ O	0.87	0.95	1.01	0.94	1.04	0.96	1.07	1.03
K ₂ O	1.00	1.21	1.42	0.61	1.24	1.33	1.60	1.36
Total	98.49	97.35	98.60	97.57	98.45	98.48	98.11	98.62
Mg# ⁽²⁾	0.45	0.41	0.38	0.50	0.40	0.40	0.36	0.37

Continuation Table OSM5:

Sample No. FGL7 - granodiorite - Bt+Amp

	Amphibole 1		Amphibole 2	Amphibole 3
	matrix		matrix	matrix
	core	rim	core	rim
SiO ₂	47.84	46.66	46.88	46.83
TiO ₂	0.77	0.83	0.70	0.69
Al ₂ O ₃	7.72	8.99	8.81	9.28
FeO _{Tot}	18.13	18.43	18.68	18.79
MnO	0.54	0.55	0.56	0.60
MgO	9.76	9.12	9.24	9.03
CaO	11.88	12.12	12.14	12.13
Na ₂ O	0.82	0.72	0.99	0.88
K ₂ O	0.70	0.86	0.77	0.72
Total	98.16	98.28	98.77	98.95
Mg#	0.51	0.48	0.48	0.48

Sample No. FGL12 - granodiorite - Bt+Amp+Grt

	Amphibole 1		Amphibole 2		Amphibole 3	
	matrix		matrix		matrix	
	core	rim	core	rim	core	rim
SiO ₂	44.85	42.52	46.16	41.07	42.18	41.59
TiO ₂	0.68	0.60	0.70	0.69	0.49	0.74
Al ₂ O ₃	10.11	12.51	8.68	14.02	12.58	13.49
FeO _{Tot}	19.01	19.26	18.66	19.85	19.56	19.61
MnO	0.54	0.42	0.55	0.56	0.44	0.44
MgO	8.14	6.91	8.79	6.37	6.70	6.41
CaO	11.86	11.87	11.81	11.66	11.97	11.81
Na ₂ O	0.89	0.93	0.78	0.90	0.94	1.02
K ₂ O	0.98	1.28	0.79	1.63	1.16	1.38
Total	97.06	96.33	96.91	96.74	96.01	96.49
Mg#	0.45	0.40	0.47	0.39	0.39	0.38

Continuation Table OSM5:

Sample No. FGL16 - enclave

	Amphibole 1			Amphibole 2	Amphibole 3		Amphibole 4	Amphibole 5	
	matrix			matrix	matrix		matrix	matrix	
	core1	core2	rim	rim	core	rim	core	core	rim
SiO ₂	41.53	41.68	41.28	42.03	41.40	41.48	41.44	41.44	41.59
TiO ₂	0.53	0.67	0.61	0.49	0.55	0.61	0.69	0.73	0.54
Al ₂ O ₃	15.20	15.11	15.25	14.89	14.78	15.23	14.79	15.13	15.15
FeO _{Tot}	20.47	20.47	20.61	20.61	20.53	20.52	20.11	20.59	20.85
MnO	0.39	0.40	0.31	0.37	0.38	0.39	0.35	0.33	0.46
MgO	5.80	5.88	5.82	5.97	5.95	6.09	5.71	5.82	5.75
CaO	11.90	11.83	11.87	11.78	12.24	11.64	11.76	11.85	11.81
Na ₂ O	1.05	1.08	1.10	1.11	1.02	1.04	1.05	1.10	1.00
K ₂ O	1.70	1.69	1.71	1.67	1.54	1.70	1.63	1.73	1.59
Total	98.58	98.80	98.56	98.91	98.40	98.71	97.53	98.73	98.73
Mg#	0.35	0.35	0.35	0.35	0.35	0.38	0.34	0.35	0.35

Table OSM6: Feldspar mineral chemistry: (1) major elements are reported in wt.%; (2) bdl: below detection limit

Sample No. FSV3 - tonalite - Bt+Grt

	Plagioclase		Plagioclase		Plagioclase		
	matrix		inclusion in garnet		Corona		
	core	rim	core	rim	Close to grt	core	close to Bt
SiO ₂ ⁽¹⁾	53.79	57.02	51.78	53.16	53.48	54.08	55.53
Al ₂ O ₃	28.73	27.92	29.92	29.32	29.60	29.11	27.94
FeO _{Tot}	bdl ⁽²⁾	bdl	0.47	0.49	bdl	0.14	0.15
CaO	12.11	10.49	13.66	12.88	12.81	12.28	9.39
Na ₂ O	4.83	6.02	3.87	4.43	4.55	4.69	6.84
K ₂ O	0.00	0.00	0.11	0.14	0.00	0.08	0.10
Total	99.46	101.45	99.80	100.42	100.45	100.37	100.17
Ab	41.93	50.96	33.68	38.04	39.12	40.69	48.25
An	58.07	49.04	65.69	61.16	60.88	58.88	51.21
Or	0.00	0.00	0.64	0.79	0.00	0.43	0.54

Sample No. FGL6 – granodiorite - Bt+Amp+Grt

	Plagioclase				
	Matrix			Matrix	
	core	core	rim	core	rim
SiO ₂	46.87	46.72	59.85	60.04	58.88
Al ₂ O ₃	34.67	34.49	26.38	25.43	25.21
FeO _{Tot}	bdl	bdl	bdl	bdl	bdl
CaO	18.55	18.75	8.38	7.55	7.65
Na ₂ O	1.28	1.28	7.08	7.49	7.04
K ₂ O	0.00	0.00	0.00	0.00	0.00
Total	101.37	101.24	101.69	100.51	98.79
Ab	11.06	10.97	60.47	64.24	62.49
An	88.94	89.03	39.53	35.76	37.51
Or	0.00	0.00	0.00	0.00	0.00

Continuation Table OSM6:

Sample No. FGL7 - granodiorite - Bt+Amp

	Plagioclase 1		Plagioclase 2		Plagioclase 3		Plagioclase 4	
	Matrix		Matrix		Matrix		Matrix	
	Core	Rim	Core	Rim	Core	Rim	Core	Rim
SiO ₂	55.43	57.39	55.78	57.24	59.53	59.12	47.12	60.39
Al ₂ O ₃	27.61	27.42	27.96	27.02	26.27	26.19	34.25	25.37
FeO _{Tot}	bdl	bdl	bdl	bdl	bdl	bdl	bdl	bdl
CaO	10.25	9.55	10.71	9.62	8.17	8.23	17.95	7.45
Na ₂ O	5.86	6.45	5.76	6.35	7.25	7.13	1.60	7.73
K ₂ O	0.16	0.16	0.13	0.21	0.36	0.17	0.00	0.13
Total	99.31	100.98	100.34	100.44	101.58	100.84	100.91	101.06
Ab	50.41	54.52	48.97	53.79	60.42	60.47	13.86	64.79
An	48.71	44.60	50.30	45.02	37.61	38.58	86.14	34.50
Or	0.88	0.89	0.73	1.19	1.97	0.94	0.00	0.71

Sample No. FGL12 – granodiorite - Bt+Amp+Grt

	Plagioclase	
	Matrix	
	core	rim
SiO ₂	56.68	56.68
Al ₂ O ₃	26.58	26.20
FeO _{Tot}	bdl	bdl
CaO	9.31	9.11
Na ₂ O	6.47	6.43
K ₂ O	0.07	0.11
Total	99.11	98.53
Ab	55.47	55.75
An	44.11	43.64
Or	0.42	0.62

Continuation Table OSM6:

Sample No.	FGL14 - granodiorite - Bt					
	Plagioclase 1		Plagioclase 2		Plagioclase 3	
	Matrix	Core	Matrix	Rim	Matrix	Rim
SiO ₂	59.31	59.58	59.29	57.43	57.51	
Al ₂ O ₃	26.26	25.41	26.30	27.31	26.57	
FeO _{Tot}	bdl	bdl	bdl	bdl	bdl	
CaO	8.35	7.69	8.04	9.59	9.07	
Na ₂ O	7.19	6.99	7.24	6.45	6.45	
K ₂ O	0.23	0.18	0.18	0.00	0.16	
Total	101.33	99.86	101.24	100.77	99.76	
Ab	60.16	61.57	61.33	54.90	55.78	
An	38.59	37.41	37.65	45.10	43.33	
Or	1.25	1.02	1.01	0.00	0.89	

Sample No.	FGL15 – granodiorite – Bt+Grt							
	Plagioclase				Plagioclase			
	Matrix		Matrix		Inclusion in garnet 1		Inclusion in garnet 2	
	Core	Rim	Core	Rim	Core	Rim	Core	Rim
SiO ₂	48.00	56.24	47.00	58.09	57.67	57.88	60.36	60.76
Al ₂ O ₃	33.76	26.72	33.49	26.32	26.35	26.18	24.02	23.82
FeO _{Tot}	bdl	bdl	bdl	bdl	0.15	bdl	0.23	0.21
CaO	16.81	9.31	16.93	8.50	8.62	8.40	5.79	5.77
Na ₂ O	1.85	6.17	1.74	6.90	6.61	6.56	8.23	8.39
K ₂ O	0.00	0.07	0.00	0.10	0.18	0.20	0.24	0.21
Total	100.43	98.51	99.16	99.91	99.59	99.22	98.88	99.16
Ab	16.62	54.31	1.66	59.16	57.49	57.88	70.99	71.62
An	83.38	45.28	84.34	40.28	41.45	40.95	27.62	27.20
Or	0.00	0.41	0.00	0.56	1.06	1.17	1.38	1.18

Continuation Table OSM6:

Sample No. FGL16 - enclave

	Plagioclase				Plagioclase					
	Matrix		Matrix		Inclusion in garnet 1					
	core	rim	core	rim	core	rim	core	rim	core	rim
SiO ₂	47.72	56.90	58.25	58.46	58.08	58.67	58.44	58.71	57.66	57.85
Al ₂ O ₃	32.48	27.28	26.71	26.65	27.63	26.33	26.59	26.45	26.66	26.20
FeO _{Tot}	bdl	bdl	bdl	bdl	0.19	0.13	bdl	bdl	bdl	bdl
CaO	17.01	9.80	8.99	8.68	9.94	8.73	8.95	8.98	9.05	8.73
Na ₂ O	1.57	6.00	6.50	6.74	4.98	6.71	6.65	6.73	6.45	6.49
K ₂ O	0.00	0.00	0.09	0.12	0.12	0.13	0.14	0.15	0.16	0.13
Total	98.90	99.97	100.53	100.64	100.93	100.71	100.77	101.02	99.98	99.40
Ab	14.25	52.21	56.36	58.03	47.17	57.75	56.90	57.11	55.80	56.91
An	85.09	47.10	43.10	41.30	52.09	41.54	42.30	42.08	43.27	42.31
Or	0.66	0.69	0.54	0.67	0.75	0.71	0.80	0.81	0.93	0.78

Sample No. FGL22 – granodiorite – Bt+Grt

	Plagioclase				Plagioclase		K-feldspato			
	Matrix		Matrix		Inclusion in garnet		Rim	Core	Rim	
	Core	Rim	Core	Rim	Core	rim				
SiO ₂	58.82	58.62	53.08	60.22	56.96	56.54	58.11	64.33	64.00	64.45
Al ₂ O ₃	26.14	26.13	29.76	25.13	27.45	26.79	26.05	17.73	17.96	18.09
FeO _{Tot}	bdl	bdl	bdl	bdl	bdl	bdl	bdl	bdl	bdl	bdl
CaO	8.26	8.26	12.92	7.60	9.91	9.72	8.55	0.00	0.14	0.00
Na ₂ O	7.02	7.21	4.71	7.57	6.35	6.26	6.79	0.72	0.58	0.89
K ₂ O	0.13	0.11	0.09	0.17	0.11	0.14	0.10	15.58	15.81	15.29
Total	100.40	100.33	100.57	100.73	100.86	99.45	99.60	98.61	98.77	99.11
Ab	60.17	60.90	39.56	63.72	53.37	53.39	58.63	6.59	5.24	8.12
An	39.11	38.51	59.93	35.34	46.01	45.80	40.81	0.00	0.71	0.00
Or	0.72	0.59	0.52	0.94	0.62	0.81	0.57	93.41	94.05	91.88

Table OSM7: Whole rock major and trace element analyses. (1) Major elements are reported in (wt.%); (2) Loss of ignition; (3) Al/(2*Ca+Na+K); (4) Mg/(Mg+Fe2+); (5) Trace elements are reported in (ppm) (part per million); (6) $Eu_N/[(Sm_N)(Gd_N)]^{1/2}$; (7) Mafic Microgranular Enclaves

Sample	FSV1	FSV3	FSV5	FGL6	FGL7	FSV9	FSV10	FGL12	FGL14
UTM points	206417 E 7913072 S	210670 E 7915909 S	220975 E 7911918 S	231076 E 7902594 S	231760 E 7898113 S	204900 E 7906475 S	204900 E 7906475 S	233128 E 7897734 S	249277 E 7877776 S
Rock Type	Tonalite	Tonalite	Granodiorite	Granodiorite	Granodiorite	MME ⁽⁷⁾	Granodiorite	Granodiorite	Granodiorite
Mineral assemblage	Bt+Grt	Bt+Grt	Bt+Grt	Bt+Amp+Grt	Bt+Amph		Bt+Amp+Grt	Bt+Amp+Grt	Bt
SiO ₂ ⁽¹⁾	62.98	63.31	71.42	65.54	63.58	53.80	62.21	63.49	68.08
TiO ₂	0.85	0.89	0.31	0.65	0.74	1.07	0.91	0.73	0.50
Al ₂ O ₃	16.43	16.73	14.68	15.80	16.15	17.89	16.67	16.24	15.28
Fe ₂ O ₃ Tot	6.94	6.51	2.73	5.49	6.15	9.80	6.49	5.94	4.42
MnO	0.17	0.08	0.04	0.10	0.10	0.19	0.10	0.11	0.09
MgO	2.05	1.85	0.51	1.83	2.27	4.25	2.30	2.20	1.46
CaO	4.64	5.06	2.82	4.38	5.16	8.57	6.09	5.11	3.52
Na ₂ O	2.58	2.32	2.89	2.92	2.69	2.32	2.52	2.84	2.80
K ₂ O	2.47	2.45	3.87	2.68	2.42	1.48	1.76	2.58	3.23
P ₂ O ₅	0.18	0.25	0.11	0.16	0.17	0.17	0.21	0.16	0.14
L.O.I ⁽²⁾	0.72	0.54	0.62	0.43	0.55	0.46	0.45	0.60	0.48
A/CNK ⁽³⁾	1.07	1.07	1.04	1.01	0.98	0.85	0.99	0.97	1.05
FeO _{Tot} + MgO	8.29	7.71	2.96	6.78	5.54	13.07	8.14	7.54	5.44
Mg# ⁽⁴⁾	0.37	0.36	0.27	0.40	0.42	0.46	0.41	0.42	0.40
Sc ⁽⁵⁾	25.0	22.4	11.2	19.1	22.3	33.9	19.2	22.3	18.1
V	80.1	69.4	25.2	87.9	105.0	189.0	113.9	95.0	80.4
Cr	21.7	19.3	11.4	22.8	34.8	41.2	25.4	36	24.1
Co	49.4	40.8	55.5	44.3	51.2	49.9	53.9	41.8	51.9
Ni	14.9	15.5	7.94	14.9	17.9	15.2	13.2	14.1	10.7
Cu	45.0	107.0	6.1	19.3	19.2	22.9	61.8	15.4	16.0
Zn	99.5	109	73.9	79.3	83.1	121	90.2	85	71.5
Rb	111	116	106	125	93.3	48.4	70.2	97.2	120
Sr	211	252	164	176	195	305	312	206	209

Continuation Table OSM7:

Y	46.2	21.9	13.1	22.1	23.3	42.6	14.5	26	40.7
Zr	162	247	175	162	168	158	179	162	128
Nb	12.9	11.8	9.08	11.7	10.5	11	9.13	11	9.33
Mo	0.47	0.49	0.65	0.51	0.68	1.61	0.61	0.65	0.49
Cs	4.37	5.2	3.82	7.91	5.91	1.2	2.27	4.39	8.85
Ba	417	588	568	277	403	358	455	465	463
La	74.8	38.7	27.9	39.5	22.2	18	32.2	29.6	32.4
Ce	147	77.5	63	79.8	46.9	52.3	61.8	60.1	65.3
Pr	15.6	8.94	6.51	8.75	5.53	8.41	7.32	6.77	8.02
Nd	56.0	33.7	24.3	31.7	23.1	38.2	27.8	26.3	31.5
Sm	8.23	6.67	4.28	5.56	5.13	9.32	4.99	5.6	6.67
Eu	1.11	1.44	1.03	1.12	1.18	1.73	1.33	1.2	1.24
Gd	5.83	5.3	3.89	5.01	4.41	8.03	3.77	4.95	6.83
Tb	0.92	0.76	0.5	0.71	0.71	1.31	0.52	0.78	1.09
Dy	7.27	4.38	2.79	4.53	4.54	7.68	2.88	4.84	6.49
Ho	1.83	0.82	0.52	0.85	0.86	1.68	0.52	0.9	1.36
Er	6.82	2.33	1.42	2.25	2.63	4.75	1.37	2.77	4.24
Tm	1.30	0.32	0.19	0.30	0.36	0.68	0.17	0.40	0.58
Yb	8.66	2	1.48	2.18	2.48	4.87	1.11	2.64	3.98
Lu	1.42	0.31	0.22	0.33	0.37	0.68	0.14	0.38	0.6
Hf	4.63	6.91	4.26	4.49	4.78	4.29	4.98	4.74	4.15
Ta	1.28	0.85	1.16	1.44	1.32	1.58	0.94	1.05	1.45
Pb	9.31	8.61	28.3	17.7	14.2	12.5	8.39	15.6	24.5
Th	21.0	9.2	9.1	13.9	6.4	0.8	5.1	10.1	11.2
U	0.98	1.08	1.62	3.96	1	0.34	0.49	1.22	1.91
ΣREE	27.3	10.2	6.6	10.4	11.2	20.3	6.2	11.9	17.3
La/Yb	8.64	19.36	18.85	18.16	8.98	3.70	29.02	11.24	8.14
Eu/Eu* ⁽⁶⁾	0.49	0.74	0.77	0.65	0.76	0.61	0.93	0.70	0.56

Continuation Table OSM7:

Sample	FGL15	FGL16	FGL17	FGL18	FGL19	FGL20	FGL22
UTM points	239932 E 7880630 S	239932 E 7880630 S	239932 E 7880630 S	239932 E 7880630 S	240224 E 7880630 S	240662 E 7877458 S	240336 E 7874500 S
Rock Type	Granodiorite	MME	MME	MME	Granodiorite	Granodiorite	Granodiorite
Mineral assemblage	Bt+Grt				Bt+Grt	Bt+Grt	Bt+Grt
SiO ₂ ⁽¹⁾	67.94	64.48	63.53	63.54	72.04	67.67	70.62
TiO ₂	0.58	0.80	0.90	0.83	0.31	0.44	0.39
Al ₂ O ₃	15.29	15.43	15.76	15.72	14.51	16.40	15.00
Fe ₂ O ₃ Tot	4.73	6.88	7.34	7.28	2.95	3.93	3.44
MnO	0.07	0.11	0.10	0.11	0.05	0.07	0.04
MgO	1.29	2.12	2.15	2.19	0.59	1.07	0.71
CaO	4.08	4.92	4.25	4.69	3.28	4.21	3.78
Na ₂ O	2.70	2.32	2.48	2.43	2.94	2.87	3.01
K ₂ O	2.74	2.33	2.77	2.57	2.88	2.83	2.56
P ₂ O ₅	0.15	0.15	0.19	0.16	0.08	0.13	0.09
L.O.I ⁽²⁾	0.44	0.44	0.53	0.48	0.35	0.37	0.35
A/CNK ⁽³⁾	1.03	1.01	1.07	1.03	1.04	1.06	1.03
FeO _{Tot} + MgO	5.54	8.32	8.75	8.74	3.25	4.61	3.80
Mg# ⁽⁴⁾	0.35	0.38	0.37	0.37	0.29	0.35	0.29
Sc ⁽⁵⁾	18.4	25.4	23.8	26.7	13.6	15.5	15.7
V	71.4	117.0	121.0	118.0	35.6	54.8	40.5
Cr	26	19.5	19.9	18.3	12.7	15.7	18.4
Co	51.7	44.9	43.7	50.1	62.5	46.4	58.2
Ni	14.8	12.4	14.8	12.3	8.75	16.1	9.95
Cu	20.8	20.2	11.7	9.3	11.6	20.1	22.4
Zn	74.8	97	112	103	64.4	55.9	59.8
Rb	95.8	118	138	123	80.8	97.8	78
Sr	202	168	150	148	157	184	185
Y	20.9	28.5	21.5	32.7	17.6	25.2	18

Continuation Table OSM7:

Zr	189	160	144	159	173	143	176
Nb	12.1	11.3	12.7	11.4	9.82	10.1	11.7
Mo	0.9	1.05	0.7	0.71	0.72	1.07	0.8
Cs	2.68	4.86	5.9	4.87	3.31	6.85	2.49
Ba	660	204	229	207	744	516	759
La	44.2	25.4	23.4	23.6	40.5	31.5	50.3
Ce	88.6	50.9	48.8	50.8	91.8	64.7	104
Pr	10.2	5.76	5.66	6.25	9.87	7.42	11.1
Nd	37.0	23.3	22.6	25.2	34.3	27.3	40.8
Sm	6.94	5.05	4.98	5.87	6.46	5.3	7.16
Eu	1.48	1.18	1.2	1.33	1.27	1.47	1.28
Gd	5.76	4.47	4.87	5.96	4.87	4.61	6.07
Tb	0.77	0.77	0.69	0.91	0.67	0.7	0.73
Dy	4.21	5.05	4.27	5.71	3.47	4.45	4.39
Ho	0.86	1.01	0.89	1.24	0.63	0.9	0.7
Er	2.11	3.06	2.32	3.53	1.68	3.19	1.82
Tm	0.29	0.43	0.32	0.52	0.27	0.40	0.25
Yb	1.95	3.06	2.13	3.5	1.58	2.77	1.46
Lu	0.28	0.47	0.29	0.53	0.26	0.41	0.29
Hf	5	4.34	4.02	4.45	5.28	4.05	4.48
Ta	1.4	1.01	1.05	1.04	1.08	1.32	1.16
Pb	14.4	9.98	11	9.07	18.1	17	14.5
Th	11.6	7.5	7.7	6.5	9.9	10.0	12.0
U	1.44	1.88	1.34	1.55	1.68	2.21	1.39
ΣREE	9.7	13.1	10.2	15.0	7.9	12.1	8.9
La/Yb	22.71	8.31	11.00	6.74	25.61	11.39	34.42
Eu/Eu* ⁽⁶⁾	0.91	0.76	0.75	0.69	0.69	0.91	0.59

APPENDIX B**Supplementary material of the manuscript presented in the chapter 5****SM1: LA-SC-ICP-MS U-Th-Pb dating**

LA-ICP-MS U-Pb dates and Lu-Hf isotopes analytical procedures and instrumental settings have been already and carefully described in Farina *et al.*, (2015) and Albert *et al.*, (2016). These are resumed here and in the following supplementary table 1

Supplementary Table 1

Data acquisition and instrumental settings for the U-Pb-Th and Lu-Hf isotope analyses

	U-Pb-Th session	Lu-Hf session
Instrument	Element 2	Thermo-Finnigan Neptune +
Scan mode	E-Scan	Static
Scanned masses	202, 204, 206, 207, 208, 232, 238	172, 173, 175, 176, 177, 178, 179, 180, 300
Mass resolution	300	300
Dwell time	4 (202), 4 (204), 14 (206), 20 (207), 10 (232), 14 (238) ms	0.52s
Integration time	0.9s	1s
Background	19s	-
Ablation time	30s	36s
Carrier gas	0.5 L/min He (+ 1.0 L/min Ar)	1.3 L/min He (+1.0 L/min Ar, 0.015 L/min N)
Laser	CETAC LSX-213 G2+	Photon machines 193
Spot size	20 μm	40 μm
Laser settings	10 Hz, 3.5 J/cm ²	5 Hz, 3 J/cm ²
Cell volume	Low (teardrop)	Low (two volume cell)

Sample preparation was already reported in the text. U, Th and Pb isotopes have been analysed by means ThermoScientific Element sector field ICP-MS coupled to a CETAC LSX-213 G2+ laser system (Frei & Gerders, 2009; Gerdes & Zeh, 2006, 2009) and). Zircons grains mounted in epoxy disc, polished and imaged under cathodoluminescence (CL) were imaged at the Universidade Federal de Ouro Preto (UFOP) (Brazil). Imaging was performed by Scanning Electron Microscopy (SEM) using JEOL 6510 equipped with Centaurus CL detector. U-Pb dating was conducted at the UFOP during one session in July 2015 via thermo-Scientific Element 2 Sector Field (SF) ICP-MS coupled to a CETAC LSX-213 G2 + ($\lambda = 213 \text{ nm}$) Nd:YAG laser. Data reduction was performed using GLITTER[®] software package (Van Achterbergh *et al.*, 2001). During the analytical session a normalization with reference zircon GJ-1 (Jackson *et al.*, 2004) was applied in order to correct laser-induced fractionation and instrumental mass discrimination.

$^{206}\text{Pb}/^{238}\text{U}$ uncertainties (2σ) were propagated by quadratic addition of the external reproducibility (2SD) obtained from the standard zircon GJ-1 during the analytical session and the within-run precision of each analysis (standard error). The validity of the applied method and age reproducibility of the obtained age data was tested doing multiple analyses on Plešovice (Sláma *et al.*, 2007) and in-house BB reference material (Santos *et al.*, 2017). Plešovice and BB secondary standards gave concordia ages of 338 ± 2 Ma (2S; $n = 13$, MSWD Conc. + Equiv. 0.27) and 562 ± 1 Ma (2S; $n = 45$, MSWD Conc. + Equiv. 0.084) respectively which are consistent, within uncertainty, with the ID-TIMS values published for Plešovice [337.3 ± 0.4 Ma (2S); Sláma *et al.*, 2007] and BB [563 ± 0.3 Ma (2S); Santos *et al.*, 2017]. Background signal, common Pb, laser-induced elemental fractionation, instrumental mass discrimination and U-Pb time dependent fractionation were corrected on the raw data using Glitter software (Van Achterbergh *et al.*, 2001). During ablation session attention was paid in monitoring the time-resolved signal in order to exclude grains domains such as epoxy resin, mineral inclusions, fractures and other zone that could cause distinct Pb/U ratios and being affected by Pb-loss. From almost 90 % of the analyses, no common Pb correction was applied since the ^{204}Pb signal was below the detection limit (20 counts per limit). Instead, for the other 10 % this correction was applied (Stacy and Kramers, 1975). LA-ICP-MS All reported uncertainties of unknowns and standards (ratios and ages) are at the 2 sigma level (Horstwood *et al.*, 2016). Concordia ellipses were generated using the Isoplot/Ex4 program (Ludwig, 2003). U-Pb dating results of the samples and secondary standards are presented in supplementary Table 2, 3, respectively.

SM2: LA-MC-ICP-MS Lu-Hf Isotope Analyses

During the same U-Pb analytical session, Lu-Hf isotope analyses were also performed by means LA-ICP-MS according to the methods already published (Gerdes & Zeh, 2006, 2009). Lu-Hf isotopic data were acquired during the same dating session at the UFOP using a multi-collector (MC)-ICP-MS Thermo-Scientific Neptune Plus system coupled to a Photon Machines composition 193 ($\lambda = 193$ nm) ArF Excimer laser ablation system. The laser spot was kept constant at 40 μm . The ablation was done onto the same U-Pb pits or otherwise, when not possible, in similar domains individuated carefully before by CL imaging. In order to inhibit oxide formation in the plasma and enhancing the signal sensitivity, nitrogen was introduced into the Ar samples carrier gas via Aridus nebulisation system. Similar to the U-Pb analyses, the integration window was processed offline in order to verify the homogeneity of the ablated zircon. During each analysis ^{172}Yb , ^{173}Yb and ^{175}Lu were measured. This allowed to correct for the isobaric interferences of Lu and Yb isotopes on mas ^{176}Lu . JWG in-house values of 0.02655 for $^{176}\text{Lu}/^{175}\text{Lu}$ ratio and 0.795051 for the $^{176}\text{Yb}/^{173}\text{Yb}$

ratio were used in order to calculate ^{176}Lu and ^{176}Yb . An exponential law and $^{172}\text{Yb}/^{173}\text{Yb}$ ratio of 1.35351 (mean of Segal *et al.*, 2003; Chu *et al.*, 2002) and $^{179}\text{Hf}/^{177}\text{Hf}$ ratios of 0.7325 (Patchett *et al.*, 1981) were used to correct instrumental biases. Yb (β_{Yb}) isotope has a mass bias that usually differs from that of the Hafnium (β_{Hf}) showing an offset of $\beta_{\text{Hf}}/\beta_{\text{Yb}}$. Thus for each analytical session, this offset was calculated by averaging the $\beta_{\text{Hf}}/\beta_{\text{Yb}}$ of multiple analyses of the Temora reference material. Regarding the behaviour of Lu mass bias, this was assumed being similar to that of Yb. The $\beta_{\text{Hf}}/\beta_{\text{Yb}}$ offset factor for Yb-rich zircons was determined from the mean β_{Yb} of each analysis while for the Yb-poor grains the correction was done taking the β_{Hf} of each integration step divided by the average $\beta_{\text{Hf}}/\beta_{\text{Yb}}$ offset factor of the whole analytical session. Thus it results that that any under- or over-correction for Yb and Lu interference on mass 176 gives an apparent correlation of the $^{176}\text{Hf}/^{177}\text{Hf}$ and $^{176}\text{Yb}/^{177}\text{Yb}$ ratios. The data reported in this study have been controlled plotting $^{176}\text{Hf}/^{177}\text{Hf}$ against $^{176}\text{Yb}/^{177}\text{Yb}$ and it is clear that irrelevant interference by Yb. This testifies that the data are reliable (Fig. SM2-1). Uncertainties are quadratic additions of the within-run precision and the reproducibility of the reference zircons, Plešovice (Sláma *et al.*, 2008), Temora (Wu *et al.*, 2006), 91500 (Blichert-Toft, 2008), Mud Tank (Woodhead & Hergt, 2005). Four reference materials were analysed before and during runs: Temora ($^{176}\text{Hf}/^{177}\text{Hf} = 0.282673 \pm 39$ (2SD), $n = 48$), Plešovice ($^{176}\text{Hf}/^{177}\text{Hf} = 0.282494 \pm 23$ (2SD), $n = 19$), Mud Tank ($^{176}\text{Hf}/^{177}\text{Hf} = 0.282520 \pm 21$ (2SD), $n = 67$). The values are in agreement within error with the recommended values for, Temora [$^{176}\text{Hf}/^{177}\text{Hf} = 0.282680 \pm 31$ (2σ); Wu *et al.*, 2006], Plešovice [$^{176}\text{Hf}/^{177}\text{Hf} = 0.282482 \pm 13$ (2σ); Sláma *et al.*, 2008], Mud Tank [$^{176}\text{Hf}/^{177}\text{Hf} = 0.282504 \pm 44$ (2σ); Woodhead & Hergt, 2005]. Irrelevant interference by Yb is also for the standards (Fig. SM2-2).

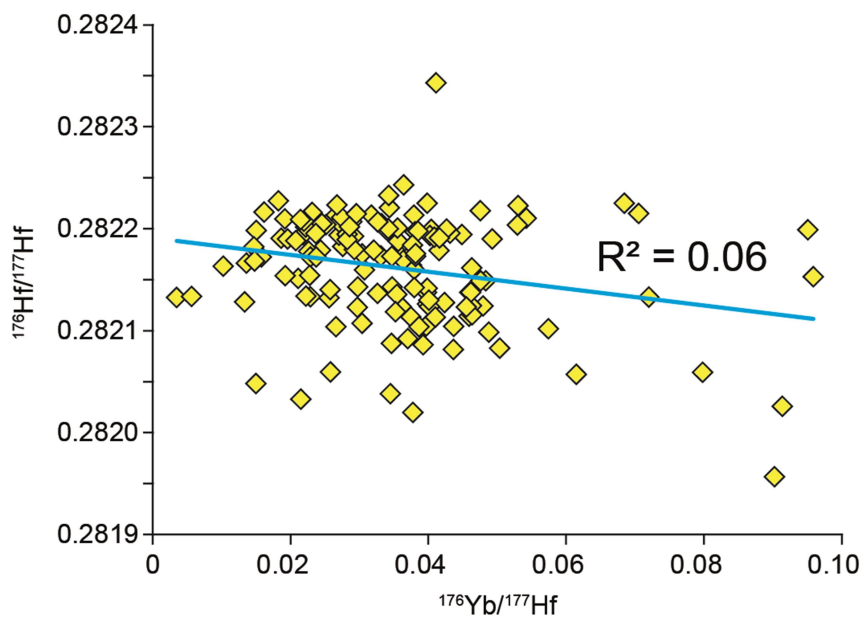


Fig. SM2-1. $^{176}\text{Yb}/^{177}\text{Hf}$ versus $^{176}\text{Hf}/^{177}\text{Hf}$ plot for the analysed Galiléia zircons

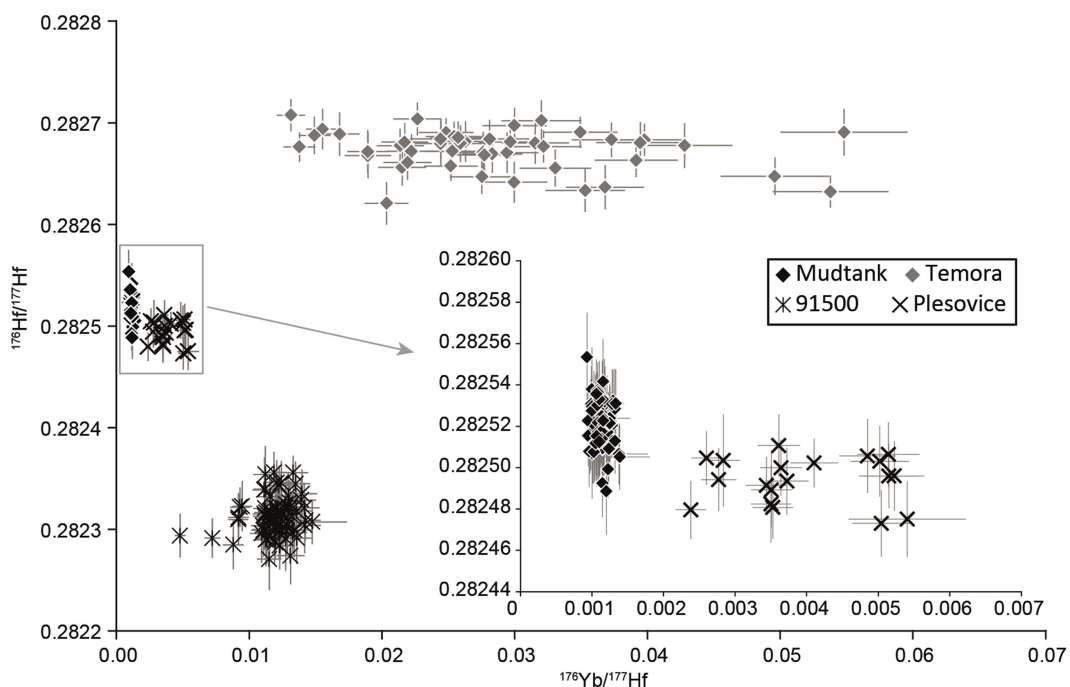


Fig. SM2-2. $^{176}\text{Yb}/^{177}\text{Hf}$ versus $^{176}\text{Hf}/^{177}\text{Hf}$ plot for the analysed standard zircons

Epsilon Hf (ϵHf) and Hf model ages were calculated using Chondritic Uniform Reservoir (CHUR) $^{176}\text{Lu}/^{177}\text{Hf}$ and $^{176}\text{Hf}/^{177}\text{Hf}$ values of 0.0336 and 0.282785 respectively (Bouvier *et al.*, 2008), “maximum” Depleted Mantle (DM) values of $^{176}\text{Lu}/^{177}\text{Hf} = 0.03933$ and $^{176}\text{Hf}/^{177}\text{Hf} = 0.283294$ (Blichert-Toft & Puchtel, 2010), a ^{176}Lu decay constant of $\lambda = 1.867 \times 10^{-11} \text{ a}^{-1}$ (Söderlund *et al.*, 2004) and a crustal source composition with a $^{176}\text{Lu}/^{177}\text{Hf}$ ratio of 0.0113 [mean of average continental crust as suggested by Taylor & McLennan (1985) and Wedepohl (1995)].

SM3: ADDITIONAL FIGURES

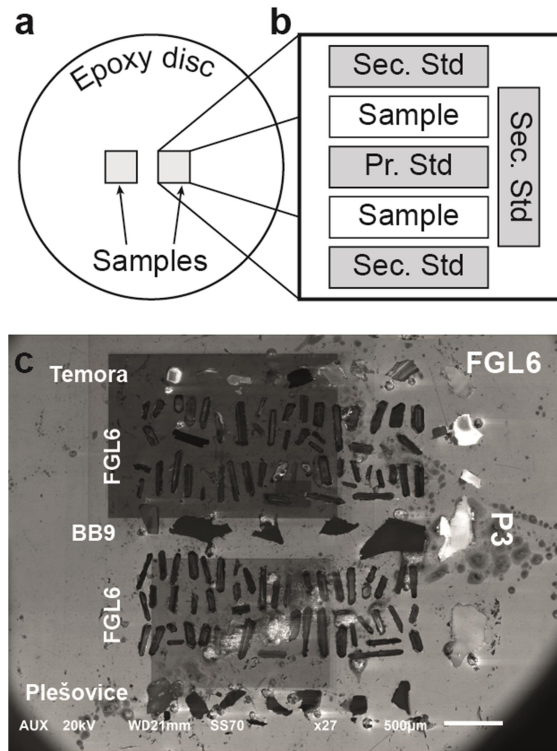


Fig. SM3-1. Example of mount set up for zircons analysed by high-precision dating

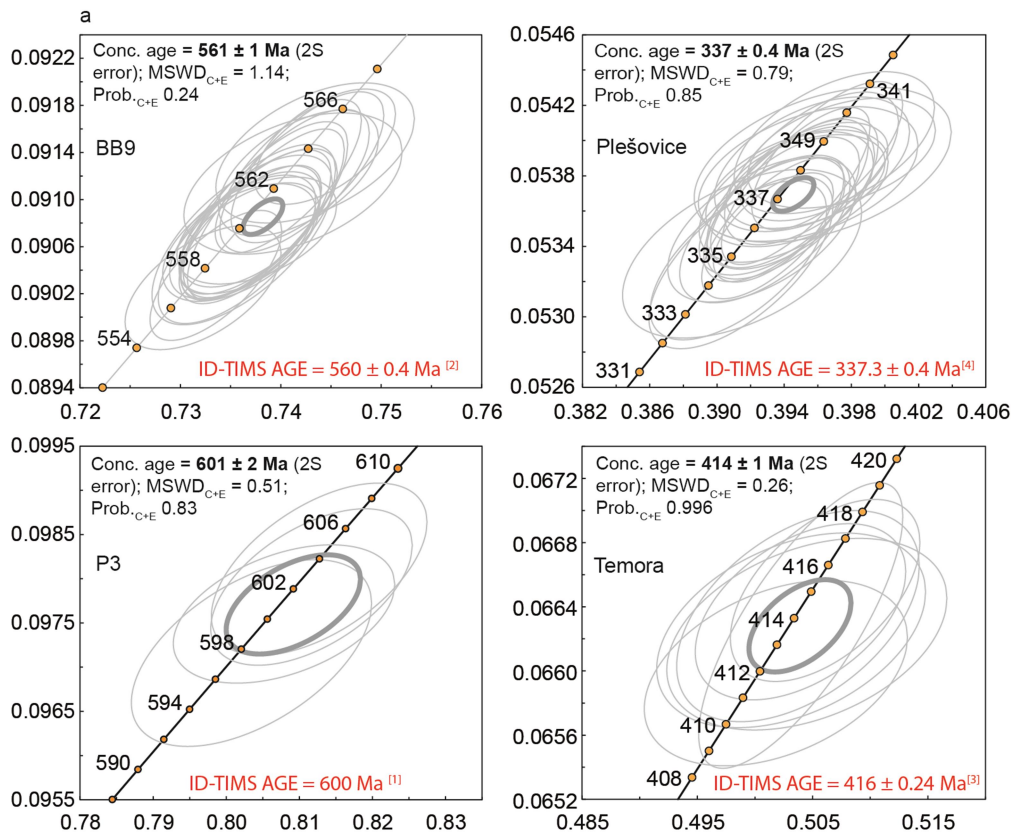


Fig. SM3-2. Concordia diagrams of the standards measured by high-precision multi collector dating. In red are reported the accepted ID-TIMS ages from: 1) Lana *et al.* (2017); 2) Santos *et al.* (2017); 3) Black *et al.* (2003); Sláma *et al.* (2008).

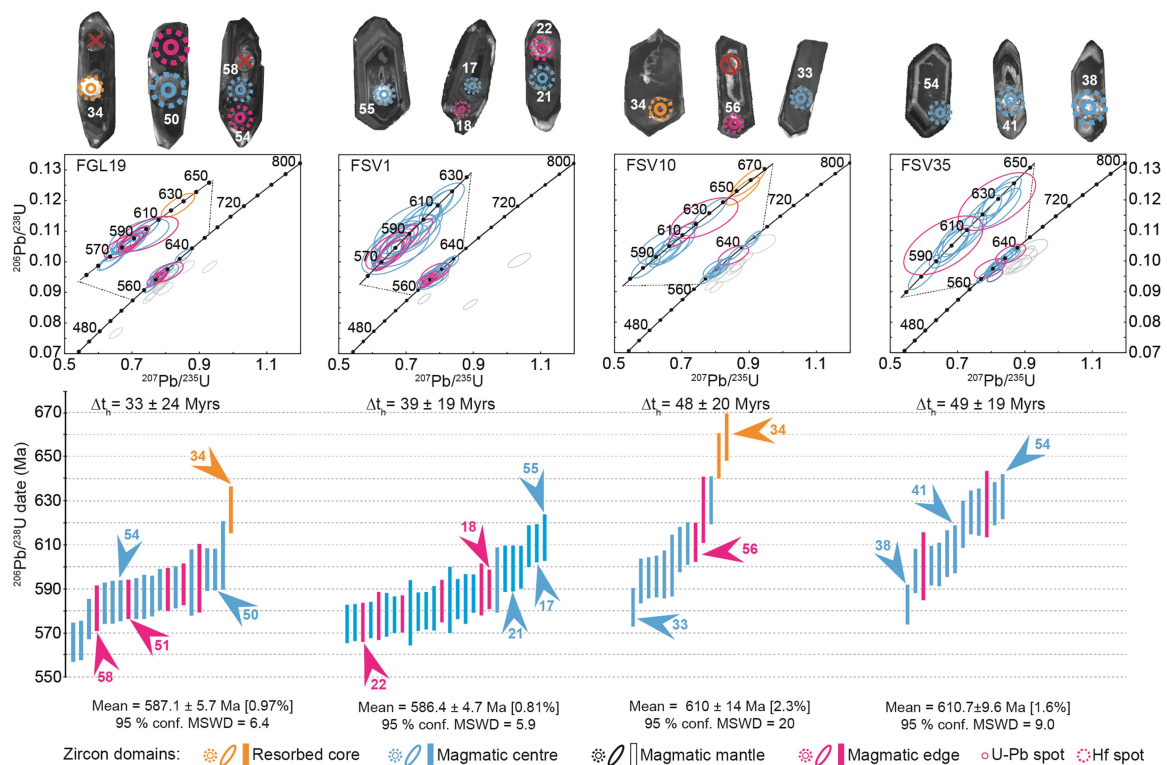


Fig. SM3-3. Zircon images, concordia diagrams and weighted mean plots of LA-SF-ICP-MS dating. Δt_h is the difference between the oldest and youngest magmatic dates for each hand sample. Ellipses and error bars are 2s.

SM4: NO Pb-LOSS IN THE GALILÉIA ZIRCONS

In literature, cases reporting evidences such as those studied here are rare (Ashwal *et al.*, 1999; Wang *et al.*, 2011). A good case is however reported for a single hand sample from a Neoproterozoic meta-leuconorite (Ashwal *et al.*, 1999) where ca. 30 dated zircons gave 100 Myrs of date dispersion (i.e. from 630 to 540 Ma). Mostly of these grains had fractures and after air-abrasion ID-TIMS dating, zircons showed a grain-size decrease as the relative date decreased. In this case, fractures and consequent Pb-loss and date reset were caused by long-lasting granulite facies metamorphism that the terrain was experiencing at the time of leuconorite intrusion (i.e. syn-magmatic deformation) (Ashwal *et al.*, 1999).

By contrast CL images have shown that Galiléia zircons are fracture-free, devoid of metamorphic overgrowths, in agreement with the weakly deformed character of the rocks, and metameric textures. Furthermore the high-precision date-pits were done in the magmatic domains and resorbed cores which have clear crystalline character.

Al, Ca, Fe, and Ba are non-stoichiometric elements which enter in the zircon crystalline structure once the grain undergoes re-equilibration due to interaction with aqueous fluids or melts (Davies *et al.*, 2015; Geisler *et al.*, 2007). This causes loss of Pb and the positive relationship between Ca and Ba and the α dose (the amount of radiation damage that zircon undergoes over time due to U and Th decay to different Pb isotopes; Davies *et al.*, 2015) indicates if zircon might have lost Pb or not (Davies *et al.*, 2015).

The α dose has been calculated as it follows (Davies *et al.*, 2015):

$$D\alpha = 8 \times \frac{cU \times NA \times 0.9928}{M_{238} \times 10^6} \times (e^{\lambda_{238}t} - 1) + 7 \times \frac{cU \times NA \times 0.0072}{M_{235} \times 10^6} \times (e^{\lambda_{235}t} - 1) + 6 \times \frac{cTh \times NA}{M_{232} \times 10^6} \times (e^{\lambda_{232}t} - 1).$$

$D\alpha$ is in units of α -decays/g. cU and cTh are the U and Th concentrations in ppm, NA is the Avogadro's number, M_{238} , M_{235} and M_{232} are the atomic weights, λ_{238} , λ_{235} and λ_{232} are the decay constants of each isotope and t is the measured zircon date.

Al and Fe were not analysed but Ca (and Ba) are enriched in the Galiléia zircons (Fig. SM4-1). Based on trace element contents and α dose, some data were excluded (Fig. 6). Nevertheless, it is possible to see that, despite some outsiders having high α dose ($> 6 \times 10^{18}$ α/g) regardless their high Ca and vice versa (Fig. SM4-1), this element once plotted against the relative zircon $^{206}Pb/^{238}U$ dates (Fig. B4-1), shows that the grains having high and below detection limit Ca content show the

same date dispersion irrespective of the calcium content. The same is seen for Ba. This argues against Pb-loss.

Pb-loss affects the U-Pb system whereas the Lu-Hf one remains closed. However, if zircons lost Pb, by plotting the measured zircon $^{176}\text{Hf}/^{177}\text{Hf}$ at present time ($t = 0$) against the relative date this would create a linear array according to the zircon date variation (e.g. Vervoort & Kemp, 2016). In Fig. 8c, Temora and Mud Tunk standards employed in our Lu-Hf analyses were used to simulate this Pb-loss-derived effect. Their $^{176}\text{Hf}/^{177}\text{Hf}_{t=0}$ was plotted against the same age variability (640 to 550 Ma) found in our study and compared the result with ours. By comparing Figs. 8b and c we do not envisage such linear trend for the Galiléia zircons.

In a fair way, we must report that few samples might appear to have lost Pb. For instance, accepting for the moment that these few samples have zircons that lost Pb, a question would be: why Hf isotopes should record Pb-loss only in these two samples whereas not in the others, despite all of them show the same date dispersion? For absurd, this would mean that i) Pb-loss was localized only in few parts of the Galiléia Batholith and ii) the dates related to Pb-loss reproduce the same date dispersion showed by the no-Pb-loss-related zircons. In our opinion this is quite unlikely to happen.

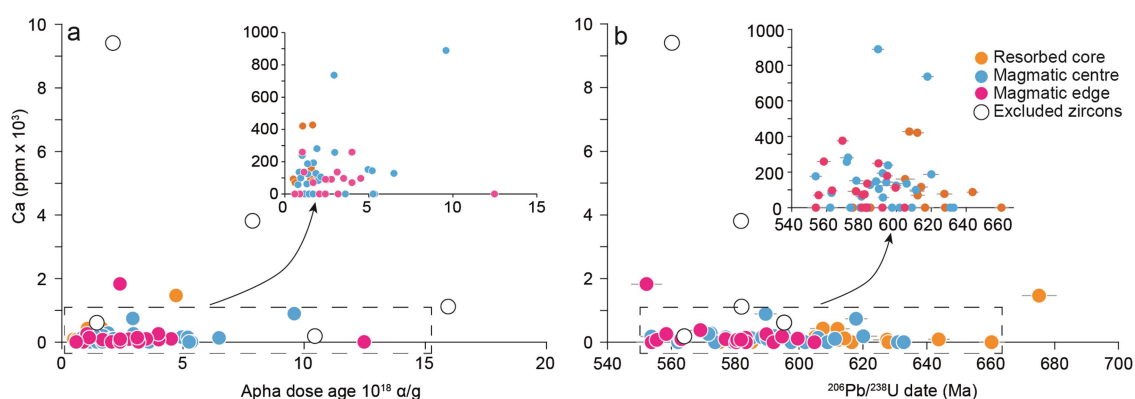


Fig. SM4-1. Zircon Ca content vs. a) alpha dose and b) $^{206}\text{Pb}/^{208}\text{U}$ high-precision date. In both images inset report the area indicated with the black dotted area.

References

Albert C., Farina F., Lana C., Stevens G., Storey C., Gerdes A., Dopico C.M., 2016. Archean crustal evolution in the Southern São Francisco craton, Brazil: Constraints from U-Pb, Lu-Hf and O isotope analyses. *Lithos*, **266–267**:64–86.

Ashwal L.D., Tucker R.D., Zinner E.K. 1999. Slow cooling of deep crustal granulites and Pb-loss in zircon. *Geochimica et Cosmochimica Acta*, 63: 2839–2851

Black L.P., Kamo S.L., Allen C.M., Aleinikoff J.N., Davis D.W., Korsch R.J., Foudoulis C., 2003. TEMORA 1: A new zircon standard for Phanerozoic U-Pb geochronology. *Chemical Geology*, **200**:155–170

Blichert-Toft J., 2008. The Hf isotopic composition of zircon reference material 91500. *Chemical Geology*, **253**:252–257.

Blichert-Toft J. & Puchtel I.S. 2010. Depleted mantle sources through time: Evidence from Lu-Hf and Sm-Nd isotope systematics of Archean komatiites. *Earth and Planetary Science Letters*, **297**:598–606

Bouvier A., Vervoort J.D., Patchett P.J. 2008. The Lu-Hf and Sm-Nd isotopic composition of CHUR: Constraints from unequilibrated chondrites and implications for the bulk composition of terrestrial planets. *Earth and Planetary Science Letters*, **273**:48–57

Davies J.H.F.L., Stern R.A., Heaman L.M., Rojas X., Walton E.L., 2015. Resolving oxygen isotopic disturbance in zircon: A case study from the low $\delta^{18}\text{O}$ Scourie dikes, NW Scotland. *American Mineralogist*, **100**:1952–1966.

Farina F., Albert C., Lana C., 2015. The Neoproterozoic transition between medium- and high-K granitoids: Clues from the Southern São Francisco Craton (Brazil). *Precambrian Research*, **266**:375–394.

Frei D. & Gerdes A. 2009. Precise and accurate in situ U–Pb dating of zircon with high sample throughput by automated LA-SF-ICP-MS. *Chemical Geology*, **261**:261–270

Geisler T., Schaltegger U., Tomaschek F. 2007. Re-equilibration of zircon in aqueous fluids and melts. *Elements*, **3**:43–50.

Gerdes A. & Zeh A. 2006. Combined U–Pb and Hf isotope LA-(MC-)ICP-MS analyses of detrital zircons: Comparison with SHRIMP and new constraints for the provenance and age of an Armorican metasediment in Central Germany. *Earth and Planetary Science Letters*, **249**:47–61

Gerdes A. & Zeh A. 2009. Zircon formation versus zircon alteration - New insights from combined U-Pb and Lu-Hf in-situ LA-ICP-MS analyses, and consequences for the interpretation of Archean zircon from the Central Zone of the Limpopo Belt. *Chemical Geology*, **261**:230–243

Horstwood M.S.A., Košler J., Gehrels G., Jackson S.E., McLean N.M. Paton C., Pearson N.J., Sircombe K., Sylvester P., Vermeesch P., Bowring J.F., Condon D.J., Schoene B. 2016. Community-Derived Standards for LA-ICP-MS U-(Th-)Pb Geochronology – Uncertainty Propagation, Age Interpretation and Data Reporting. *Geostandards Geoanalytical Research*, **40**:311–332.

Jackson S.E., Pearson N.J., Griffin W.L., Belousova E.A. 2004. The application of laser ablation-inductively coupled plasma-mass spectrometry to in situ U-Pb zircon geochronology. *Chemical Geology*, **211**:47–69

Ludwig K.R. 2003 Isoplot/EX Version 3.00: A Geochronological Toolkit for Microsoft Excel. Berkeley Geochronology Center, Berkeley, CA.

Santos M.M., Lana C., Scholz R., Buick I., Schmitz M.D., Kamo S.L., Gerdes A., Corfu F., Tapster S., Lancaster P., Storey C.D., Basei M.A.S., Tohver E., Alkmim A., Nalini H., Krambrock K., Fantini C., Wiedenbeck M., 2017. A New Appraisal of Sri Lankan BB Zircon as a Reference Material for LA-ICP-MS U-Pb Geochronology and Lu-Hf Isotope Tracing. *Geostandards Geoanalytical Research*, **41**:335–358

Segal I., Halicz L., Platzner I.T., 2003. Accurate isotope ratio measurements of ytterbium by multiple collection inductively coupled plasma mass spectrometry applying erbium and hafnium in an improved double external normalization procedure. *Journal of Analytical Atomic Spectrometry*, **18**:1217

Sláma J., Košler J., Condon D.J., Crowley J.L., Gerdes A., Hanchar J.M., Horstwood M.S.A., Morris G.A., Nasdala L., Norberg N., Schaltegger U., Schoene B., Tubrett M.N., Whitehouse M.J., 2008. Plešovice zircon - A new natural reference material for U-Pb and Hf isotopic microanalysis. *Chemical Geology*, **249**:1–35

Söderlund U., Patchett P.J., Vervoort J.D., Isachsen C.E., 2004. The ^{176}Lu decay constant determined by Lu-Hf and U-Pb isotope systematics of Precambrian mafic intrusions. *Earth and Planetary Science Letters*, **219**:311–324

Stacey J.S. & Kramers J.D., 1975. Approximation of terrestrial lead isotope evolution by a two stage model. *Earth and Planetary Science Letters*, **26**:207–221.

Taylor S. & McLennan S., 1995. The geochemical evolution of the continental crust. *Review in Geophysics*, **33**:241–265.

Van Achterbergh E., Ryan C.G., Jackson S.E., Griffin W.L., 2001. Data reduction software for LA-ICP-MS: appendix. In: Sylvester, P.J. (Ed.), *Laser Ablation-ICP Mass Spectrometry in the Earth Sciences: Principles and Applications*, vol. 29. *Mineralogical Association of Canada (MAC) Short Course Series*, Ottawa, Ontario, Canada, pp. 239–243.

Vervoort J.D. & Kemp, A.I.S. 2016. Clarifying the zircon Hf isotope record of crust-mantle evolution. *Chemical Geology*, **425**:65–75.

Wang Y., Liu D., Dong C., Liu S., Wang S., Yang E. 2011. U–Th–Pb behavior of zircons under high-grade metamorphic conditions: A case study of zircon dating of meta-diorite near Qixia, eastern Shandong. *Geoscience Frontiers*, **2**:137–146.

Wedepohl K.H. 1995. INGERSON LECTURE The composition of the continental crust. *Geochimica et Cosmochimica Acta* **59**: 1217–1232

Woodhead J.D. & Hergt J.M. 2005. A Preliminary Appraisal of Seven Natural Zircon Reference Materials for In Situ Hf Isotope Determination. *Geostandards Geoanalytical Research*, **29**:183–195

Wu F.-Y., Yang Y.-H., Xie L.-W., Yang J.-H., Xu P., 2006. Hf isotopic compositions of the standard zircons and baddeleyites used in U–Pb geochronology. *Chemical Geology*, **234**:105–126

Table 1. LA-SF-ICP-MS U-Pb Galiléia zircon dates; (a) Data corrected for common Pb; (b) Concordance calculated as $(^{206}\text{Pb}/^{238}\text{U}/^{207}\text{Pb}/^{206}\text{Pb}) * 100$; (c) Error correlation defined as the quotient of the propagated errors of the $^{206}\text{Pb}/^{238}\text{U}$ and the $^{207}\text{Pb}/^{235}\text{U}$ ratio

Sample	Spot position	U	Th/U	204 Corrected Ratios ^a						204 corrected ages							
		ppm		$^{207}\text{Pb}/^{206}\text{Pb}$	2s	$^{206}\text{Pb}/^{238}\text{U}$	2s	$^{207}\text{Pb}/^{235}\text{U}$	2s	RHO ^c	$^{207}\text{Pb}/^{206}\text{Pb}$	2s	$^{206}\text{Pb}/^{238}\text{U}$	2s	$^{207}\text{Pb}/^{235}\text{U}$	2s	Conc ^b
FGL19	centre	479	0.31	0.0596	1.125	0.0917	1.635	0.7532	1.985	0.824	587	24	566	9	570	9	99
FGL19	centre	687	0.20	0.0597	1.139	0.0919	1.633	0.7561	1.991	0.820	592	25	567	9	572	9	99
FGL19	centre	517	0.25	0.0593	1.158	0.0935	1.643	0.7642	2.010	0.817	577	25	576	9	576	9	100
FGL19	edge	537	0.15	0.0592	2.003	0.0943	1.851	0.7701	2.727	0.679	575	44	581	10	580	12	100
FGL19	centre	232	0.30	0.0594	1.263	0.0947	1.668	0.7752	2.093	0.797	580	27	583	9	583	9	100
FGL19	centre	303	0.20	0.0600	1.266	0.0948	1.730	0.7848	2.144	0.807	605	27	584	10	588	10	99
FGL19	centre	675	0.21	0.0594	1.207	0.0949	1.654	0.7775	2.048	0.808	582	26	585	9	584	9	100
FGL19	edge	1177	0.14	0.0598	1.088	0.0950	1.579	0.7831	1.917	0.824	595	24	585	9	587	9	100
FGL19	centre	322	0.41	0.0599	1.169	0.0951	1.641	0.7850	2.015	0.814	599	25	586	9	588	9	100
FGL19	centre	290	0.36	0.0593	1.754	0.0952	1.770	0.7788	2.491	0.710	579	38	586	10	585	11	100
FGL19	centre	288	0.40	0.0595	1.177	0.0953	1.637	0.7815	2.016	0.812	585	26	587	9	586	9	100
FGL19	centre	382	0.21	0.0596	1.124	0.0958	1.650	0.7869	1.996	0.826	589	24	590	9	589	9	100
FGL19	edge	262	0.33	0.0596	1.259	0.0958	1.733	0.7868	2.142	0.809	588	27	590	10	589	10	100
FGL19	centre	127	0.35	0.0597	1.308	0.0960	1.688	0.7891	2.136	0.791	591	28	591	10	591	10	100
FGL19	edge	196	0.31	0.0596	1.207	0.0962	1.664	0.7908	2.056	0.809	590	26	592	9	592	9	100
FGL19	centre	212	0.27	0.0599	3.560	0.0963	2.634	0.7955	4.428	0.595	600	77	593	15	594	20	100
FGL19	centre	169	0.35	0.0606	3.586	0.0967	2.716	0.8076	4.498	0.604	625	77	595	15	601	21	99
FGL19	centre	162	0.33	0.0599	1.270	0.0973	1.685	0.8030	2.110	0.799	598	28	599	10	599	10	100
FGL19	centre	433	0.21	0.0598	1.304	0.0973	1.644	0.8026	2.098	0.784	597	28	599	9	598	10	100
FGL19	centre	169	0.35	0.0606	3.586	0.0967	2.716	0.8076	4.498	0.604	625	77	605	15	601	21	99
FGL19	resorbed	181	0.13	0.0606	1.518	0.1019	1.766	0.8518	2.329	0.758	626	33	626	11	626	11	100

Continuation Table 1

Sample	Spot position	U ppm	Th/U	204 Corrected Ratios ^a						204 corrected ages							
				²⁰⁷ Pb/ ²⁰⁶ Pb	2s	²⁰⁶ Pb/ ²³⁸ U	2s	²⁰⁷ Pb/ ²³⁵ U	2s	RHO ^c	²⁰⁷ Pb/ ²⁰⁶ Pb	2s	²⁰⁶ Pb/ ²³⁸ U	2s	²⁰⁷ Pb/ ²³⁵ U	2s	Conc ^b
FGL22	centre	827	0.12	0.0600	1.066	0.0936	1.667	0.7746	1.979	0.842	605	23	577	9	582	9	99
FGL22	edge	495	0.29	0.0593	1.247	0.0940	1.638	0.7692	2.059	0.795	579	27	579	9	579	9	100
FGL22	centre	255	0.22	0.0598	1.254	0.0943	1.824	0.7779	2.213	0.824	597	27	581	10	584	10	99
FGL22	edge	192	0.43	0.0596	1.191	0.0953	1.722	0.7828	2.094	0.822	589	26	587	10	587	9	100
FGL22	centre	296	0.27	0.0596	1.124	0.0956	1.695	0.7853	2.034	0.833	589	24	588	10	588	9	100
FGL22	centre	380	0.30	0.0597	1.814	0.0969	1.925	0.7972	2.645	0.728	592	39	596	11	595	12	100
FGL22	edge	227	0.23	0.0598	1.343	0.0971	1.669	0.8001	2.142	0.779	595	29	598	10	597	10	100
FGL22	centre	160	0.27	0.0605	3.521	0.0972	2.687	0.8104	4.429	0.607	620	76	598	15	603	20	99
FGL22	centre	241	0.55	0.0602	1.380	0.0987	1.905	0.8185	2.352	0.810	609	30	607	11	607	11	100
FGL22	centre	121	0.29	0.0604	3.547	0.0989	2.681	0.8238	4.446	0.603	619	77	608	16	610	21	100
FGL22	centre	85	0.40	0.0612	1.634	0.1019	1.826	0.8594	2.451	0.745	646	35	625	11	630	12	99
FGL22	resorbed	198	0.35	0.0611	1.146	0.1043	1.706	0.8784	2.055	0.830	641	25	640	10	640	10	100
													49	20			
FGL26	centre	175	0.36	0.0588	1.259	0.0913	1.753	0.7397	2.158	0.812	559	27	563	9	562	9	100
FGL26	centre	485	0.23	0.0590	1.204	0.0921	1.460	0.7492	1.892	0.772	566	26	568	8	568	8	100
FGL26	centre	125	0.71	0.0586	1.212	0.0934	1.628	0.7546	2.029	0.802	552	26	576	9	571	9	101
FGL26	resorbed	79	0.39	0.0593	1.871	0.0949	1.854	0.7766	2.634	0.704	580	41	585	10	584	12	100
FGL26	edge	162	0.21	0.0599	1.320	0.0952	1.533	0.7859	2.023	0.758	599	29	586	9	589	9	100
FGL26	centre	541	0.27	0.0595	1.091	0.0953	1.579	0.7821	1.919	0.823	587	24	587	9	587	9	100
FGL26	centre	379	0.22	0.0596	1.107	0.0962	1.559	0.7908	1.912	0.815	589	24	592	9	592	9	100
FGL26	centre	72	0.40	0.0588	6.809	0.0972	4.362	0.7877	8.086	0.539	558	148	598	25	590	37	101
FGL26	centre	141	0.34	0.0612	2.420	0.0992	2.115	0.8366	3.214	0.658	646	52	610	12	617	15	99
FGL26	centre	417	0.22	0.0603	1.486	0.1010	1.829	0.8394	2.356	0.776	614	32	620	11	619	11	100
FGL26	centre	345	0.19	0.0604	1.238	0.1014	1.758	0.8449	2.150	0.818	619	27	623	10	622	10	100
FGL26	centre	425	0.29	0.0607	1.136	0.1018	1.729	0.8524	2.069	0.836	630	24	625	10	626	10	100
FGL26	resorbed	58	0.23	0.0635	2.504	0.1172	2.150	1.0259	3.301	0.651	725	53	714	15	717	17	100

Continuation Table 1

Sample	Spot position	U ppm	Th/U	204 Corrected Ratios ^a						204 corrected ages							
				²⁰⁷ Pb/ ²⁰⁶ Pb	2s	²⁰⁶ Pb/ ²³⁸ U	2s	²⁰⁷ Pb/ ²³⁵ U	2s	RHO ^c	²⁰⁷ Pb/ ²⁰⁶ Pb	2s	²⁰⁶ Pb/ ²³⁸ U	2s	²⁰⁷ Pb/ ²³⁵ U	2s	Conc ^b
<i>FGL40</i>	<i>centre</i>	548	0.19	0.0585	1.077	0.0890	1.574	0.7178	1.907	0.825	549	24	549	8	549	8	100
<i>FGL40</i>	<i>centre</i>	327	0.32	0.0587	1.124	0.0903	1.551	0.7307	1.915	0.810	556	25	557	8	557	8	100
<i>FGL40</i>	<i>mantle</i>	999	0.43	0.0589	1.014	0.0904	1.508	0.7347	1.817	0.830	565	22	558	8	559	8	100
<i>FGL40</i>	<i>centre</i>	738	0.26	0.0591	1.016	0.0907	1.499	0.7391	1.811	0.828	570	22	560	8	562	8	100
<i>FGL40</i>	<i>centre</i>	152	0.34	0.0592	1.386	0.0930	1.678	0.7586	2.176	0.771	573	30	573	9	573	10	100
<i>FGL40</i>	<i>centre</i>	260	0.36	0.0592	1.232	0.0935	1.562	0.7635	1.989	0.785	576	27	576	9	576	9	100
<i>FGL40</i>	<i>centre</i>	477	0.56	0.0592	1.148	0.0937	1.537	0.7651	1.919	0.801	576	25	577	8	577	8	100
<i>FGL40</i>	<i>edge</i>	131	0.48	0.0601	3.753	0.0940	2.849	0.7783	4.712	0.605	606	81	579	16	585	21	99
<i>FGL40</i>	<i>centre</i>	430	0.18	0.0594	1.279	0.0942	1.635	0.7714	2.076	0.788	582	28	580	9	581	9	100
<i>FGL40</i>	<i>edge</i>	153	0.46	0.0593	1.753	0.0942	1.975	0.7704	2.641	0.748	579	38	580	11	580	12	100
<i>FGL40</i>	<i>centre</i>	446	0.18	0.0593	1.079	0.0943	1.528	0.7710	1.870	0.817	579	23	581	8	580	8	100
<i>FGL40</i>	<i>centre</i>	340	0.45	0.0598	1.355	0.0943	1.548	0.7775	2.057	0.753	596	29	581	9	584	9	99
<i>FGL40</i>	<i>edge</i>	460	0.42	0.0594	1.060	0.0945	1.524	0.7741	1.856	0.821	582	23	582	8	582	8	100
<i>FGL40</i>	<i>edge</i>	131	0.65	0.0595	1.463	0.0946	1.670	0.7756	2.220	0.752	584	32	583	9	583	10	100
<i>FGL40</i>	<i>edge</i>	287	0.25	0.0595	1.580	0.0947	1.648	0.7766	2.283	0.722	585	34	583	9	584	10	100
<i>FGL40</i>	<i>centre</i>	82	0.36	0.0592	2.230	0.0952	1.940	0.7768	2.956	0.656	575	48	586	11	584	13	100
<i>FGL40</i>	<i>resorbed</i>	185	0.67	0.0598	1.955	0.0952	1.848	0.7856	2.691	0.687	598	42	586	10	589	12	100
<i>FGL40</i>	<i>centre</i>	625	0.36	0.0598	3.524	0.0955	2.593	0.7868	4.375	0.593	595	76	588	15	589	20	100
<i>FGL40</i>	<i>centre</i>	271	0.59	0.0599	1.536	0.0975	1.806	0.8047	2.371	0.762	600	33	599	10	599	11	100
<i>FGL40</i>	<i>edge</i>	102	0.23	0.0603	2.139	0.0989	1.961	0.8225	2.902	0.676	614	46	608	11	609	13	100
<i>FGL40</i>	<i>core</i>	216	0.48	0.0602	1.362	0.0996	1.667	0.8268	2.152	0.774	611	29	612	10	612	10	100
<i>FGL6</i>	<i>centre</i>	470	0.26	0.0592	3.596	0.0923	2.696	0.7533	4.495	0.600	575	78	569	15	570	20	100
<i>FGL6</i>	<i>edge</i>	311	0.36	0.0583	1.169	0.0924	1.604	0.7429	1.985	0.808	543	26	569	9	564	9	101
<i>FGL6</i>	<i>centre</i>	455	0.19	0.0597	1.172	0.0937	1.601	0.7712	1.985	0.807	593	25	577	9	580	9	99
<i>FGL6</i>	<i>centre</i>	884	0.24	0.0600	1.151	0.0942	1.593	0.7785	1.965	0.811	602	25	580	9	585	9	99

Continuation Table 1

Sample	Spot position	U	Th/U	204 Corrected Ratios a						204 corrected ages							
		ppm		²⁰⁷ Pb/ ²⁰⁶ Pb	2s	²⁰⁶ Pb/ ²³⁸ U	2s	²⁰⁷ Pb/ ²³⁵ U	2s	RHO ^c	²⁰⁷ Pb/ ²⁰⁶ Pb	2s	²⁰⁶ Pb/ ²³⁸ U	2s	²⁰⁷ Pb/ ²³⁵ U	2s	Conc b
<i>FGL6</i>	<i>centre</i>	682	0.15	0.0607	1.137	0.0971	1.586	0.8121	1.952	0.813	628	25	597	9	604	9	99
<i>FGL6</i>	<i>centre</i>	532	0.13	0.0597	1.105	0.0981	1.570	0.8073	1.920	0.818	593	24	603	9	601	9	100
<i>FGL6</i>	<i>centre</i>	234	0.48	0.0594	1.196	0.0985	1.605	0.8058	2.001	0.802	580	26	605	9	600	9	101
<i>FGL6</i>	<i>centre</i>	260	0.37	0.0600	1.217	0.0992	1.613	0.8205	2.020	0.798	603	26	610	9	608	9	100
<i>FGL6</i>	<i>centre</i>	310	0.49	0.0595	1.216	0.0992	1.612	0.8140	2.019	0.798	585	26	610	9	605	9	101
<i>FGL6</i>	<i>centre</i>	74	0.67	0.0594	4.034	0.1004	2.903	0.8223	4.970	0.584	582	88	617	17	609	23	101
<i>FGL6</i>	<i>centre</i>	453	0.20	0.0596	1.209	0.1007	1.608	0.8270	2.012	0.799	587	26	619	9	612	9	101
<i>FGL6</i>	<i>centre</i>	342	0.30	0.0596	3.572	0.1018	2.540	0.8367	4.383	0.580	589	77	625	15	617	20	101
<i>FGL6</i>	<i>centre</i>	229	0.32	0.0608	1.317	0.1021	1.646	0.8551	2.108	0.781	630	28	627	10	627	10	100
<i>FGL6</i>	<i>resorbed</i>	213	0.45	0.0601	1.181	0.1024	1.602	0.8491	1.990	0.805	609	26	628	10	624	9	101
<i>FGL6</i>	<i>resorbed</i>	288	0.27	0.0606	1.166	0.1047	1.608	0.8743	1.986	0.810	624	25	642	10	638	9	101
<i>FSV1</i>	<i>centre</i>	448	0.56	0.0592	1.318	0.0932	1.589	0.7602	2.064	0.770	574	29	574	9	574	9	100
<i>FSV1</i>	<i>centre</i>	419	0.32	0.0593	1.113	0.0933	1.522	0.7627	1.886	0.807	578	24	575	8	576	8	100
<i>FSV1</i>	<i>edge</i>	215	0.17	0.0593	1.299	0.0933	1.608	0.7623	2.067	0.778	577	28	575	9	575	9	100
<i>FSV1</i>	<i>centre</i>	340	0.21	0.0592	1.166	0.0935	1.498	0.7626	1.898	0.789	574	25	576	8	576	8	100
<i>FSV1</i>	<i>edge</i>	192	0.25	0.0589	2.297	0.0938	1.969	0.7617	3.026	0.651	563	50	578	11	575	13	101
<i>FSV1</i>	<i>centre</i>	185	0.53	0.0592	1.979	0.0939	1.799	0.7657	2.674	0.673	573	43	578	10	577	12	100
<i>FSV1</i>	<i>centre</i>	234	0.51	0.0592	1.249	0.0939	1.513	0.7668	1.962	0.771	576	27	578	8	578	9	100
<i>FSV1</i>	<i>edge</i>	265	0.18	0.0594	1.314	0.0939	1.533	0.7690	2.019	0.759	581	29	579	8	579	9	100
<i>FSV1</i>	<i>centre</i>	133	0.59	0.0595	3.610	0.0940	2.659	0.7707	4.484	0.593	584	78	579	15	580	20	100
<i>FSV1</i>	<i>centre</i>	650	0.33	0.0593	1.450	0.0941	1.573	0.7696	2.139	0.735	579	32	580	9	580	9	100
<i>FSV1</i>	<i>centre</i>	186	0.57	0.0594	1.230	0.0942	1.529	0.7706	1.962	0.779	580	27	580	8	580	9	100
<i>FSV1</i>	<i>centre</i>	217	0.95	0.0592	1.819	0.0944	1.807	0.7700	2.564	0.705	574	40	581	10	580	11	100
<i>FSV1</i>	<i>edge</i>	199	0.12	0.0592	1.861	0.0949	1.726	0.7748	2.538	0.680	575	40	584	10	582	11	100
<i>FSV1</i>	<i>centre</i>	142	0.45	0.0598	3.704	0.0950	2.683	0.7829	4.574	0.587	596	80	585	15	587	21	100

Continuation Table 1

Sample	Spot position	U ppm	Th/U	204 Corrected Ratios ^a						204 corrected ages							
				²⁰⁷ Pb/ ²⁰⁶ Pb	2s	²⁰⁶ Pb/ ²³⁸ U	2s	²⁰⁷ Pb/ ²³⁵ U	2s	RHO ^c	²⁰⁷ Pb/ ²⁰⁶ Pb	2s	²⁰⁶ Pb/ ²³⁸ U	2s	²⁰⁷ Pb/ ²³⁵ U	2s	Conc b
<i>FSV1</i>	<i>centre</i>	176	0.11	0.0595	1.278	0.0951	1.620	0.7797	2.063	0.785	585	28	585	9	585	9	100
<i>FSV1</i>	<i>centre</i>	320	0.37	0.0591	2.492	0.0951	2.011	0.7747	3.202	0.628	571	54	585	11	582	14	101
<i>FSV1</i>	<i>centre</i>	227	0.45	0.0596	1.309	0.0955	1.550	0.7847	2.029	0.764	589	28	588	9	588	9	100
<i>FSV1</i>	<i>edge</i>	224	0.16	0.0604	1.192	0.0958	1.587	0.7975	1.985	0.799	617	26	590	9	595	9	99
<i>FSV1</i>	<i>centre</i>	205	0.49	0.0599	2.536	0.0958	2.082	0.7907	3.281	0.634	599	55	590	12	592	15	100
<i>FSV1</i>	<i>edge</i>	187	0.37	0.0591	3.606	0.0965	2.590	0.7869	4.440	0.583	572	78	594	15	589	20	101
<i>FSV1</i>	<i>centre</i>	150	0.35	0.0595	2.048	0.0974	1.834	0.7990	2.749	0.667	586	44	599	10	596	12	100
<i>FSV1</i>	<i>centre</i>	214	0.55	0.0598	1.755	0.0974	1.828	0.8035	2.534	0.721	598	38	599	10	599	12	100
<i>FSV1</i>	<i>centre</i>	136	0.34	0.0598	1.672	0.0975	1.702	0.8042	2.386	0.713	596	36	600	10	599	11	100
<i>FSV1</i>	<i>centre</i>	281	0.17	0.0601	1.360	0.0991	1.629	0.8217	2.122	0.768	608	29	609	9	609	10	100
<i>FSV1</i>	<i>centre</i>	983	0.22	0.0602	1.063	0.0993	1.490	0.8242	1.831	0.814	610	23	610	9	610	8	100
<i>FSV1</i>	<i>centre</i>	115	0.26	0.0604	1.905	0.0998	1.804	0.8302	2.624	0.688	617	41	613	11	614	12	100
<i>FSV10</i>	<i>centre</i>	319	0.24	0.0595	1.339	0.0944	1.593	0.7744	2.081	0.765	585	29	582	9	582	9	100
<i>FSV10</i>	<i>centre</i>	292	0.23	0.0603	1.245	0.0964	1.805	0.8010	2.192	0.823	613	27	593	10	597	10	99
<i>FSV10</i>	<i>centre</i>	304	0.26	0.0601	1.198	0.0967	1.655	0.8011	2.043	0.810	608	26	595	9	597	9	100
<i>FSV10</i>	<i>centre</i>	404	0.33	0.0595	1.143	0.0968	1.674	0.7936	2.027	0.826	585	25	595	10	593	9	100
<i>FSV10</i>	<i>centre</i>	158	0.60	0.0606	1.503	0.0969	1.919	0.8093	2.437	0.787	624	32	596	11	602	11	99
<i>FSV10</i>	<i>centre</i>	355	0.24	0.0596	3.046	0.0976	2.452	0.8018	3.910	0.627	588	66	600	14	598	18	100
<i>FSV10</i>	<i>centre</i>	388	0.23	0.0600	1.346	0.0988	1.787	0.8181	2.237	0.799	605	29	608	10	607	10	100
<i>FSV10</i>	<i>centre</i>	1375	0.22	0.0602	1.097	0.0994	1.671	0.8241	1.999	0.836	609	24	611	10	610	9	100
<i>FSV10</i>	<i>edge</i>	2980	0.45	0.0602	1.180	0.0994	1.549	0.8245	1.948	0.795	609	26	611	9	611	9	100
<i>FSV10</i>	<i>edge</i>	643	0.33	0.0607	3.535	0.1019	2.525	0.8533	4.345	0.581	629	76	626	15	626	21	100
<i>FSV10</i>	<i>centre</i>	1029	0.11	0.0607	1.184	0.1027	1.815	0.8597	2.167	0.838	630	26	630	11	630	10	100
<i>FSV10</i>	<i>resorbed</i>	744	0.49	0.0619	1.115	0.1061	1.678	0.9054	2.014	0.833	670	24	650	10	655	10	99
<i>FSV10</i>	<i>resorbed</i>	2713	0.31	0.0615	1.116	0.1076	1.720	0.9122	2.050	0.839	657	24	659	11	658	10	100

Continuation Table 1

Sample	Spot position	U	Th/U	204 Corrected Ratios ^a							204 corrected ages						
		ppm		²⁰⁷ Pb/ ²⁰⁶ Pb	2s	²⁰⁶ Pb/ ²³⁸ U	2s	²⁰⁷ Pb/ ²³⁵ U	2s	RHO ^c	²⁰⁷ Pb/ ²⁰⁶ Pb	2s	²⁰⁶ Pb/ ²³⁸ U	2s	²⁰⁷ Pb/ ²³⁵ U	2s	Conc ^b
FSV35	centre	233	0.46	0.0594	1.146	0.0946	1.628	0.7743	1.990	0.818	580	25	583	9	582	9	100
FSV35	centre	138	0.31	0.0599	1.503	0.0972	1.770	0.8026	2.322	0.762	600	33	598	10	598	11	100
FSV35	edge	214	0.41	0.0592	3.860	0.0976	2.702	0.7961	4.712	0.573	574	84	600	16	595	21	101
FSV35	centre	3305	0.31	0.0600	1.007	0.0976	1.579	0.8082	1.873	0.843	605	22	600	9	601	9	100
FSV35	centre	393	0.53	0.0598	1.192	0.0977	1.737	0.8058	2.107	0.825	597	26	601	10	600	10	100
FSV35	centre	216	0.28	0.0599	1.701	0.0985	1.839	0.8142	2.505	0.734	601	37	606	11	605	11	100
FSV35	centre	140	0.49	0.0602	1.744	0.0989	1.881	0.8207	2.565	0.733	611	38	608	11	608	12	100
FSV35	centre	182	0.39	0.0604	1.390	0.1008	1.825	0.8402	2.294	0.796	619	30	619	11	619	11	100
FSV35	centre	453	0.41	0.0616	1.264	0.1017	1.681	0.8640	2.103	0.799	660	27	625	10	632	10	99
FSV35	centre	633	0.41	0.0608	1.251	0.1018	1.808	0.8524	2.199	0.822	630	27	625	11	626	10	100
FSV35	edge	398	0.58	0.0608	3.454	0.1024	2.526	0.8583	4.279	0.590	632	74	628	15	629	20	100
FSV35	centre	209	0.36	0.0607	1.235	0.1024	1.640	0.8576	2.053	0.799	630	27	629	10	629	10	100
FSV35	centre	208	0.06	0.0609	1.315	0.1030	1.709	0.8638	2.157	0.793	634	28	632	10	632	10	100

Table 2. LA-SF-ICP-MS U-Pb standard dates; (a) Data corrected for common Pb; (b) Concordance calculated as $(^{206}\text{Pb}/^{238}\text{U}/^{207}\text{Pb}/^{206}\text{Pb}) * 100$; (c) Error correlation defined as the quotient of the propagated errors of the $^{206}\text{Pb}/^{238}\text{U}$ and the $^{207}\text{Pb}/^{235}\text{U}$ ratio; STD1 primary standard; STD2 secondary standard.

	U	Th/U	204 Corrected Ratios ^a							204 corrected ages						
<i>GJI</i>	ppm		$^{207}\text{Pb}/^{206}\text{Pb}$	2s	$^{206}\text{Pb}/^{238}\text{U}$	2s	$^{207}\text{Pb}/^{235}\text{U}$	2s	RHO ^c	$^{207}\text{Pb}/^{206}\text{Pb}$	2s	$^{206}\text{Pb}/^{238}\text{U}$	2s	$^{207}\text{Pb}/^{235}\text{U}$	2s	Conc ^b
STD1	303	0.02	0.0604	3.491	0.099	2.549	0.825	4.322	0.590	619	75	609	15	611	20	100
STD1	308	0.02	0.0605	1.108	0.099	1.580	0.823	1.929	0.819	620	24	607	9	610	9	100
STD1	304	0.02	0.0602	1.114	0.098	1.564	0.817	1.920	0.815	609	24	605	9	606	9	100
STD1	317	0.02	0.0607	1.214	0.099	1.630	0.830	2.032	0.802	627	26	610	9	613	9	99
STD1	339	0.02	0.0605	1.074	0.098	1.636	0.816	1.957	0.836	623	23	601	9	606	9	99
STD1	312	0.02	0.0600	1.067	0.099	1.623	0.815	1.943	0.836	603	23	606	9	605	9	100
STD1	310	0.02	0.0596	1.177	0.098	1.638	0.804	2.017	0.812	589	26	602	9	599	9	100
STD1	307	0.02	0.0596	1.156	0.099	1.664	0.815	2.026	0.821	589	25	610	10	605	9	101
STD1	324	0.02	0.0600	1.619	0.098	1.766	0.806	2.396	0.737	602	35	600	10	600	11	100
STD1	305	0.02	0.0598	1.070	0.097	1.603	0.803	1.927	0.832	598	23	599	9	599	9	100
STD1	331	0.02	0.0599	1.201	0.098	1.644	0.811	2.036	0.808	601	26	604	9	603	9	100
STD1	309	0.02	0.0602	3.498	0.099	2.606	0.820	4.362	0.597	611	76	607	15	608	20	100
STD1	274	0.02	0.0599	1.619	0.100	1.816	0.828	2.433	0.747	600	35	616	11	612	11	101
STD1	305	0.02	0.0600	1.875	0.100	1.902	0.825	2.671	0.712	603	41	613	11	611	12	100
BB																
STD2	591	0.15	0.0589	1.275	0.091	1.666	0.737	2.098	0.794	565	28	560	9	561	9	100
STD2	558	0.15	0.0584	1.095	0.092	1.637	0.738	1.970	0.831	546	24	565	9	561	9	101
STD2	478	0.15	0.0593	1.777	0.091	1.788	0.742	2.521	0.709	578	39	560	10	564	11	99
STD2	406	0.14	0.0581	1.171	0.090	1.548	0.724	1.941	0.798	532	26	558	8	553	8	101
STD2	447	0.14	0.0586	1.463	0.090	1.753	0.728	2.284	0.768	554	32	556	9	555	10	100
STD2	532	0.15	0.0586	1.167	0.092	1.593	0.744	1.975	0.807	551	25	568	9	565	9	101
STD2	520	0.15	0.0586	1.058	0.092	1.585	0.744	1.905	0.832	552	23	568	9	565	8	101

Continuation Table 2

STD1 GJI	U	Th/U	204 Corrected Ratios ^a						204 corrected ages							
	ppm		²⁰⁷ Pb/ ²⁰⁶ Pb	2s	²⁰⁶ Pb/ ²³⁸ U	2s	²⁰⁷ Pb/ ²³⁵ U	2s	RHO ^c	²⁰⁷ Pb/ ²⁰⁶ Pb	2s	²⁰⁶ Pb/ ²³⁸ U	2s	²⁰⁷ Pb/ ²³⁵ U	2s	Conc ^b
STD1	310	0.02	0.0607	1.1203	0.0987	1.5191	0.8264	1.8875	0.8048	629	24	607	9	612	9	99
STD1	295	0.02	0.0594	1.1456	0.0984	1.5442	0.8056	1.9228	0.8031	580	25	605	9	600	9	101
STD1	301	0.02	0.0598	1.1425	0.0967	1.5316	0.7980	1.9107	0.8016	597	25	595	9	596	9	100
STD1	293	0.02	0.0599	1.6105	0.0993	1.6793	0.8206	2.3267	0.7217	602	35	610	10	608	11	100
STD1	307	0.02	0.0598	1.5707	0.0979	1.6689	0.8074	2.2918	0.7282	597	34	602	10	601	10	100
STD1	319	0.02	0.0602	1.3653	0.0993	1.5955	0.8243	2.0999	0.7598	611	30	610	9	610	10	100
STD1	316	0.02	0.0593	1.1977	0.0983	1.5674	0.8030	1.9726	0.7946	577	26	604	9	599	9	101
STD1	328	0.02	0.0607	1.8349	0.0990	1.7731	0.8288	2.5516	0.6949	629	40	609	10	613	12	99
STD1	321	0.02	0.0604	1.8035	0.0992	1.7313	0.8260	2.5000	0.6925	619	39	609	10	611	12	100
STD1	295	0.02	0.0599	1.1358	0.0981	1.4683	0.8096	1.8564	0.7910	599	25	603	8	602	8	100
STD1	279	0.02	0.0595	1.1425	0.0979	1.4716	0.8030	1.8631	0.7899	586	25	602	8	599	8	101
STD1	289	0.02	0.0598	1.1375	0.0980	1.4694	0.8078	1.8582	0.7907	596	25	603	8	601	8	100
STD1	284	0.02	0.0600	1.1496	0.0983	1.4854	0.8134	1.8783	0.7908	604	25	604	9	604	9	100
STD1	298	0.02	0.0601	1.1320	0.0996	1.5066	0.8246	1.8845	0.7995	606	24	612	9	611	9	100
STD1	300	0.02	0.0599	2.3368	0.0981	1.9380	0.8095	3.0359	0.6384	599	51	603	11	602	14	100
STD1	316	0.02	0.0598	3.5391	0.1000	2.4993	0.8245	4.3326	0.5769	596	77	615	15	611	20	101
STD1	316	0.02	0.0599	1.1513	0.0982	1.4866	0.8115	1.8803	0.7906	601	25	604	9	603	9	100
STD1	299	0.02	0.0601	3.5244	0.0998	2.5058	0.8271	4.3243	0.5795	608	76	613	15	612	20	100
STD1	354	0.02	0.0596	3.5578	0.0996	2.5229	0.8177	4.3615	0.5784	588	77	612	15	607	20	101
STD1	346	0.02	0.0594	3.5656	0.0984	2.5409	0.8062	4.3784	0.5803	583	77	605	15	600	20	101
STD1	300	0.02	0.0606	1.9255	0.0992	1.7689	0.8291	2.6147	0.6765	626	42	610	10	613	12	99
STD1	280	0.02	0.0603	1.1273	0.0977	1.4938	0.8129	1.8714	0.7982	615	24	601	9	604	9	100
STD1	284	0.02	0.0602	1.1299	0.0978	1.5136	0.8113	1.8889	0.8013	610	24	601	9	603	9	100
STD1	277	0.02	0.0599	1.1360	0.0992	1.4918	0.8188	1.8751	0.7956	599	25	610	9	607	9	100
STD1	278	0.02	0.0601	1.1808	0.0982	1.5269	0.8145	1.9302	0.7911	608	26	604	9	605	9	100

Continuation Table 2

	U	Th/U	204 Corrected Ratios ^a							204 corrected ages						
	ppm		²⁰⁷ Pb/ ²⁰⁶ Pb	2s	²⁰⁶ Pb/ ²³⁸ U	2s	²⁰⁷ Pb/ ²³⁵ U	2s	RHO ^c	²⁰⁷ Pb/ ²⁰⁶ Pb	2s	²⁰⁶ Pb/ ²³⁸ U	2s	²⁰⁷ Pb/ ²³⁵ U	2s	Conc ^b
<i>STDI GJI</i>																
STD1	303	0.02	0.0594	1.2956	0.0991	1.6554	0.8118	2.1021	0.7875	583	28	609	10	603	10	101
STD1	313	0.02	0.0596	1.2917	0.0973	1.6658	0.7993	2.1080	0.7902	589	28	598	10	596	10	100
STD1	289	0.02	0.0599	1.4028	0.0997	1.7046	0.8234	2.2076	0.7721	599	30	613	10	610	10	100
STD1	273	0.02	0.0591	2.3921	0.0997	2.0601	0.8132	3.1569	0.6526	573	52	613	12	604	14	101
<i>Plešovice</i>																
STD2	388	0.11	0.0534	1.2914	0.0548	1.6073	0.4033	2.0618	0.7796	347	29	344	5	344	6	100
STD2	336	0.11	0.0531	1.8793	0.0536	2.0694	0.3922	2.7954	0.7403	332	43	337	7	336	8	100
STD2	392	0.09	0.0536	1.4889	0.0532	1.7412	0.3928	2.2909	0.7600	352	34	334	6	336	7	99
STD2	378	0.09	0.0534	1.6540	0.0520	1.8592	0.3824	2.4884	0.7471	345	37	327	6	329	7	99
<i>BB</i>																
STD2	439	0.17	0.0584	1.0961	0.0911	1.4494	0.7332	1.8172	0.7976	544	24	562	8	558	8	101
STD2	423	0.17	0.0590	1.1965	0.0902	1.4618	0.7346	1.8891	0.7738	569	26	557	8	559	8	100
STD2	436	0.16	0.0585	1.0948	0.0905	1.4802	0.7297	1.8410	0.8040	547	24	559	8	556	8	100
STD2	429	0.16	0.0585	1.9041	0.0904	1.7881	0.7286	2.6121	0.6846	547	42	558	10	556	11	100
STD2	426	0.16	0.0583	1.0970	0.0915	1.4860	0.7362	1.8471	0.8045	543	24	565	8	560	8	101

Continuation Table 2

<i>GJI</i>	U	Th/U	204 Corrected Ratios a							204 corrected ages						
	ppm		²⁰⁷ Pb/ ²⁰⁶ Pb	2s	²⁰⁶ Pb/ ²³⁸ U	2s	²⁰⁷ Pb/ ²³⁵ U	2s	RHO c	²⁰⁷ Pb/ ²⁰⁶ Pb	2s	²⁰⁶ Pb/ ²³⁸ U	2s	²⁰⁷ Pb/ ²³⁵ U	2s	Conc b
STD1	325	0.021	0.060	1.127	0.098	1.645	0.820	1.994	0.825	616	24	606	10	608	9	100
STD1	343	0.021	0.061	1.165	0.097	1.723	0.819	2.080	0.828	637	25	600	10	608	10	99
STD1	344	0.021	0.061	1.156	0.099	1.703	0.823	2.059	0.827	623	25	606	10	610	9	99
STD1	318	0.021	0.060	1.149	0.098	1.660	0.808	2.019	0.822	605	25	600	10	601	9	100
STD1	307	0.021	0.060	1.332	0.099	1.714	0.818	2.171	0.790	611	29	606	10	607	10	100
STD1	309	0.021	0.060	1.137	0.099	1.666	0.810	2.017	0.826	588	25	606	10	602	9	101
STD1	272	0.021	0.060	1.221	0.098	1.700	0.808	2.093	0.812	589	26	605	10	601	10	101
STD1	287	0.021	0.060	2.707	0.098	2.253	0.815	3.522	0.640	608	59	605	13	606	16	100
STD1	284	0.021	0.060	1.273	0.099	1.707	0.819	2.130	0.802	601	28	609	10	607	10	100
STD1	290	0.021	0.059	1.177	0.099	1.699	0.811	2.067	0.822	585	26	608	10	603	9	101
STD1	343	0.019	0.060	1.121	0.098	1.555	0.806	1.917	0.811	596	24	601	9	600	9	100
STD1	332	0.019	0.060	1.105	0.098	1.571	0.807	1.921	0.818	594	24	603	9	601	9	100
STD1	285	0.019	0.060	1.738	0.098	1.731	0.820	2.453	0.706	621	37	605	10	608	11	99
STD1	345	0.019	0.060	1.116	0.099	1.598	0.818	1.949	0.820	605	24	608	9	607	9	100
STD1	339	0.018	0.059	1.111	0.098	1.590	0.803	1.940	0.820	581	24	603	9	599	9	101
STD1	313	0.019	0.061	1.105	0.099	1.603	0.824	1.947	0.823	626	24	606	9	610	9	99
STD1	300	0.019	0.060	1.319	0.098	1.642	0.810	2.106	0.780	595	29	604	9	602	10	100
STD1	290	0.019	0.061	1.123	0.100	1.607	0.831	1.960	0.820	623	24	612	9	614	9	100
STD1	292	0.018	0.060	1.867	0.099	1.838	0.818	2.620	0.701	606	40	607	11	607	12	100
STD1	275	0.019	0.060	1.442	0.099	1.709	0.816	2.236	0.764	603	31	607	10	606	10	100
STD1	288	0.018	0.059	1.179	0.098	1.621	0.805	2.004	0.809	582	26	604	9	600	9	101
STD1	291	0.019	0.060	1.956	0.099	1.879	0.818	2.713	0.693	598	42	609	11	607	12	100

Continuation Table 2

BB	U	Th/U	204 Corrected Ratios ^a						204 corrected ages							
	ppm		²⁰⁷ Pb/ ²⁰⁶ Pb	2s	²⁰⁶ Pb/ ²³⁸ U	2s	²⁰⁷ Pb/ ²³⁵ U	2s	RHO ^c	²⁰⁷ Pb/ ²⁰⁶ Pb	2s	²⁰⁶ Pb/ ²³⁸ U	2s	²⁰⁷ Pb/ ²³⁵ U	2s	Conc ^b
STD2	545	0.15	0.059	1.098	0.092	1.683	0.747	2.009	0.837	575	24	565	9	567	9	100
STD2	428	0.15	0.058	1.149	0.091	1.640	0.736	2.002	0.819	542	25	564	9	560	9	101
STD2	423	0.15	0.059	1.681	0.092	1.828	0.746	2.484	0.736	550	37	570	10	566	11	101
STD2	405	0.16	0.059	1.151	0.092	1.670	0.751	2.028	0.823	570	25	569	9	569	9	100
STD2	537	0.13	0.059	1.068	0.090	1.556	0.732	1.887	0.824	567	23	556	8	558	8	100
STD2	518	0.14	0.058	1.066	0.091	1.564	0.728	1.893	0.826	536	23	560	8	555	8	101
STD2	509	0.13	0.059	1.455	0.091	1.658	0.738	2.206	0.752	557	32	562	9	561	10	100
STD2	511	0.13	0.059	1.086	0.090	1.572	0.734	1.911	0.823	566	24	557	8	559	8	100
STD2	510	0.14	0.059	1.072	0.090	1.571	0.732	1.902	0.826	558	23	558	8	558	8	100
STD2	514	0.14	0.059	1.071	0.091	1.569	0.734	1.900	0.826	560	23	559	8	559	8	100
STD2	512	0.14	0.059	1.074	0.091	1.576	0.739	1.907	0.826	555	23	564	9	562	8	100
STD2	556	0.14	0.060	1.297	0.092	1.670	0.754	2.114	0.790	587	28	566	9	570	9	99
STD2	499	0.14	0.059	1.190	0.092	1.614	0.749	2.006	0.805	564	26	568	9	568	9	100
STD2	501	0.14	0.058	1.839	0.092	1.838	0.745	2.600	0.707	548	40	569	10	565	11	101
STD2	433	0.14	0.059	1.122	0.090	1.622	0.730	1.972	0.822	560	24	556	9	556	8	100

GJI

STD1	324	0.02	0.0602	1.130	0.0988	1.620	0.8196	1.975	0.820	610	24	607	9	608	9	100
STD1	334	0.02	0.0607	1.121	0.0983	1.607	0.8226	1.959	0.820	628	24	605	9	609	9	99
STD1	318	0.02	0.0594	1.128	0.0994	1.610	0.8142	1.965	0.819	582	24	611	9	605	9	101
STD1	300	0.02	0.0594	2.227	0.0980	1.985	0.8023	2.983	0.665	581	48	603	11	598	14	101
STD1	293	0.02	0.0602	1.130	0.0993	1.612	0.8235	1.969	0.819	610	24	610	9	610	9	100
STD1	294	0.02	0.0597	1.139	0.0990	1.616	0.8150	1.977	0.817	593	25	609	9	605	9	101
STD1	284	0.02	0.0599	1.816	0.0997	1.827	0.8236	2.576	0.709	600	39	613	11	610	12	100
STD1	305	0.02	0.0602	2.353	0.0981	2.057	0.8139	3.126	0.658	609	51	603	12	605	14	100

Continuation Table 2

<i>GJI</i>	U		204 Corrected Ratios ^a							204 corrected ages						
	ppm	Th/U	²⁰⁷ Pb/ ²⁰⁶ Pb	2s	²⁰⁶ Pb/ ²³⁸ U	2s	²⁰⁷ Pb/ ²³⁵ U	2s	RHO ^c	²⁰⁷ Pb/ ²⁰⁶ Pb	2s	²⁰⁶ Pb/ ²³⁸ U	2s	²⁰⁷ Pb/ ²³⁵ U	2s	Conc ^b
STD1	312	0.02	0.0588	1.157	0.0988	1.619	0.8011	1.990	0.814	559	25	608	9	597	9	102
STD1	320	0.02	0.0604	1.175	0.0988	1.640	0.8230	2.017	0.813	619	25	607	10	610	9	100
STD1	297	0.02	0.0608	1.243	0.0986	1.659	0.8270	2.073	0.800	633	27	606	10	612	10	99
STD1	315	0.02	0.0605	1.190	0.0988	1.640	0.8240	2.026	0.809	622	26	607	10	610	9	99
STD1	312	0.02	0.0595	1.196	0.0982	1.650	0.8063	2.038	0.810	587	26	604	10	600	9	101
STD1	328	0.02	0.0602	1.097	0.0989	1.678	0.8202	2.005	0.837	609	24	608	10	608	9	100
STD1	330	0.02	0.0602	1.113	0.1000	1.679	0.8304	2.015	0.834	611	24	615	10	614	9	100
STD1	305	0.02	0.0600	1.117	0.0989	1.678	0.8177	2.016	0.832	602	24	608	10	607	9	100
STD1	299	0.02	0.0605	1.689	0.1000	1.860	0.8344	2.512	0.740	623	36	614	11	616	12	100
STD1	304	0.02	0.0596	1.141	0.0991	1.696	0.8141	2.044	0.830	589	25	609	10	605	9	101
STD1	292	0.02	0.0601	1.148	0.0993	1.693	0.8222	2.046	0.828	606	25	610	10	609	9	100
STD1	298	0.02	0.0610	1.165	0.0981	1.693	0.8241	2.055	0.824	637	25	603	10	610	9	99
STD1	307	0.02	0.0602	1.180	0.0981	1.693	0.8135	2.064	0.820	610	26	603	10	604	9	100
STD1	339	0.02	0.0603	1.112	0.0996	1.688	0.8271	2.021	0.835	613	24	612	10	612	9	100
STD1	299	0.02	0.0601	1.132	0.0993	1.673	0.8222	2.020	0.828	606	24	610	10	609	9	100
STD1	313	0.02	0.0602	1.130	0.0989	1.678	0.8205	2.023	0.829	609	24	608	10	608	9	100
STD1	308	0.02	0.0606	1.311	0.0984	1.754	0.8216	2.190	0.801	624	28	605	10	609	10	99
STD1	309	0.02	0.0598	1.137	0.0992	1.693	0.8180	2.040	0.830	596	25	610	10	607	9	100
STD1	301	0.02	0.0599	1.153	0.0998	1.704	0.8233	2.057	0.828	599	25	613	10	610	9	101
STD1	315	0.02	0.0590	2.290	0.0985	2.074	0.8019	3.090	0.671	569	50	606	12	598	14	101
STD1	301	0.02	0.0604	2.505	0.0989	2.175	0.8239	3.317	0.656	619	54	608	13	610	15	100
STD1	299	0.02	0.0593	2.012	0.0995	1.969	0.8144	2.815	0.699	580	44	612	11	605	13	101
STD1	312	0.02	0.0603	1.268	0.0982	1.740	0.8168	2.153	0.808	616	27	604	10	606	10	100
STD1	303	0.02	0.0595	1.160	0.0994	1.710	0.8150	2.067	0.828	584	25	611	10	605	9	101
STD1	294	0.02	0.0594	1.414	0.0981	1.781	0.8038	2.274	0.783	582	31	603	10	599	10	101

Continuation Table 2

<i>GJI</i>	U Th/U		204 Corrected Ratios ^a						204 corrected ages							
	ppm		²⁰⁷ Pb/ ²⁰⁶ Pb	2s	²⁰⁶ Pb/ ²³⁸ U	2s	²⁰⁷ Pb/ ²³⁵ U	2s	RHO ^c	²⁰⁷ Pb/ ²⁰⁶ Pb	2s	²⁰⁶ Pb/ ²³⁸ U	2s	²⁰⁷ Pb/ ²³⁵ U	2s	Conc ^b
STD1	289	0.02	0.0599	1.202	0.0983	1.647	0.8122	2.039	0.808	600	26	605	10	604	9	100
STD1	288	0.02	0.0604	1.666	0.0980	1.779	0.8168	2.437	0.730	619	36	603	10	606	11	99
STD1	263	0.02	0.0606	1.341	0.0997	1.683	0.8335	2.152	0.782	625	29	613	10	616	10	100
STD1	290	0.02	0.0604	1.453	0.1002	1.746	0.8352	2.271	0.769	619	31	616	10	616	11	100
STD1	267	0.02	0.0599	1.236	0.0992	1.674	0.8185	2.081	0.805	599	27	609	10	607	10	100
STD1	315	0.02	0.0604	1.288	0.1006	1.756	0.8374	2.178	0.806	616	28	618	10	618	10	100
STD1	393	0.02	0.0601	1.670	0.0996	1.935	0.8245	2.556	0.757	606	36	612	11	611	12	100
STD1	328	0.02	0.0603	2.291	0.0976	2.078	0.8118	3.093	0.672	615	49	600	12	603	14	99
STD1	338	0.02	0.0607	1.185	0.0978	1.717	0.8192	2.087	0.823	630	26	602	10	608	10	99
BB																
STD2	366	0.14	0.0590	1.357	0.0923	1.582	0.7504	2.084	0.759	566	30	569	9	568	9	100
STD2	505	0.15	0.0579	2.379	0.0915	2.079	0.7308	3.159	0.658	526	52	565	11	557	14	101
STD2	399	0.15	0.0592	1.199	0.0917	1.571	0.7486	1.976	0.795	575	26	565	9	567	9	100
STD2	361	0.15	0.0583	1.321	0.0917	1.592	0.7369	2.069	0.770	540	29	566	9	561	9	101
STD2	386	0.15	0.0587	1.227	0.0914	1.575	0.7397	1.997	0.789	555	27	564	9	562	9	100
STD2	506	0.14	0.0586	1.922	0.0922	1.932	0.7448	2.726	0.709	553	42	568	11	565	12	101
STD2	468	0.14	0.0583	2.121	0.0923	2.003	0.7416	2.917	0.687	541	46	569	11	563	13	101
STD2	485	0.14	0.0590	1.102	0.0923	1.668	0.7506	1.999	0.834	566	24	569	9	569	9	100
STD2	498	0.14	0.0584	1.926	0.0916	1.958	0.7372	2.747	0.713	545	42	565	11	561	12	101
STD2	484	0.14	0.0594	1.259	0.0911	1.712	0.7457	2.125	0.806	581	27	562	9	566	9	99
STD2	507	0.14	0.0579	1.276	0.0906	1.731	0.7230	2.150	0.805	525	28	559	9	552	9	101
STD2	515	0.14	0.0587	1.841	0.0909	1.927	0.7349	2.665	0.723	555	40	561	10	559	12	100
STD2	523	0.14	0.0593	1.113	0.0899	1.691	0.7346	2.025	0.835	577	24	555	9	559	9	99
STD2	518	0.14	0.0585	1.793	0.0902	1.905	0.7273	2.616	0.728	549	39	556	10	555	11	100
STD2	477	0.14	0.0593	1.148	0.0922	1.692	0.7532	2.044	0.828	576	25	569	9	570	9	100
STD2	429	0.14	0.0592	1.184	0.0903	1.655	0.7365	2.035	0.813	573	26	557	9	560	9	99

Continuation Table 2

<i>GJI</i>	U	Th/U	204 Corrected Ratios ^a							204 corrected ages						
	ppm		²⁰⁷ Pb/ ²⁰⁶ Pb	2s	²⁰⁶ Pb/ ²³⁸ U	2s	²⁰⁷ Pb/ ²³⁵ U	2s	RHO ^c	²⁰⁷ Pb/ ²⁰⁶ Pb	2s	²⁰⁶ Pb/ ²³⁸ U	2s	²⁰⁷ Pb/ ²³⁵ U	2s	Conc ^b
STD1	311	0.02	0.0604	1.142	0.097	1.646	0.810	2.003	0.822	618	25	598	9	602	9	99
STD1	285	0.02	0.0608	3.477	0.099	2.592	0.833	4.337	0.598	634	75	610	15	615	20	99
STD1	308	0.02	0.0595	1.142	0.100	1.644	0.819	2.002	0.821	587	25	613	10	607	9	101
STD1	294	0.02	0.0599	1.153	0.098	1.641	0.805	2.005	0.818	599	25	600	9	599	9	100
STD1	295	0.02	0.0603	2.728	0.099	2.235	0.824	3.526	0.634	615	59	609	13	610	16	100
STD1	311	0.02	0.0595	3.548	0.099	2.604	0.815	4.401	0.592	587	77	610	15	605	20	101
STD1	303	0.02	0.0596	2.359	0.098	2.061	0.809	3.132	0.658	590	51	605	12	602	14	101
STD1	320	0.02	0.0592	2.342	0.098	2.067	0.801	3.124	0.662	574	51	604	12	598	14	101
STD1	324	0.02	0.0598	3.544	0.099	2.614	0.820	4.404	0.594	596	77	611	15	608	20	101
STD1	307	0.02	0.0594	1.196	0.099	1.659	0.809	2.045	0.811	581	26	608	10	602	9	101
STD1	320	0.02	0.0606	1.173	0.098	1.672	0.819	2.042	0.819	623	25	603	10	607	9	99
STD1	1092	0.23	0.0600	1.116	0.098	1.639	0.808	1.983	0.826	604	24	601	9	601	9	100
STD1	260	0.02	0.0602	1.213	0.099	1.599	0.820	2.007	0.797	610	26	607	9	608	9	100
STD1	264	0.02	0.0599	1.236	0.100	1.604	0.826	2.025	0.792	599	27	615	9	611	9	101
STD1	286	0.02	0.0600	2.604	0.099	2.117	0.815	3.356	0.631	603	56	606	12	605	15	100
STD1	290	0.02	0.0595	2.308	0.100	1.974	0.817	3.036	0.650	586	50	612	12	607	14	101
STD1	289	0.02	0.0606	1.915	0.097	1.835	0.815	2.653	0.692	626	41	600	11	605	12	99
STD1	302	0.02	0.0591	1.185	0.099	1.599	0.805	1.990	0.803	569	26	608	9	599	9	101
STD1	292	0.02	0.0598	1.188	0.099	1.579	0.814	1.976	0.799	596	26	607	9	605	9	100
STD1	298	0.02	0.0596	1.253	0.099	1.605	0.809	2.036	0.788	588	27	606	9	602	9	101
STD1	322	0.02	0.0598	2.532	0.098	2.102	0.812	3.291	0.639	597	55	605	12	604	15	100
STD1	315	0.02	0.0605	1.173	0.099	1.599	0.825	1.983	0.806	622	25	607	9	611	9	99
STD1	294	0.02	0.0594	1.195	0.098	1.615	0.801	2.009	0.804	582	26	602	9	598	9	101
STD1	322	0.02	0.0591	1.493	0.099	1.726	0.803	2.282	0.756	570	32	606	10	599	10	101
STD1	326	0.02	0.0601	1.198	0.097	1.643	0.807	2.033	0.808	608	26	599	9	601	9	100
STD1	333	0.02	0.0603	1.193	0.099	1.659	0.822	2.044	0.812	615	26	608	10	609	9	100

Continuation Table 2

<i>GJI</i>	U	Th/U	204 Corrected Ratios ^a							204 corrected ages						
	ppm		²⁰⁷ Pb/ ²⁰⁶ Pb 2s	²⁰⁶ Pb/ ²³⁸ U 2s	²⁰⁷ Pb/ ²³⁵ U 2s	RHO ^c	²⁰⁷ Pb/ ²⁰⁶ Pb 2s	²⁰⁶ Pb/ ²³⁸ U 2s	²⁰⁷ Pb/ ²³⁵ U 2s	Conc ^b						
STD1	333	0.02	0.0603	1.193	0.099	1.659	0.822	2.044	0.812	615	26	608	10	609	9	100
STD1	344	0.02	0.0601	1.198	0.098	1.658	0.809	2.046	0.811	606	26	601	10	602	9	100
STD1	341	0.02	0.0598	2.325	0.099	2.052	0.819	3.101	0.662	595	50	611	12	608	14	101
STD1	356	0.02	0.0605	1.207	0.100	1.676	0.836	2.066	0.812	621	26	616	10	617	10	100
<i>Plešovice</i>																
STD2	363	0.11	0.0528	1.591	0.054	1.910	0.393	2.486	0.768	321	36	339	6	337	7	101
STD2	396	0.11	0.0534	1.387	0.054	1.773	0.394	2.251	0.788	347	31	336	6	337	6	100
STD2	406	0.10	0.0528	1.212	0.054	1.630	0.393	2.031	0.803	321	28	339	5	337	6	101
STD2	398	0.10	0.0540	1.223	0.054	1.630	0.402	2.037	0.800	370	28	339	5	343	6	99
STD2	498	0.09	0.0536	1.194	0.054	1.561	0.398	1.965	0.794	354	27	338	5	340	6	99
STD2	506	0.09	0.0538	1.247	0.054	1.596	0.399	2.025	0.788	361	28	338	5	341	6	99

Table 3. High-precision LA-MC-ICP-MS U-Pb Galiléia zircon dates; (a) The mean ^{207}Pb signal in counts per second (cps) was within-run background corrected; (b) U, Th and Th/U ratio calculated relative to the GJ-1 reference; (c) Pbc is the total amount of common Pb; initial Pb using Stacey and Kramers (1975) model; (d) Corrected for background, within-run Pb/U fractionation and common Pb; $^{207}\text{Pb}/^{235}\text{U}$ calculated using $^{207}\text{Pb}/^{206}\text{Pb}/(^{238}\text{U}/^{206}\text{Pb}\times 1/137.88)$; (e) Error correlation defined as the quotient of the propagated errors of the $^{206}\text{Pb}/^{238}\text{U}$ and the $^{207}\text{Pb}/^{235}\text{U}$ ratio; (f) Concordance calculated as $(^{206}\text{Pb}/^{238}\text{U}/^{207}\text{Pb}/^{206}\text{Pb})\times 100$.

Sample	Spot position	^{207}Pb (cps) (a)	U (ppm) (b)	Pb (ppm) (b)	Th/U (b)	^{206}Pbc (%) (c)	$^{206}\text{Pb}/^{238}\text{U}$ (d)	$\pm 2s$ (%)	$^{207}\text{Pb}/^{238}\text{U}$ (d)	$\pm 2s$ (%)	$^{207}\text{Pb}/^{206}\text{Pb}$ (d)	$\pm 2s$ (%)	RHO (e)	$^{206}\text{Pb}/^{238}\text{U}$	$\pm 2s$	$^{207}\text{Pb}/^{235}\text{U}$	$\pm 2s$	$^{207}\text{Pb}/^{206}\text{Pb}$	$\pm 2s$	disc (f)
FGL6	centre	7868	445	40	0.28	0.374	0.090	0.8	0.728	1.1	0.059	0.8	0.699	554	4	555	5	560	18	99
FGL6	edge	13783	843	73	0.18	0.430	0.090	1.0	0.732	1.2	0.059	0.8	0.768	556	5	558	5	562	17	99
FGL6	centre	3299	194	18	0.30	0.265	0.091	0.7	0.741	1.1	0.059	0.9	0.655	562	4	563	5	567	19	99
FGL6	centre	3200	186	17	0.24	0.761	0.091	0.6	0.742	1.5	0.059	1.3	0.440	563	3	564	6	567	28	99
FGL6	edge	12354	714	65	0.28	0.415	0.091	0.4	0.745	0.9	0.059	0.8	0.456	564	2	566	4	574	17	98
FGL6	edge	9956	591	54	0.25	0.179	0.092	0.7	0.753	0.9	0.059	0.6	0.755	569	4	570	4	573	12	99
FGL6	centre	7155	410	43	0.72	0.182	0.093	0.3	0.758	0.7	0.059	0.6	0.503	572	2	573	3	577	12	99
FGL6	res	1369	80	8	0.31	0.000	0.093	0.7	0.762	1.0	0.059	0.8	0.651	575	4	575	5	574	17	100
FGL6	centre	5925	329	30	0.21	0.242	0.094	0.7	0.767	1.0	0.059	0.8	0.685	577	4	578	5	582	16	99
FGL6	edge	3833	224	21	0.28	0.354	0.094	0.6	0.771	1.0	0.059	0.8	0.606	580	3	581	5	581	18	100
FGL6	edge	12886	758	69	0.20	0.203	0.094	0.5	0.773	0.8	0.059	0.6	0.689	581	3	581	3	585	12	99
FGL6	centre	6150	350	32	0.16	1.280	0.094	0.6	0.774	2.0	0.059	1.9	0.280	581	3	582	9	585	42	99
FGL6	edge	7050	412	39	0.29	0.645	0.094	0.4	0.775	1.2	0.060	1.1	0.336	582	2	583	5	587	24	99
FGL6	resorbed	1299	73	7	0.29	0.222	0.095	0.7	0.781	1.2	0.060	1.0	0.561	585	4	586	5	588	22	99
FGL6	core	5541	316	30	0.24	0.764	0.096	1.5	0.787	2.0	0.060	1.3	0.769	590	9	590	9	590	28	100
FGL6	edge	8406	488	45	0.17	0.128	0.096	0.7	0.790	0.8	0.060	0.5	0.787	590	4	591	4	596	11	99
FGL6	centre	4551	264	26	0.37	0.137	0.096	0.6	0.789	0.9	0.060	0.7	0.654	590	3	591	4	594	14	99
FGL6	edge	4983	286	28	0.37	0.660	0.096	0.5	0.792	1.2	0.060	1.1	0.385	592	3	593	6	594	25	100
FGL6	centre	9813	560	55	0.35	0.172	0.097	0.6	0.796	0.8	0.060	0.5	0.746	594	3	595	4	597	12	100
FGL6	edge	3177	185	18	0.22	0.000	0.097	0.6	0.798	0.9	0.060	0.7	0.644	595	3	596	4	599	15	99
FGL6	edge	9028	524	51	0.29	0.000	0.097	0.6	0.802	0.8	0.060	0.5	0.775	598	4	598	4	599	11	100
FGL6	edge	7180	393	36	0.13	0.135	0.097	0.6	0.806	0.8	0.060	0.5	0.710	600	3	600	4	602	12	100
FGL6	centre	3396	197	20	0.51	0.392	0.098	0.5	0.810	1.1	0.060	1.0	0.428	602	3	602	5	604	21	100
FGL6	resorbed	5634	315	30	0.18	0.708	0.098	0.9	0.816	1.5	0.060	1.2	0.611	605	5	606	7	608	26	100

Continuation Table 3.

Sampl e	Spot position	²⁰⁷ Pb (cps) (a)	U (ppm) (b)	Pb (ppm) (b)	Th/U (b)	²⁰⁶ Pbc (%) (c)	²⁰⁶ Pb/ ²³⁸ U (d)	±2s (%)	²⁰⁷ Pb/ ²³⁸ U (d)	±2s (%)	²⁰⁷ Pb/ ²⁰⁶ Pb (d)	±2s (%)	RHO (e)	²⁰⁶ Pb/ ²³⁸ U	±2s	²⁰⁷ Pb/ ²³⁵ U	±2s	²⁰⁷ Pb/ ²⁰⁶ Pb	±2s	disc (f)
FGL6	resorbed	5634	315	30	0.18	0.708	0.098	0.9	0.816	1.5	0.060	1.2	0.611	605	5	606	7	608	26	100
FGL6	resorbed	1884	103	11	0.69	1.233	0.100	0.7	0.831	2.1	0.060	2.0	0.313	614	4	614	10	615	43	100
FGL6	centre	4840	268	27	0.36	0.062	0.101	0.5	0.839	0.8	0.060	0.6	0.648	618	3	618	4	620	13	100
FGL6	resorbed	5100	284	29	0.29	0.158	0.102	0.7	0.852	0.9	0.061	0.6	0.716	625	4	625	4	627	14	100
FGL6	centre	1742	98	10	0.35	0.352	0.103	0.7	0.866	1.1	0.061	0.9	0.618	633	4	633	5	634	19	100
FGL6	resorbed	5098	281	29	0.24	0.095	0.104	0.4	0.875	0.7	0.061	0.6	0.583	638	3	638	4	639	13	100
FGL6	resorbed	11593	654	70	0.19	1.242	0.110	0.8	0.945	2.207	0.062	2.0	0.385	675	5	675	11	676	44	100
FGL12	edge	4844	282	25	0.26	0.109	0.089	0.9	0.725	1.1	0.059	0.6	0.821	552	5	553	5	558	14	99
FGL12	edge	6798	406	36	0.26	0.000	0.090	0.9	0.727	1.1	0.059	0.5	0.858	554	5	555	5	558	12	99
FGL12	edge	4811	304	27	0.21	0.623	0.090	0.6	0.730	1.2	0.059	1.1	0.502	556	3	557	5	562	24	99
FGL12	edge	4376	251	22	0.20	0.909	0.090	0.7	0.736	1.6	0.059	1.5	0.453	558	4	560	7	566	32	99
FGL12	edge	8189	461	42	0.31	1.274	0.091	0.5	0.743	2.0	0.059	1.9	0.264	563	3	564	9	569	42	99
FGL12	centre	3526	208	21	0.58	0.059	0.093	0.8	0.759	1.0	0.059	0.6	0.812	572	5	574	5	578	13	99
FGL12	centre	2543	150	15	0.54	0.154	0.093	0.6	0.761	1.1	0.059	0.9	0.531	574	3	574	5	577	20	99
FGL12	resorbed	1126	65	6	0.42	0.375	0.094	0.8	0.768	1.6	0.060	1.4	0.483	577	4	579	7	586	30	98
FGL12	edge	6004	341	31	0.21	0.000	0.094	0.9	0.768	1.1	0.059	0.6	0.808	577	5	579	5	585	14	99
FGL12	centre	1685	96	10	0.67	1.362	0.094	0.6	0.771	2.2	0.059	2.2	0.255	579	3	580	10	584	47	99
FGL12	centre	1602	93	9	0.60	0.000	0.094	0.6	0.772	1.3	0.059	1.2	0.467	580	3	581	6	585	25	99
FGL12	edge	9804	573	52	0.17	0.000	0.095	0.6	0.776	0.8	0.060	0.5	0.725	582	3	583	3	587	11	99
FGL12	edge	4940	286	27	0.34	0.598	0.095	0.9	0.777	1.4	0.060	1.1	0.639	583	5	584	6	587	24	99
FGL12	edge	7015	408	39	0.33	0.235	0.095	0.6	0.778	0.9	0.060	0.7	0.683	583	3	585	4	589	15	99
FGL12	centre	4720	271	26	0.31	0.128	0.095	0.6	0.778	1.0	0.060	0.8	0.599	583	3	584	4	588	17	99

Continuation Table 3.

Sample	Spot position	²⁰⁷ Pb (cps) (a)	U (ppm) (b)	Pb (ppm) (b)	Th/U (b)	²⁰⁶ Pbc (%) (c)	²⁰⁶ Pb/ ²³⁸ U ±2s (%) (d)	²⁰⁷ Pb/ ²³⁸ U ±2s (%) (d)	²⁰⁷ Pb/ ²⁰⁶ Pb ±2s (%) (d)	RHO (e)	²⁰⁶ Pb/ ²³⁸ U ±2s	²⁰⁷ Pb/ ²³⁵ U ±2s	²⁰⁷ Pb/ ²⁰⁶ Pb ±2s	disc (f)						
FGL12	centre	3121	182	18	0.47	0.000	0.095	0.6	0.778	1.0	0.060	0.8	0.598	584	3	584	4	587	17	99
FGL12	centre	3079	157	16	0.48	0.683	0.095	0.6	0.783	2.3	0.060	2.2	0.244	585	3	587	10	597	48	98
FGL12	centre	8362	495	50	0.50	0.251	0.096	0.7	0.787	0.9	0.060	0.6	0.778	588	4	589	4	592	13	99
FGL12	centre	1710	103	10	0.23	0.000	0.096	0.6	0.791	1.2	0.060	1.0	0.513	592	3	592	5	590	22	100
FGL12	centre	1490	85	8	0.38	0.000	0.096	0.5	0.794	1.0	0.060	0.8	0.541	592	3	593	4	597	18	99
FGL12	centre	2192	124	12	0.40	0.054	0.097	0.5	0.798	1.0	0.060	0.8	0.498	595	3	596	4	598	18	99
FGL12	centre	2038	104	10	0.21	0.953	0.098	1.7	0.805	2.4	0.060	1.7	0.689	600	9	600	11	599	38	100
FGL12	edge	1694	96	10	0.39	0.181	0.098	0.6	0.815	1.2	0.060	1.0	0.503	605	3	605	5	606	22	100
FGL12	centre	1001	57	6	0.72	0.189	0.099	0.8	0.818	1.5	0.060	1.3	0.498	606	4	607	7	610	28	99
FGL12	resorbed	3190	180	19	0.56	0.500	0.099	0.7	0.820	1.2	0.060	1.0	0.576	607	4	608	6	611	21	99
FGL12	centre	4747	271	28	0.54	0.812	0.099	0.7	0.823	1.5	0.060	1.3	0.485	609	4	610	7	613	29	99
FGL12	centre	3692	202	20	0.36	1.439	0.099	0.6	0.827	2.3	0.060	2.2	0.278	611	4	612	10	615	47	99
FGL12	resorbed	1486	86	9	0.40	0.000	0.100	0.7	0.828	1.2	0.060	0.9	0.609	612	4	612	5	614	20	100
FGL12	resorbed	1633	95	10	0.33	0.372	0.100	0.6	0.828	1.2	0.060	1.0	0.538	612	4	612	6	613	22	100
FGL12	resorbed	655	38	4	0.38	0.132	0.100	0.7	0.828	1.8	0.060	1.6	0.380	612	4	613	8	615	35	100
FGL12	resorbed	4146	254	25	0.27	0.000	0.100	0.8	0.835	1.1	0.060	0.7	0.758	617	5	617	5	617	15	100
FGL12	centre	2133	127	13	0.49	0.000	0.101	0.8	0.843	1.2	0.061	0.9	0.685	620	5	621	6	624	19	99
FGL12	resorbed	1760	101	11	0.57	1.173	0.102	0.7	0.856	2.0	0.061	1.9	0.369	628	4	628	9	628	40	100
FGL12	resorbed	1972	113	12	0.44	0.136	0.102	0.6	0.857	1.0	0.061	0.9	0.538	628	3	628	5	630	19	100
FGL12	centre	1755	97	10	0.51	0.303	0.103	0.7	0.862	1.3	0.061	1.0	0.568	631	4	631	6	633	22	100
FGL12	resorbed	1817	103	11	0.45	0.583	0.105		0.885	1.4	0.061	1.3	0.381	644	3	644	7	643	29	100
FGL12	resorbed	1522	87	10	0.40	0.042	0.108	0.6	0.916	1.2	0.062	1.0	0.531	660	4	660	6	660	22	100

Table 4. High-precision LA-MC-ICP-MS U-Pb standards dates; (a) The mean ^{207}Pb signal in counts per second (cps) was within-run background corrected; (b) U, Th and Th/U ratio calculated relative to the GJ-1 reference; (c) Pbc is the total amount of common Pb; initial Pb using Stacey and Kramers (1975) model; (d) Corrected for background, within-run Pb/U fractionation and common Pb; $^{207}\text{Pb}/^{235}\text{U}$ calculated using $^{207}\text{Pb}/^{206}\text{Pb}/(^{238}\text{U}/^{206}\text{Pb}\times 1/137.88)$; (e) Error correlation defined as the quotient of the propagated errors of the $^{206}\text{Pb}/^{238}\text{U}$ and the $^{207}\text{Pb}/^{235}\text{U}$ ratio; (f) Concordance calculated as $(^{206}\text{Pb}/^{238}\text{U}/^{207}\text{Pb}/^{206}\text{Pb})\times 100$.

Sample	^{207}Pb (a) (cps)	U (b) (ppm)	Pb (b) (ppm)	Th/U (b)	^{206}Pbc (c) (%)	$^{206}\text{Pb}/^{238}\text{U}$ (d) (%)	$\pm 2s$	$^{207}\text{Pb}/^{238}\text{U}$ (d) (%)	$\pm 2s$	$^{207}\text{Pb}/^{206}\text{Pb}$ (d) (%)	$\pm 2s$	RHO (e)	$^{206}\text{Pb}/^{238}\text{U}$ $\pm 2s$	$^{207}\text{Pb}/^{235}\text{U}$ $\pm 2s$	$^{207}\text{Pb}/^{206}\text{Pb}$ $\pm 2s$	disc (f)			
P3	865	48	4.61	0.22	0.24	0.098	0.74	0.812	1.39	0.060	1.18	0.53	602	4	603	6	608	25	99
P3	851	49	4.67	0.23	0.14	0.098	0.81	0.813	1.48	0.060	1.24	0.55	603	5	604	7	606	27	99
P3	747	42	3.97	0.23	0.26	0.097	0.89	0.803	1.67	0.060	1.42	0.53	598	5	599	8	603	31	99
P3	686	39	3.68	0.22	0.21	0.098	0.65	0.808	1.53	0.060	1.39	0.43	600	4	601	7	605	30	99
BB9	6929	435	39.5	0.29	0.000	0.091	0.58	0.741	0.80	0.059	0.55	0.728	563	3	563	3	564	12	100
BB9	7321	460	41.6	0.29	0.183	0.091	0.57	0.738	0.83	0.059	0.61	0.685	560	3	561	4	564	13	99
BB9	6720	411	37.4	0.30	0.178	0.091	0.55	0.741	0.82	0.059	0.61	0.665	562	3	563	4	567	13	99
BB9	6660	411	37.5	0.30	0.190	0.091	0.57	0.743	0.84	0.059	0.61	0.686	563	3	564	4	568	13	99
BB9	6847	419	38.2	0.30	0.638	0.091	0.54	0.741	1.20	0.059	1.07	0.449	562	3	563	5	567	23	99
BB9	5537	340	30.8	0.30	0.220	0.091	0.57	0.738	0.85	0.059	0.63	0.672	560	3	561	4	565	14	99
BB9	4970	310	28.1	0.29	0.246	0.091	0.48	0.742	0.88	0.059	0.74	0.545	563	3	563	4	566	16	99
BB9	5947	366	33.1	0.29	0.144	0.091	0.42	0.737	0.77	0.059	0.65	0.549	560	2	561	3	565	14	99
BB9	4930	302	27.3	0.30	0.184	0.091	0.45	0.736	0.85	0.059	0.72	0.531	559	2	560	4	563	16	99
BB9	5486	336	30.6	0.29	0.139	0.091	0.44	0.744	0.77	0.059	0.63	0.568	564	2	565	3	568	14	99
BB9	5860	354	32.2	0.30	0.240	0.091	0.41	0.738	0.88	0.059	0.78	0.465	560	2	561	4	566	17	99
BB9	5624	345	31.3	0.31	0.144	0.091	0.53	0.737	0.79	0.059	0.58	0.673	560	3	561	3	564	13	99
BB9	6341	384	35.0	0.31	0.134	0.091	0.65	0.739	0.86	0.059	0.57	0.755	561	4	562	4	565	12	99
BB9	5812	354	32.1	0.31	0.159	0.091	0.47	0.736	0.81	0.059	0.66	0.585	560	3	560	3	563	14	99
BB9	5581	341	31.0	0.31	0.173	0.091	0.60	0.736	0.90	0.059	0.67	0.672	559	3	560	4	563	14	99
BB9	5419	330	29.9	0.31	0.185	0.091	0.44	0.737	0.77	0.059	0.63	0.572	560	2	561	3	564	14	99
BB9	4618	277	25.4	0.31	0.513	0.091	0.53	0.743	1.09	0.059	0.95	0.490	564	3	564	5	567	21	99
BB9	4858	293	26.6	0.30	0.194	0.091	0.57	0.738	0.86	0.059	0.65	0.663	560	3	561	4	563	14	99
BB9	4884	301	27.3	0.30	0.000	0.091	0.68	0.738	0.92	0.059	0.62	0.742	561	4	561	4	564	13	99

Continuation Table 4.

Sample	²⁰⁷ Pb (cps) (a)	U (ppm) (b)	Pb (ppm) (b)	Th/U (b)	²⁰⁶ Pbc (%) (c)	²⁰⁶ Pb/ ²³⁸ U (d)	±2s (%) (d)	²⁰⁷ Pb/ ²³⁸ U (d)	±2s (%) (d)	²⁰⁷ Pb/ ²⁰⁶ Pb (d)	±2s (%) (d)	RHO (e)	²⁰⁶ Pb/ ²³⁸ U (d)	±2s (d)	²⁰⁷ Pb/ ²³⁵ U (d)	±2s (d)	²⁰⁷ Pb/ ²⁰⁶ Pb (d)	±2s (d)	disc (f)
BB9	4952	304	28	0.30	0.17	0.091	0.649	0.7	0.998	0.059	0.758	0.7	559	3	560	4	563	17	99
Plešovice	4564	525	26	0.09	0.00	0.054	0.473	0.4	0.742	0.053	0.571	0.6	336	2	337	2	342	13	98
Plešovice	3182	369	18	0.07	0.19	0.053	0.691	0.4	1.098	0.053	0.853	0.6	335	2	335	3	338	19	99
Plešovice	2428	279	14	0.07	0.14	0.054	0.657	0.4	1.069	0.053	0.844	0.6	338	2	338	3	341	19	99
Plešovice	4283	484	24	0.09	0.12	0.054	0.636	0.4	0.925	0.053	0.672	0.7	339	2	339	3	344	15	99
Plešovice	4086	464	23	0.08	0.77	0.054	0.666	0.4	1.578	0.053	1.430	0.4	338	2	339	5	344	32	98
Plešovice	3717	430	22	0.08	0.14	0.054	0.701	0.4	1.017	0.053	0.736	0.7	337	2	337	3	340	17	99
Plešovice	3746	429	22	0.09	0.19	0.054	0.698	0.4	1.060	0.053	0.798	0.7	337	2	338	3	342	18	99
Plešovice	2242	256	13	0.08	0.44	0.054	0.610	0.4	1.228	0.053	1.066	0.5	339	2	339	4	343	24	99
Plešovice	3873	441	22	0.08	0.01	0.054	0.611	0.4	0.879	0.053	0.631	0.7	336	2	337	3	342	14	98
Plešovice	1958	222	11	0.08	0.16	0.053	0.639	0.4	1.056	0.053	0.840	0.6	336	2	336	3	340	19	99
Plešovice	2710	312	16	0.08	0.13	0.054	0.404	0.4	0.978	0.053	0.890	0.4	338	1	338	3	342	20	99
Plešovice	2701	313	16	0.08	0.15	0.054	0.508	0.4	0.902	0.053	0.746	0.6	336	2	337	3	339	17	99
Plešovice	2034	235	12	0.07	0.15	0.054	0.617	0.4	1.033	0.053	0.829	0.6	337	2	338	3	341	19	99
Plešovice	2256	255	13	0.07	0.55	0.054	0.580	0.4	1.350	0.053	1.219	0.4	338	2	338	4	341	28	99
Plešovice	2202	254	13	0.08	0.17	0.054	0.579	0.4	1.199	0.053	1.050	0.5	338	2	338	3	340	24	99
Plešovice	2086	239	12	0.08	0.12	0.054	0.504	0.4	1.123	0.053	1.004	0.4	337	2	338	3	341	23	99
Plešovice	2628	300	15	0.09	0.13	0.054	0.423	0.4	0.908	0.053	0.803	0.5	338	1	339	3	343	18	99
Plešovice	2277	264	13	0.08	0.13	0.054	0.563	0.4	1.074	0.053	0.915	0.5	337	2	337	3	339	21	99
Plešovice	1998	235	12	0.08	0.22	0.053	0.628	0.4	1.164	0.053	0.980	0.5	336	2	336	3	339	22	99
Plešovice	2126	250	12	0.09	0.56	0.053	0.732	0.4	1.485	0.053	1.292	0.5	335	2	335	4	338	29	99
Plešovice	2873	328	16	0.08	0.21	0.053	0.750	0.4	1.145	0.053	0.865	0.7	335	2	335	3	340	20	99
Plešovice	2904	338	17	0.09	0.00	0.054	0.677	0.4	0.915	0.053	0.615	0.7	337	2	338	3	340	14	99
Plešovice	3921	413	21	0.11	0.40	0.054	0.473	0.4	1.149	0.053	1.047	0.4	339	2	340	3	348	24	97
Plešovice	3305	387	19	0.08	0.16	0.054	0.565	0.4	0.918	0.053	0.724	0.6	337	2	337	3	340	16	99

Continuation Table 4.

Sample	²⁰⁷ Pb (a)	U (b)	Pb (b)	Th/U (b)	²⁰⁶ Pbc (%) (c)	²⁰⁶ Pb/ ²³⁸ U (d)	±2s (%) (d)	²⁰⁷ Pb/ ²³⁸ U (d)	±2s (%) (d)	²⁰⁷ Pb/ ²⁰⁶ Pb (d)	±2s (%) (d)	RHO (e)	²⁰⁶ Pb/ ²³⁸ U (d)	±2s (d)	²⁰⁷ Pb/ ²³⁵ U (d)	±2s (d)	²⁰⁷ Pb/ ²⁰⁶ Pb (d)	±2s (d)	disc (f)
Temora	878	76	5	0.43	0.70	0.066	0.748	0.5	1.894	0.055	1.740	0.4	414	3	414	6	415	39	100
Temora	841	71	5	0.43	0.20	0.067	0.697	0.5	1.327	0.055	1.129	0.5	415	3	416	5	420	25	99
Temora	528	47	3	0.34	0.23	0.066	0.810	0.5	1.707	0.055	1.503	0.5	414	3	414	6	415	34	100
Temora	624	54	4	0.43	0.39	0.066	0.736	0.5	1.968	0.055	1.825	0.4	413	3	415	7	422	41	98
Temora	1037	93	6	0.43	0.10	0.066	0.676	0.5	1.481	0.055	1.318	0.5	414	3	414	5	415	29	100
Temora	1056	95	7	0.44	0.01	0.066	1.097	0.5	1.436	0.055	0.926	0.8	414	4	414	5	418	21	99
Temora	885	75	5	0.44	0.40	0.066	0.716	0.5	1.859	0.055	1.715	0.4	412	3	413	6	419	38	98

Table 5. Lu-Hf Galiléia zircon isotopes; High-precision LA-MC-ICP-MS U-Pb standards dates; (a) $^{176}\text{Yb}/^{177}\text{Hf} = (^{176}\text{Yb}/^{173}\text{Yb})_{\text{true}} \times (^{173}\text{Yb}/^{177}\text{Hf})_{\text{meas}} \times (M^{173}(\text{Yb})/M^{177}(\text{Hf}))_{\text{b(Hf)}}$, $\text{b(Hf)} = \ln(^{179}\text{Hf}/^{177}\text{Hf}_{\text{true}} / ^{179}\text{Hf}/^{177}\text{Hf}_{\text{meas}}) / \ln(M^{179}(\text{Hf})/M^{177}(\text{Hf}))$, M=mass of respective isotope. The $^{176}\text{Lu}/^{177}\text{Hf}$ were calculated in a similar way by using the $^{175}\text{Lu}/^{177}\text{Hf}$ and b(Yb) ; (b) Mean Hf signal in volt; (c) Uncertainties are quadratic additions of the within-run precision and the daily reproducibility of the zircon standards; (d) Initial $^{176}\text{Hf}/^{177}\text{Hf}$ and ϵHf calculated using the $^{206}\text{Pb}/^{238}\text{U}$ age determined by LA-ICP-MS dating (see column s), and the CHUR parameters: $^{176}\text{Lu}/^{177}\text{Hf} = 0.0336$, and $^{176}\text{Hf}/^{177}\text{Hf} = 0.282785$ (Bouvier *et al.*, 2008); (e) Two stage "maximum" model age in billion years using the measured $^{176}\text{Lu}/^{177}\text{Hf}$ of each spot, the value of $^{176}\text{Lu}/^{177}\text{Hf} = 0.0113$ (mean of average of continental crust (Taylor and McLennan, 1995)); (f) $^{206}\text{Pb}/^{238}\text{U}$ age determined by LA-SF-ICP-MS dating.

Sample	Spot posititon	$^{176}\text{Yb}/^{177}\text{Hf}$ a	$\pm 2\text{s}$	$^{176}\text{Lu}/^{177}\text{Hf}$ a	$\pm 2\text{s}$	$^{178}\text{Hf}/^{177}\text{Hf}$	$^{180}\text{Hf}/^{177}\text{Hf}$	(V) SigHf b	$^{176}\text{Hf}/^{177}\text{Hf}$	$\pm 2\text{s}$ c	$^{176}\text{Hf}/^{177}\text{Hf}_{(t)}$ ^d	$\epsilon\text{Hf}^{(t)}$ d	$\pm 2\text{s}$ e	(Ga) TDM2 e	$^{206}\text{Pb}/^{238}\text{U}$ age (Ma) f	$\pm 2\text{s}$
FGL19	centre	0.04639	54	0.00143	14	1.46726	1.88601	13	0.282131	18	0.282115	-10	0.72	2.0	593	15
FGL19	centre	0.04020	35	0.00135	10	1.46722	1.88656	13	0.282138	22	0.282123	-10	0.72	2.0	591	10
FGL19	centre	0.03266	33	0.00107	9	1.46717	1.88627	15	0.282148	19	0.282136	-10	0.72	2.0	576	9
FGL19	centre	0.05746	64	0.00198	20	1.46719	1.88609	13	0.282123	20	0.282102	-11	0.72	2.0	586	10
FGL19	centre	0.03984	35	0.00135	10	1.46723	1.88643	14	0.282157	22	0.282141	-9	0.72	1.9	599	10
FGL19	centre	0.02979	30	0.00101	9	1.46723	1.88666	15	0.282154	15	0.282143	-10	0.72	1.9	590	9
FGL19	centre	0.03478	36	0.00117	10	1.46721	1.88619	15	0.282156	18	0.282143	-10	0.72	1.9	584	10
FGL19	centre	0.04113	35	0.00139	9	1.46724	1.88598	15	0.282359	39	0.282343	-2	0.72	1.6	599	9
FGL19	centre	0.02561	21	0.00086	6	1.46722	1.88636	14	0.282142	19	0.282132	-10	0.72	2.0	585	9
FGL19	centre	0.01500	24	0.00050	8	1.46723	1.88570	13	0.282054	24	0.282048	-13	0.71	2.1	586	9
FGL19	centre	0.04237	45	0.00141	13	1.46725	1.88644	16	0.282142	15	0.282127	-11	0.72	2.0	566	9
FGL19	centre	0.04838	55	0.00163	17	1.46724	1.88572	15	0.282166	17	0.282149	-10	0.72	1.9	567	9
FGL19	centre	0.04763	46	0.00158	13	1.46721	1.88634	12	0.282166	15	0.282149	-10	0.72	1.9	583	9
FGL19	centre	0.03612	33	0.00121	9	1.46720	1.88638	14	0.282137	17	0.282123	-10	0.72	2.0	605	15
FGL19	edge	0.04368	38	0.00148	9	1.46727	1.88637	13	0.282098	15	0.282082	-12	0.71	2.1	592	9
FGL19	edge	0.04009	39	0.00130	11	1.46726	1.88597	17	0.282144	18	0.282130	-10	0.72	2.0	585	9
FGL19	edge	0.03043	26	0.00104	7	1.46721	1.88642	14	0.282119	16	0.282107	-11	0.72	2.0	590	10
FGL19	edge	0.04104	34	0.00138	9	1.46722	1.88639	20	0.282128	13	0.282113	-11	0.72	2.0	581	10
FGL19	edge	0.04633	39	0.00156	11	1.46719	1.88631	12	0.282179	20	0.282162	-9	0.72	1.9	595	15
FGL19	resorbed	0.02227	21	0.00076	6	1.46724	1.88630	13	0.282143	15	0.282134	-9	0.72	1.9	626	11

Continuation table 5

Sample	Spot posititon	$^{176}\text{Yb}/^{177}\text{Hf}$ a	$\pm 2s$	$^{176}\text{Lu}/^{177}\text{Hf}$ a	$\pm 2s$	$^{178}\text{Hf}/^{177}\text{Hf}$	$^{180}\text{Hf}/^{177}\text{Hf}$	(V) SigHf b	$^{176}\text{Hf}/^{177}\text{Hf}$ c	$\pm 2s$	$^{176}\text{Hf}/^{177}\text{Hf}_{(t)}$ d	$\epsilon\text{Hf}^{(t)}$ d	$\pm 2s$ c	(Ga) TDM2 e	$^{206}\text{Pb}/^{238}\text{U}$ age (Ma) f	$\pm 2s$
FGL22	centre	0.03545	46	0.00120	14	1.46721	1.88627	13	0.282149	18	0.282135	-10	0.72	2.0	581	10
FGL22	centre	0.03799	32	0.00126	8	1.46718	1.88606	14	0.282174	16	0.282160	-9	0.72	1.9	588	10
FGL22	centre	0.03795	38	0.00126	11	1.46722	1.88602	13	0.282156	19	0.282142	-9	0.72	1.9	598	15
FGL22	centre	0.04372	41	0.00144	12	1.46719	1.88617	14	0.282120	15	0.282104	-11	0.72	2.0	608	16
FGL22	centre	0.03315	38	0.00107	9	1.46722	1.88572	14	0.282186	19	0.282173	-8	0.72	1.9	625	11
FGL22	centre	0.03451	32	0.00112	9	1.46720	1.88634	10	0.282051	18	0.282038	-13	0.71	2.1	607	11
FGL22	centre	0.04882	48	0.00165	14	1.46719	1.88684	14	0.282117	19	0.282099	-11	0.72	2.0	596	11
FGL22	edge	0.02659	30	0.00087	8	1.46715	1.88624	16	0.282113	16	0.282104	-11	0.72	2.0	598	10
FGL22	edge	0.03469	31	0.00114	9	1.46725	1.88695	12	0.282100	19	0.282087	-12	0.71	2.0	587	10
FGL22	edge	0.04617	40	0.00158	10	1.46724	1.88677	15	0.282155	17	0.282137	-10	0.72	2.0	579	9
FGL22	resorbed	0.09587	147	0.00313	46	1.46725	1.88684	17	0.282190	17	0.282153	-8	0.72	1.9	640	10
FGL26	centre	0.02113	22	0.00076	7	1.46726	1.88580	16	0.282160	17	0.282151	-9	0.72	1.9	610	12
FGL26	centre	0.03976	42	0.00148	13	1.46720	1.88578	15	0.282154	17	0.282138	-10	0.72	2.0	587	9
FGL26	centre	0.02150	29	0.00081	9	1.46722	1.88614	11	0.282042	20	0.282033	-14	0.71	2.2	576	9
FGL26	centre	0.01337	11	0.00048	3	1.46726	1.88616	14	0.282133	20	0.282128	-10	0.72	2.0	598	25
FGL26	edge	0.03759	35	0.00137	10	1.46725	1.88566	16	0.282179	20	0.282164	-9	0.72	1.9	586	9
FGL26	centre	0.04797	40	0.00176	12	1.46723	1.88624	19	0.282143	17	0.282124	-11	0.72	2.0	568	8
FGL26	centre	0.03598	30	0.00136	8	1.46721	1.88589	18	0.282188	15	0.282173	-8	0.72	1.9	592	9
FGL26	centre	0.03704	42	0.00139	14	1.46723	1.88581	18	0.282108	14	0.282092	-11	0.72	2.0	623	10
FGL26	centre	0.07981	100	0.00269	31	1.46719	1.88622	21	0.282091	13	0.282059	-12	0.71	2.1	625	10
FGL26	centre	0.04160	39	0.00151	12	1.46721	1.88592	15	0.282195	17	0.282179	-9	0.72	1.9	563	9
FGL26	resorbed	0.02292	28	0.00085	9	1.46724	1.88576	16	0.282145	14	0.282133	-7	0.72	1.9	714	15

Continuation table 5

Sample	Spot posititon	$^{176}\text{Yb}/^{177}\text{Hf}$ a	$\pm 2s$	$^{176}\text{Lu}/^{177}\text{Hf}$ a	$\pm 2s$	$^{178}\text{Hf}/^{177}\text{Hf}$	$^{180}\text{Hf}/^{177}\text{Hf}$	(V) SigHf b	$^{176}\text{Hf}/^{177}\text{Hf}$ c	$\pm 2s$	$^{176}\text{Hf}/^{177}\text{Hf}_{(t)}$ d	$\epsilon\text{Hf}^{(t)}$ d	$\pm 2s$ c	(Ga) TDM2 e	$^{206}\text{Pb}/^{238}\text{U}$ age (Ma) f	$\pm 2s$
FGL40	centre	0.02220	40	0.00078	13	1.46720	1.88644	12	0.282210	17	0.282202	-8	0.72	1.8	586	11
FGL40	centre	0.03809	33	0.00143	10	1.46713	1.88672	13	0.282212	17	0.282197	-8	0.72	1.9	560	8
FGL40	centre	0.03411	30	0.00127	8	1.46718	1.88651	12	0.282212	20	0.282198	-8	0.72	1.8	581	8
FGL40	centre	0.03816	35	0.00139	11	1.46721	1.88666	12	0.282188	17	0.282173	-9	0.72	1.9	580	9
FGL40	centre	0.02957	30	0.00102	8	1.46719	1.88688	13	0.282226	17	0.282215	-7	0.72	1.8	612	10
FGL40	centre	0.02456	22	0.00087	6	1.46717	1.88711	12	0.282215	16	0.282205	-7	0.72	1.8	599	10
FGL40	centre	0.02746	30	0.00097	9	1.46721	1.88668	13	0.282222	19	0.282211	-7	0.72	1.8	588	15
FGL40	centre	0.03643	33	0.00134	9	1.46720	1.88712	11	0.282257	21	0.282243	-6	0.72	1.8	581	9
FGL40	centre	0.04023	34	0.00146	10	1.46720	1.88725	12	0.282209	20	0.282193	-8	0.72	1.9	576	9
FGL40	centre	0.03566	31	0.00130	9	1.46718	1.88677	12	0.282201	16	0.282188	-9	0.72	1.9	557	8
FGL40	centre	0.03852	42	0.00143	13	1.46723	1.88672	12	0.282213	18	0.282197	-8	0.72	1.8	577	8
FGL40	centre	0.01920	18	0.00072	5	1.46719	1.88672	12	0.282217	18	0.282210	-8	0.72	1.8	573	9
FGL40	edge	0.02930	24	0.00112	7	1.46719	1.88659	13	0.282192	18	0.282180	-8	0.72	1.9	608	11
FGL40	edge	0.03775	37	0.00139	12	1.46719	1.88669	13	0.282198	18	0.282184	-9	0.72	1.9	549	8
FGL40	edge	0.02822	29	0.00095	8	1.46720	1.88675	15	0.282205	20	0.282195	-8	0.72	1.8	582	8
FGL40	edge	0.01503	17	0.00050	5	1.46717	1.88669	12	0.282203	17	0.282198	-8	0.72	1.8	580	11
FGL40	edge	0.03427	29	0.00121	8	1.46716	1.88670	11	0.282246	17	0.282233	-7	0.72	1.8	579	16
FGL40	edge	0.01826	22	0.00062	7	1.46719	1.88677	13	0.282234	17	0.282227	-7	0.72	1.8	583	9
FGL40	mantle	0.03421	36	0.00124	10	1.46721	1.88680	14	0.282213	15	0.282200	-8	0.72	1.8	558	8
FGL40	mantle	0.02076	17	0.00076	5	1.46716	1.88675	13	0.282196	18	0.282188	-8	0.72	1.9	583	9
FGL40	resorbed	0.03556	32	0.00126	9	1.46715	1.88654	11	0.282214	19	0.282200	-8	0.72	1.8	586	10

Continuation table 5

Sample	Spot posititon	$^{176}\text{Yb}/^{177}\text{Hf}$ a	$\pm 2s$	$^{176}\text{Lu}/^{177}\text{Hf}$ a	$\pm 2s$	$^{178}\text{Hf}/^{177}\text{Hf}$	$^{180}\text{Hf}/^{177}\text{Hf}$	(V) SigHf b	$^{176}\text{Hf}/^{177}\text{Hf}$ c	$\pm 2s$	$^{176}\text{Hf}/^{177}\text{Hf}_{(t)}$ d	$\epsilon\text{Hf}^{(t)}$ d	$\pm 2s$ c	(Ga) TDM2 e	$^{206}\text{Pb}/^{238}\text{U}$ age (Ma) f	$\pm 2s$
FGL6	centre	0.04315	54	0.00157	17	1.46716	1.88618	15	0.282213	16	0.282196	-7	0.72	1.8	603	9
FGL6	centre	0.02705	26	0.00100	8	1.46721	1.88644	13	0.282205	15	0.282193	-7	0.72	1.8	610	9
FGL6	centre	0.03793	31	0.00141	9	1.46723	1.88663	15	0.282229	15	0.282213	-7	0.72	1.8	597	9
FGL6	centre	0.02758	25	0.00106	8	1.46721	1.88635	15	0.282195	15	0.282183	-8	0.72	1.9	605	9
FGL6	centre	0.04488	46	0.00165	14	1.46719	1.88640	14	0.282212	16	0.282194	-8	0.72	1.8	577	9
FGL6	centre	0.04181	37	0.00148	10	1.46718	1.88676	14	0.282208	17	0.282192	-8	0.72	1.9	580	9
FGL6	centre	0.04047	36	0.00158	11	1.46719	1.88664	10	0.282217	20	0.282199	-7	0.72	1.8	617	17
FGL6	centre	0.02811	23	0.00109	7	1.46719	1.88664	13	0.282217	20	0.282204	-7	0.72	1.8	610	15
FGL6	centre	0.03177	34	0.00118	11	1.46720	1.88649	14	0.282227	16	0.282213	-6	0.72	1.8	625	9
FGL6	centre	0.01618	18	0.00065	6	1.46721	1.88642	15	0.282224	15	0.282216	-6	0.72	1.8	619	9
FGL6	centre	0.02315	31	0.00086	11	1.46719	1.88660	14	0.282225	17	0.282216	-7	0.72	1.8	569	15
FGL6	centre	0.03434	40	0.00126	13	1.46717	1.88625	16	0.282235	17	0.282220	-6	0.72	1.8	627	10
FGL6	edge	0.02892	27	0.00110	8	1.46721	1.88646	13	0.282219	16	0.282207	-8	0.72	1.8	569	9
FGL6	resorbed	0.03322	28	0.00124	8	1.46720	1.88622	14	0.282220	16	0.282205	-6	0.72	1.8	642	10
FGL6	resorbed	0.02639	22	0.00097	6	1.46717	1.88659	14	0.282223	15	0.282211	-6	0.72	1.8	628	10
FSV1	centre	0.03780	45	0.00139	15	1.46720	1.88682	11	0.282035	23	0.282020	-14	0.71	2.2	579	15
FSV1	centre	0.03866	33	0.00147	10	1.46718	1.88665	13	0.282120	16	0.282104	-11	0.72	2.0	580	8
FSV1	centre	0.03525	50	0.00136	18	1.46715	1.88683	18	0.282134	15	0.282118	-10	0.72	2.0	610	9
FSV1	edge	0.00566	6	0.00020	2	1.46720	1.88704	14	0.282136	15	0.282134	-10	0.72	2.0	590	9
FSV1	centre	0.02196	25	0.00082	8	1.46722	1.88661	13	0.282216	16	0.282207	-8	0.72	1.8	578	10
FSV1	edge	0.02822	38	0.00109	13	1.46722	1.88619	14	0.282201	17	0.282189	-8	0.72	1.9	578	11
FSV1	centre	0.02376	28	0.00086	10	1.46721	1.88698	17	0.282182	15	0.282172	-8	0.72	1.9	599	10
FSV1	edge	0.03816	35	0.00139	11	1.46714	1.88653	14	0.282190	18	0.282175	-9	0.72	1.9	575	9
FSV1	centre	0.02974	28	0.00110	8	1.46723	1.88673	13	0.282135	20	0.282123	-11	0.72	2.0	578	8
FSV1	centre	0.03210	37	0.00116	12	1.46721	1.88674	13	0.282191	15	0.282179	-9	0.72	1.9	576	8

Continuation table 5

Sample	Spot posititon	$^{176}\text{Yb}/^{177}\text{Hf}$ a	$\pm 2s$	$^{176}\text{Lu}/^{177}\text{Hf}$ a	$\pm 2s$	$^{178}\text{Hf}/^{177}\text{Hf}$	$^{180}\text{Hf}/^{177}\text{Hf}$	(V) SigHf b	$^{176}\text{Hf}/^{177}\text{Hf}$	$\pm 2s$ c	$^{176}\text{Hf}/^{177}\text{Hf}_{(t)}$ ^d	$\epsilon\text{Hf}^{(t)}$ d	$\pm 2s$ c	(Ga) TDM2 e	$^{206}\text{Pb}/^{238}\text{U}$ age (Ma) f	$\pm 2s$
FSV1	centre	0.00351	3	0.00013	1	1.46723	1.88660	15	0.282134	20	0.282132	-10	0.72	2.0	585	9
FSV1	centre	0.07204	67	0.00275	21	1.46726	1.88655	11	0.282163	19	0.282133	-10	0.72	2.0	581	10
FSV1	centre	0.02290	24	0.00086	8	1.46717	1.88643	15	0.282182	15	0.282172	-9	0.72	1.9	585	11
FSV1	centre	0.01470	14	0.00058	4	1.46723	1.88639	16	0.282189	18	0.282182	-8	0.72	1.9	609	9
FSV1	edge	0.02281	21	0.00085	6	1.46721	1.88661	13	0.282164	16	0.282154	-9	0.72	1.9	590	12
FSV1	centre	0.01480	14	0.00056	5	1.46722	1.88652	16	0.282174	17	0.282168	-9	0.72	1.9	594	15
FSV1	centre	0.02677	25	0.00101	8	1.46721	1.88680	14	0.282234	18	0.282223	-7	0.72	1.8	574	9
FSV1	centre	0.02575	24	0.00099	8	1.46719	1.88630	12	0.282151	21	0.282140	-9	0.72	1.9	599	10
FSV1	centre	0.04555	54	0.00179	19	1.46727	1.88594	11	0.282143	18	0.282123	-10	0.72	2.0	585	15
FSV1	centre	0.02370	21	0.00088	6	1.46727	1.88594	16	0.282205	11	0.282195	-8	0.72	1.8	575	8
FSV1	centre	0.01927	39	0.00074	13	1.46720	1.88661	15	0.282162	19	0.282154	-9	0.72	1.9	613	11
FSV1	edge	0.01023	9	0.00035	3	1.46722	1.88653	14	0.282167	13	0.282163	-9	0.72	1.9	579	8
FSV1	centre	0.02145	21	0.00080	7	1.46717	1.88600	13	0.282218	18	0.282209	-7	0.72	1.8	588	9
FSV1	centre	0.02263	29	0.00081	10	1.46718	1.88614	15	0.282187	15	0.282178	-9	0.72	1.9	580	9
FSV1	centre	0.03473	33	0.00129	10	1.46722	1.88634	12	0.282187	20	0.282173	-8	0.72	1.9	600	10
FSV10	centre	0.03989	37	0.00137	11	1.46717	1.88597	13	0.282142	16	0.282126	-10	0.72	2.0	608	10
FSV10	centre	0.04605	49	0.00154	15	1.46721	1.88639	14	0.282154	16	0.282137	-10	0.72	2.0	582	9
FSV10	centre	0.03077	33	0.00106	9	1.46721	1.88684	14	0.282171	19	0.282159	-9	0.72	1.9	600	14
FSV10	centre	0.09137	77	0.00296	19	1.46722	1.88674	16	0.282059	17	0.282026	-14	0.71	2.2	595	9
FSV10	centre	0.05037	50	0.00166	14	1.46724	1.88626	16	0.282102	17	0.282083	-11	0.72	2.0	611	10
FSV10	centre	0.02580	26	0.00085	7	1.46723	1.88615	12	0.282069	21	0.282059	-12	0.71	2.1	596	11
FSV10	centre	0.04629	40	0.00155	11	1.46722	1.88615	16	0.282142	13	0.282124	-10	0.72	2.0	595	10
FSV10	centre	0.03970	32	0.00134	8	1.46727	1.88563	18	0.282120	18	0.282104	-10	0.72	2.0	630	11
FSV10	centre	0.06151	57	0.00208	16	1.46718	1.88655	16	0.282080	20	0.282057	-13	0.71	2.1	593	10
FSV10	edge	0.03748	34	0.00126	9	1.46721	1.88658	13	0.282128	19	0.282114	-10	0.72	2.0	611	9

Continuation table 5

Sample	Spot posititon	$^{176}\text{Yb}/^{177}\text{Hf}$ a	$\pm 2s$	$^{176}\text{Lu}/^{177}\text{Hf}$ a	$\pm 2s$	$^{178}\text{Hf}/^{177}\text{Hf}$	$^{180}\text{Hf}/^{177}\text{Hf}$	(V) SigHf b	$^{176}\text{Hf}/^{177}\text{Hf}$ c	$\pm 2s$	$^{176}\text{Hf}/^{177}\text{Hf}_{(t)}$ d	$\epsilon\text{Hf}^{(t)}$ d	$\pm 2s$ c	(Ga) TDM2 e	$^{206}\text{Pb}/^{238}\text{U}$ age (Ma) f	$\pm 2s$
FSV10	edge	0.03928	32	0.00133	8	1.46727	1.88619	19	0.282102	16	0.282086	-11	0.72	2.0	626	15
FSV10	resorbed	0.09025	78	0.00283	20	1.46719	1.88668	22	0.281992	15	0.281957	-15	0.71	2.3	659	11
FSV10	resorbed	0.04592	38	0.00152	10	1.46725	1.88622	14	0.282133	16	0.282114	-9	0.72	2.0	650	10
FSV35	centre	0.02519	22	0.00095	6	1.46722	1.88628	11	0.282215	18	0.282204	-7	0.72	1.8	625	10
FSV35	centre	0.03044	26	0.00114	7	1.46715	1.88631	12	0.282189	17	0.282175	-8	0.72	1.9	625	11
FSV35	centre	0.03699	36	0.00135	11	1.46727	1.88664	11	0.282186	23	0.282171	-8	0.72	1.9	601	10
FSV35	edge	0.01958	22	0.00073	7	1.46720	1.88636	13	0.282198	19	0.282190	-8	0.72	1.8	600	16
FSV35	centre	0.01363	27	0.00043	8	1.46721	1.88665	13	0.282171	15	0.282166	-9	0.72	1.9	600	9
FSV35	edge	0.01579	13	0.00067	4	1.46719	1.88667	13	0.282180	16	0.282172	-8	0.72	1.9	628	15
FSV35	centre	0.02843	23	0.00105	7	1.46718	1.88649	12	0.282204	19	0.282193	-8	0.72	1.8	583	9
FSV35	centre	0.03639	33	0.00133	10	1.46719	1.88636	11	0.282184	19	0.282169	-8	0.72	1.9	608	11
FSV35	centre	0.02439	23	0.00092	7	1.46715	1.88658	13	0.282189	18	0.282179	-8	0.72	1.9	598	10
FSV35	centre	0.01866	18	0.00075	6	1.46717	1.88603	14	0.282200	15	0.282191	-7	0.72	1.8	632	10
FSV35	centre	0.02916	31	0.00108	9	1.46719	1.88654	12	0.282205	18	0.282192	-7	0.72	1.8	629	10
FSV35	centre	0.02188	18	0.00081	5	1.46718	1.88651	12	0.282203	22	0.282194	-7	0.72	1.8	606	11
FSV35	centre	0.02708	23	0.00100	6	1.46722	1.88682	12	0.282218	17	0.282206	-7	0.72	1.8	619	11

Table 6. Lu-Hf standard zircon isotopes; High-precision LA-MC-ICP-MS U-Pb standards dates; (a) $^{176}\text{Yb}/^{177}\text{Hf} = (^{176}\text{Yb}/^{173}\text{Yb})_{\text{true}} \times (^{173}\text{Yb}/^{177}\text{Hf})_{\text{meas}} \times (M^{173}(\text{Yb})/M^{177}(\text{Hf}))_{\text{b(Hf)}}$, $\text{b(Hf)} = \ln(^{179}\text{Hf}/^{177}\text{Hf}_{\text{true}} / ^{179}\text{Hf}/^{177}\text{Hf}_{\text{meas}}) / \ln(M^{179}(\text{Hf})/M^{177}(\text{Hf}))$, M=mass of respective isotope. The $^{176}\text{Lu}/^{177}\text{Hf}$ were calculated in a similar way by using the $^{175}\text{Lu}/^{177}\text{Hf}$ and b(Yb) ; (b) Mean Hf signal in volt; (c) Uncertainties are quadratic additions of the within-run precision and the daily reproducibility of the zircon standards; (d) Initial $^{176}\text{Hf}/^{177}\text{Hf}$ and ϵHf calculated using the $^{206}\text{Pb}/^{238}\text{U}$ age determined by LA-ICP-MS dating (see column s), and the CHUR parameters: $^{176}\text{Lu}/^{177}\text{Hf} = 0.0336$, and $^{176}\text{Hf}/^{177}\text{Hf} = 0.282785$ (Bouvier *et al.*, 2008); (e) Two stage "maximum" model age in billion years using the measured $^{176}\text{Lu}/^{177}\text{Hf}$ of each spot, the value of $^{176}\text{Lu}/^{177}\text{Hf} = 0.0113$ (mean of average of continental crust (Taylor and McLennan, 1995)); (f) $^{206}\text{Pb}/^{238}\text{U}$ age determined by LA-SF-ICP-MS dating.

Standard Mud Tank September 28th, 2015	$^{176}\text{Yb}/^{177}\text{Hf}$ a	$\pm 2\text{s}$	$^{176}\text{Lu}/^{177}\text{Hf}$ a	$\pm 2\text{s}$	$^{178}\text{Hf}/^{177}\text{Hf}$	$^{180}\text{Hf}/^{177}\text{Hf}$	(V) SigHf b	$^{176}\text{Hf}/^{177}\text{Hf}$ c	$\pm 2\text{s}$	$^{176}\text{Hf}/^{177}\text{Hf}_{(t)}$ ^d	$\epsilon\text{Hf}^{(t)}$ ^d	$\pm 2\text{s}$ ^c	(Ga) TDM2 e	$^{206}\text{Pb}/^{238}\text{U}$ age (Ma) f	$\pm 2\text{s}$
Mud Tank	0.00116	1.0	0.00003	0.19	1.46724	1.88666	7	0.282519	20	0.282519	7	0.72	1.0	732	1
Mud Tank	0.00103	0.9	0.00003	0.17	1.46723	1.88664	7	0.282515	21	0.282514	7	0.72	1.0	732	1
Mud Tank	0.00116	1.0	0.00003	0.19	1.46718	1.88620	8	0.282542	20	0.282541	8	0.72	0.9	732	1
Mud Tank	0.00107	1.1	0.00003	0.18	1.46716	1.88645	8	0.282525	21	0.282525	7	0.72	1.0	732	1
Mud Tank	0.00117	1.0	0.00003	0.22	1.46729	1.88639	8	0.282530	22	0.282530	7	0.72	0.9	732	1
Mud Tank	0.00100	0.8	0.00003	0.18	1.46718	1.88656	8	0.282507	22	0.282506	7	0.72	1.0	732	1
Mud Tank	0.00093	0.8	0.00003	0.16	1.46724	1.88659	9	0.282553	21	0.282553	8	0.72	0.9	732	1
Mud Tank	0.00103	0.8	0.00003	0.18	1.46719	1.88625	11	0.282520	18	0.282520	7	0.72	1.0	732	1
Mud Tank	0.00099	0.8	0.00003	0.16	1.46726	1.88631	11	0.282517	18	0.282516	7	0.72	1.0	732	1
Mud Tank	0.00116	0.9	0.00003	0.20	1.46720	1.88658	9	0.282511	20	0.282511	7	0.72	1.0	732	1
Mud Tank	0.00121	1.0	0.00003	0.21	1.46717	1.88631	9	0.282523	21	0.282523	7	0.72	1.0	732	1
Mud Tank	0.00118	1.0	0.00003	0.20	1.46723	1.88634	9	0.282525	19	0.282524	7	0.72	1.0	732	1
Mud Tank	0.00107	1.0	0.00003	0.18	1.46720	1.88646	10	0.282514	19	0.282513	7	0.72	1.0	732	1
Mud Tank	0.00101	0.8	0.00003	0.17	1.46730	1.88642	9	0.282512	20	0.282512	7	0.72	1.0	732	1
Mud Tank	0.00100	0.8	0.00003	0.17	1.46719	1.88655	9	0.282524	19	0.282524	7	0.72	1.0	732	1
Mud Tank	0.00111	0.9	0.00003	0.18	1.46720	1.88649	9	0.282519	20	0.282518	7	0.72	1.0	732	1

Continuation Table 6

Standard Mud Tank <i>September 29th, 2015</i>	$^{176}\text{Yb}/^{177}\text{Hf}$ a	$\pm 2s$	$^{176}\text{Lu}/^{177}\text{Hf}$ a	$\pm 2s$	$^{178}\text{Hf}/^{177}\text{Hf}$	$^{180}\text{Hf}/^{177}\text{Hf}$	(V) SigHf b	$^{176}\text{Hf}/^{177}\text{Hf}$	$\pm 2s$ c	$^{176}\text{Hf}/^{177}\text{Hf}_{(t)}$ ^d	$\epsilon\text{Hf}_{(t)}$ ^d	$\pm 2s$ ^c	(Ga) TDM2 e	$^{206}\text{Pb}/^{238}\text{U}$ age (Ma) ^f	$\pm 2s$
Mud Tank	0.00096	0.8	0.00003	0.17	1.46725	1.88641	14	0.282508	17	0.282507	7	0.72	1.0	732	1
Mud Tank	0.00111	0.9	0.00003	0.20	1.46724	1.88645	13	0.282515	16	0.282515	7	0.72	1.0	732	1
Mud Tank	0.00101	0.8	0.00003	0.18	1.46720	1.88644	14	0.282521	14	0.282520	7	0.72	1.0	732	1
Mud Tank	0.00138	4.0	0.00003	0.41	1.46725	1.88620	13	0.282507	15	0.282506	7	0.72	1.0	732	1
Mud Tank	0.00098	0.8	0.00003	0.17	1.46723	1.88629	13	0.282527	15	0.282527	7	0.72	0.9	732	1
Mud Tank	0.00109	0.9	0.00003	0.19	1.46723	1.88623	13	0.282511	19	0.282511	7	0.72	1.0	732	1
Mud Tank	0.00104	0.8	0.00003	0.19	1.46725	1.88613	14	0.282522	18	0.282521	7	0.72	1.0	732	1
Mud Tank	0.00114	0.9	0.00003	0.20	1.46726	1.88620	14	0.282534	18	0.282533	7	0.72	0.9	732	1
Mud Tank	0.00113	0.9	0.00003	0.20	1.46724	1.88652	13	0.282521	15	0.282520	7	0.72	1.0	732	1
Mud Tank	0.00103	0.8	0.00003	0.19	1.46725	1.88636	13	0.282532	14	0.282532	7	0.72	0.9	732	1
Mud Tank	0.00100	0.8	0.00003	0.18	1.46725	1.88631	13	0.282538	20	0.282537	8	0.72	0.9	732	1
Mud Tank	0.00139	4.2	0.00004	0.35	1.46724	1.88630	12	0.282505	16	0.282505	6	0.72	1.0	732	1
Mud Tank	0.00104	0.8	0.00003	0.19	1.46722	1.88626	13	0.282513	14	0.282513	7	0.72	1.0	732	1
Mud Tank	0.00112	0.9	0.00003	0.20	1.46723	1.88612	13	0.282521	21	0.282520	7	0.72	1.0	732	1
Mud Tank	0.00111	0.9	0.00003	0.20	1.46722	1.88589	14	0.282518	22	0.282517	7	0.72	1.0	732	1
Mud Tank	0.00108	0.9	0.00003	0.19	1.46720	1.88618	14	0.282537	14	0.282537	8	0.72	0.9	732	1
Mud Tank	0.00115	0.9	0.00003	0.20	1.46728	1.88615	16	0.282509	16	0.282509	7	0.72	1.0	732	1
Mud Tank	0.00098	0.8	0.00003	0.18	1.46728	1.88623	16	0.282516	14	0.282516	7	0.72	1.0	732	1
Mud Tank	0.00105	0.8	0.00003	0.19	1.46725	1.88631	16	0.282532	12	0.282532	7	0.72	0.9	732	1
Mud Tank	0.00100	0.8	0.00003	0.17	1.46724	1.88594	18	0.282523	15	0.282522	7	0.72	1.0	732	1
Mud Tank	0.00109	0.9	0.00003	0.19	1.46721	1.88593	15	0.282513	13	0.282513	7	0.72	1.0	732	1
<i>September 30th, 2015</i>															
Mud Tank	0.00125	2.8	0.00003	0.27	1.46727	1.88612	14	0.282524	16	0.282523	7	0.72	1.0	732	1
Mud Tank	0.00109	0.9	0.00003	0.19	1.46725	1.88621	14	0.282511	16	0.282511	7	0.72	1.0	732	1
Mud Tank	0.00114	0.9	0.00003	0.20	1.46722	1.88593	14	0.282525	17	0.282524	7	0.72	1.0	732	1
Mud Tank	0.00120	1.3	0.00003	0.21	1.46721	1.88600	14	0.282516	18	0.282515	7	0.72	1.0	732	1
Mud Tank	0.00120	1.4	0.00003	0.21	1.46722	1.88613	15	0.282522	14	0.282522	7	0.72	1.0	732	1
Mud Tank	0.00132	1.1	0.00004	0.25	1.46720	1.88622	13	0.282513	16	0.282512	7	0.72	1.0	732	1

Continuation Table 6

Standard Mud Tank <i>September 30th, 2015</i>	$^{176}\text{Yb}/^{177}\text{Hf}$ a	$\pm 2s$	$^{176}\text{Lu}/^{177}\text{Hf}$ a	$\pm 2s$	$^{178}\text{Hf}/^{177}\text{Hf}$	$^{180}\text{Hf}/^{177}\text{Hf}$	(V) SigHf b	$^{176}\text{Hf}/^{177}\text{Hf}$ c	$\pm 2s$	$^{176}\text{Hf}/^{177}\text{Hf}_{(t)}$ d	$\epsilon\text{Hf}^{(t)}$ d	$\pm 2s$ c	(Ga) TDM2 e	$^{206}\text{Pb}/^{238}\text{U}$ age (Ma) f	$\pm 2s$
Mud Tank	0.00132	1.1	0.00004	0.25	1.46725	1.88632	13	0.282528	19	0.282528	7	0.72	0.9	732	1
Mud Tank	0.00107	0.9	0.00003	0.19	1.46726	1.88633	13	0.282509	18	0.282509	7	0.72	1.0	732	1
Mud Tank	0.00107	0.9	0.00003	0.19	1.46720	1.88636	15	0.282521	16	0.282521	7	0.72	1.0	732	1
Mud Tank	0.00097	0.8	0.00003	0.17	1.46719	1.88635	13	0.282516	19	0.282516	7	0.72	1.0	732	1
Mud Tank	0.00094	0.8	0.00003	0.17	1.46722	1.88640	13	0.282523	16	0.282522	7	0.72	1.0	732	1
Mud Tank	0.00105	0.9	0.00003	0.18	1.46722	1.88629	13	0.282520	14	0.282520	7	0.72	1.0	732	1
Mud Tank	0.00095	0.8	0.00003	0.17	1.46728	1.88610	14	0.282515	15	0.282515	7	0.72	1.0	732	1
Mud Tank	0.00104	0.9	0.00003	0.18	1.46723	1.88617	16	0.282512	15	0.282512	7	0.72	1.0	732	1
Mud Tank	0.00130	1.1	0.00004	0.24	1.46719	1.88618	15	0.282532	15	0.282532	7	0.72	0.9	732	1
Mud Tank	0.00122	1.0	0.00004	0.22	1.46724	1.88643	15	0.282499	14	0.282499	6	0.72	1.0	732	1
Mud Tank	0.00123	1.1	0.00004	0.22	1.46720	1.88626	16	0.282519	17	0.282519	7	0.72	1.0	732	1
Mud Tank	0.00115	0.9	0.00003	0.21	1.46719	1.88631	13	0.282509	16	0.282509	7	0.72	1.0	732	1
Mud Tank	0.00125	1.0	0.00004	0.22	1.46720	1.88626	13	0.282521	18	0.282520	7	0.72	1.0	732	1
Mud Tank	0.00115	0.9	0.00003	0.20	1.46721	1.88639	14	0.282492	16	0.282492	6	0.72	1.0	732	1
Mud Tank	0.00099	0.8	0.00003	0.17	1.46727	1.88638	13	0.282531	18	0.282530	7	0.72	0.9	732	1
Mud Tank	0.00103	0.8	0.00003	0.17	1.46726	1.88665	13	0.282508	15	0.282507	7	0.72	1.0	732	1
Mud Tank	0.00100	0.8	0.00003	0.17	1.46723	1.88648	13	0.282530	14	0.282529	7	0.72	0.9	732	1
Mud Tank	0.00106	1.3	0.00003	0.19	1.46720	1.88656	11	0.282512	16	0.282512	7	0.72	1.0	732	1
Mud Tank	0.00100	0.8	0.00003	0.18	1.46723	1.88615	13	0.282527	17	0.282527	7	0.72	0.9	732	1
Mud Tank	0.00114	0.9	0.00003	0.20	1.46725	1.88651	12	0.282514	15	0.282514	7	0.72	1.0	732	1
Mud Tank	0.00111	1.0	0.00003	0.20	1.46726	1.88644	13	0.282512	16	0.282512	7	0.72	1.0	732	1
Mud Tank	0.00109	0.9	0.00003	0.19	1.46724	1.88652	12	0.282517	16	0.282517	7	0.72	1.0	732	1
Mud Tank	0.00109	0.9	0.00003	0.18	1.46725	1.88643	13	0.282522	18	0.282521	7	0.72	1.0	732	1
Mud Tank	0.00105	0.9	0.00003	0.18	1.46722	1.88631	13	0.282512	18	0.282511	7	0.72	1.0	732	1
<i>October 2nd, 2015</i>															
Mud Tank	0.00128	1.0	0.00003	0.20	1.46724	1.88617	12	0.282521	16	0.282520	7	0.72	1.0	732	1
Mud Tank	0.00120	1.0	0.00003	0.19	1.46719	1.88630	12	0.282489	21	0.282488	6	0.72	1.0	732	1
Mud Tank	0.00122	1.0	0.00003	0.20	1.46724	1.88593	12	0.282517	16	0.282517	7	0.72	1.0	732	1

Continuation Table 6

Standard Mud Tank <i>September 30th, 2015</i>	$^{176}\text{Yb}/^{177}\text{Hf}$ a	$\pm 2s$	$^{176}\text{Lu}/^{177}\text{Hf}$ a	$\pm 2s$	$^{178}\text{Hf}/^{177}\text{Hf}$	$^{180}\text{Hf}/^{177}\text{Hf}$	(V) SigHf b	$^{176}\text{Hf}/^{177}\text{Hf}$ c	$\pm 2s$	$^{176}\text{Hf}/^{177}\text{Hf}_{(t)}$ d	$\epsilon\text{Hf}^{(t)}$ d	$\pm 2s$ c	(Ga) TDM2 e	$^{206}\text{Pb}/^{238}\text{U}$ age (Ma) f	$\pm 2s$
Mud Tank	0.00132	1.1	0.00004	0.25	1.46725	1.88632	13	0.282528	19	0.282528	7	0.72	0.9	732	1
Mud Tank	0.00107	0.9	0.00003	0.19	1.46726	1.88633	13	0.282509	18	0.282509	7	0.72	1.0	732	1
Mud Tank	0.00107	0.9	0.00003	0.19	1.46720	1.88636	15	0.282521	16	0.282521	7	0.72	1.0	732	1
Mud Tank	0.00097	0.8	0.00003	0.17	1.46719	1.88635	13	0.282516	19	0.282516	7	0.72	1.0	732	1
Mud Tank	0.00094	0.8	0.00003	0.17	1.46722	1.88640	13	0.282523	16	0.282522	7	0.72	1.0	732	1
Mud Tank	0.00105	0.9	0.00003	0.18	1.46722	1.88629	13	0.282520	14	0.282520	7	0.72	1.0	732	1
Mud Tank	0.00095	0.8	0.00003	0.17	1.46728	1.88610	14	0.282515	15	0.282515	7	0.72	1.0	732	1
Mud Tank	0.00104	0.9	0.00003	0.18	1.46723	1.88617	16	0.282512	15	0.282512	7	0.72	1.0	732	1
Mud Tank	0.00130	1.1	0.00004	0.24	1.46719	1.88618	15	0.282532	15	0.282532	7	0.72	0.9	732	1
Mud Tank	0.00122	1.0	0.00004	0.22	1.46724	1.88643	15	0.282499	14	0.282499	6	0.72	1.0	732	1
Mud Tank	0.00123	1.1	0.00004	0.22	1.46720	1.88626	16	0.282519	17	0.282519	7	0.72	1.0	732	1
Mud Tank	0.00115	0.9	0.00003	0.21	1.46719	1.88631	13	0.282509	16	0.282509	7	0.72	1.0	732	1
Mud Tank	0.00125	1.0	0.00004	0.22	1.46720	1.88626	13	0.282521	18	0.282520	7	0.72	1.0	732	1
Mud Tank	0.00115	0.9	0.00003	0.20	1.46721	1.88639	14	0.282492	16	0.282492	6	0.72	1.0	732	1
Mud Tank	0.00099	0.8	0.00003	0.17	1.46727	1.88638	13	0.282531	18	0.282530	7	0.72	0.9	732	1
Mud Tank	0.00103	0.8	0.00003	0.17	1.46726	1.88665	13	0.282508	15	0.282507	7	0.72	1.0	732	1
Mud Tank	0.00100	0.8	0.00003	0.17	1.46723	1.88648	13	0.282530	14	0.282529	7	0.72	0.9	732	1
Mud Tank	0.00106	1.3	0.00003	0.19	1.46720	1.88656	11	0.282512	16	0.282512	7	0.72	1.0	732	1
Mud Tank	0.00100	0.8	0.00003	0.18	1.46723	1.88615	13	0.282527	17	0.282527	7	0.72	0.9	732	1
Mud Tank	0.00114	0.9	0.00003	0.20	1.46725	1.88651	12	0.282514	15	0.282514	7	0.72	1.0	732	1
Mud Tank	0.00111	1.0	0.00003	0.20	1.46726	1.88644	13	0.282512	16	0.282512	7	0.72	1.0	732	1
Mud Tank	0.00109	0.9	0.00003	0.19	1.46724	1.88652	12	0.282517	16	0.282517	7	0.72	1.0	732	1
Mud Tank	0.00109	0.9	0.00003	0.18	1.46725	1.88643	13	0.282522	18	0.282521	7	0.72	1.0	732	1
Mud Tank	0.00105	0.9	0.00003	0.18	1.46722	1.88631	13	0.282512	18	0.282511	7	0.72	1.0	732	1
<i>October 2nd, 2015</i>															
Mud Tank	0.00128	1.0	0.00003	0.20	1.46724	1.88617	12	0.282521	16	0.282520	7	0.72	1.0	732	1
Mud Tank	0.00120	1.0	0.00003	0.19	1.46719	1.88630	12	0.282489	21	0.282488	6	0.72	1.0	732	1
Mud Tank	0.00122	1.0	0.00003	0.20	1.46724	1.88593	12	0.282517	16	0.282517	7	0.72	1.0	732	1

Continuation Table 6

Standard Mud Tank <i>September 30th, 2015</i>	$^{176}\text{Yb}/^{177}\text{Hf}$ a	$\pm 2s$	$^{176}\text{Lu}/^{177}\text{Hf}$ a	$\pm 2s$	$^{178}\text{Hf}/^{177}\text{Hf}$	$^{180}\text{Hf}/^{177}\text{Hf}$	(V) SigHf b	$^{176}\text{Hf}/^{177}\text{Hf}$ c	$\pm 2s$	$^{176}\text{Hf}/^{177}\text{Hf}$ f _(t) ^d	$\epsilon\text{Hf}^{(t)}$ d	$\pm 2s$ ^c	(Ga) TDM2 e	$^{206}\text{Pb}/^{238}\text{U}$ age (Ma) f	$\pm 2s$
Mud Tank	0.00118	1.0	0.00003	0.18	1.46721	1.88603	13	0.282532	17	0.282532	7	0.72	0.9	732	1
Mud Tank	0.00118	1.0	0.00003	0.18	1.46721	1.88603	13	0.282532	17	0.282532	7	0.72	0.9	732	1
Mud Tank	0.00117	1.0	0.00003	0.18	1.46722	1.88584	14	0.282521	24	0.282520	7	0.72	1.0	732	1
Mud Tank	0.00125	1.0	0.00003	0.20	1.46727	1.88614	13	0.282521	18	0.282521	7	0.72	1.0	732	1
Mud Tank	0.00128	1.1	0.00003	0.21	1.46719	1.88641	13	0.282531	17	0.282530	7	0.72	0.9	732	1
Mud Tank	0.00108	0.9	0.00003	0.17	1.46717	1.88596	15	0.282517	15	0.282517	7	0.72	1.0	732	1
Mud Tank	0.00108	0.9	0.00003	0.17	1.46725	1.88626	15	0.282530	16	0.282530	7	0.72	0.9	732	1
Mud Tank	0.00133	1.2	0.00003	0.21	1.46727	1.88615	15	0.282531	16	0.282531	7	0.72	0.9	732	1
Mud Tank	0.00110	0.9	0.00003	0.17	1.46719	1.88635	13	0.282533	19	0.282533	7	0.72	0.9	732	1
Mud Tank	0.00125	1.1	0.00003	0.18	1.46726	1.88622	13	0.282521	18	0.282521	7	0.72	1.0	732	1
Mud Tank	0.00117	1.0	0.00003	0.18	1.46719	1.88618	13	0.282523	16	0.282523	7	0.72	1.0	732	1
Mud Tank	0.00125	1.0	0.00003	0.20	1.46727	1.88633	14	0.282521	16	0.282521	7	0.72	1.0	732	1
Mud Tank	0.00113	0.9	0.00003	0.18	1.46721	1.88643	15	0.282518	15	0.282517	7	0.72	1.0	732	1
Mud Tank	0.00114	0.9	0.00003	0.18	1.46723	1.88625	15	0.282514	17	0.282514	7	0.72	1.0	732	1
Mud Tank	0.00124	1.1	0.00003	0.19	1.46724	1.88631	15	0.282509	16	0.282509	7	0.72	1.0	732	1
Mud Tank	0.00107	0.9	0.00003	0.17	1.46722	1.88629	14	0.282515	16	0.282515	7	0.72	1.0	732	1
Mud Tank	0.00108	0.9	0.00003	0.17	1.46723	1.88645	15	0.282536	15	0.282536	8	0.72	0.9	732	1
Mud Tank	0.00106	0.9	0.00003	0.17	1.46721	1.88627	15	0.282536	17	0.282535	8	0.72	0.9	732	1
Mud Tank	0.00116	0.9	0.00003	0.18	1.46719	1.88619	14	0.282523	20	0.282522	7	0.72	1.0	732	1
Mud Tank	0.00110	0.9	0.00003	0.17	1.46717	1.88630	14	0.282513	17	0.282512	7	0.72	1.0	732	1

Continuation Table 6

Standard Mud Tank <i>September 28th, 2015</i>	$^{176}\text{Yb}/^{177}\text{Hf}$ a	$\pm 2s$	$^{176}\text{Lu}/^{177}\text{Hf}$ a	$\pm 2s$	$^{178}\text{Hf}/^{177}\text{Hf}$	$^{180}\text{Hf}/^{177}\text{Hf}$	(V) SigHf b	$^{176}\text{Hf}/^{177}\text{Hf}$	$\pm 2s$ c	$^{176}\text{Hf}/^{177}\text{Hf}$ $f_{(t)}$ d	$\epsilon\text{Hf}^{(t)}$ d	$\pm 2s$ c	(Ga) TDM2 e	$^{206}\text{Pb}/^{238}\text{U}$ age (Ma) f	$\pm 2s$
91500	0.01197	10.5	0.00043	2.60	1.46723	1.88609	4	0.282321	34	0.282312	7	0.72	1.2	1065	1
91500	0.01120	9.0	0.00042	2.54	1.46725	1.88649	4	0.282321	33	0.282312	7	0.72	1.2	1065	1
91500	0.01114	9.0	0.00042	2.52	1.46724	1.88609	5	0.282339	32	0.282330	8	0.72	1.2	1065	1
91500	0.01232	9.9	0.00045	2.74	1.46715	1.88616	5	0.282300	29	0.282291	6	0.72	1.3	1065	1
91500	0.01218	9.8	0.00046	2.75	1.46718	1.88619	5	0.282319	31	0.282310	7	0.72	1.2	1065	1
91500	0.01288	10.8	0.00047	2.93	1.46722	1.88605	5	0.282312	24	0.282302	7	0.72	1.2	1065	1
91500	0.01161	9.4	0.00043	2.59	1.46726	1.88629	5	0.282310	26	0.282302	7	0.72	1.2	1065	1
91500	0.01151	9.2	0.00043	2.59	1.46721	1.88622	6	0.282271	31	0.282262	5	0.72	1.3	1065	1
91500	0.01246	10.0	0.00047	2.84	1.46723	1.88587	5	0.282316	27	0.282307	7	0.72	1.2	1065	1
91500	0.01210	9.7	0.00046	2.78	1.46724	1.88635	5	0.282321	26	0.282312	7	0.72	1.2	1065	1
91500	0.01095	8.8	0.00041	2.46	1.46718	1.88627	5	0.282296	29	0.282288	6	0.72	1.3	1065	1
91500	0.01118	9.0	0.00042	2.52	1.46714	1.88637	5	0.282313	21	0.282305	7	0.72	1.2	1065	1
<i>September 29th, 2015</i>															
91500	0.01191	9.6	0.00045	2.74	1.46719	1.88629	7	0.282302	25	0.282293	6	0.72	1.3	1065	1
91500	0.01122	9.0	0.00042	2.59	1.46723	1.88611	7	0.282354	28	0.282346	8	0.72	1.2	1065	1
91500	0.01157	9.3	0.00043	2.63	1.46720	1.88587	8	0.282332	19	0.282324	8	0.72	1.2	1065	1
91500	0.01475	26.3	0.00047	2.93	1.46723	1.88621	7	0.282307	22	0.282298	7	0.72	1.3	1065	1
91500	0.01254	10.1	0.00046	2.75	1.46726	1.88653	7	0.282302	22	0.282292	6	0.72	1.3	1065	1
91500	0.01238	10.0	0.00046	2.76	1.46716	1.88640	6	0.282314	23	0.282305	7	0.72	1.2	1065	1
91500	0.01331	11.3	0.00049	3.20	1.46718	1.88609	7	0.282356	17	0.282346	8	0.72	1.2	1065	1
91500	0.01350	11.1	0.00050	3.18	1.46722	1.88620	7	0.282345	22	0.282335	8	0.72	1.2	1065	1
91500	0.01415	11.5	0.00052	3.28	1.46725	1.88605	8	0.282321	25	0.282311	7	0.72	1.2	1065	1
91500	0.01418	12.3	0.00051	3.19	1.46723	1.88602	7	0.282304	27	0.282294	7	0.72	1.3	1065	1
91500	0.01116	9.0	0.00042	2.52	1.46723	1.88603	8	0.282315	25	0.282307	7	0.72	1.2	1065	1
91500	0.01124	9.1	0.00042	2.54	1.46724	1.88626	8	0.282340	20	0.282331	8	0.72	1.2	1065	1
91500	0.01138	9.1	0.00042	2.55	1.46726	1.88625	8	0.282312	21	0.282303	7	0.72	1.2	1065	1
91500	0.01272	10.2	0.00045	2.74	1.46726	1.88626	7	0.282321	23	0.282312	7	0.72	1.2	1065	1
91500	0.01211	9.8	0.00045	2.71	1.46727	1.88635	7	0.282317	25	0.282309	7	0.72	1.2	1065	1

Continuation Table 6

Standard Mud Tank <i>September 28th, 2015</i>	$^{176}\text{Yb}/^{177}\text{Hf}$ a	$\pm 2s$	$^{176}\text{Lu}/^{177}\text{Hf}$ a	$\pm 2s$	$^{178}\text{Hf}/^{177}\text{Hf}$	$^{180}\text{Hf}/^{177}\text{Hf}$	(V) SigHf b	$^{176}\text{Hf}/^{177}\text{Hf}$	$\pm 2s$ c	$^{176}\text{Hf}/^{177}\text{Hf}$ $f(t)$ d	$\epsilon\text{Hf}(t)$ d	$\pm 2s$ c	(Ga) TDM2 e	$^{206}\text{Pb}/^{238}\text{U}$ age (Ma) f	$\pm 2s$
91500	0.01197	10.5	0.00043	2.60	1.46723	1.88609	4	0.282321	34	0.282312	7	0.72	1.2	1065	1
91500	0.01120	9.0	0.00042	2.54	1.46725	1.88649	4	0.282321	33	0.282312	7	0.72	1.2	1065	1
91500	0.01114	9.0	0.00042	2.52	1.46724	1.88609	5	0.282339	32	0.282330	8	0.72	1.2	1065	1
91500	0.01232	9.9	0.00045	2.74	1.46715	1.88616	5	0.282300	29	0.282291	6	0.72	1.3	1065	1
91500	0.01218	9.8	0.00046	2.75	1.46718	1.88619	5	0.282319	31	0.282310	7	0.72	1.2	1065	1
91500	0.01288	10.8	0.00047	2.93	1.46722	1.88605	5	0.282312	24	0.282302	7	0.72	1.2	1065	1
91500	0.01161	9.4	0.00043	2.59	1.46726	1.88629	5	0.282310	26	0.282302	7	0.72	1.2	1065	1
91500	0.01151	9.2	0.00043	2.59	1.46721	1.88622	6	0.282271	31	0.282262	5	0.72	1.3	1065	1
91500	0.01246	10.0	0.00047	2.84	1.46723	1.88587	5	0.282316	27	0.282307	7	0.72	1.2	1065	1
91500	0.01210	9.7	0.00046	2.78	1.46724	1.88635	5	0.282321	26	0.282312	7	0.72	1.2	1065	1
91500	0.01095	8.8	0.00041	2.46	1.46718	1.88627	5	0.282296	29	0.282288	6	0.72	1.3	1065	1
91500	0.01118	9.0	0.00042	2.52	1.46714	1.88637	5	0.282313	21	0.282305	7	0.72	1.2	1065	1
<i>September 29th, 2015</i>															
91500	0.01191	9.6	0.00045	2.74	1.46719	1.88629	7	0.282302	25	0.282293	6	0.72	1.3	1065	1
91500	0.01122	9.0	0.00042	2.59	1.46723	1.88611	7	0.282354	28	0.282346	8	0.72	1.2	1065	1
91500	0.01157	9.3	0.00043	2.63	1.46720	1.88587	8	0.282332	19	0.282324	8	0.72	1.2	1065	1
91500	0.01475	26.3	0.00047	2.93	1.46723	1.88621	7	0.282307	22	0.282298	7	0.72	1.3	1065	1
91500	0.01254	10.1	0.00046	2.75	1.46726	1.88653	7	0.282302	22	0.282292	6	0.72	1.3	1065	1
91500	0.01238	10.0	0.00046	2.76	1.46716	1.88640	6	0.282314	23	0.282305	7	0.72	1.2	1065	1
91500	0.01331	11.3	0.00049	3.20	1.46718	1.88609	7	0.282356	17	0.282346	8	0.72	1.2	1065	1
91500	0.01350	11.1	0.00050	3.18	1.46722	1.88620	7	0.282345	22	0.282335	8	0.72	1.2	1065	1
91500	0.01415	11.5	0.00052	3.28	1.46725	1.88605	8	0.282321	25	0.282311	7	0.72	1.2	1065	1
91500	0.01418	12.3	0.00051	3.19	1.46723	1.88602	7	0.282304	27	0.282294	7	0.72	1.3	1065	1
91500	0.01116	9.0	0.00042	2.52	1.46723	1.88603	8	0.282315	25	0.282307	7	0.72	1.2	1065	1
91500	0.01124	9.1	0.00042	2.54	1.46724	1.88626	8	0.282340	20	0.282331	8	0.72	1.2	1065	1
91500	0.01138	9.1	0.00042	2.55	1.46726	1.88625	8	0.282312	21	0.282303	7	0.72	1.2	1065	1
91500	0.01272	10.2	0.00045	2.74	1.46726	1.88626	7	0.282321	23	0.282312	7	0.72	1.2	1065	1
91500	0.01211	9.8	0.00045	2.71	1.46727	1.88635	7	0.282317	25	0.282309	7	0.72	1.2	1065	1

Continuation Table 6

Standard Mud Tank <i>September 29th, 2015</i>	$^{176}\text{Yb}/^{177}\text{Hf}$ a	$\pm 2s$	$^{176}\text{Lu}/^{177}\text{Hf}$ a	$\pm 2s$	$^{178}\text{Hf}/^{177}\text{Hf}$	$^{180}\text{Hf}/^{177}\text{Hf}$	(V) SigHf b	$^{176}\text{Hf}/^{177}\text{Hf}$	$\pm 2s$ c	$^{176}\text{Hf}/^{177}\text{Hf}$ $f(t)$ d	$\epsilon\text{Hf}(t)$ d	$\pm 2s$ c	(Ga) TDM2 e	$^{206}\text{Pb}/^{238}\text{U}$ age (Ma) f	$\pm 2s$
91500	0.01176	9.5	0.00044	2.63	1.46726	1.88632	7	0.282310	26	0.282302	7	0.72	1.2	1065	1
91500	0.01298	10.5	0.00045	2.72	1.46723	1.88627	8	0.282320	27	0.282311	7	0.72	1.2	1065	1
91500	0.01208	9.7	0.00046	2.76	1.46729	1.88595	7	0.282346	22	0.282337	8	0.72	1.2	1065	1
91500	0.01398	11.3	0.00052	3.26	1.46719	1.88607	8	0.282335	24	0.282324	8	0.72	1.2	1065	1
91500	0.01357	11.0	0.00051	3.17	1.46721	1.88597	8	0.282318	20	0.282308	7	0.72	1.2	1065	1
91500	0.01275	10.3	0.00047	2.91	1.46719	1.88595	9	0.282291	32	0.282282	6	0.72	1.3	1065	1
<i>September 30th, 2015</i>															
91500	0.00722	5.9	0.00027	1.65	1.46721	1.88622	10	0.282291	19	0.282286	6	0.72	1.3	1065	1
91500	0.00930	7.5	0.00035	2.09	1.46718	1.88640	10	0.282322	19	0.282315	7	0.72	1.2	1065	1
91500	0.00946	7.6	0.00035	2.12	1.46724	1.88613	10	0.282323	25	0.282316	7	0.72	1.2	1065	1
91500	0.01288	10.4	0.00047	2.92	1.46724	1.88628	7	0.282304	21	0.282295	7	0.72	1.3	1065	1
91500	0.01160	9.4	0.00042	2.61	1.46720	1.88641	7	0.282318	22	0.282310	7	0.72	1.2	1065	1
91500	0.01392	11.3	0.00051	3.22	1.46721	1.88616	7	0.282329	22	0.282319	7	0.72	1.2	1065	1
91500	0.01129	9.1	0.00042	2.53	1.46724	1.88627	8	0.282317	21	0.282308	7	0.72	1.2	1065	1
91500	0.01164	9.8	0.00043	2.75	1.46718	1.88600	9	0.282316	19	0.282307	7	0.72	1.2	1065	1
91500	0.00479	4.0	0.00018	1.10	1.46719	1.88615	8	0.282294	22	0.282290	6	0.72	1.3	1065	1
91500	0.01283	10.4	0.00047	2.91	1.46726	1.88600	8	0.282299	25	0.282289	6	0.72	1.3	1065	1
91500	0.01230	9.9	0.00046	2.80	1.46718	1.88622	8	0.282284	23	0.282275	6	0.72	1.3	1065	1
91500	0.01304	10.6	0.00049	3.07	1.46720	1.88605	7	0.282326	22	0.282317	7	0.72	1.2	1065	1
91500	0.01198	9.6	0.00045	2.77	1.46716	1.88623	7	0.282301	28	0.282292	6	0.72	1.3	1065	1
91500	0.01115	9.0	0.00042	2.60	1.46717	1.88641	7	0.282300	20	0.282291	6	0.72	1.3	1065	1
91500	0.01104	8.9	0.00041	2.46	1.46718	1.88633	9	0.282304	20	0.282295	7	0.72	1.3	1065	1
91500	0.01151	9.3	0.00042	2.53	1.46721	1.88628	9	0.282292	16	0.282284	6	0.72	1.3	1065	1
91500	0.01153	9.2	0.00043	2.58	1.46719	1.88615	9	0.282303	18	0.282294	7	0.72	1.3	1065	1
91500	0.01125	9.1	0.00042	2.54	1.46728	1.88635	8	0.282290	26	0.282281	6	0.72	1.3	1065	1
91500	0.01134	9.1	0.00042	2.56	1.46725	1.88639	8	0.282291	25	0.282282	6	0.72	1.3	1065	1
91500	0.01108	9.0	0.00041	2.50	1.46719	1.88604	8	0.282299	26	0.282291	6	0.72	1.3	1065	1
91500	0.01324	10.8	0.00049	3.09	1.46721	1.88613	8	0.282312	23	0.282303	7	0.72	1.2	1065	1

Continuation Table 6

Standard Mud Tank <i>September 29th, 2015</i>	$^{176}\text{Yb}/^{177}\text{Hf}$ a	$\pm 2s$	$^{176}\text{Lu}/^{177}\text{Hf}$ a	$\pm 2s$	$^{178}\text{Hf}/^{177}\text{Hf}$	$^{180}\text{Hf}/^{177}\text{Hf}$	(V) SigHf b	$^{176}\text{Hf}/^{177}\text{Hf}$	$\pm 2s$ c	$^{176}\text{Hf}/^{177}\text{Hf}$ $f(t)$ d	$\epsilon\text{Hf}(t)$ d	$\pm 2s$ c	(Ga) TDM2 e	$^{206}\text{Pb}/^{238}\text{U}$ age (Ma) f	$\pm 2s$
91500	0.01176	9.5	0.00044	2.63	1.46726	1.88632	7	0.282310	26	0.282302	7	0.72	1.2	1065	1
91500	0.01298	10.5	0.00045	2.72	1.46723	1.88627	8	0.282320	27	0.282311	7	0.72	1.2	1065	1
91500	0.01208	9.7	0.00046	2.76	1.46729	1.88595	7	0.282346	22	0.282337	8	0.72	1.2	1065	1
91500	0.01398	11.3	0.00052	3.26	1.46719	1.88607	8	0.282335	24	0.282324	8	0.72	1.2	1065	1
91500	0.01357	11.0	0.00051	3.17	1.46721	1.88597	8	0.282318	20	0.282308	7	0.72	1.2	1065	1
91500	0.01275	10.3	0.00047	2.91	1.46719	1.88595	9	0.282291	32	0.282282	6	0.72	1.3	1065	1
<i>September 30th, 2015</i>															
91500	0.00722	5.9	0.00027	1.65	1.46721	1.88622	10	0.282291	19	0.282286	6	0.72	1.3	1065	1
91500	0.00930	7.5	0.00035	2.09	1.46718	1.88640	10	0.282322	19	0.282315	7	0.72	1.2	1065	1
91500	0.00946	7.6	0.00035	2.12	1.46724	1.88613	10	0.282323	25	0.282316	7	0.72	1.2	1065	1
91500	0.01288	10.4	0.00047	2.92	1.46724	1.88628	7	0.282304	21	0.282295	7	0.72	1.3	1065	1
91500	0.01160	9.4	0.00042	2.61	1.46720	1.88641	7	0.282318	22	0.282310	7	0.72	1.2	1065	1
91500	0.01392	11.3	0.00051	3.22	1.46721	1.88616	7	0.282329	22	0.282319	7	0.72	1.2	1065	1
91500	0.01129	9.1	0.00042	2.53	1.46724	1.88627	8	0.282317	21	0.282308	7	0.72	1.2	1065	1
91500	0.01164	9.8	0.00043	2.75	1.46718	1.88600	9	0.282316	19	0.282307	7	0.72	1.2	1065	1
91500	0.00479	4.0	0.00018	1.10	1.46719	1.88615	8	0.282294	22	0.282290	6	0.72	1.3	1065	1
91500	0.01283	10.4	0.00047	2.91	1.46726	1.88600	8	0.282299	25	0.282289	6	0.72	1.3	1065	1
91500	0.01230	9.9	0.00046	2.80	1.46718	1.88622	8	0.282284	23	0.282275	6	0.72	1.3	1065	1
91500	0.01304	10.6	0.00049	3.07	1.46720	1.88605	7	0.282326	22	0.282317	7	0.72	1.2	1065	1
91500	0.01198	9.6	0.00045	2.77	1.46716	1.88623	7	0.282301	28	0.282292	6	0.72	1.3	1065	1
91500	0.01115	9.0	0.00042	2.60	1.46717	1.88641	7	0.282300	20	0.282291	6	0.72	1.3	1065	1
91500	0.01104	8.9	0.00041	2.46	1.46718	1.88633	9	0.282304	20	0.282295	7	0.72	1.3	1065	1
91500	0.01151	9.3	0.00042	2.53	1.46721	1.88628	9	0.282292	16	0.282284	6	0.72	1.3	1065	1
91500	0.01153	9.2	0.00043	2.58	1.46719	1.88615	9	0.282303	18	0.282294	7	0.72	1.3	1065	1
91500	0.01125	9.1	0.00042	2.54	1.46728	1.88635	8	0.282290	26	0.282281	6	0.72	1.3	1065	1
91500	0.01134	9.1	0.00042	2.56	1.46725	1.88639	8	0.282291	25	0.282282	6	0.72	1.3	1065	1
91500	0.01108	9.0	0.00041	2.50	1.46719	1.88604	8	0.282299	26	0.282291	6	0.72	1.3	1065	1
91500	0.01324	10.8	0.00049	3.09	1.46721	1.88613	8	0.282312	23	0.282303	7	0.72	1.2	1065	1

Continuation Table 6

Standard Mud Tank <i>September 30th, 2015</i>	$^{176}\text{Yb}/^{177}\text{Hf}$ a	$\pm 2s$	$^{176}\text{Lu}/^{177}\text{Hf}$ a	$\pm 2s$	$^{178}\text{Hf}/^{177}\text{Hf}$	$^{180}\text{Hf}/^{177}\text{Hf}$	(V) SigHf b	$^{176}\text{Hf}/^{177}\text{Hf}$ c	$\pm 2s$	$^{176}\text{Hf}/^{177}\text{Hf}$ f _(t) ^d	$\epsilon\text{Hf}^{(t)}$ d	$\pm 2s$ ^c	(Ga) TDM2 e	$^{206}\text{Pb}/^{238}\text{U}$ age (Ma) f	$\pm 2s$
91500	0.01327	10.8	0.00049	3.12	1.46716	1.88622	7	0.282297	20	0.282287	6	0.72	1.3	1065	1
91500	0.01173	9.4	0.00043	2.67	1.46725	1.88611	8	0.282313	23	0.282304	7	0.72	1.2	1065	1
91500	0.01424	11.5	0.00051	3.22	1.46718	1.88611	9	0.282309	20	0.282299	7	0.72	1.3	1065	1
91500	0.01236	9.9	0.00045	2.70	1.46727	1.88645	8	0.282299	21	0.282290	6	0.72	1.3	1065	1
91500	0.01207	9.7	0.00043	2.65	1.46720	1.88616	8	0.282305	23	0.282296	7	0.72	1.3	1065	1
<i>October 2nd, 2015</i>															
91500	0.01289	10.4	0.00042	2.56	1.46724	1.88589	7	0.282303	25	0.282294	7	0.72	1.3	1065	1
91500	0.01294	10.4	0.00043	2.57	1.46725	1.88604	6	0.282333	23	0.282324	8	0.72	1.2	1065	1
91500	0.01340	12.4	0.00042	2.58	1.46719	1.88605	7	0.282299	27	0.282291	6	0.72	1.3	1065	1
91500	0.00880	7.8	0.00029	2.01	1.46722	1.88633	6	0.282285	24	0.282279	6	0.72	1.3	1065	1
91500	0.00919	7.5	0.00030	1.90	1.46723	1.88640	6	0.282310	25	0.282304	7	0.72	1.2	1065	1
91500	0.00921	7.7	0.00031	1.96	1.46724	1.88620	6	0.282312	24	0.282306	7	0.72	1.2	1065	1
91500	0.01242	10.0	0.00042	2.58	1.46716	1.88624	7	0.282346	21	0.282338	8	0.72	1.2	1065	1
91500	0.01225	9.9	0.00042	2.52	1.46720	1.88645	7	0.282297	25	0.282288	6	0.72	1.3	1065	1
91500	0.01232	9.9	0.00042	2.57	1.46724	1.88620	8	0.282312	19	0.282303	7	0.72	1.2	1065	1
91500	0.01187	9.6	0.00040	2.40	1.46723	1.88601	8	0.282356	20	0.282348	8	0.72	1.2	1065	1
91500	0.01225	10.0	0.00041	2.46	1.46717	1.88618	9	0.282343	20	0.282335	8	0.72	1.2	1065	1
91500	0.01359	10.9	0.00045	2.77	1.46722	1.88615	7	0.282291	26	0.282282	6	0.72	1.3	1065	1
91500	0.01312	10.5	0.00044	2.70	1.46720	1.88671	7	0.282274	28	0.282265	5	0.72	1.3	1065	1
91500	0.01308	10.7	0.00044	2.68	1.46717	1.88626	7	0.282322	21	0.282313	7	0.72	1.2	1065	1
91500	0.01237	10.0	0.00040	2.43	1.46726	1.88632	7	0.282305	22	0.282297	7	0.72	1.3	1065	1
91500	0.01192	9.6	0.00039	2.36	1.46717	1.88615	9	0.282289	23	0.282281	6	0.72	1.3	1065	1
91500	0.01196	9.7	0.00040	2.40	1.46720	1.88625	8	0.282287	16	0.282279	6	0.72	1.3	1065	1
91500	0.01214	9.8	0.00041	2.47	1.46724	1.88620	8	0.282303	17	0.282294	7	0.72	1.3	1065	1
91500	0.01193	9.6	0.00040	2.44	1.46722	1.88622	8	0.282309	23	0.282301	7	0.72	1.2	1065	1
91500	0.01277	10.3	0.00042	2.55	1.46721	1.88626	8	0.282325	25	0.282317	7	0.72	1.2	1065	1

Continuation Table 6

Standard Mud Tank <i>September 30th, 2015</i>	$^{176}\text{Yb}/^{177}\text{Hf}$ a	$\pm 2s$	$^{176}\text{Lu}/^{177}\text{Hf}$ a	$\pm 2s$	$^{178}\text{Hf}/^{177}\text{Hf}$	$^{180}\text{Hf}/^{177}\text{Hf}$	(V) SigHf b	$^{176}\text{Hf}/^{177}\text{Hf}$ c	$\pm 2s$	$^{176}\text{Hf}/^{177}\text{Hf}$ f _(t) ^d	$\epsilon\text{Hf}^{(t)}$ d	$\pm 2s$ ^c	(Ga) TDM2 e	$^{206}\text{Pb}/^{238}\text{U}$ age (Ma) f	$\pm 2s$
91500	0.01327	10.8	0.00049	3.12	1.46716	1.88622	7	0.282297	20	0.282287	6	0.72	1.3	1065	1
91500	0.01173	9.4	0.00043	2.67	1.46725	1.88611	8	0.282313	23	0.282304	7	0.72	1.2	1065	1
91500	0.01424	11.5	0.00051	3.22	1.46718	1.88611	9	0.282309	20	0.282299	7	0.72	1.3	1065	1
91500	0.01236	9.9	0.00045	2.70	1.46727	1.88645	8	0.282299	21	0.282290	6	0.72	1.3	1065	1
91500	0.01207	9.7	0.00043	2.65	1.46720	1.88616	8	0.282305	23	0.282296	7	0.72	1.3	1065	1
<i>October 2nd, 2015</i>															
91500	0.01289	10.4	0.00042	2.56	1.46724	1.88589	7	0.282303	25	0.282294	7	0.72	1.3	1065	1
91500	0.01294	10.4	0.00043	2.57	1.46725	1.88604	6	0.282333	23	0.282324	8	0.72	1.2	1065	1
91500	0.01340	12.4	0.00042	2.58	1.46719	1.88605	7	0.282299	27	0.282291	6	0.72	1.3	1065	1
91500	0.00880	7.8	0.00029	2.01	1.46722	1.88633	6	0.282285	24	0.282279	6	0.72	1.3	1065	1
91500	0.00919	7.5	0.00030	1.90	1.46723	1.88640	6	0.282310	25	0.282304	7	0.72	1.2	1065	1
91500	0.00921	7.7	0.00031	1.96	1.46724	1.88620	6	0.282312	24	0.282306	7	0.72	1.2	1065	1
91500	0.01242	10.0	0.00042	2.58	1.46716	1.88624	7	0.282346	21	0.282338	8	0.72	1.2	1065	1
91500	0.01225	9.9	0.00042	2.52	1.46720	1.88645	7	0.282297	25	0.282288	6	0.72	1.3	1065	1
91500	0.01232	9.9	0.00042	2.57	1.46724	1.88620	8	0.282312	19	0.282303	7	0.72	1.2	1065	1
91500	0.01187	9.6	0.00040	2.40	1.46723	1.88601	8	0.282356	20	0.282348	8	0.72	1.2	1065	1
91500	0.01225	10.0	0.00041	2.46	1.46717	1.88618	9	0.282343	20	0.282335	8	0.72	1.2	1065	1
91500	0.01359	10.9	0.00045	2.77	1.46722	1.88615	7	0.282291	26	0.282282	6	0.72	1.3	1065	1
91500	0.01312	10.5	0.00044	2.70	1.46720	1.88671	7	0.282274	28	0.282265	5	0.72	1.3	1065	1
91500	0.01308	10.7	0.00044	2.68	1.46717	1.88626	7	0.282322	21	0.282313	7	0.72	1.2	1065	1
91500	0.01237	10.0	0.00040	2.43	1.46726	1.88632	7	0.282305	22	0.282297	7	0.72	1.3	1065	1
91500	0.01192	9.6	0.00039	2.36	1.46717	1.88615	9	0.282289	23	0.282281	6	0.72	1.3	1065	1
91500	0.01196	9.7	0.00040	2.40	1.46720	1.88625	8	0.282287	16	0.282279	6	0.72	1.3	1065	1
91500	0.01214	9.8	0.00041	2.47	1.46724	1.88620	8	0.282303	17	0.282294	7	0.72	1.3	1065	1
91500	0.01193	9.6	0.00040	2.44	1.46722	1.88622	8	0.282309	23	0.282301	7	0.72	1.2	1065	1
91500	0.01277	10.3	0.00042	2.55	1.46721	1.88626	8	0.282325	25	0.282317	7	0.72	1.2	1065	1

Continuation Table 6

Standard Mud Tank <i>September</i> <i>28th, 2015</i>	$^{176}\text{Yb}/^{177}\text{Hf}$ a	$\pm 2s$	$^{176}\text{Lu}/^{177}\text{Hf}$ a	$\pm 2s$	$^{178}\text{Hf}/^{177}\text{Hf}$	$^{180}\text{Hf}/^{177}\text{Hf}$	(V) SigHf b	$^{176}\text{Hf}/^{177}\text{Hf}$ c	$\pm 2s$	$^{176}\text{Hf}/^{177}\text{Hf}$ $f_{(t)}$ ^d	$\epsilon\text{Hf}^{(t)}$ d	$\pm 2s$ ^c	(Ga) TDM2 e	$^{206}\text{Pb}/^{238}\text{U}$ age (Ma) f	$\pm 2s$
Temora	0.03681	29.5	0.00131	7.87	1.46717	1.88637	8	0.282637	22	0.282626	4	0.72	0.9	416	1
Temora	0.02943	23.6	0.00115	6.94	1.46714	1.88601	9	0.282671	20	0.282662	5	0.72	0.8	416	1
Temora	0.02443	19.6	0.00090	5.44	1.46720	1.88647	8	0.282680	22	0.282673	5	0.72	0.8	416	1
Temora	0.02997	24.9	0.00117	7.47	1.46724	1.88649	8	0.282642	20	0.282632	4	0.72	0.9	416	1
Temora	0.02035	16.5	0.00074	4.53	1.46724	1.88635	7	0.282621	21	0.282615	3	0.72	0.9	416	1
<i>September</i> <i>29th, 2015</i>															
Temora	0.03916	31.3	0.00143	8.57	1.46724	1.88695	10	0.282663	17	0.282652	5	0.72	0.8	416	1
Temora	0.02484	20.7	0.00101	6.52	1.46722	1.88656	12	0.282690	14	0.282683	6	0.72	0.8	416	1
Temora	0.01553	12.5	0.00060	3.63	1.46722	1.88646	11	0.282694	20	0.282689	6	0.72	0.8	416	1
Temora	0.01682	14.9	0.00066	4.70	1.46722	1.88666	10	0.282689	21	0.282684	6	0.72	0.8	416	1
Temora	0.04280	36.0	0.00153	9.89	1.46727	1.88658	9	0.282678	22	0.282666	5	0.72	0.8	416	1
Temora	0.05482	47.9	0.00189	13.0	1.46724	1.88654	10	0.282691	23	0.282676	5	0.72	0.8	416	1
Temora	0.03156	25.3	0.00113	6.81	1.46722	1.88625	10	0.282680	21	0.282671	5	0.72	0.8	416	1
Temora	0.03730	29.9	0.00132	7.95	1.46728	1.88628	14	0.282683	17	0.282673	5	0.72	0.8	416	1
Temora	0.02998	24.2	0.00117	7.14	1.46722	1.88635	17	0.282697	18	0.282688	6	0.72	0.8	416	1
Temora	0.03495	28.0	0.00129	7.79	1.46725	1.88626	13	0.282691	15	0.282681	6	0.72	0.8	416	1
<i>September</i> <i>30th, 2015</i>															
Temora	0.02138	17.8	0.00082	5.19	1.46718	1.88608	16	0.282677	17	0.282671	5	0.72	0.8	416	1
Temora	0.03307	26.8	0.00122	7.48	1.46726	1.88662	10	0.282655	18	0.282646	4	0.72	0.8	416	1
Temora	0.02630	21.3	0.00106	6.47	1.46716	1.88592	13	0.282682	20	0.282673	5	0.72	0.8	416	1
Temora	0.02763	23.5	0.00107	7.51	1.46721	1.88616	13	0.282671	20	0.282663	5	0.72	0.8	416	1
Temora	0.02832	22.7	0.00115	6.91	1.46718	1.88662	11	0.282669	18	0.282660	5	0.72	0.8	416	1
Temora	0.01379	11.9	0.00059	3.76	1.46725	1.88646	12	0.282676	15	0.282672	5	0.72	0.8	416	1
Temora	0.02772	22.4	0.00108	6.51	1.46726	1.88646	12	0.282668	19	0.282660	5	0.72	0.8	416	1

Continuation Table 6

Standard Mud Tank <i>September 30th, 2015</i>	$^{176}\text{Yb}/^{177}\text{Hf}$ a	$\pm 2s$	$^{176}\text{Lu}/^{177}\text{Hf}$ a	$\pm 2s$	$^{178}\text{Hf}/^{177}\text{Hf}$	$^{180}\text{Hf}/^{177}\text{Hf}$	(V) SigHf b	$^{176}\text{Hf}/^{177}\text{Hf}$ c	$\pm 2s$	$^{176}\text{Hf}/^{177}\text{Hf}$ f(t) d	$\epsilon\text{Hf}^{(t)}$ d	$\pm 2s$ ^c	(Ga) TDM2 e	$^{206}\text{Pb}/^{238}\text{U}$ age (Ma) f	$\pm 2s$
Temora	0.04960	40.9	0.00192	12	1.46724	1.88624	11	0.282647	19	0.282632	4	0.72	0.9	416	1
Temora	0.01895	17.6	0.00080	5.80	1.46726	1.88573	13	0.282668	22	0.282662	5	0.72	0.8	416	1
Temora	0.03532	29.9	0.00133	8.96	1.46726	1.88624	10	0.282633	21	0.282623	4	0.72	0.9	416	1
Temora	0.02753	24.3	0.00109	7.40	1.46723	1.88630	11	0.282647	17	0.282638	4	0.72	0.9	416	1
Temora	0.05380	43.6	0.00200	12.	1.46725	1.88621	12	0.282632	16	0.282617	3	0.72	0.9	416	1
Temora	0.02530	20.4	0.00100	6.06	1.46721	1.88633	10	0.282672	16	0.282664	5	0.72	0.8	416	1
Temora	0.02812	29.9	0.00107	8.70	1.46724	1.88706	11	0.282684	19	0.282676	5	0.72	0.8	416	1
Temora	0.01492	12.0	0.00057	3.48	1.46718	1.88617	13	0.282688	18	0.282683	6	0.72	0.8	416	1
Temora	0.03202	30.0	0.00120	8.71	1.46723	1.88649	12	0.282702	20	0.282693	6	0.72	0.8	416	1
Temora	0.03218	28.6	0.00120	8.00	1.46722	1.88656	12	0.282677	16	0.282667	5	0.72	0.8	416	1
Temora	0.01894	15.5	0.00073	4.43	1.46725	1.88637	10	0.282672	21	0.282666	5	0.72	0.8	416	1
<i>October 2nd, 2015</i>															
Temora	0.02443	28.6	0.00083	7.97	1.46723	1.88642	12	0.282684	19	0.282678	5	0.72	0.8	416	1
Temora	0.02268	18.2	0.00080	4.85	1.46725	1.88645	12	0.282704	16	0.282697	6	0.72	0.7	416	1
Temora	0.01315	10.7	0.00045	2.79	1.46727	1.88602	15	0.282708	16	0.282704	6	0.72	0.7	416	1
Temora	0.02152	18.0	0.00073	4.86	1.46727	1.88606	16	0.282656	18	0.282650	5	0.72	0.8	416	1
Temora	0.02223	18.1	0.00070	4.42	1.46727	1.88588	12	0.282672	17	0.282666	5	0.72	0.8	416	1
Temora	0.02545	21.6	0.00090	5.93	1.46721	1.88603	14	0.282686	15	0.282679	6	0.72	0.8	416	1
Temora	0.02591	20.8	0.00089	5.33	1.46721	1.88619	14	0.282680	18	0.282673	5	0.72	0.8	416	1
Temora	0.02574	20.9	0.00093	5.70	1.46717	1.88671	11	0.282685	16	0.282678	5	0.72	0.8	416	1
Temora	0.02521	20.2	0.00092	5.55	1.46721	1.88666	12	0.282658	14	0.282650	5	0.72	0.8	416	1
Temora	0.02193	18.1	0.00084	5.17	1.46718	1.88668	13	0.282661	17	0.282654	5	0.72	0.8	416	1
Temora	0.02968	23.8	0.00106	6.35	1.46722	1.88617	13	0.282681	16	0.282673	5	0.72	0.8	416	1
Temora	0.03979	31.9	0.00134	8.09	1.46724	1.88632	14	0.282683	16	0.282673	5	0.72	0.8	416	1
Temora	0.02172	17.4	0.00078	4.75	1.46723	1.88633	12	0.282681	19	0.282675	5	0.72	0.8	416	1
Temora	0.03947	33.2	0.00138	8.94	1.46720	1.88615	14	0.282680	20	0.282670	5	0.72	0.8	416	1
Temora	0.01426	11.5	0.00053	3.35	1.46723	1.88601	15	0.282667	16	0.282663	5	0.72	0.8	416	1

Continuation Table 6

Standard Mud Tank <i>September 28th, 2015</i>	$^{176}\text{Yb}/^{177}\text{Hf}$ a	$\pm 2s$	$^{176}\text{Lu}/^{177}\text{Hf}$ a	$\pm 2s$	$^{178}\text{Hf}/^{177}\text{Hf}$	$^{180}\text{Hf}/^{177}\text{Hf}$	(V) SigHf b	$^{176}\text{Hf}/^{177}\text{Hf}$ c	$\pm 2s$	$^{176}\text{Hf}/^{177}\text{Hf}$ f _(t) ^d	$\epsilon\text{Hf}^{(t)}$ d	$\pm 2s$ ^c	(Ga) TDM2 e	$^{206}\text{Pb}/^{238}\text{U}$ age (Ma) f	$\pm 2s$
Plešovice	0.00504	4.0	0.00012	0.74	1.46718	1.88651	12	0.282473	16	0.282472	-4	0.72	1.2	337	1
Plešovice	0.00515	4.1	0.00013	0.76	1.46722	1.88657	13	0.282496	16	0.282495	-3	0.72	1.2	337	1
Plešovice	0.00283	2.3	0.00007	0.43	1.46726	1.88639	10	0.282503	22	0.282503	-2	0.72	1.2	337	1
<i>September 30th, 2015</i>															
Plešovice	0.00344	2.9	0.00009	0.57	1.46719	1.88659	12	0.282491	14	0.282491	-3	0.72	1.2	337	1
Plešovice	0.00351	2.8	0.00009	0.55	1.46717	1.88689	12	0.282489	18	0.282489	-3	0.72	1.2	337	1
Plešovice	0.00277	2.4	0.00007	0.50	1.46722	1.88667	13	0.282494	15	0.282494	-3	0.72	1.2	337	1
Plešovice	0.00238	2.1	0.00006	0.42	1.46722	1.88661	13	0.282480	14	0.282479	-3	0.72	1.2	337	1
<i>October 2nd , 2015</i>															
Plešovice	0.00541	8.2	0.00011	0.84	1.46727	1.88662	12	0.282475	18	0.282474	-3	0.72	1.2	337	1
Plešovice	0.00522	4.2	0.00012	0.7	1.46721	1.88632	12	0.282496	17	0.282495	-3	0.72	1.2	337	1
Plešovice	0.00502	4.1	0.00011	0.67	1.46725	1.88670	13	0.282503	17	0.282502	-2	0.72	1.2	337	1
Plešovice	0.00350	2.8	0.00008	0.51	1.46719	1.88682	13	0.282482	19	0.282482	-3	0.72	1.2	337	1
Plešovice	0.00364	2.9	0.00008	0.49	1.46715	1.88651	14	0.282500	14	0.282499	-3	0.72	1.2	337	1
Plešovice	0.00353	2.8	0.00008	0.47	1.46723	1.88653	14	0.282481	15	0.282480	-3	0.72	1.2	337	1
Plešovice	0.00260	2.1	0.00006	0.35	1.46723	1.88611	17	0.282505	13	0.282504	-2	0.72	1.2	337	1
Plešovice	0.00410	3.3	0.00009	0.57	1.46721	1.88596	20	0.282502	12	0.282502	-3	0.72	1.2	337	1
Plešovice	0.00373	3.0	0.00008	0.50	1.46725	1.88616	18	0.282493	16	0.282493	-3	0.72	1.2	337	1
Plešovice	0.00514	4.3	0.00012	0.78	1.46720	1.88620	17	0.282506	16	0.282506	-2	0.72	1.2	337	1
Plešovice	0.00485	3.9	0.00011	0.64	1.46721	1.88660	13	0.282506	18	0.282505	-2	0.72	1.2	337	1
Plešovice	0.00361	3.0	0.00008	0.51	1.46726	1.88607	18	0.282511	15	0.282510	-2	0.72	1.1	337	1

Table 7: Whole rock major and trace element analyses. (1) Major elements are reported in (wt.%); (2) Loss of ignition; (3) Al/(2*Ca+Na+K); (4) Mg/(Mg+Fe²⁺); (5) Trace elements are reported in (ppm) (part per million); (6) Eu_N/[(Sm_N)(Gd_N)]^{1/2}; (7) Mafic Microgranular Enclaves

Sample	FGL24	FGL25	FGL26	FGL28	FGL31	FGL32	FSV35	FGL40
UTM points	240523 E 7879396 S	237898 E 7875897 S	238127 E 7864600 S	238718 E 7874187 S	238427 E 7864843 S	238420 E 7882709 S	214287 E 7917718 S	239526 E 7879396 S
Mineral assemblage	Bt+Grt	Bt+Grt	Bt+Amp+Grt	MME	MME	Bt+Amp+Grt	Bt+Amp+Grt	Bt+Grt
SiO ₂ ⁽¹⁾	72.19	64.06	60.71	58.00	64.42	66.42	58.83	69.30
TiO ₂	0.32	0.71	0.96	0.90	0.82	0.59	1.04	0.35
Al ₂ O ₃	14.47	16.80	16.38	16.11	16.19	15.75	17.43	15.40
Fe ₂ O ₃ Tot	2.78	5.50	7.75	9.13	6.24	4.77	7.94	3.41
MnO	0.06	0.09	0.13	0.12	0.09	0.09	0.14	0.07
MgO	0.70	1.77	2.35	4.01	1.81	1.75	3.03	0.78
CaO	2.68	5.17	6.29	6.10	4.09	4.29	6.66	3.08
Na ₂ O	3.34	2.88	2.74	2.13	2.55	2.70	2.26	3.30
K ₂ O	2.98	2.34	1.83	2.67	2.33	2.91	2.06	3.69
P ₂ O ₅	0.09	0.16	0.24	0.17	0.16	0.13	0.19	0.10
L.O.I. ⁽²⁾	0.41	0.52	0.61	0.66	1.31	0.60	0.43	0.53
A/CNK ⁽³⁾	1.07	1.01	0.91	0.92	1.15	1.02	0.97	1.03
FeO _{Tot} + MgO	3.20	6.72	9.33	12.22	7.42	6.04	10.18	3.85
Mg# ⁽⁴⁾	0.330	0.39	0.38	0.47	0.36	0.42	0.43	0.31
Sc ⁽⁵⁾	14.6	21.8	29.3	27.9	25.8	19.3	27.0	14.7
V	42.1	93.1	150	149	91.5	80.6	137	48.3
Cr	17.2	25.1	17.0	102	22.3	32.3	33.8	10.9
Co	46.9	37.0	38.1	42.1	43.3	46.4	45.0	43.6
Ni	7.56	12.1	9.4	26.9	10.6	12.4	14.8	6.73
Cu	3.22	10.2	15.2	6.15	18.4	16.1	15.3	7.37
Zn	42.9	72.2	92.8	123	88.2	64.1	94.1	56.2
Rb	119	81.1	55.3	89.3	143	98.2	80.4	118
Sr	128	209	252	162	154	163	190	155

Continuation Table 7

Y	21.0	25.1	46.2	36.2	19.2	22.6	25.3	19.0
Zr	116	183	209	142	193	152	152	114
Nb	7.78	10.6	13.0	9.51	11.8	9.48	10.1	8.48
Mo	0.355	0.795	1.13	0.602	0.693	0.497	0.678	0.615
Cs	12.0	3.31	1.56	2.62	5.98	6.45	3.71	5.02
Ba	738	517	636	483	435	451	360	449
La	23.1	35.0	14.2	13.0	18.8	24.9	9.40	16.3
Ce	48.9	67.1	37.2	35.5	47.3	49.2	23.5	33.8
Pr	5.69	8.35	5.67	5.16	4.66	5.67	3.33	4.16
Nd	22.0	32.2	27.7	24.6	18.4	22.1	16.5	17.0
Sm	4.23	6.28	8.34	6.94	3.83	4.44	4.35	4.22
Eu	0.955	1.39	1.74	1.35	1.36	0.950	1.20	1.05
Gd	3.80	5.59	9.16	6.83	3.66	4.20	4.69	3.41
Tb	0.674	0.796	1.60	1.05	0.548	0.607	0.716	0.576
Dy	3.98	4.93	9.38	6.73	3.70	4.11	4.76	3.22
Ho	0.731	0.948	1.87	1.36	0.772	0.821	1.01	0.690
Er	2.01	2.87	5.11	4.03	2.30	2.44	2.79	1.77
Tm	0.262	0.431	0.646	0.553	0.272	0.355	0.365	0.259
Yb	2.18	2.51	4.49	3.65	2.18	2.44	2.71	1.93
Lu	0.233	0.384	0.551	0.512	0.306	0.425	0.361	0.281
Hf	3.83	5.09	5.45	3.74	5.55	4.52	3.82	3.40
Ta	1.16	0.97	0.89	0.76	1.11	1.21	0.88	1.20
Pb	14.7	13.2	8.06	6.92	10.4	20.0	8.32	21.8
Th	7.77	8.73	2.26	1.92	10.0	9.34	1.85	6.44
U	1.95	1.31	0.697	0.511	0.980	1.82	0.599	1.71
ΣREE	119	169	128	111	108	123	75.7	88.7
La/Yb	1.96	2.14	1.39	1.41	3.19	2.31	2.12	2.63
Eu/Eu* ⁽⁶⁾	0.73	0.72	0.61	0.60	1.11	0.67	0.82	0.84

Table 8. Trace element analyses (in ppm) for the Galiléia zircons. Note that trace analyses were performed only on high-precision concordant dates. *b.d.l.*: below detection limit

Sample	FGL22																
Spot domain	edge	edge	edge	edge	edge	edge	edge	edge	edge	edge	edge	edge	centre	centre	centre	centre	centre
²⁰⁶ Pb/ ²³⁸ U age (Ma)	552	554	556	558	563	577	582	583	583	583	605	572	574	579	580	584	585
2S	4.83	4.83	3.34	3.95	2.86	4.84	3.08	5.15	3.50	3.26	3.47	4.62	3.21	3.16	3.43	3.28	3.15
⁴⁴ Ca	1823	<i>b.d.l.</i>	70	259	96	91	<i>b.d.l.</i>	<i>b.d.l.</i>	135	<i>b.d.l.</i>	<i>b.d.l.</i>	281	<i>b.d.l.</i>	<i>b.d.l.</i>	62	<i>b.d.l.</i>	128
⁴⁵ Sc	546	424	419	481	495	413	539	600	492	882	410	548	370	463	466	729	774
⁴⁷ Ti	983	855	868	870	749	918	986	959	1004	1026	987	1022	909	1063	962	989	1096
⁸⁹ Y	1161	895	1010	1128	1439	1093	1255	1205	1074	1387	497	1315	650	1041	1246	1107	1301
⁹⁰ Zr	210496	165690	193594	164768	180720	185199	204189	212825	205856	212854	199401	217165	176037	215028	205958	206412	226065
⁹³ Nb	6.42	3.74	5.06	3.48	9.55	5.70	4.21	6.58	4.69	6.63	4.63	4.24	4.42	4.87	4.38	4.79	5.19
¹³⁷ Ba	1.98	2.59	1.59	2.78	1.28	3.66	2.89	1.59	2.83	2.10	1.26	2.18	1.69	2.01	1.56	1.51	3.29
¹³⁹ La	2.98	<i>b.d.l.</i>	0.90	0.73	0.90	<i>b.d.l.</i>	0.69	0.49	0.49	0.54	<i>b.d.l.</i>	<i>b.d.l.</i>	0.53	<i>b.d.l.</i>	<i>b.d.l.</i>	<i>b.d.l.</i>	0.94
¹⁴⁰ Ce	10.51	3.57	3.87	2.84	7.92	3.20	1.95	6.29	2.79	5.36	2.66	8.12	3.23	6.60	6.01	1.49	3.46
¹⁴¹ Pr	1.27	0.44	0.37	<0.233	<0.231	<0.227	<0.181	<0.187	<0.172	<0.189	0.43	0.31	<0.215	0.25	<0.198	<0.190	<0.221
¹⁴⁶ Nd	7.85	0.65	0.55	1.72	1.59	0.51	<i>b.d.l.</i>	1.04	2.12	1.07	<0.37	4.26	<i>b.d.l.</i>	2.87	3.34	1.20	2.82
¹⁴⁷ Sm	4.93	2.08	0.81	1.42	3.10	2.02	1.66	0.96	5.16	3.80	<0.69	9.25	1.93	7.41	7.82	4.14	4.95
¹⁵³ Eu	<0.156	<0.210	0.19	<0.152	0.43	0.32	<0.165	<0.196	0.98	0.68	0.29	1.44	<0.219	1.06	1.21	0.45	0.81
¹⁵⁷ Gd	16.35	7.93	12.89	8.84	25.32	8.57	13.40	22.76	16.21	21.82	6.44	35.30	4.15	22.34	35.45	14.37	27.10
¹⁵⁹ Tb	5.44	4.17	4.85	5.33	11.54	5.28	7.80	9.47	6.92	9.79	1.76	12.06	4.27	7.42	12.17	5.79	9.02
¹⁶³ Dy	105.94	58.79	67.38	75.00	179.65	78.61	115.48	129.12	112.08	179.40	38.52	194.21	53.34	120.48	152.25	99.16	155.92
¹⁶⁵ Ho	37.14	25.18	27.47	32.04	70.84	33.62	48.70	54.69	35.87	61.85	13.32	59.44	21.94	38.54	52.44	34.03	50.47
¹⁶⁶ Er	223.84	120.74	134.05	159.69	347.89	168.24	239.20	256.44	188.66	346.94	74.98	298.45	99.77	191.83	221.28	193.05	262.76
¹⁶⁹ Tm	37.18	26.66	22.73	35.00	57.73	37.92	55.87	41.70	27.77	56.06	11.27	45.23	20.84	27.45	32.26	32.17	40.55
¹⁷² Yb	463.60	247.23	239.12	314.37	599.02	361.25	533.24	435.47	337.69	687.04	146.58	527.89	199.39	326.61	317.16	410.29	494.44
¹⁷⁵ Lu	65.04	43.85	39.12	56.41	91.51	65.39	91.55	70.75	44.11	92.33	20.56	67.79	34.21	42.51	49.27	55.76	64.66
¹⁷⁸ Hf	6287	4720	5964	4797	5856	5477	5430	5907	5483	5797	5420	5627	5363	5477	5517	5178	5865
¹⁸¹ Ta	1.49	0.51	1.68	0.70	3.27	2.54	1.14	1.76	0.66	0.97	0.74	0.60	1.09	0.62	0.54	0.72	0.86
²³² Th	79.62	38.77	56.09	40.53	188.28	52.22	56.45	121.47	64.18	123.01	23.47	128.51	47.90	71.50	92.02	46.26	99.93
²³⁸ U	262.15	89.83	183.85	108.63	462.24	332.35	233.40	229.91	103.81	238.81	61.88	158.39	134.23	92.51	105.34	122.85	171.50
Apha dose	2.41	0.89	1.69	1.04	4.52	2.77	2.06	2.41	1.14	2.48	0.59	1.92	1.27	1.10	1.31	1.18	1.85

Continuation Table 8

Sample	FGL22															
Spot domain	centre	centre	centre	centre	centre	centre	centre	centre	centre	centre	centre	resorbed	resorbed	resorbed	resorbed	resorbed
²⁰⁶ Pb/ ²³⁸ U age (Ma)	588	592	592	595	600	606	609	611	620	631	577	607	612	612	612	617
2S	4.11	3.43	2.99	2.77	9.47	4.36	4.34	3.67	4.79	4.29	4.21	4.05	4.22	3.79	3.95	4.73
⁴⁴ Ca	148	193	57	238	124	135	<i>b.d.l.</i>	99	187	<i>b.d.l.</i>	92	427	92	420	70	<i>b.d.l.</i>
⁴⁵ Sc	523	554	502	394	477	532	426	687	436	1203	504	396	624	502	510	570
⁴⁷ Ti	928	1002	930	919	915	1101	965	1083	915	2174	986	949	1051	1052	878	160
⁸⁹ Y	1551	1235	1075	954	1103	1191	1032	1040	1263	2729	894	984	1237	1104	874	1014
⁹⁰ Zr	200448	200441	184485	193856	197707	225971	198574	221628	201204	433880	203149	191333	216955	213100	196216	226103
⁹³ Nb	6.64	3.64	2.73	4.09	4.82	4.44	5.50	4.44	4.22	11.76	3.89	4.73	4.46	3.98	4.30	4.81
¹³⁷ Ba	<i>b.d.l.</i>	2.42	1.58	1.72	2.04	<i>b.d.l.</i>	2.62	3.35	0.98	4.35	2.69	<i>b.d.l.</i>	<i>b.d.l.</i>	1.36	2.67	2.78
¹³⁹ La	5.39	<i>b.d.l.</i>	<i>b.d.l.</i>	<i>b.d.l.</i>	0.81	<i>b.d.l.</i>	<i>b.d.l.</i>	<i>b.d.l.</i>	<i>b.d.l.</i>	<i>b.d.l.</i>	0.55	0.68	<i>b.d.l.</i>	2.07	<i>b.d.l.</i>	<i>b.d.l.</i>
¹⁴⁰ Ce	15.39	1.33	1.07	2.94	1.82	6.43	3.65	2.56	5.41	10.26	2.95	3.88	2.91	7.30	2.29	2.58
¹⁴¹ Pr	1.53	<0.206	0.35	<0.252	<0.210	0.46	0.30	<0.214	<0.214	<0.47	<0.219	<0.216	<0.207	0.58	0.35	0.19
¹⁴⁶ Nd	6.12	1.63	0.98	0.77	<0.41	4.61	0.46	0.97	2.65	3.25	1.08	1.94	1.41	3.86	1.67	1.44
¹⁴⁷ Sm	8.99	3.26	3.94	3.71	2.45	7.32	3.06	2.21	3.68	10.20	1.32	4.61	3.35	3.43	2.41	<0.80
¹⁵³ Eu	0.82	0.24	<0.234	0.67	0.17	2.08	0.62	0.26	0.58	1.75	<0.202	0.89	0.51	0.58	<0.207	0.29
¹⁵⁷ Gd	37.15	13.39	11.97	14.51	20.62	23.53	16.28	15.34	29.08	32.14	11.54	13.85	13.44	13.16	17.62	12.00
¹⁵⁹ Tb	12.41	8.72	6.33	5.51	5.18	8.16	5.66	5.95	9.68	16.34	4.07	7.84	7.84	7.62	4.55	4.06
¹⁶³ Dy	227.61	114.95	87.13	73.61	81.73	124.64	98.53	95.82	113.15	246.86	66.36	104.15	108.83	90.28	61.76	71.07
¹⁶⁵ Ho	73.94	46.12	32.12	28.31	33.82	36.56	32.56	30.78	41.95	100.95	22.03	38.29	42.91	33.62	24.66	24.53
¹⁶⁶ Er	396.81	230.30	148.06	130.85	164.02	191.81	173.56	174.22	183.01	480.63	116.93	173.80	210.30	151.41	113.57	138.97
¹⁶⁹ Tm	62.92	51.11	32.91	21.02	27.27	27.15	25.43	27.63	28.12	104.30	17.89	34.64	46.28	33.23	16.70	23.14
¹⁷² Yb	760.16	472.50	293.09	211.68	279.81	326.78	320.48	358.74	272.98	960.03	229.68	313.40	425.72	292.57	182.95	294.98
¹⁷⁵ Lu	98.67	80.92	51.32	34.76	47.79	42.30	41.99	49.69	42.40	165.10	32.30	51.86	73.11	49.37	30.21	39.97
¹⁷⁸ Hf	5945	4926	4535	5928	5878	5239	5284	5854	5928	<i>b.d.l.</i>	5599	4800	4876	4885	5538	5915
¹⁸¹ Ta	1.09	0.85	0.41	0.84	1.13	0.57	0.91	0.46	0.79	1.76	0.43	1.14	0.81	0.72	0.98	0.37
²³² Th	225.98	56.34	34.65	54.91	44.82	66.05	69.91	42.63	82.96	158.81	27.12	78.54	60.46	50.56	34.11	38.26
²³⁸ U	519.38	185.79	78.93	96.25	149.07	64.17	140.12	94.48	117.97	361.41	46.90	162.25	159.81	104.20	56.29	105.38
Apha dose	5.16	1.71	0.79	1.03	1.37	0.86	1.44	0.95	1.35	3.60	0.50	1.66	1.54	1.07	0.61	1.00

Continuation Table 8

Sample	FGL22			
Spot domain	resorbed	resorbed	resorbed	resorbed
²⁰⁶ Pb/ ²³⁸ U age (Ma)	628	628	644	660
2S	4.44	3.30	3.36	4.05
⁴⁴ Ca	77	<i>b.d.l.</i>	87	<i>b.d.l.</i>
⁴⁵ Sc	453	496	548	518
⁴⁷ Ti	914	1061	998	1030
⁸⁹ Y	1285	1008	1150	1234
⁹⁰ Zr	182740	209495	202158	205088
⁹³ Nb	3.66	5.13	4.74	3.61
¹³⁷ Ba	1.22	1.30	1.82	2.31
¹³⁹ La	<i>b.d.l.</i>	<i>b.d.l.</i>	0.78	<i>b.d.l.</i>
¹⁴⁰ Ce	5.07	3.00	3.31	1.11
¹⁴¹ Pr	0.29	0.24	0.30	0.23
¹⁴⁶ Nd	2.96	0.95	1.22	2.60
¹⁴⁷ Sm	6.41	1.69	3.45	3.98
¹⁵³ Eu	1.54	0.43	0.37	0.69
¹⁵⁷ Gd	23.85	13.15	14.72	19.57
¹⁵⁹ Tb	12.82	5.01	7.67	9.93
¹⁶³ Dy	163.86	84.48	112.60	131.23
¹⁶⁵ Ho	57.79	28.43	45.91	47.34
¹⁶⁶ Er	260.40	160.16	223.43	209.70
¹⁶⁹ Tm	52.47	26.04	50.86	41.76
¹⁷² Yb	439.89	325.81	470.37	383.81
¹⁷⁵ Lu	74.01	45.25	80.44	64.39
¹⁷⁸ Hf	4522	6026	5216	4813
¹⁸¹ Ta	0.49	0.86	1.27	0.45
²³² Th	106.49	55.44	74.22	52.34
²³⁸ U	139.70	139.17	275.94	84.04
Apha dose	1.65	1.35	2.48	0.93

Continuation Table 8

Sample	FGL6																
Spot domain	edge	edge	edge	edge	edge	edge	edge	edge	edge	edge	centre	centre	centre	centre	centre	centre	centre
²⁰⁶ Pb/ ²³⁸ U age (Ma)	569	580	581	582	590	592	595	600	598	554	562	563	572	577	590	590	594
² S	4	3	3	2	4	3	3	3	4	4	4	3	2	4	9	3	3
⁴⁴ Ca	375	<i>b.d.l.</i>	72	75	249	<i>b.d.l.</i>	178	112	176	128	82	257	151	889	105	143	<i>b.d.l.</i>
⁴⁵ Sc	385	369	352	373	451	321	541	401	379	469	426	676	393	445	331	455	359
⁴⁷ Ti	854	910	816	862	1695	1104	1633	1559	1062	1571	1161	1522	944	1794	827	1636	1017
⁸⁹ Y	869	520	962	775	1221	766	1432	945	1069	1497	1014	1556	1313	1305	713	1143	1133
⁹⁰ Zr	184164	183882	161834	184069	237271	163414	223915	231345	178440	229021	187113	227076	155717	208514	159757	242624	174693
⁹³ Nb	5.11	4.35	4.56	4.15	7.61	3.94	6.21	4.26	4.93	5.39	4.77	5.33	4.24	6.88	3.69	5.39	4.62
¹³⁷ Ba	1.32	1.61	1.68	0.92	<i>b.d.l.</i>	<i>b.d.l.</i>	2.62	3.75	2.79	3.74	2.10	<i>b.d.l.</i>	<i>b.d.l.</i>	3.92	2.33	2.60	1.97
¹³⁹ La	0.42	3.15	<i>b.d.l.</i>	<i>b.d.l.</i>	1.40	0.81	<i>b.d.l.</i>	<i>b.d.l.</i>	<i>b.d.l.</i>	5.75	<i>b.d.l.</i>	0.49	<i>b.d.l.</i>	2.35	<i>b.d.l.</i>	0.66	1.04
¹⁴⁰ Ce	5.67	17.18	4.23	2.38	8.16	8.79	7.89	5.05	5.49	61.32	4.92	1.34	6.64	12.33	2.90	7.41	5.49
¹⁴¹ Pr	0.49	1.44	<0.214	<0.221	0.63	0.73	<i>b.d.l.</i>	0.55	0.29	5.32	<0.197	<i>b.d.l.</i>	0.20	0.76	0.41	0.34	<0.197
¹⁴⁶ Nd	1.20	7.64	1.34	0.65	6.00	2.34	1.27	3.10	1.30	34.52	0.74	2.01	1.94	7.64	1.25	1.66	1.45
¹⁴⁷ Sm	1.28	5.28	<0.77	2.73	5.00	3.06	2.12	5.15	1.70	18.03	1.84	5.37	3.15	7.37	1.18	3.57	3.53
¹⁵³ Eu	0.37	1.52	<0.203	<0.128	0.63	0.43	0.88	1.09	0.31	14.64	0.59	0.44	1.15	1.30	0.77	0.80	0.48
¹⁵⁷ Gd	13.38	15.54	5.26	15.99	16.84	7.82	19.81	19.31	11.11	57.47	9.52	34.10	15.21	25.88	8.93	22.68	13.51
¹⁵⁹ Tb	4.28	2.58	2.90	4.00	6.04	5.55	8.88	5.94	5.85	17.74	4.02	15.36	6.13	9.39	2.28	8.79	6.58
¹⁶³ Dy	58.30	42.36	51.94	63.19	84.07	58.20	121.62	69.80	79.41	180.42	61.98	195.26	87.16	112.70	39.59	105.73	85.67
¹⁶⁵ Ho	24.34	15.39	22.43	22.88	31.89	23.16	47.54	24.80	29.99	58.29	26.30	72.98	32.44	41.89	16.71	38.61	35.09
¹⁶⁶ Er	123.98	79.10	119.30	105.53	179.41	119.44	250.41	134.46	147.59	270.94	128.69	354.19	167.95	211.98	85.20	206.35	169.82
¹⁶⁹ Tm	22.31	15.22	21.43	18.55	34.73	20.45	42.68	24.51	23.51	44.18	21.10	56.00	28.86	35.40	14.61	34.30	27.18
¹⁷² Yb	252.13	207.49	288.43	193.28	429.13	223.46	444.70	267.21	307.38	453.60	289.65	564.78	404.90	377.43	191.74	379.30	379.19
¹⁷⁵ Lu	44.09	41.62	57.50	31.31	74.74	42.55	76.80	48.57	50.00	76.66	49.13	91.38	71.91	64.80	40.39	66.76	63.44
¹⁷⁸ Hf	5787	5976	5853	5889	8036	7383	6175	7055	5324	6931	5165	7117	4941	6652	6093	7054	5056
¹⁸¹ Ta	1.87	0.77	1.25	1.18	3.10	0.85	0.83	0.88	1.98	0.85	0.86	0.51	0.68	1.58	0.51	0.83	1.67
²³² Th	118	82	97	101	115	141	127	107	184	267	69	89	341	250	67	180	163
²³⁸ U	447	474	395	247	1589	318	322	397	620	667	215	330	403	1097	237	561	593
Apha dose	4.00	4.00	3.50	2.42	12.48	3.18	3.12	3.57	5.67	6.50	1.99	2.97	4.96	9.60	2.15	5.21	5.35

Continuation Table 8

Sample	FGL6							
Spot domain	centre	centre	centre	resorbed	resorbed	resorbed	resorbed	resorbed
206Pb/238U age (Ma)	602	618	633	575	585	605	614	675
2S	3	3	4	4	4	5	4	5
⁴⁴ Ca	<i>b.d.l.</i>	736	<i>b.d.l.</i>	<i>b.d.l.</i>	<i>b.d.l.</i>	160	116	1465
⁴⁵ Sc	441	365	515	411	423	488	447	365
⁴⁷ Ti	1680	1244	1609	907	882	1014	1637	824
⁸⁹ Y	1465	939	1089	639	641	1199	1070	839
⁹⁰ Zr	250662	182029	238216	179696	167554	178300	228666	185552
⁹³ Nb	5.05	3.45	3.91	4.00	3.51	4.19	4.27	3.81
¹³⁷ Ba	3.11	4.78	1.56	1.66	1.92	0.97	2.29	2.06
¹³⁹ La	<i>b.d.l.</i>	2.42	0.69	0.58	<i>b.d.l.</i>	<i>b.d.l.</i>	1.12	1.85
¹⁴⁰ Ce	9.62	7.80	4.69	2.85	2.43	3.70	6.87	8.77
¹⁴¹ Pr	0.70	0.65	<i>b.d.l.</i>	<0.215	0.36	0.53	0.26	1.25
¹⁴⁶ Nd	6.20	3.54	0.49	0.87	1.05	2.95	2.13	6.78
¹⁴⁷ Sm	9.97	3.48	2.03	1.59	1.69	6.28	3.95	5.04
¹⁵³ Eu	2.43	0.67	0.49	0.50	0.29	1.14	0.80	3.54
¹⁵⁷ Gd	48.98	24.02	16.09	7.41	9.30	32.60	19.74	19.68
¹⁵⁹ Tb	15.43	6.21	6.23	2.24	2.47	11.88	6.56	6.09
¹⁶³ Dy	182.65	71.57	79.18	41.52	42.93	160.51	87.31	80.98
¹⁶⁵ Ho	65.64	23.54	29.99	18.49	18.17	54.28	29.67	28.24
¹⁶⁶ Er	328.00	125.28	156.35	89.96	92.45	249.25	143.35	139.79
¹⁶⁹ Tm	57.06	20.66	25.76	17.44	17.92	34.86	23.35	23.27
¹⁷² Yb	613.25	217.65	280.48	217.41	228.76	423.37	237.93	257.68
¹⁷⁵ Lu	108.39	39.09	48.33	46.87	46.23	65.35	40.36	42.97
¹⁷⁸ Hf	6143	6274	6430	5526	5563	5047	6121	6061
¹⁸¹ Ta	0.61	0.72	0.54	0.49	0.40	0.64	0.29	1.19
²³² Th	310	125	63	34	27	87	103	115
²³⁸ U	468	297	176	126	91	143	166	546
Apha dose	5.26	2.93	1.67	1.13	0.83	1.57	1.83	4.72

Table 9. Trace element of the standard materials used during Galiléia zircon trace element analyses.

Standard BHVO Analyses n°	9	10	29	30	49	50	69	70	89	90	109	110	129	130	149	150	169	170
⁴⁴ Ca	47302	44290	54761	55828	52601	49892	50130	50274	52674	50682	49093	47518	49541	47619	42285	44837	59592	53834
⁴⁵ Sc	31	32	31	33	37	34	27	31	33	33	31	24	30	30	24	25	32	27
⁴⁷ Ti	14511	14989	13526	15921	16693	17006	14069	14638	14821	14765	14622	11608	13895	13896	10678	9995	18175	17129
⁸⁹ Y	19	22	22	21	24	23	20	20	20	22	22	17	20	19	18	19	23	20
⁹⁰ Zr	141	148	150	150	162	152	138	131	147	150	153	121	135	129	128	123	143	134
⁹³ Nb	18	18	18	19	17	17	15	14	18	18	18	15	16	17	14	14	17	17
¹³⁷ Ba	126	125	124	132	155	147	124	134	128	128	133	108	129	128	103	100	127	129
¹³⁹ La	15	15	14	14	17	17	14	15	15	16	15	12	14	14	12	12	14	15
¹⁴⁰ Ce	38	40	38	41	41	38	34	35	42	41	41	31	38	36	31	31	40	38
¹⁴¹ Pr	5.02	5.35	5.04	6.11	5.70	4.82	5.23	4.85	5.29	5.58	5.22	4.33	4.98	5.57	4.20	3.51	4.99	4.59
¹⁴⁶ Nd	23.4	24.4	23.3	24.1	23.2	23.9	18.8	19.7	24.8	25.8	24.7	20.0	23.1	21.9	20.3	18.9	25.1	24.0
¹⁴⁷ Sm	4.84	4.85	7.97	6.41	7.22	4.83	5.02	4.25	6.00	6.80	6.35	4.78	5.15	4.55	4.23	4.52	6.45	6.34
¹⁵³ Eu	1.74	2.34	1.84	2.01	2.11	1.92	1.93	1.45	2.35	1.91	2.08	1.36	1.52	1.90	1.79	1.29	1.69	1.39
¹⁵⁷ Gd			7.27	4.42	4.36	5.84	6.45	6.45	9.96	3.11	6.76	6.76	5.74	5.74	3.63	3.63	4.39	
¹⁵⁹ Tb	0.81	0.78	1.04	1.01	1.04	0.66	1.23	1.24	0.82	0.95	0.76	0.76	0.88	0.92	1.02	1.08	1.07	
¹⁶³ Dy	4.37	4.56	3.25	5.64	5.37	5.02	4.38	4.71	4.48	5.24	5.47	3.35	6.10	6.54	4.33	4.35	4.81	3.51
¹⁶⁵ Ho	1.02	0.88	0.77	1.02	0.95	0.68	0.99	1.11	0.56	0.96	0.97	0.63	0.42	0.63	0.99	1.13	0.90	1.16
¹⁶⁶ Er	2.25	1.54	1.49	1.94	2.29	1.75	2.55	2.99	1.40	2.10	2.34	2.35	1.56	4.18	2.26	1.38	3.38	1.94
¹⁶⁹ Tm	0.15	0.32	0.25	0.35	0.15	0.46	0.21	0.26	0.37	0.47	0.30	0.26	0.33	0.24	0.33	0.27	0.31	0.31
¹⁷² Yb	1.89	2.31	1.56	2.12	2.53	2.58	1.47	1.41	1.32	1.35	1.95	1.95	1.84	1.84	1.82	1.82	1.85	1.27
¹⁷⁵ Lu	0.33	0.09	0.28	0.29	0.40	0.40	0.19	0.13	0.22	0.29	0.23	0.23	0.24	0.24	0.32	0.23		
¹⁷⁸ Hf	2.98	4.06	3.81	4.18	4.19	3.42	3.98	5.08	3.87	4.06	5.59	2.68	4.28	3.11	4.72	2.84	4.08	3.04
¹⁸¹ Ta	0.90	1.08	0.97	0.95	1.14	0.96	0.69	1.29	1.23	0.86	1.10	0.64	0.80	1.08	0.96	1.11	1.04	1.12
²³² Th	1.02	1.03	0.99	0.91	1.17	0.88	0.73	0.90	1.63	1.48	1.13	0.82	1.31	0.89	1.06	1.25	1.02	1.12
²³⁸ U	0.50	0.61	0.53	0.45	0.53	0.60	0.43	0.40	0.56	0.36	0.33	0.47	0.72	0.37	0.30	0.50	0.57	0.59

Continuation Table 9

Standard Analyses <i>n</i> ^o	BHVO						<i>BHVO</i>	<i>MEAN</i>	<i>SD</i>	<i>RSD</i>
	<i>189</i>	<i>190</i>	<i>209</i>	<i>210</i>	<i>229</i>	<i>230</i>				
⁴⁴ Ca	51462	51467	36567	39576	55662	59237	44000	49864	5622	8.87
⁴⁵ Sc	22	22	16	16	26	29	29.600	28.056	5.381	5.21
⁴⁷ Ti	10424	9853	11059	9883	16409	17589	16165	14006	2619	5.35
⁸⁹ Y	16	16	12	12	19	23	22.10	19.59	3.18	6.16
⁹⁰ Zr	115	109	90	86	149	159	155.00	135.16	19.99	6.76
⁹³ Nb	13	11	9	9	15	18	16.90	15.70	2.81	5.59
¹³⁷ Ba	88	85	84	83	138	160	129.00	121.63	21.47	5.66
¹³⁹ La	12	10	8	9	15	16	15.20	13.64	2.24	6.08
¹⁴⁰ Ce	29	27	22	22	37	42	37.50	35.54	5.90	6.02
¹⁴¹ Pr	3.74	3.23	2.47	2.40	4.16	5.35	5.00	4.66	0.98	4.75
¹⁴⁶ Nd	18.7	17.2	13.4	14.2	23.0	25.7	23.50	21.74	3.47	6.26
¹⁴⁷ Sm	1.40	4.78	5.08	2.56	6.35	3.23	5.75	5.16	1.48	3.48
¹⁵³ Eu	1.30	1.64	1.29	1.59	1.85	2.44	2.01	1.78	0.34	5.22
¹⁵⁷ Gd		5.36	4.99	4.84	5.98	7.86	5.50	5.68	1.63	3.48
¹⁵⁹ Tb	0.88	0.58	0.62	0.62	0.65	1.22	0.85	0.90	0.20	4.43
¹⁶³ Dy	4.73	4.70	4.18	4.28	6.50	7.20	4.92	4.88	0.99	4.91
¹⁶⁵ Ho	0.45	0.70	0.43	0.30	1.20	1.28	0.91	0.84	0.28	3.04
¹⁶⁶ Er	1.89	1.99	0.98	1.80	2.68	2.60	2.28	2.15	0.70	3.08
¹⁶⁹ Tm	0.51	0.30	0.06	0.11	0.45	0.45	0.29	0.30	0.12	2.58
¹⁷² Yb	2.64	2.60	1.60	1.24	1.99	2.70	1.96	1.90	0.46	4.13
¹⁷⁵ Lu	0.17	0.19	0.16	0.18	0.21	0.56	0.25	0.25	0.10	2.42
¹⁷⁸ Hf	4.91	2.21	2.10	2.01	3.17	2.94	4.02	3.64	0.95	3.82
¹⁸¹ Ta	1.44	1.15	1.10	0.99	0.41	1.33	0.96	1.01	0.23	4.46
²³² Th	1.11	0.91	0.58	0.78	0.84	1.03	1.10	1.02	0.23	4.38
²³⁸ U	0.37	0.41	0.35	0.23	0.50	0.47	0.45	0.46	0.11	4.08

Continuation Table 9

<i>Standard Analyses</i>	<i>BCR</i>																	
<i>n^o</i>	<i>7</i>	<i>8</i>	<i>27</i>	<i>28</i>	<i>47</i>	<i>48</i>	<i>67</i>	<i>68</i>	<i>87</i>	<i>88</i>	<i>107</i>	<i>108</i>	<i>127</i>	<i>128</i>	<i>147</i>	<i>148</i>	<i>167</i>	<i>168</i>
⁴⁴ Ca	42662	41932	48230	47176	43562	45291	45476	45672	47284	43878	44512	44326	43579	46271	45518	44633	49331	51571
⁴⁵ Sc	31.76	32.46	32.34	31.45	32.95	34.58	32.37	28.11	30.74	31.51	33.59	32.16	31.68	29.87	33.24	33.21	37.23	35.53
⁴⁷ Ti	12982	12671	13644	13022	14253	14221	12579	11267	12104	12876	14304	13036	10727	12791	14567	14235	15882	16835
⁸⁹ Y	30.47	30.64	32.73	32.55	33.11	32.78	31.03	29.48	31.10	30.68	32.18	32.44	30.20	30.38	34.01	31.81	35.86	33.59
⁹⁰ Zr	169	167	174	178	183	176	165	164	172	174	177	165	147	148	161	232	193	186
⁹³ Nb	10.98	10.69	11.61	11.12	11.56	11.93	10.98	9.93	11.13	10.45	10.94	11.88	11.33	11.47	10.28	11.33	12.63	12.53
¹³⁷ Ba	636	628	664	660	673	683	625	608	648	633	659	649	612	632	672	671	772	733
¹³⁹ La	24.25	24.43	25.86	25.86	26.66	27.32	22.85	23.57	26.44	23.83	25.04	25.10	24.20	24.43	26.03	25.75	28.31	29.25
¹⁴⁰ Ce	49.81	50.50	52.77	52.93	54.26	51.91	50.71	49.12	52.15	48.30	53.25	52.30	49.97	51.05	53.69	51.28	61.45	59.52
¹⁴¹ Pr	6.23	6.37	6.73	6.15	6.45	6.55	6.35	6.13	6.38	6.34	6.91	5.85	5.82	6.40	6.45	6.81	8.13	6.94
¹⁴⁶ Nd	26.85	27.95	27.72	27.88	29.58	29.17	26.62	25.02	27.91	26.59	27.95	27.95	25.92	26.98	28.14	29.37	31.91	31.97
¹⁴⁷ Sm	4.81	6.52	6.68	7.22	5.12	9.34	5.31	5.47	4.77	6.55	7.15	6.77	6.67	5.60	6.67	6.30	6.62	6.87
¹⁵³ Eu	1.84	2.04	2.19	1.73	1.92	2.21	2.07	1.60	2.20	1.39	2.10	2.11	1.91	2.03	1.81	2.06	2.72	2.56
¹⁵⁷ Gd	4.07	7.36	4.72	9.12	5.89	6.60	5.94	6.85	4.94	4.39	7.43	8.52	4.57	5.34	5.67	9.70		8.84
¹⁵⁹ Tb	0.95	0.87	0.90	1.12	1.11	0.54	1.54	0.65	1.45	0.89	0.92	0.58	0.78	0.97	0.88	1.21	1.32	0.65
¹⁶³ Dy	5.93	6.32	6.25	5.18	5.97	5.40	6.33	5.98	5.02	5.80	5.51	7.35	5.96	5.73	6.72	5.27	6.68	7.08
¹⁶⁵ Ho	1.06	1.30	1.30	1.19	1.18	1.48	0.84	1.34	0.97	1.20	1.30	1.37	1.08	0.96	1.32	1.48	1.64	1.21
¹⁶⁶ Er	3.13	2.10	3.57	4.36	2.89	3.50	3.29	3.49	2.93	3.28	2.79	4.16	2.82	3.22	4.19	2.94	3.02	4.31
¹⁶⁹ Tm	0.41	0.32	0.61	0.55	0.58	0.52	0.36	0.42	0.59	0.37	0.53	0.39	0.52	0.25	0.58	0.53	0.44	0.36
¹⁷² Yb	3.35	3.06	4.27	2.84	4.33	3.19	2.72	3.28	3.04	2.42	3.22	4.85	4.01	2.33	3.01	4.16	5.14	3.61
¹⁷⁵ Lu	0.42	0.40	0.51	0.58	0.50	0.65	0.32	0.44	0.62	0.37	0.46	0.47	0.44	0.38	0.55	0.55	0.44	0.55
¹⁷⁸ Hf	4.65	3.93	4.67	4.63	5.06	4.39	4.28	4.16	3.27	4.45	5.17	5.00	3.88	4.05	4.87	5.08	4.31	5.03
¹⁸¹ Ta	0.77	0.53	0.59	0.59	0.64	0.55	0.73	0.56	1.07	0.57	0.34	0.50	0.68	0.68	0.51	0.62	0.95	0.63
²³² Th	5.43	5.12	6.46	5.63	6.97	5.39	5.30	4.97	5.54	5.54	5.93	5.63	5.43	5.27	5.31	6.63	6.31	6.47
²³⁸ U	1.76	1.54	1.70	1.76	1.92	1.52	1.93	1.39	1.62	1.44	1.92	1.77	1.64	1.74	1.66	1.72	1.98	1.97

Continuation Table 9

<i>Standard</i>	<i>BCR</i>									
<i>Analyses n°</i>	<i>187</i>	<i>188</i>	<i>207</i>	<i>208</i>	<i>227</i>	<i>228</i>	<i>BCR</i>	<i>MEAN</i>	<i>SD</i>	<i>RSD</i>
⁴⁴ Ca	39604	39494	44500	29189	57813	48498	45000	45000	5074	8.87
⁴⁵ Sc	30.12	25.12	34.90	22.25	36.67	34.18	32.00	32.00	3.34	9.59
⁴⁷ Ti	9481	10122	16303	7884	13883	14250	13080	13080	2100	6.23
⁸⁹ Y	28.39	28.56	35.08	19.60	37.58	34.14	31.60	31.60	3.39	9.32
⁹⁰ Zr	154	154	189	109	209	180	172.0	172.0	23.1	7.44
⁹³ Nb	9.69	9.55	11.51	7.12	13.11	12.67	11.10	11.10	1.25	8.87
¹³⁷ Ba	539	544	713	417	756	702	1.18	647.00	73.88	8.76
¹³⁹ La	21.15	21.68	27.44	16.16	28.52	28.28	647	25.10	2.84	8.85
¹⁴⁰ Ce	41.73	43.29	54.30	33.41	60.19	58.10	25.10	51.50	5.98	8.61
¹⁴¹ Pr	5.17	5.24	7.69	4.16	6.86	6.77	51.50	6.37	0.80	8.00
¹⁴⁶ Nd	22.79	23.73	29.25	17.37	34.15	29.63	6.37	27.60	3.32	8.32
¹⁴⁷ Sm	6.26	5.50	7.56	4.41	6.19	7.08	27.60	6.31	1.07	5.88
¹⁵³ Eu	1.20	1.33	1.66	1.46	2.69	1.98	6.31	1.95	0.39	4.94
¹⁵⁷ Gd	4.94	5.18	4.46	4.16	11.83	4.83	1.95	6.32	2.08	3.04
¹⁵⁹ Tb	0.66	1.21	0.91	0.32	1.53	1.08	6.32	0.96	0.31	3.05
¹⁶³ Dy	3.57	6.35	5.67	3.79	6.41	7.81	0.96	5.92	0.97	6.13
¹⁶⁵ Ho	0.88	1.12	1.36	0.82	1.39	1.27	5.92	1.21	0.21	5.71
¹⁶⁶ Er	3.16	2.67	5.03	1.78	3.57	2.78	1.21	3.29	0.73	4.49
¹⁶⁹ Tm	0.39	0.69	0.74	0.41	0.26	0.47	3.29	0.47	0.13	3.70
¹⁷² Yb	2.01	2.77	4.27	1.00	4.80	3.45	0.47	3.38	0.98	3.46
¹⁷⁵ Lu	0.36	0.58	0.51	0.33		0.61	3.38	0.48	0.10	5.01
¹⁷⁸ Hf	3.69	4.85	5.52	2.74	4.85	4.77	0.48	4.47	0.65	6.93
¹⁸¹ Ta	0.61	0.28	0.37	0.35	0.85	0.92	4.47	0.62	0.20	3.17
²³² Th	4.90	4.96	6.13	3.74	6.62	6.15	10.10	5.66	0.72	7.86
²³⁸ U	1.50	1.32	1.59	1.12	2.13	1.93	5.66	1.69	0.24	7.06

Continuation Table 9

*Standard NIST610**Analyses*

<i>n</i> ^o	<i>4</i>	<i>5</i>	<i>6</i>	<i>24</i>	<i>25</i>	<i>26</i>	<i>44</i>	<i>45</i>	<i>46</i>	<i>64</i>	<i>65</i>	<i>66</i>	<i>84</i>	<i>85</i>	<i>86</i>	<i>104</i>	<i>105</i>	<i>106</i>
⁴⁴ Ca	71125	73255	71805	79572	77017	73640	80636	76796	80311	80681	77718	82083	81020	79640	81390	83463	80127	80706
⁴⁵ Sc	511	525	518	521	526	506	522	500	507	470	464	477	485	481	483	473	462	478
⁴⁷ Ti	277	285	267	270	246	312	60	55	53	52	42	46	44	54	44	48	45	47
⁸⁹ Y	515	484	485	480	484	480	500	468	478	449	447	457	483	469	464	471	451	462
⁹⁰ Zr	457	476	458	469	459	442	464	442	464	414	408	410	459	463	448	461	417	430
⁹³ Nb	486	489	489	499	490	482	522	478	497	458	461	459	497	480	467	478	454	464
¹³⁷ Ba	431	452	433	443	436	430	492	442	453	408	421	406	473	469	455	497	443	446
¹³⁹ La	452	457	454	465	455	447	483	454	472	429	425	431	468	452	449	463	439	444
¹⁴⁰ Ce	499	508	486	495	495	483	496	472	490	439	453	449	499	485	479	488	460	462
¹⁴¹ Pr	525	531	508	478	487	473	497	468	474	440	431	449	472	464	454	464	440	447
¹⁴⁶ Nd	450	461	457	453	455	446	474	448	463	416	416	428	457	450	439	448	425	427
¹⁴⁷ Sm	474	491	474	464	484	483	493	450	454	426	424	438	458	453	429	442	422	436
¹⁵³ Eu	458	467	466	470	468	457	491	467	476	433	431	436	462	458	441	457	431	427
¹⁵⁷ Gd	435	460	467	459	463	459	518	482	484	450	444	460	499	512	483	513	476	461
¹⁵⁹ Tb	449	462	461	453	455	445	485	443	465	424	417	434	471	463	446	461	434	441
¹⁶³ Dy	471	475	478	470	481	480	489	461	466	430	423	437	470	472	456	464	445	455
¹⁶⁵ Ho	488	494	484	492	485	478	508	467	491	443	447	458	483	485	469	487	455	458
¹⁶⁶ Er	480	490	486	494	486	468	492	455	477	425	431	449	459	471	434	465	430	443
¹⁶⁹ Tm	459	478	471	468	471	467	495	457	476	435	440	441	473	471	451	471	454	443
¹⁷² Yb	496	495	485	506	495	474	507	473	510	438	433	452	489	471	459	469	447	448
¹⁷⁵ Lu	475	483	477	490	480	476	502	468	489	437	438	460	484	479	467	477	450	453
¹⁷⁸ Hf	431	441	438	441	440	433	452	432	448	399	399	420	409	417	416	419	388	396
¹⁸¹ Ta	520	524	525	538	518	519	548	500	506	460	464	482	508	506	488	500	473	475
²³² Th	481	486	477	492	475	480	505	466	487	436	429	447	483	484	461	476	450	457
²³⁸ U	489	503	489	506	499	499	538	496	516	464	469	471	517	501	484	493	468	472

Continuation Table 9

Standard *NIST610*

Analyses

<i>n</i> ^o	124	125	126	144	145	146	164	165	166	184	185	186	204	205	206	224	225	226
⁴⁴ Ca	86123	82933	81744	86619	82361	85867	82845	83478	84987	81908	84126	80121	63635	57609	56973	86214	83462	80735
⁴⁵ Sc	469	460	448	475	461	486	474	467	487	464	471	452	374	364	341	479	488	493
⁴⁷ Ti	314	312	284	317	308	283	289	298	337	283	322	252	171	147	153	213	202	227
⁸⁹ Y	457	454	425	471	454	472	451	449	469	439	447	432	351	345	319	450	446	451
⁹⁰ Zr	414	399	382	427	415	431	418	419	448	407	425	403	338	319	305	422	428	430
⁹³ Nb	461	449	436	482	479	483	457	450	471	448	458	435	361	353	330	460	462	468
¹³⁷ Ba	426	423	413	451	433	456	418	395	428	411	389	394	331	315	286	410	423	423
¹³⁹ La	448	435	423	463	459	469	443	430	456	420	435	419	335	327	307	428	427	434
¹⁴⁰ Ce	464	451	436	479	470	485	456	448	474	441	449	432	357	343	318	457	450	458
¹⁴¹ Pr	457	440	421	464	453	459	438	430	457	422	436	416	345	334	310	441	438	445
¹⁴⁶ Nd	431	416	405	439	436	438	420	413	437	405	414	403	331	322	301	424	423	427
¹⁴⁷ Sm	425	404	396	439	425	432	425	419	453	406	417	404	344	338	314	419	435	431
¹⁵³ Eu	437	430	404	448	449	457	428	429	447	422	428	413	347	326	312	437	427	444
¹⁵⁷ Gd	397	401	374	396	406	397	441	422	440	409	424	420	333	314	288	411	401	409
¹⁵⁹ Tb	431	421	399	442	436	439	426	420	450	408	412	401	333	319	300	429	423	429
¹⁶³ Dy	433	413	408	444	429	452	431	428	456	429	437	421	346	338	313	445	452	443
¹⁶⁵ Ho	450	434	419	451	447	456	448	449	469	432	448	428	352	346	324	456	458	457
¹⁶⁶ Er	427	418	402	441	433	431	456	444	468	424	430	418	338	328	311	435	442	441
¹⁶⁹ Tm	433	422	413	444	436	443	442	430	458	422	430	426	344	334	314	442	447	451
¹⁷² Yb	464	454	440	469	472	480	456	444	475	439	448	420	368	367	338	466	481	481
¹⁷⁵ Lu	449	441	429	457	457	467	455	447	468	426	441	433	345	335	320	448	433	448
¹⁷⁸ Hf	395	380	370	394	394	391	394	386	406	377	389	380	308	307	283	385	390	397
¹⁸¹ Ta	469	459	435	470	475	478	485	480	503	468	481	465	382	374	342	485	491	490
²³² Th	451	439	430	469	460	474	437	436	467	424	439	430	353	344	321	451	448	453
²³⁸ U	463	448	427	477	468	477	466	453	478	448	457	449	363	361	326	469	461	471

Continuation Table 9

Standard	<i>NIST 610</i>		
	<i>MEAN</i>	<i>SD</i>	<i>RSD</i>
⁴⁴ Ca	78964.6	7147.3	11.0
⁴⁵ Sc	474.0	40.9	11.6
⁴⁷ Ti	193.3	112.2	1.7
⁸⁹ Y	453.0	39.9	11.4
⁹⁰ Zr	424.2	39.2	10.8
⁹³ Nb	460.9	39.4	11.7
¹³⁷ Ba	423.7	42.9	9.9
¹³⁹ La	436.0	38.3	11.4
¹⁴⁰ Ce	458.5	41.9	10.9
¹⁴¹ Pr	447.4	44.9	10.0
¹⁴⁶ Nd	425.0	37.5	11.3
¹⁴⁷ Sm	431.1	39.5	10.9
¹⁵³ Eu	435.5	38.1	11.4
¹⁵⁷ Gd	433.5	52.7	8.2
¹⁵⁹ Tb	428.5	39.5	10.8
¹⁶³ Dy	440.0	39.0	11.3
¹⁶⁵ Ho	452.6	40.2	11.3
¹⁶⁶ Er	439.5	42.3	10.4
¹⁶⁹ Tm	440.3	38.5	11.4
¹⁷² Yb	458.5	38.1	12.0
¹⁷⁵ Lu	449.6	40.4	11.1
¹⁷⁸ Hf	398.5	37.7	10.6
¹⁸¹ Ta	480.1	42.7	11.2
²³² Th	449.9	39.8	11.3
²³⁸ U	467.7	42.8	10.9

Continuation Table 9

*Standard NIST612**Analyses*

<i>n</i> ^o	2	3	21	22	23	41	42	43	41	42	43	61	62	81	87	83	81	82
⁴⁴ Ca	82514	78215	89900	88886	82656	88011	85242	90091	86570	83847	88616	87511	81168	83447	88274	83411	84318	89196
⁴⁵ Sc	38.86	40.82	38.19	40.72	46.40	42.94	37.33	41.94	43.17	37.53	42.17	40.29	37.55	45.46	39.33	42.37	45.08	39.01
⁴⁷ Ti	54.03	23.45	104.03	39.16	24.01	56.35	62.56	31.53	11.11	12.34	6.22	10.17	8.62	1417	1417	1417	1276	1276
⁸⁹ Y	38.09	37.04	38.37	38.23	39.26	38.06	38.28	38.79	38.98	39.19	39.71	36.48	37.26	40.03	36.79	37.44	40.45	37.18
⁹⁰ Zr	35.11	38.72	31.91	35.98	35.40	35.92	38.23	35.15	35.74	38.05	34.98	31.22	38.50	40.07	32.73	35.87	42.39	34.62
⁹³ Nb	37.32	38.76	38.51	38.75	39.28	36.90	36.50	38.64	38.42	38.01	40.24	36.32	37.47	37.42	37.63	39.09	37.56	37.77
¹³⁷ Ba	40.46	34.10	37.67	35.97	37.49	39.74	40.78	36.44	42.62	43.73	39.07	38.48	38.96	30.12	35.33	32.46	32.03	37.56
¹³⁹ La	33.58	36.92	35.15	36.54	36.47	36.08	35.07	36.37	37.88	36.81	38.18	31.96	33.95	36.32	35.06	35.73	37.06	35.78
¹⁴⁰ Ce	36.29	36.91	38.87	41.47	38.31	38.10	39.30	38.13	39.20	40.44	39.23	35.64	38.12	38.63	35.95	39.17	39.68	36.93
¹⁴¹ Pr	37.27	36.68	36.59	38.11	37.18	37.17	36.48	37.98	38.97	38.25	39.82	33.96	35.80	35.72	37.38	37.34	35.90	37.57
¹⁴⁶ Nd	35.02	36.87	35.44	37.02	33.99	34.15	34.32	35.23	35.85	36.02	36.99	34.46	36.05	34.58	34.45	33.75	35.15	35.01
¹⁴⁷ Sm	38.20	35.94	35.22	37.28	38.35	37.43	31.21	41.44	37.38	31.18	41.40	35.71	35.69	39.73	34.03	39.34	39.59	33.91
¹⁵³ Eu	34.93	34.11	34.12	36.23	35.10	34.37	32.70	34.14	36.35	34.57	36.10	32.78	34.06	33.38	34.53	33.73	33.16	34.30
¹⁵⁷ Gd	35.34	33.39	39.33	40.79	38.13	30.87	36.94	41.96	34.18	40.90	46.46	40.41	39.09	29.19	32.22	32.53	30.40	33.55
¹⁵⁹ Tb	35.45	35.15	35.10	37.36	35.75	37.05	36.29	35.54	38.85	38.05	37.26	34.56	35.62	33.04	34.71	35.65	33.99	35.70
¹⁶³ Dy	34.83	35.20	35.20	39.13	34.80	37.40	36.81	35.51	38.62	38.01	36.67	33.77	37.29	33.13	36.21	34.46	33.66	36.79
¹⁶⁵ Ho	37.38	36.12	39.62	40.94	36.13	38.00	36.59	38.98	39.47	38.00	40.49	36.45	37.92	37.28	36.28	37.14	37.54	36.54
¹⁶⁶ Er	37.97	36.69	36.00	40.38	36.89	40.86	35.24	35.97	41.99	36.21	36.96	33.74	36.68	36.85	36.96	39.88	36.67	36.78
¹⁶⁹ Tm	36.67	38.53	36.41	39.77	37.57	39.13	36.25	36.50	40.95	37.94	38.20	35.16	37.43	35.88	37.21	37.89	36.24	37.58
¹⁷² Yb	41.15	39.36	41.16	43.13	40.91	35.23	37.79	41.24	36.42	39.06	42.63	36.15	41.84	41.47	40.64	42.01	41.65	40.82
¹⁷⁵ Lu	37.97	37.75	37.77	39.86	35.59	38.92	37.98	36.23	40.01	39.05	37.26	36.83	37.43	35.86	37.44	37.91	36.50	38.11
¹⁷⁸ Hf	34.96	36.47	35.22	35.57	34.99	36.14	34.40	30.68	37.80	35.98	32.09	33.32	35.91	36.21	34.87	32.32	34.95	33.66
¹⁸¹ Ta	39.48	39.62	38.22	40.68	41.13	40.85	38.78	39.70	41.66	39.55	40.49	37.25	38.97	40.20	41.21	38.97	40.55	41.57
²³² Th	37.35	38.43	37.50	38.81	34.49	38.21	37.19	36.32	39.60	38.55	37.64	37.20	37.35	35.50	35.38	36.86	36.36	36.24
²³⁸ U	36.06	37.41	36.07	41.60	35.61	36.57	37.61	37.36	38.50	39.61	39.34	36.92	35.10	35.51	36.22	36.31	35.48	36.19

Continuation Table 9

*Standard NIST612**Analyses*

<i>n</i> ^o	83	101	102	103	122	122	141	142	143	161	162	163	161	162	163	181	182	183	201
⁴⁴ Ca	84282	85700	85107	89630	79834	83086	85239	78131	78762	92507	89568	91442	88244	85440	87228	83846	86793	86722	85012
⁴⁵ Sc	42.02	41.10	37.59	43.73	38.45	38.85	36.55	38.50	42.23	42.01	42.83	46.42	39.48	40.26	43.63	42.35	40.09	41.87	42.68
⁴⁷ Ti	1275.63	5.64	6.67	<4.26	6.78	44.31	<28.32	58.36	<26.53	66.87	77.68	55.34	63.41	73.66	52.48	98.05	44.72	31.11	<23.64
⁸⁹ Y	37.83	37.45	38.74	39.15	37.02	37.69	36.44	32.99	35.35	41.50	41.53	43.11	37.94	37.97	39.41	36.03	36.50	36.35	40.29
⁹⁰ Zr	37.95	37.40	35.76	34.84	28.24	26.89	34.84	28.84	34.08	36.98	47.65	41.22	34.95	45.03	38.96	28.77	31.07	37.34	39.31
⁹³ Nb	39.23	36.31	36.33	39.75	39.96	40.72	35.86	34.03	34.33	42.04	40.24	40.54	39.05	37.39	37.66	36.41	36.75	37.85	40.43
¹³⁷ Ba	34.51	39.28	42.06	38.40	40.66	39.47	34.50	31.62	31.60	43.77	43.71	40.69	39.80	39.76	37.01	33.48	37.36	36.37	40.03
¹³⁹ La	36.45	35.09	36.33	34.86	34.68	35.73	33.06	33.25	31.67	40.81	38.55	37.32	37.39	35.31	34.19	33.35	33.46	36.04	38.25
¹⁴⁰ Ce	40.23	35.71	36.70	39.53	39.14	39.14	36.07	36.64	34.01	41.25	39.00	42.35	38.84	36.73	39.88	37.43	36.22	38.16	39.97
¹⁴¹ Pr	37.52	37.97	37.61	37.15	36.55	37.24	35.58	33.76	32.63	41.36	39.95	40.61	38.21	36.91	37.52	35.50	36.01	36.93	37.60
¹⁴⁶ Nd	34.31	35.38	36.45	36.77	33.83	34.02	33.62	32.54	32.74	38.69	37.74	37.38	35.89	35.02	34.68	33.65	33.22	34.43	37.41
¹⁴⁷ Sm	39.20	37.87	37.22	36.07	33.34	33.11	37.39	32.48	34.35	39.69	42.52	39.31	37.13	39.77	36.77	33.68	34.33	38.12	36.73
¹⁵³ Eu	33.51	35.88	36.17	33.80	34.47	34.86	31.94	32.23	31.45	38.06	37.62	35.38	35.30	34.89	32.82	32.45	32.63	35.86	35.99
¹⁵⁷ Gd	33.87	30.53	40.51	36.85	50.47	43.48	36.82	30.10	34.41	41.50	38.11	33.64	40.79	37.46	33.07	35.90	29.22	29.33	43.12
¹⁵⁹ Tb	36.67	37.50	35.03	36.05	36.78	36.00	35.37	32.17	31.78	39.68	38.09	39.37	36.31	34.85	36.02	34.93	33.83	36.46	38.08
¹⁶³ Dy	35.01	34.95	34.57	36.90	40.94	39.73	33.05	32.41	33.13	39.11	35.75	39.33	36.82	33.66	37.03	36.55	33.39	35.00	39.04
¹⁶⁵ Ho	37.41	37.86	37.98	38.95	38.97	38.12	35.76	33.75	33.78	43.27	42.38	39.75	40.00	39.17	36.74	35.51	38.38	37.41	39.90
¹⁶⁶ Er	39.68	37.15	35.79	37.05	38.98	38.66	36.66	32.79	34.29	43.29	37.81	40.09	40.89	35.71	37.87	34.30	33.44	40.21	39.07
¹⁶⁹ Tm	38.26	38.27	38.24	36.60	37.76	37.15	35.93	34.54	32.04	41.86	40.90	42.25	38.53	37.64	38.88	34.86	33.97	38.03	39.01
¹⁷² Yb	42.19	37.64	37.24	39.49	40.59	41.46	36.14	36.36	32.89	46.91	42.01	47.32	42.24	37.83	42.61	37.93	36.52	44.28	39.10
¹⁷⁵ Lu	38.58	37.91	37.41	38.21	37.39	37.24	36.44	33.43	33.42	43.94	39.72	41.73	39.80	35.98	37.81	35.49	35.37	37.67	40.68
¹⁷⁸ Hf	31.19	36.76	32.13	37.98	37.24	36.58	35.38	27.89	33.03	38.52	36.53	36.84	35.23	33.41	33.70	32.27	35.21	38.04	37.62
¹⁸¹ Ta	39.30	39.52	38.47	38.80	40.28	39.93	39.25	36.56	35.45	43.56	42.38	42.06	40.94	39.83	39.53	39.01	37.84	40.74	40.42
²³² Th	37.75	36.94	38.26	37.78	37.41	37.51	34.18	32.57	33.80	43.14	41.11	40.29	38.66	36.83	36.10	36.09	36.54	36.93	41.42
²³⁸ U	36.28	37.92	37.38	37.83	39.36	38.22	37.47	34.11	31.95	40.21	37.37	42.33	38.23	35.52	40.25	36.60	33.83	36.68	38.17

Continuation Table 9

<i>Standard Analyses n^o</i>	<i>NIST612</i>								<i>NIST612</i>		
	<i>202</i>	<i>203</i>	<i>201</i>	<i>202</i>	<i>203</i>	<i>221</i>	<i>222</i>	<i>223</i>	<i>MEAN</i>	<i>SD</i>	<i>RSD</i>
⁴⁴ Ca	82845	82194	84911	82746	82096	88015	87466	87627	85474.35	3445.35	24.81
⁴⁵ Sc	39.66	39.47	42.61	39.59	39.40	42.85	39.13	42.81	41.01	2.46	16.69
⁴⁷ Ti	40.74	26.89	28.87	28.87	19.06	<17.10	23.17	234.77	240.24	473.05	0.51
⁸⁹ Y	40.25	39.44	39.07	39.04	38.26	38.64	37.84	36.56	38.27	1.77	21.64
⁹⁰ Zr	39.03	28.09	38.47	38.20	27.49	38.99	30.85	42.29	35.87	4.56	7.86
⁹³ Nb	39.11	38.06	39.59	38.30	37.27	40.14	37.56	35.82	38.12	1.69	22.57
¹³⁷ Ba	37.11	39.25	39.30	36.43	38.53	41.11	36.14	35.05	37.78	3.37	11.22
¹³⁹ La	38.23	35.75	36.69	36.67	34.29	36.13	35.36	35.44	35.76	1.80	19.87
¹⁴⁰ Ce	40.34	37.51	39.13	39.49	36.72	38.72	39.34	36.66	38.34	1.75	21.89
¹⁴¹ Pr	37.97	37.93	36.74	37.11	37.07	37.89	37.41	36.82	37.19	1.59	23.40
¹⁴⁶ Nd	37.46	35.10	36.38	36.43	34.13	36.14	33.44	34.70	35.24	1.44	24.48
¹⁴⁷ Sm	37.96	36.23	36.56	37.78	36.06	41.19	32.87	36.27	36.82	2.72	13.54
¹⁵³ Eu	37.32	33.18	35.24	36.54	32.48	35.85	33.58	33.26	34.48	1.57	21.95
¹⁵⁷ Gd	37.29	43.24	39.55	34.20	39.65	37.27	36.06	33.65	36.79	4.82	7.64
¹⁵⁹ Tb	36.18	36.59	37.03	35.18	35.58	34.71	34.89	38.25	35.97	1.68	21.39
¹⁶³ Dy	37.95	34.08	38.46	37.39	33.57	35.78	33.59	36.89	36.03	2.12	16.99
¹⁶⁵ Ho	38.44	35.92	39.33	37.89	35.40	38.31	38.30	38.43	37.96	1.92	19.74
¹⁶⁶ Er	39.49	36.61	37.23	37.63	34.88	38.97	36.93	39.72	37.51	2.29	16.39
¹⁶⁹ Tm	40.01	37.43	38.13	39.11	36.59	37.82	36.25	37.49	37.62	1.96	19.20
¹⁷² Yb	40.68	39.40	39.76	41.37	40.08	39.33	37.92	41.24	40.07	2.85	14.06
¹⁷⁵ Lu	38.65	38.39	38.96	37.01	36.76	37.86	38.15	37.65	37.78	1.88	20.07
¹⁷⁸ Hf	36.34	31.75	36.64	35.40	30.93	35.47	35.33	35.36	34.85	2.28	15.30
¹⁸¹ Ta	41.20	38.47	39.10	39.86	37.21	40.39	41.11	41.52	39.81	1.56	25.52
²³² Th	37.77	35.25	40.67	37.08	34.62	38.31	36.15	37.07	37.32	2.03	18.40
²³⁸ U	38.84	36.78	37.24	37.90	35.88	37.65	38.12	36.26	37.24	1.93	19.32

APPENDIX C

Abstract to conferences

List of contributions

- I. Narduzzi F., Farina F., Stevens G., Lana C., Nalini Jr. H.A. (2015). Magmatic garnets in Cordilleran-type granitoids: evidence for crystallization in the lower crust. The 8th Hutton Symposium on Granites and Related rocks 2015, Florianópolis, Brazil. (presentation and poster)
- II. Narduzzi F., Farina F., Stevens G., Teixeira L., Lana C., Nalini Jr. H.A. (2016). From high (> 0.8 GPa) to low (ca. 0.5 GPa) pressure crystallization: evidence from the grossular-rich magmatic garnets of the Galiléia batholith, Brazil. 48^o Congresso Brasileiro de Geologia 2016, Porto Alegre, Brazil. (presentation).
- III. Narduzzi F., Farina F., Lana C., Stevens G., Alkmim A., Nalini Jr. H.A. (2017). Extreme U-Pb zircon age variability in the lower crustal Galiléia Batholith (SE Brazil). Goldschmidt 2017, Paris. (presentation).



Florianoópolis, Brazil, September 20-25th, 2015

The 8th Hutton Symposium on Granites and Related Rocks

PT.054

Magmatic garnets in Cordilleran-type granitoids: evidence for crystallization in the lower crust.

Narduzzi F¹, Farina F¹, Stevens G², Lana C¹, Nalini Jr HA¹ - ¹Universidade Federal De Ouro Preto - Departamento de Geologia, ²Stellenbosch University - Department of Earth Sciences

The Galiléia batholith (ca. 30000 km²), located in the westernmost part of the Araçuaí Orogen (Brazil), is a Neoproterozoic (600 – 575 Ma) weakly to moderately foliated calc-alkaline metaluminous (ASI 0.97 – 1.07) granite characterized by the widespread occurrence of both garnet and epidote. Garnets form 1 to 6 mm diameter skeletal and euhedral crystals, and although absent in some rocks, they are widespread in the host granite reaching up to 5 %. Occasionally they occur in the mafic enclaves as well. The lack of a pervasive well-defined foliation in the rock, the occurrence of garnet inclusions hosted within cm-sized alkali-feldspar in porphyric phases of the batholith, as well as the fact that mineral inclusions in garnet constitutes the same assemblage that occurs in the matrix of the granite, supports a magmatic origin for these crystals. In addition, a variety of resorption textures indicates that garnet crystals experienced periods of disequilibrium with the granitic melt. Garnets are exceptionally high in grossular (24 - 43 mol %) and spessartine (9 - 19 mol %), very low in pyrope (< 7 mol %), and are unzoned. Moreover, grossular content does not vary with respect to CaO, Y_N and (La/Yb)_N whole rock variability. Other minerals are reabsorbed epidotes usually rimming allanites, and having low (9 – 23 mol %) Ps ([Pistacite: Fe³⁺/(Fe³⁺+Al)*100]) content, rare zoisite (FeO_{tot} < 2 wt %) inclusions in garnets and white micas, chemically similar to low Si-phengites (Si ≈ 3.2 a.f.u.). As revealed by the experiments on metaluminous systems, the presence of garnet+epidote/zoisite+white mica supports granite crystallization above 0.8 GPa. Considering this high-pressure mineralogical assemblage, combined with pressure estimates for the metamorphism of the intruded metasedimentary rock (medium amphibolite-facies, ca. 0.6 GPa), we propose a “two-stage crystallization model” for the Galiléia granitoids. Firstly, they started crystallizing in the lower crust, in an already thickened continental crust, at possibly 0.8 – 1.0 GPa (ca. 24 - 30 km), according to white mica geobarometry. Then, in agreement with resorbed garnets and pressure estimates from the country rocks, the granite reach the depth of final emplacement at 0.6 – 0.7 GPa. Furthermore, since epidotes are a last-stage phase and their resorbed textures are similar to experiments for epidote dissolution kinetics in granitic magmas, this may suggest that this last step was fast (< 10³ years), enough also for garnet preservation. Where garnets lack, different and plausible slow intrusion rates are supposedly involved. Finally, the most striking characteristic of the Galiléia garnets is their high-grossular content. Geochemically, they are similar if not identical to other magmatic garnets reported from small metaluminous granitic bodies in Alaska and China. Here, we have the great and quite rare possibility to study these high-grossular magmatic garnets and in turn, their metaluminous granitoid hosts, that until now have never been studied in detail.

The authors acknowledge support from FAPEMIG (apoio a participacao em eventos) and CNPq.

FROM HIGH (> 0.8 GPa) TO LOW (CA. 0.5 GPa) PRESSURE CRYSTALLIZATION: EVIDENCE FROM THE GROSSULAR-RICH MAGMATIC GARNETS OF THE GALILÉIA BATHOLITH, BRAZIL

Narduzzi, F.^{1,3}; Farina, F.^{1,2}; Stevens, G.^{1,3}; Teixeira, L.^{1,3}; Lana, C.¹; Nalini, Jr. H.A.¹

¹Universidade Federal de Ouro Preto (Brazil); ²University of Geneva (Switzerland); ³University of Stellenbosch (South Africa)

In S-type magma generation, the incongruent melting of mica-bearing metasediments produces peraluminous melts, which are in equilibrium with Al-rich minerals such as garnet. Consequently, when S-type granites are sufficiently femic, either cordierite or garnet crystallize in addition to biotite. In contrast, incongruent melting of intermediate rocks to form I-type granites, produces peritectic clinopyroxene and a less peraluminous melt. Such magmas crystallize hornblende and/or pyroxene in addition to biotite. In such rocks, garnet crystallization is very rare and of special petrogenetic significance. The Neoproterozoic (630 – 575 Ma) Galiléia batholith (ca. 30000 km²), located in the Araçuaí Orogen, is a weakly to moderately foliated calc-alkaline Cordilleran-type granitic body, hosting mafic enclaves up to 4 - 5 m², and displaying SiO₂ and CaO contents between 62 to 72 wt% and 2.8 to 6.1 wt%, respectively. Despite its weakly peraluminous to metaluminous (ASI 0.97 – 1.07) character and the presence of hornblende, the batholith is characterized by the widespread occurrence of garnet (grossular 25 – 43 mol%) and epidote. Garnet forms euhedral and anhedral crystals up to 6 mm across. Three main lines of evidence suggest a magmatic origin for these crystals: i) presence of garnet inclusions in sub-idiomorphic alkali-feldspar crystals in undeformed granites, ii) the occurrence of mineral inclusions in garnet which match the matrix minerals in the sample; iii) the widespread garnet distribution irrespective of the degree of matrix deformation. Furthermore, garnet does not appear to be inherited from the source or wall rock, because the Galiléia rocks and garnet-free Cordilleran-type granites have similar Σ HREE content, both ranging from ca. 1 to 10 ppm. Epidote inclusions in garnet have the same Pistacite content (9 – 23 mol %) as matrix epidote. Likewise, low Si-phengite-like white mica inclusions (Si \approx 3.2 a.f.u.) show similar petrographic and chemical features with white mica in the matrix. Overall, this suggest that these minerals are also magmatic. Crystallization experiments on calc-alkaline metaluminous systems show that grossular-rich garnets are indicative of high pressures (> 0.8 GPa). The coexistence with other high pressure minerals such as epidote, white mica, as well as the rare occurrence of zoisite (FeO_{tot} < 2 wt %), as inclusions in garnet suggest that the Galiléia granitoids started crystallizing in the lower crust at ca. 30 km depth. Plagioclase + quartz coronas around garnet indicate that garnet was in disequilibrium during the evolution of the magmatic system, suggesting a two stage emplacement history for the batholith: the first one took place at 0.8 – 1.0 GPa, followed by a second crystallization stage at pressure of ca. 0.5 GPa, and temperature < 700 °C. These last P-T conditions are recorded by the host metasediments. The Galiléia grossular-rich garnets have higher CaO content than the experimental garnet referred above and have compositions similar to some metamorphic and/or peritectic garnets from ultra-high pressure (> 1.5 GPa) rocks. This suggests that during the Galiléia granitoid genesis, the Araçuaí orogen was already over-thickened favouring a continental-continental collision setting, instead of oceanic subduction.

KEY WORDS: GROSSULAR-RICH MAGMATIC GARNETS; GALILÉIA METALUMINOUS GRANITOIDES; ARAÇUAÍ OROGEN

Goldschmidt2017 Abstract

Extreme U-Pb zircon age variability in the lower crustal Galiléia Batholith (SE Brazil)

F. NARDUZZI¹*, F. FARINA², C. LANA¹, G. STEVENS³, A.
ALKMIM¹, H.A.JR. NALINI¹

¹Applied Isotope Research Group, Ouro Preto Univ., Minas
Gerais, Brazil (*narduzzi13@gmail.com)

²Department of Earth Sci, Geneva Univ., Switzerland

³Centre for Crustal Petrology, Stellenbosch Univ., South
Africa

The garnet-epidote-bearing cordilleran-type Galiléia Batholith (30000 km²) appears to have been assembled in the lower crust (> 0.8 GPa) between ca. 630 and ca. 570 Ma [1]. New U-Pb zircon LA-ICP-MS dating on metaluminous to peraluminous granitoids from the batholith disclose an intriguingly long potential crystallization history, that is consistent with the proposed >10kbar crystallisation indicated by the mineralogy and mineral chemistry of the rocks [1]. In most cases, the scatter of U-Pb zircon dates from a single sample cannot be explained by analytical uncertainties alone, yielding weighted mean dates with considerable over-dispersion (MSWD >> 1). In individual samples, the ages of oscillatory zoned, magmatic zircon, appears to record between ca. 20 to 50 Myrs of crystallisation suggesting extremely protracted zircon crystallisation. Hf isotopic compositions of the same zircon crystals show negative values, with ϵ_{Hf} from -6 up to -16, and scattered behaviour, varying from 4 up to 10 ϵ_{Hf} units per sample. Zircon ages and ϵ_{Hf} are correlated, with ϵ_{Hf} decreasing in young crystals, while zircon Th/U ratios appear to increase through time. The rare occurrence of dissolution textures in zircon suggest that the magma was kept near Zr-saturation for ca. 50 Myr. Collectively, these data suggest that the Galiléia batholith was incrementally assembled over an extended period of time in a magmatic system that became progressively less radiogenic in Hf and enriched in Th. Overall, this might have been assisted by the fact that the Galiléia Batholith was emplaced in the lower crust, as indicated by the coexistence of garnet, epidote and phengite in some samples.

[1] Narduzzi *et al.* (2017) *Lithos* 282-283, 82-97. FN acknowledge CNPQ, FAPEMIG and PROPP-UFOP financial support.